Eddy Circulation, Heat and Salt Balances, and Ocean Metabolism: Observations from a Seaglider-Mooring Array at Ocean Station Papa

Noel Adolfson Pelland

A dissertation submitted in partial fulfillment of the
requirements for the degree of

Doctor of Philosophy

University of Washington

2015

Reading Committee:

Charles C. Eriksen, Chair

Meghan F. Cronin

Craig M. Lee

Steven R. Emerson

Program Authorized to Offer Degree:
School of Oceanography

University of Washington

Abstract

Eddy Circulation, Heat and Salt Balances, and Ocean Metabolism: Observations from a Seaglider-Mooring Array at Ocean Station Papa

Noel Adolfson Pelland

Chair of the Supervisory Committee:
Professor Charles C. Eriksen
School of Oceanography

Seagliders were deployed at Ocean Station Papa (OSP; 50°N, 145°W) in the southern Gulf of Alaska, augmenting a NOAA Ocean Climate Stations surface fluxes mooring and subsurface ADCP, from 8 June 2008 to 21 January 2010. Seagliders provided increased resolution of the three-dimensional temperature, salinity, and dissolved oxygen field surrounding the mooring, resolving horizontal gradients at scales relevant to local advection. This thesis concerns the analysis and interpretation of results from this time series, with application to 1) observations of eddy circulation unusual in comparison to typical conditions at OSP, 2) quantitative analysis of the temperature and salinity balances in the upper 200 m using least-squares methods, and 3) diagnosis of the balance of kinematics and net metabolism in the balance of dissolved oxygen. Geostrophic velocities estimated using Seaglider were moderate and poleward during 2008 before rotating counterclockwise and weakening in early 2009. Coinciding with the chance in horizontal circulation were observations of strong horizontal water mass gradients, downward isopycnal displacements, and vertical finestructure circumstantially consistent with subsurface thermohaline fronts. A likely explanation is the presence of a mesoscale anticylonic eddy; oxygen characteristics in the permanent pycnocline suggest that this feature originated to the south or west of OSP. A least-squares method was used to determine the velocity and diffusivity that best explained the integrated temperature and

salinity balances. The least-squares solution velocity and diffusivity elements were in good agreement with *a priori* estimates or, in the case of diffusivity, with general expectations about the vertical structure and magnitude of turbulent mixing coefficients in the upper ocean. Using the solution elements, the vertically- and temporally-integrated heat and salt balances were closed with mean square error that was a small fraction of the total variance. In the top 120 m, the surface heat input was balanced by cooling due to vertical advection; the resulting excess of salt was removed by horizontal advection. This combination of terms is contrary to the climatological concept of flow at OSP. The oxygen budget had similar character to the temperature budget shallower than 100 m and the salinity budget at greater depths. Horizontal advection was unimportant in the oxygen budget in the surface layer, but was a leading term deeper. Robust estimates of respiration were formed in the region deeper than the surface layer and shallower than the permanent pycnocline, giving a net apparent oxygen utilization of $\sim$1.2 mol O_2 m^{-2} yr^{-1} (0.8 mol C m^{-2} yr^{-1}). Given previously estimated rates of net community productivity of C in the surface layer in summer, this rate indicates that 30-50% of the organic carbon produced there during each growing season is respired before it can reach the deep ocean.

TABLE OF CONTENTS

LIST OF FIGURES

Figure Number Page

LIST OF TABLES

ACKNOWLEDGMENTS

This work would not be possible without the generous support of the National Science Foundation through grants OCE-0628663 and OCE-1129090, which funded Seaglider observations at Ocean Station Papa and my analyses of these data.

I am indebted to the work of the NOAA Pacific Marine Environmental Laboratory Ocean Climate Stations group, including Keith Ronnholm and Jennifer Keene, for their deployment and maintenance of the Papa surface mooring and their assistance in Seaglider operations.

I want to thank Marie Robert for her leadership of the Fisheries and Oceans Canada Line P program, which has made this series of observations possible, and for her convening and nurturing of the invaluable annual Line P meeting.

Seth Bushinsky and Chuck Stump assisted in Seaglider deployments at Papa and I am most grateful for their efforts. I would also like to thank the officers and crew of the CCGS *John P. Tully* and R/V *Thomas G. Thompson* for their professionalism and capability in handling Seaglider operations while on station.

Matthew Alford, Jody Klymak, and John Mickett helpfully provided the acoustic Doppler current profiler data used in this thesis, and I am grateful for their willingness to share the data and to John Mickett for taking extra time to discuss the processing and data quality of this instrument.

Thanks also to the technicians and students of the Emerson (University of Washington) and Hamme (University of Victoria) research groups who performed oxygen measurements at Station Papa and generously provided their results for use in this study.

Discussions with several colleagues at the Line P and Station P science meetings, and here at the University of Washington, were immensely helpful in improving my understanding

of the dynamics and history of study of the Gulf of Alaska, and for refining the research directions and questions addressed in this thesis. Particular thanks go to Bill Crawford, Patrick Cummins, Jody Klymak, Christina Schallenberg, Frank Whitney, Seth Bushinsky, Andrea Fassbender, Hilary Palevsky, Eric D'Asaro, and Ramsey Harcourt.

During my time at the University of Washington, I have sincerely appreciated the very capable School of Oceanography administrative staff, who have always been patient, eager to answer questions, helpful, and generally extremely good at their jobs in all of my encounters with them. In particular, I want to thank Su Tipple, Kittie Tucker, and Chantavy Manikham, though there are many others. I would also like to single out Michelle Townsend and Luanne Thompson, first for their guidance and help, but also for creating such a positive impression of the program as the first two people I met when investigating potential graduate schools.

I have watched with admiration and great appreciation as Kirk O'Donnell, Bill Fredericks, and Jim Bennett have deployed, maintained, and operated gliders throughout my career as a graduate student at the University of Washington, including those participating in the field campaign described in this thesis. Beyond their acumen as engineers and glider operators, they have all been excellent mentors and friends, willing to take me under their wing during field operations or glider piloting, and I greatly appreciate all that they have done for me and for Seaglider operations at the University during my time there.

My committee has played an enormous role in supporting and encouraging me, providing feedback and constructive criticism, and in general, greatly contributing to my growth as a scientist during my time at the University of Washington. I thank Steve Riser for his thoughtful questions, his interest in my career, and his support for me that has been unwavering since he first met me as a prospective student. I thank Craig Lee for his invaluable advice regarding glider sampling and for always being willing to take time for a meeting or to give his thoughts on career choices. Steve Emerson has played an important role in encouraging me to always strive for a greater understanding of other disciplines in oceanography,

and helped me start this project through his reading and criticism of the initial proposal. Chris Bretherton has been an excellent addition through his incisive questions and healthy skepticism. In particular, I would like to thank Jeremy Sterling and Meghan Cronin, who for extended periods of my graduate studies, have devoted amounts of time, energy, and mentorship to my work that would ordinarily only be reserved for someone in an advisory role. I have enjoyed greatly my times spent in conversation with them about science topics or otherwise and look forward to working with them in the future, hopefully for years to come.

Thanks to my advisor, Charlie Eriksen, for his mentorship, advice, his openness to my ideas, and for his willingness to trust me to take on a project such as this one and make it truly my own. I value our working relationship, his mentorship and friendship, and his dry sense of humor. I remember fondly sitting in his office as a prospective student and hearing him describe the Washington coast Seaglider time series that would go on to become the first project that I worked on as a graduate student. It was perhaps the first moment I could easily point to as one in which I experienced that rare excitement of peering into the unknown, which has hooked me on ocean science and kept me coming back. I have heard it said that "one cannot break down the door into science, one must be handed the keys." Thanks to Charlie for handing me the keys and giving me my entrance to the world of oceanography.

Finally, there are not enough words to express my gratitude to my friends and colleagues in oceanography, who continue to challenge and inspire me, in addition to being great friends. Among many others, thanks to Andrea Fassbender and Kirsten Feifel for long, enjoyable discussions. Thanks to Seth Bushinsky for our many adventures and a healthy dose of office commiseration whenever it was needed. Thanks to my longtime officemates and friends Sally Warner and Tom Connolly who, in addition to being terrific people, are superlative scientists that I have always looked up to. And of course, thanks to my great friend Nick Beaird, for

looking out for me, and for making it a pleasure just to come to the office every day.

DEDICATION

This thesis is dedicated to those who have raised me and instilled in me the qualities that have helped me complete this thesis and succeed during my time at the University of Washington: my family. I owe them everything for teaching me the necessity of hard work, the satisfaction that comes with a job well done, the value of being a good communicator, and so much else. To state simply that they have supported me through the difficult times during my graduate studies would be the gravest understatement. It suffices to say that I do not know where I would be without them. Thanks to Lynnda, Brooke and Rob, Sophie and Nick, Lisa and Morgan, Alec and Porter, my sister Micaela, and my amazing parents Bob and Molly. This thesis is dedicated to them.

Chapter 1

INTRODUCTION AND BACKGROUND

The region of the North Pacific Ocean surrounding the southern Gulf of Alaska and west coast of North America features marked cross-shore heterogeneity in the character of the surface circulation, atmospheric forcing, and freshwater input to the surface ocean. Along the west coast of North America, alongshore wind stress creates a complex and seasonally-varying set of boundary currents, resulting in increased mesoscale kinetic energy (KE) within the coastal transition zone near the continental margin [158, 100]. Baroclinic instabilities and interactions with topography extract kinetic and potential energy from these flows, generating eddies that either radiate westward into the interior of the subarctic or subtropical gyres or become embedded within the strong coastal currents, moving meridionally along the boundary [172, 23, 97]. Within the Gulf of Alaska, along the British Columbia and Alaska coasts, these vortices and meanders promote biological activity by stirring shelf and basin waters in which primary productivity is limited by different nutrients, or by creating a retentive ecosystem that persists within the center of isolated vortices for many months or longer [23]. Within the northern California Current System, off the Washington coast, eddies are one prominent mechanism for the western spread of warm, saline water carried northward by the California Undercurrent into the relatively cool and fresh interior region [123]. Near the coast in both regions, freshwater outflow from coastal rivers acts to stabilize the upper water column, and winter winds are less intense, leading to reduced winter mixed layer depths in the near-coastal region in comparison to the interior [92, 76]. North of Vancouver Island, upwelling winds become less prominent in the seasonal cycle, transitioning to the downwelling-dominated region in the Gulf of Alaska [157]. Despite the fundamental difference in alongshore wind stress forcing, both the boundary region between the subtropics

and subarctic along the Washington and British Columbia Coast and the eastern Gulf of Alaska support diverse and productive ecosystems [18, 172].

In contrast to the energetic coastal region, the weak and poorly rectified interior circulation of the North Pacific Current (NPC) features much lower KE values [158, 11]. The mean interior flow is dominated by the eastward-flowing North Pacific Current (NPC) that bifurcates as it reaches the continent, such that a portion of these waters turns northward to join the Alaska Current, the poleward eastern boundary current of the cyclonic Alaska Gyre, while another portion travels south, linking to the equatorward-flowing California Current, the eastern boundary current of the subtropical North Pacific Gyre. Alterations in wind stress forcing influence the strength of this circulation, orientation of the NPC, latitude of its bifurcation, and the relative proportion of waters entering the subtropical or subpolar gyre [59, 22, 28]. Horizontal gradients are weak in the interior and surface or subsurface fronts are uncommon. Eddy KE is at a minimum near the center of the Gulf of Alaska, within the North Pacific "Eddy Desert" [11, 19], but shows a seasonal cycle that may reflect a consistent seasonal input of eddy energy from the eastern boundary of the Gulf of Alaska [11, 156]. At interannual or decadal time scales, temperature anomalies near the gyre interior correlate with major North Pacific climate indices (*e.g.*, the Pacific Decadal Oscillation [PDO; 99], or El Niño-Southern Oscillation [ENSO; 126]) and appear to result from anomalous air-sea interaction within the interior of the gyre, with temperature anomalies propagating towards shore over a period of years [22].

These two contrasting subregions of the NPC bifurcation zone are linked by a set of oceanographic stations that extends through both coastal and interior waters, known as the Line P program, which is currently administered in a cooperation between the Canada Department of Fisheries and Oceans and the Canadian Coast Guard [56]. Established following World War II, Line P has seen regular oceanographic sampling from 1956 to the present day. The array of stations in Line P extends from the entrance to the Strait of Juan de Fuca on its eastern (inshore) edge, to station P26, also known as Ocean Station Papa (OSP; 50°N, 145°W), 1400 km from shore on its western edge. The annual cycle and typical proper-

ties along Line P have been well-documented [173]. On average, temperature gradients at mid-depth are everywhere eastward, reflecting the transition between cool, fresh subarctic water and warm, saline continental slope water. At the surface along Line P, poleward cross-track flow is dominant along the western portion, reflecting the eastern limb of the Gulf of Alaska gyre, while inshore of ∼250 km, seasonal variations are apparent, with the northward-flowing Davidson Current in November-April and the equatorward shelf-break jet present in May-September [173].

A Seaglider transect along Line P in January-April 2010 illustrates the differences in hydrography and character of the mesoscale circulation between the inshore and offshore regions (Fig. 1.1). As will be described in Chapter 2, Seagliders navigate through the water while performing a series of dive-climb cycles from 0-1000 m depth; it is possible to obtain an estimate of the average current sampled by the vehicle during each cycle, which is plotted in the top panel of Figure 1.1. This depth-averaged current can be used to provide a reference velocity for relative cross-track geostrophic velocities, which are contoured in gray and white in the lower panel of Figure 1.1, along with density (magenta contours) and "spice" [55] (background colors), which is approximately equal to the temperature or salinity anomaly along an isopycnal. Seaglider 144's crossing shows elevated energy in both the depth-averaged currents and the cross-track component of current, with the strength of currents increasing steadily towards shore inshore of about 800 km west of P1. Numerous eddies are evident, including a mesoscale anticyclone centered at ∼600 km from P1, and spice is observed to increase towards shore across a series of subsurface fronts. In comparison, the region near OSP is much more quiescent, with a dimished influence of coastal water at depth.

In recent years, time series of Seaglider measurements have provided important insight into physical and biological processes within the inshore portion of the domain discussed here. Seagliders sampling within the coastal transition zone (0-200 km from the continental shelf break) during 2003-09 have given important insight regarding the frequency and characteristics of coastal eddies, the seasonal appearance of the subsurface chlorophyll maximum, and relationships between seasonal structure of the upper ocean and foraging behavior of

top-level predators [125, 123, 124]. In 2008, a second time series was initiated at the opposite end of Line P: beginning June 2008 and extending into January 2010 (immediately prior to the Line P section shown in Fig. 1.1), three Seaglider missions were carried out at OSP, augmenting the array of moored sensors deployed there, first and foremost by sampling horizontal gradients at the scale relevant to local advection. The motivation for these deployments was to increase the resolution and understanding of heat and freshwater budgets at OSP, with a secondary goal of investigating the cycling of dissolved oxygen in the upper ocean and the role of horizontal advection in this tracer. This thesis concerns the analysis and interpretation of this Seaglider time series at OSP with the above goals in mind over the course of three chapters.

1.1 Overview of Research

Chapter 2 describes the equipment present at OSP and data collection methods employed during the course of the Seaglider surveys, and gives details regarding the methods for estimating horizontal gradients in scalar variables in monthly intervals. This chapter gives an overview of the observed geostrophic circulation, including comparisons to the concurrently-deployed acoustic Doppler current profiler instrument. Both absolute velocity and vertical shear are found to be in good agreement, confirming the ability of the Seaglider surveys to reliably estimate horizontal gradients and 0-1000 m depth-average current in the survey configuration in this study. This chapter provides evidence for the presence of a mesoscale eddy at OSP, which is consistent with the presence of anomalous (westward) circulation, strong water mass gradients that differ greatly from those estimated from a climatology, circumstantial evidence of horizontal intrusions typical of subsurface thermohaline fronts, and downward isopycnal displacements that are anomalous in comparison to the full oceanographic record at OSP. The possible origins of this feature are also discussed.

Chapter 3 quantitatively investigates the heat and salinity balances in the upper 200 m of the water column using a least-squares method that is designed to find the three-dimensional circulation and vertical diffusivity that minimizes the error in the integrated balances. This

chapter describes the implementation of this method in detail, and examines the accuracy of the solution and the agreement between the solution elements and prior estimates of horizontal circulation or known vertical structure of turbulent diffusivity. The diffusivity is shown to have a consistent structure month-to-month, with a rapid increase in diffusivity above the depth of maximum stratification in each month. The solution reproduces seasonal variability in the temperature and salinity records and closes the vertically-integrated budgets of each variable with small errors when integrated over the top 120 m or the depth range 120-200 m. During the Seaglider surveys, the net input of heat from the atmosphere to the ocean is offset by upwelling of cool water, and the corresponding excess of salt is removed by horizontal advection in the top 120 m. This is contrary to the typical concept of circulation at OSP in which the salinity balance is mainly in the vertical and seasonal horizontal advection cools the top 120 m [147, 84].

In Chapter 4, the three-dimensional circulation and vertical diffusivity from Chapter 3 is applied to the balance of dissolved oxygen throughout the upper 200 m. It is shown that, unlike temperature or salinity, the budget of dissolved oxygen has large terms in both the halocline/permanent pycnocline (like salinity) and also the surface layer and upper transition layer (like temperature). The most important result of this chapter is the estimation of respiration deeper than the surface layer but shallower than the permanent pycnocline. This respiration represents organic carbon that leaves the surface layer but not the upper ocean over an annual cycle, and thus in future studies considering only the SL, a correction must be applied to account for this. This Chapter furthermore investigates the kinematics of dissolved oxygen in the top 120 m, finding that while horizontal advection is not particularly important in the surface layer, it becomes a leading term deeper than the surface layer. Its measurement is likely important for future top 120 m annual net community production estimates, although the presence of an infrequent eddy may mean the estimates of horizontal advection computed here are not representative of climatology.

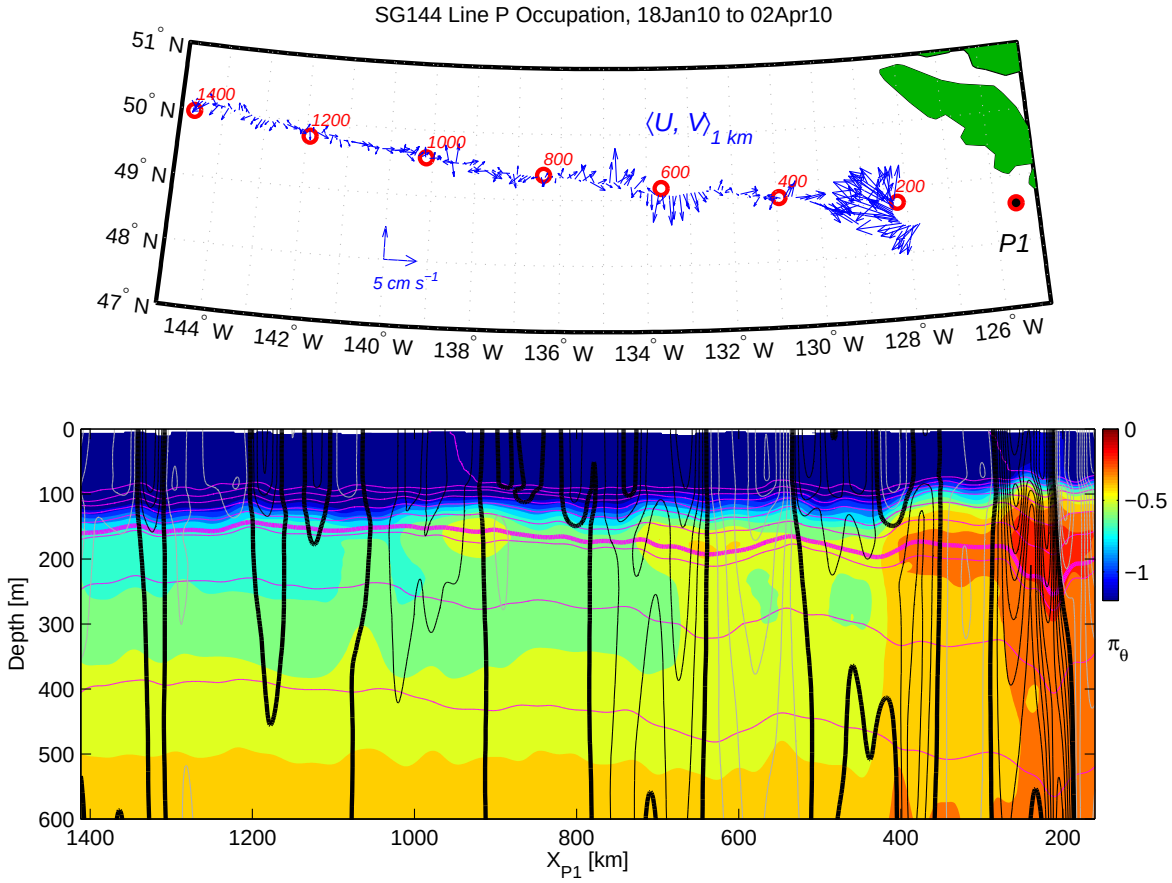

Figure 1.1: Seaglider 144 (SG144) transect along Line P, 21 January-2 April 2010. Seaglider 144 began at Ocean Station Papa (50°N, 145°W) and proceeded to the east before recovery near 128°W. Top panel shows plan view of Line P, with farthest inshore station (P1) labeled at left, and markers placed along Line P every 200 km offshore from P1. Blue vectors indicate 0-1000 m depth-averaged current reported by SG144 on each of its dive-climb cycles (scale at lower left). Lower panel shows density contours (magenta), estimated cross-track geostrophic circulation (black indicates poleward, gray equatorward, 2 cm s^{-1} contour interval), and "spice" π_θ [55] (colors, scale at right) versus depth and distance west from station P1 (X_{P1}).

Chapter 2

EDDY CIRCULATION, WATER MASS PROPERTIES, AND VERTICAL FINESTRUCTURE

with Charles C. Eriksen, Meghan F. Cronin, Steven R. Emerson

2.1 Introduction

The southern Gulf of Alaska in the Northeast Pacific Ocean is the site of one of the longest and highest-quality records of open ocean measurements in the world, the Ocean Station Papa (OSP) time series [50°N, 145°W; 56]. Ocean Station Papa lies at the southern edge of the cyclonic Gulf of Alaska (GOA) gyre (Fig. 2.1), which is bounded to the east by the North American coast, to the north and west by the coast of Alaska, and to the south by the broad, eastward-flowing Subarctic Current/North Pacific Current that forms the boundary between the GOA and the adjacent anticyclonic subtropical Northeast Pacific gyre [173, 59]. The GOA is characterized by a moderately strong, perennially poleward eastern boundary current (the Alaska Current), an intense and highly rectified western boundary current that runs southwestward along the southern Aleutian slope (the Alaska Stream), and weak velocity and mesoscale energy within the interior of the gyre [154, 158, 119]. Despite the weak interior currents, mesoscale eddies and meanders are still ubiquitous, and the ratio of eddy kinetic energy to mean kinetic energy in the eastern GOA is comparable to other regions in the North Pacific Ocean [158, 119]. The most prominent of these eddies are formed largely from instabilities or flow-topography interaction along the North American continental margin, and transport coastal water and associated nutrient, heat, and freshwater signatures seaward [158, 22, 19, 123, 97]. The southern GOA is characterized by mean positive wind stress curl, net surface heat flux into the upper ocean on the order of 30 W m^{-2} [147, 84], and net

moisture flux into the ocean (precipitation minus evaporation) of $\sim$1 m yr^{-1}, similar to much of the subarctic North Pacific [136]. Both the surface wind stress and net heat flux have strong seasonal cycles: in the summer, downward heat flux and weak surface wind stress prevail, while strong storms are more common in the fall and winter, and weak surface heat loss is characteristic of the months November-March [84, 173].

From the mid-1950s onward, several ships of the Canadian Coast Guard, overseen by the Institute of Ocean Sciences (IOS; later part of Department of Fisheries and Oceans [DFO] Canada) occupied the OSP site through the Canadian Weathership program nearly continuously until 1981, collecting atmospheric and oceanographic measurements in addition to providing search-and-rescue and communications functions to passing ships and transcontinental airliners. Since 1981, when the weathership program was discontinued, IOS, DFO Canada, and the Canadian Coast Guard have partnered to regularly revisit the OSP site, making several visits per year as part of occupations of Line P, a set of oceanographic stations established between the Strait of Juan de Fuca entrance and OSP. Today, the CCGS *John P. Tully* visits OSP three times annually (early summer, late summer, and winter when conditions allow; `http://www.pac.dfo-mpo.gc.ca/science/oceans/data-donnees/line-p/index-eng.html`).

The weak circulation at OSP, combined with the extensive duration and quality of its oceanographic record, have made it an attractive natural laboratory for the study of boundary layer dynamics, transfer of kinetic energy between atmosphere and ocean in mid-latitudes, surface gas exchange, and the biological carbon pump. Observational studies at OSP or in nearby locations have paid particular attention to short-term, storm-induced changes in sea surface temperature (SST), mixed-layer depth (MLD), and potential energy, wind work on the upper ocean and generation of near-inertial waves, and wind-driven mixing in the stratified transition region immediately deeper than the mixed layer [*e.g.,* 34, 35, 87, 118, 85, 32, 38, 2]. The years of shipboard measurements have also well-characterized the annual cycle at OSP [147, 84, 173], which has made it an important location for development and testing of one-dimensional numerical models, and their ability to

replicate the seasonal cycle of upper-ocean structure based on atmospheric inputs of heat, freshwater, and momentum [36, 35, 102, 61, 7, 86, 84, 105, 76, 155]. In parallel, advances in understanding of the boundary layer at OSP have allowed investigators to study the annual cycles of dissolved gases or nutrients in the subarctic surface ocean; through greater understanding of the physical influence on the evolution of these variables it is possible to isolate the biological contribution, which can be related to the net biologically-driven export of carbon from the surface ocean. Studies of net community production at OSP have utilized budgets of biologically active and inert dissolved gases [39, 40, 42], measurements of nitrate drawdown [178], isotopic methods reflecting particulate export from the surface ocean [17], ocean carbon dioxide [7], and coupled physical-biological models [152, 105].

Like other ocean time series sites, OSP has also been a testbed and proving ground for new ocean vessels, technologies or observing strategies. In the 1960s, the Canadian Coast Guard commissioned two vessels specifically designed, built, and outfitted for the scientific, communications, and search-and-rescue work required of Weatherships at OSP, the CCGS *Vancouver* and CCGS *Quadra* [6]. Later, OSP saw some of the first use of Climate Air-Sea Interaction Drifting (CASID) buoys, deployed during the Storm Transfer and Response [87] and Ocean Storms Experiments [85], and and the deployment and validation of several types of drifters during Ocean Storms and the World Ocean Circulation Experiment (WOCE) Heavy Weather component in 1989 to test drifter survival in difficult weather conditions [166]. The Gulf of Alaska was also the first region to reach the target density for the Argo array of autonomous profiling floats in 2003 [59, 58]. Continuing this progression, beginning in June 2007 OSP has been the site of a well-instrumented NOAA surface mooring, originally deployed as part of an investigation of the surface ocean carbon cycle at OSP [41] but continuing as an OceanSITES time series [26] and as part of the Pacific Marine Environmental Laboratory Ocean Climate Stations (OCS) program (`http://www.pmel.noaa.gov/ocs/`). Two upward-looking ADCP moorings were also deployed in 2008 and 2009 [2] and a surface Waverider buoy from 2011-on [153].

From June 2008 to January 2010, the mooring array was augmented by three successive

single-vehicle Seaglider autonomous underwater glider missions, with each repeatedly following a bowtie-shaped survey track whose corners formed a 50x50km box. These Seaglider surveys represent another important observational milestone for OSP, in that the vehicles provided estimates of the horizontal gradients of temperature, salinity, and dissolved oxygen in the top 1000 m in the area surrounding the mooring, along with well-resolved vertical profiles of these variables over the course of 18 successive months. Previous mesoscale upper-ocean horizontal gradients of temperature and salinity had been collected at OSP either from individual shipboard cruises and surveys, or drifting buoy and moored deployments with maximum duration of a few months [87, 119, 104, 160]. The primary scientific goals of the glider deployments were twofold: 1) resolve horizontal gradients through the top kilometer of the oceanic water column to estimate vertical geostrophic shear and horizontal tracer advection, and 2) estimate vertical advection and diffusion in order to describe the evolution of heat, freshwater, and dissolved oxygen. These goals were accomplished by exploiting the 4-dimensional description of temperature and salinity to infer monthly diffusion and vertical motion.

Augmentation of moored sites with mobile autonomous vehicles represents extension of moored time series oceanography to spatial structure on scales relevant to temporal evolution so that the fates of heat, freshwater, and other quantities involved in active exchange between ocean and atmosphere can be better estimated without requiring the presence of a research vessel. This, in turn, potentially enhances the ability of time series to diagnose climatically-important seasonal and interannual upper-ocean anomalies that have significant implications for regional weather patterns and the marine food web, such as the North Pacific Warm Anomaly of 2013-2015, near the center of which OSP resides [169, 171, 12]. In this way, an array of the type employed in this study serves as an important foundational piece in what may be a more common observing system in the near future. Mooring-glider combinations of greater complexity are now being deployed as part of the National Science Foundation Ocean Observatories Initiative, including at Station Papa.

Analysis and interpretation of the Seaglider surveys at OSP proceeds throughout the

following three chapters. This chapter gives an overview report that includes details regarding the duration of observation of each platform, the methods used to estimate horizontal gradients from Seaglider data, the estimated geostrophic circulation, and observed water mass properties. Quantitative analyses of the heat, salinity, and dissolved oxygen mass balances in the upper 200 m, and interpretation of oxygen residuals in terms of rates of oceanic metabolism, are left to chapters 2 and 3. In this chapter, it is shown that flow near OSP during the observing period was dominated by an eddy-like circulation at odds with the circulation that the mean field in Figure 2.1 implies. The circulation pattern detected was only intermittently detectable from satellite sea-surface height, emphasizing the potential role that autonomous observations can play in resolving features at the mesoscale and submesoscale. The water mass properties within the interior of the eddy-like feature were warm and saline relative to background conditions, though oxygen concentrations indicate that this feature must have originated to the south and west of OSP, rather than along the coast of North America as might be expected. These results, though anomalous relative to the 2007-on moored time series, are consistent with the overall picture of the southern Gulf of Alaska as a low-energy but still eddy-abundant region, in which the persistent weak eastward flow of the North Pacific Current is frequently masked by itinerant vortices, potentially carrying water and associated water mass signatures that may differ considerably from those found in the central subarctic. Section 2.2 describes the moored and Seaglider data and processing steps, along with the methods used to estimate horizontal gradients surrounding OSP. Section 2.3 describes the estimated geostrophic circulation and water mass properties. Section 2.4 discusses these results and possible origins of the phenomena observed at OSP in 2008-2010, while Section 2.5 provides a summary.

2.2 Data and Methods

2.2.1 Moored Array

The NOAA OCS installation at OSP consists of a single taut-line mooring with sensors designed to sample atmospheric properties, mixed layer properties, and temperature T and salinity S profiles in the top 300 m. Beginning in summer 2007, the mooring has been deployed and recovered in June of each year from the CCGS *Tully* in cooperation with IOS (DFO) Line P program. The mooring location alternates years between two sites near OSP. In deployments beginning in odd years, the target mooring site is 50°08′N, 144°50′W, while in even years it is to the southwest at 50°03′N, 144°53′W (Fig. 2.2a). The taut line results in little displacement of the surface buoy from its target position, with watch circle radius of 1.4 km and maximum displacement from the nominal position of 8 km over the course of the time series to this date (M.F. Cronin, N.A. Pelland, S.R. Emerson, and W.R. Crawford, Estimating diffusivity from the mixed layer heat and salt balances in the North Pacific, manuscript submitted to Journal of Geophysical Research-Oceans). During overlap with the Seaglider surveys, the mooring line parted at its connection to the bridle on 11 November 2008; the drifting buoy and surface instruments were recovered in the Strait of Juan de Fuca in January 2009. High-resolution post-processed surface data and daily-average telemetered subsurface data are available from the onset of the Seaglider time series on 8 June 2008 until mooring break. No mooring data are available from 11 November 2008 until deployment of the successor mooring on 14 June 2009 (Fig. 2.2c).

The buoy atmospheric measurements include wind speed and direction from a sonic anemometer at 4 m height, air temperature, relative humidity, and barometric pressure at 2.5 m, and short- and long-wave radiation and rain rate at 3.5 m. The buoy also samples sea-surface temperature and salinity at 1.2 m depth. Cronin et al. [24] describe the sampling strategies for these measurements at a similarly-configured Kuroshio Extension Observatory (KEO) mooring. Measurement errors are discussed by Kubota et al. [81]. This study employs net surface heat and moisture fluxes from these observations and their contributions

to errors in surface heat flux components estimated by Cronin et al. (submitted manuscript); briefly, latent and sensible heat fluxes were computed using the Coupled Ocean-Atmosphere Respose Experiment (COARE) 3.0 algorithm [49] with warm layer and coolskin corrections, while net solar and longwave radiation were estimated using the measured downwelling values and a seasonal cycle for surface albedo based on the International Satellite Cloud Climatology Project (ISCCP; `http://isccp.giss.nasa.gov/`). Rain guage measurements were corrected for wind effects following [137]. Cronin et al. [24] and Cronin et al. (submitted manuscript) describe these procedures in further detail. Subsurface measurements along the OSP mooring line include point observations of temperature T, salinity S, and vector current meter measurements of eastward u and northward v velocity components at multiple depths. In 2009, during overlap with the Seaglider time series, T was measured at 16 depths from the surface to 300 m (1.2, 5, 10, 20, 25, 30, 36, 60, 80, 100, 120, 150, 175, 200, 300 m), S was measured at 12 depths from the surface to 200 m (1.2, 10, 20, 25, 30, 36, 45, 60, 80, 100, 120, 200 m), and a current meter sampled horizontal velocity at 35 m depth.

This study also employs data from a subsurface ADCP mooring deployed near OSP during June 2008-June 2010; Alford et al. [2] summarized these results and used them to investigate the generation and downward propagation of near-inertial wave packets. During both years, a 75 kHZ up-looking unit was mounted at 800 m, giving ensemble velocity profiles in 16 m vertical bins every 30 minutes. A second up-looking, higher-frequency unit was mounted at 130 m from June 2008 (300 kHz) and 200 m (150 kHz) from June 2009 onwards. These units estimated ensemble profiles in 4 m vertical bins also every 30 minutes. The top 10% of the upper unit profile was discarded due to blanking. Weak acoustic scattering levels led to large gaps in the upper instrument record during the second year, extending up to 100 m depth from the surface at times [2]. The dedicated ADCP mooring was independent of the OSP surface mooring and was not affected by the failure of the latter in November 2008. The location of this mooring in each deployment year is indicated in Figure 2.2a.

Finally, Seaglider geostrophic velocities are also compared to the AVISO mapped Absolute Dynamic Topography (ADT) all-satellite gridded product (`http://aviso.altimetry.`

fr/index.php?id=1271). This product covers the time period 1993-2014 and is computed as the sum of satellite sea level anomaly and a mean dynamic topography as described in [142] and [131]. The mean dynamic topography of Figure 2.1 was obtained by taking the time-average of this dataset during the 1993-2014 period in the North Pacific Ocean.

2.2.2 Seaglider Surveys and Processing

Two individual Seaglider [47] AUVs were deployed at OSP in three consecutive missions. Seaglider (SG) 144 was deployed from 8 June-30 August 3008, SG120 from 30 August 2008 to 14 June 2009, and SG144 again from 14 June 2009 to 21 January 2010. SG120 ceased sampling due to a low battery state on 4 June 2009, hence there was a 10-day gap in sampling prior to the deployment of SG144 by the CCGS *Tully* on 14 June. On 21 January 2010, SG144 departed OSP and proceeded inshore along Line P before recovery on 2 April approximately 200 km from the inshore terminus of Line P.

The Seagliders profiled from the surface to 1000 m and back, using a buoyancy engine to travel with profile-average speeds of ∼20-30 cm s^{-1} through the water along an approximately 1:3 (vertical:horizontal) glide slope. During a typical dive-climb cycle, these vehicles traveled 6 km horizontally through the water over 8 hours. After each cycle, they acquired Global Positioning System (GPS) fixes at the surface, chose the heading with which to approach their next assigned navigational target, and attempted to maintain the heading during the subsequent cycle. Turns were executed at 5 minute intervals if heading deviated beyond a prescribed deadband from the target bearing. When a vehicle found that it had closed to within a prescribed radius of the target, it proceeded to the next one in its onboard list. Seagliders at OSP were instructed to repeat a series of five targets arranged in a 'bowtie' pattern inscribed in a 50×50 km box centered on the 2009 mooring site (Fig. 2.2a). The configuration of the glider navigation pattern was similar to that of surveys previously conducted at the Station A Long-Term Oligotrophic Habitat Assessment portion of HOT [111, 43]. Vehicles proceeded through the targets in the order NW-SW-NE-SE-NW, and repeated this pattern on average once every 14.5 days, resulting in 38 complete and two

partial circuits during the survey time series (Fig. 2.2a, b, d). Seagliders executed 36-59 dive-climb cycles to complete each survey circuit, with a median of 43. A total of 1707 cycles were performed (3414 profiles collected) between 8 June 2008 and SG144's departure on 21 January 2010.

Each vehicle was equipped with custom SeaBird Electronics (SBE) temperature and conductivity sensors mounted within a cylindrical duct atop a dorsal sting. These sensors were calibrated by SBE before and after each OSP deployment. In these and most Seaglider configurations, flow through the conductivity cell and past the thermistor is induced by flow past the vehicle as it glides. Measurements of salinity S were computed from measurements of T and conductivity, with corrections applied for position differences between the thermistor and conductivity cell and thermal inertia of the conductivity cell. These corrections were applied iteratively: from the steady flight equations of Eriksen et al. [47], vehicle speed was estimated from a first guess at seawater density and vehicle buoyancy, the thermal inertia correction was then applied based on this speed, a new seawater density and vehicle buoyancy and speed estimate was obtained, and the process repeated until a convergent solution was obtained. Where necessary, offsets were applied to measurements of conductivity in order to give better agreement between deep T-S measurements from Seagliders and those collected from Conductivity-Temperature-Depth (CTD) casts performed by the CCGS *Tully* and R/V *Thomas G. Thompson* (Appendix A). There was insufficient evidence to support any offset in thermistor readings between the platforms.

In the high-stratification summer and fall transition layer immediately beneath the surface mixed layer, vertical temperature gradients were large enough that the thermal inertia correction scheme was not sufficient to give accurate measurements of S, evidenced by large excursions in T-S that did not match the observed water mass structure in the CCGS *Tully*, R/V *Thompson*, or OSP mooring profiles. These were corrected by exploiting the nearly linear T-S relation shallower than the permanent pycnocline at OSP; for profiles within a specified time range, S was interpolated as a function of T between shallow and deep anchor points located in the mixed layer and permanent pycnocline, respectively. Appendix B

describes the details of this procedure.

Each vehicle was also equipped with a Western Environmental Technologies (WET Laboratories) ECO-BB2F "puck"-style sensor, sampling optical backscatter on two wavelengths and fluorescence on a single wavelength, and two dissolved oxygen sensors, a SeaBird SBE-43 Clark-type sensor and an Aanderaa Instruments 3830 oxygen optode. Chapter 4 discusses the results from the oxygen optodes from each vehicle. With the exception of September 2008, Seagliders collected samples from all instruments every 10 seconds while profiling from the surface to 80 m, every 20 seconds from 80 m to 150 m, every 30 seconds from 150 m to 300 m, and every minute when profiling between 300 m and 1000 m. This resulted in a mean vertical spacing between samples in each zone of, respectively, 0.93 m (0-80 m depth), 1.49 m (80-150 m), 2.30 m (150-300 m), and 4.17 m (300-1000 m). Within each SG profile, all scalar variables including T, S, in-situ density ρ, potential temperature referenced to the sea surface θ, and potential density ρ_θ were bin-averaged in depth, with bin depth intervals that approximately reflect the SG sampling frequency in each vertical zone: vertical bin spacing was every 2 m from the surface to 150 m, every 5 m from 150 m to 300 m, and every 20 m at greater depths.

The iterative solution described above gives an estimate of vehicle velocity through water at each sample point. Integrating this estimate across a dive-climb cycle gives an estimate of displacement through still water during that cycle. The difference between observed final displacement (climb end minus dive start location) and displacement through water divided by the cycle duration gives an estimate of time-averaged current experienced by the vehicle over that cycle. This is equated to 0-1000 m depth-averaged current (DAC) since the vehicle vertical velocity is approximately constant throughout each cycle. Independent of errors induced by onboard compass calibration, DAC samples are considered accurate to within $\sim$1 cm s^{-1} on each cycle [47].

2.2.3 Estimates of Horizontal Gradients

Seaglider profiles were sorted into time intervals corresponding to the calendar month in which they were collected. These first of these intervals extends from 8 June-30 June 2008, and the last from 1 January-21 January 2010; all intervals between these two extend from the first to the last day of each month.

The horizontal gradients within each monthly interval were estimated using ordinary linear regression curve fitting. Within each interval, and at each depth bin level, the record of each scalar variable (*e.g.,* potential temperature) was fit with a regression model of the form

$$\hat{\theta} = A + B(x - x_0) + C(y - y_0) + D(t - t_0) + E(t - t_0)^2 \tag{2.1}$$

where (x, y) are zonal and meridional coordinates of each sample, (x_0, y_0) are the coordinates at the center of the track pattern (the mooring location after June 2009), t is the time of each sample, t_0 is the mid-point of each monthly interval, and $\hat{\theta}$ indicates the scalar variable value predicted by the regression fit. The regression coefficients B and C were taken to be the zonal and meridional components of the gradient of the scalar variable in that monthly interval.

The monthly interval width corresponds to approximately the amount of time required for a Seaglider to perform two complete circuits of the bowtie survey track. As such, its corresponding frequency of 1 cycle per month represents the Nyquist frequency associated with the time to complete each circuit, and is taken to be the shortest time scale on which horizontal gradients can be reliably resolved by the spatial survey. The form of the regression equation including the quadratic term in time was chosen as the best compromise between adequately explaining the variance in each monthly interval and not over-fitting the data with more complex spatial terms (Appendix C). Estimating the regression fit (2.1) in non-overlapping monthly bins ensures that the estimates of the components of the gradient are fully independent from one another.

The above procedure was altered in the top 100 m for scalar variables also sampled by

the mooring after June 2009. At each depth level of moored sampling in the top 100 m, the mooring time record was removed from Seaglider-sampled variables, giving an anomaly field

$$\theta_a(z,t) = \theta_{\mathrm{SG}}(z,t) - \theta_{\mathrm{moor}}(z,t) \tag{2.2}$$

where θ_{SG} represents the Seaglider sampling record at depth z, θ_{moor} is the moored sampling record, low-pass filtered to remove inertial or higher frequencies, and θ_a is the anomaly between the two. A planar fit of the form

$$\hat{\theta}_a = A + B(x - x_0) + C(y - y_0) \tag{2.3}$$

was then performed on the anomaly variable and the coefficients B and C taken to be the spatial gradients in that time and depth interval. The gradients were then linearly interpolated in depth from the coarser mooring instrument depth levels onto the Seaglider depth bin levels.

This procedure was designed to, where possible, reduce errors associated with storms and atmospheric phenomena that alter surface layer depth and/or temperature over broad horizontal scales but short time periods, such as during "episodic cooling" events in which strong shear at the mixed layer base results in diffusive transport of heat from the mixed layer to thermocline over a time period of 1-2 days [87, 85, 38]. These phenomena occur at time scales that are much shorter than the 14.5 day repeat time of Seaglider spatial surveys. This type of low-wavenumber, high-frequency phenomena could be smeared onto the glider spatial record, resulting in apparent spatial gradients across the transect pattern during a single survey that are actually a result of rapid time variability. Performing a fit to the scalar variable anomalies (2.2) rather than the total value is one potential method of removing the rapid time variability, if it can be assumed that the scalar field near the OSP survey region can be expressed as a linear superposition of spatially- and temporally-varying components. In other words, the high-frequency phenomena observed by the mooring are assumed to be

coherent across the pattern, and it is further assumed that the horizontal gradient is unaltered by these phenomena. As will be shown in Chapter 3, the budget of potential temperature is least well-resolved in the lower boundary layer during summer and fall 2008, but for the same region and seasons the errors are substantially reduced in 2009, when the mooring was present and its time record could be removed from the Seaglider sampling record. This suggests, though does not prove, that the assumptions above are satisfied and that removing the mooring time record does improve the estimates of horizontal gradients of temperature in the boundary layer. The salinity budget does not show the same differential error between 2008 and 2009, suggesting that salinity is not strongly affected by this procedure, which may reflect weaker time variance in S relative to spatial variability in the upper ocean (Chapter 3).

The horizontal gradients of *in situ* density ρ estimated by the above procedure were used to estimate vertical shear of eastward u_g and northward v_g components of geostrophic velocity in each monthly interval using the thermal wind equations

$$\frac{\partial u_g}{\partial z} = -\frac{g}{\rho f}\frac{\partial \rho}{\partial y}, \ \frac{\partial v_g}{\partial z} = \frac{g}{\rho f}\frac{\partial \rho}{\partial x}, \tag{2.4}$$

where g is the gravitational acceleration, and $f = 1.1172 \times 10^{-4}$ s^{-1} is the Coriolis parameter at 50°N. Estimating vertical shear using observed density gradients defines the vertical profile of geostrophic velocity in each month to within a constant of integration. Seaglider surveys provide an estimate of this constant, albeit indirectly, in the form of monthly-averaged eastward U and northward V components of 0-1000 m DAC (Section 2.2.2). Thus profiles of absolute velocity can be constructed by adding a constant to the geostrophic velocity relative to 1000 m, whose value is equal to the difference between the observed DAC and the 0-1000

m average of the relative velocity:

$$u_g(z,t) = \int_{-H}^{z} -\frac{g}{\rho f}\frac{\partial \rho}{\partial y}(z',t)\mathrm{d}z' + \left(U(t) - \frac{1}{H}\int_{-H}^{0}\int_{-H}^{z} -\frac{g}{\rho f}\frac{\partial \rho}{\partial y}(z',t)\mathrm{d}z'\mathrm{d}z \right) \tag{2.5}$$

$$v_g(z,t) = \int_{-H}^{z} \frac{g}{\rho f}\frac{\partial \rho}{\partial x}(z',t)\mathrm{d}z' + \left(V(t) - \frac{1}{H}\int_{-H}^{0}\int_{-H}^{z} \frac{g}{\rho f}\frac{\partial \rho}{\partial x}(z',t)\mathrm{d}z'\mathrm{d}z \right). \tag{2.6}$$

Equations (2.5) and (2.6) assume that monthly DAC components $U(t)$, $V(t)$ include negligible contribution from surface Ekman flow. Based on the 10 m wind speeds shown in Figure 2.2, a characteristic magnitude of the surface stress $|\tau| = \rho_a C_d u_{10}^2$ is 0.15 N m^{-2}, based on $u_{10} = 10$ m s^{-1}, atmospheric density $\rho_a = 1.25$ kg m^{-3}, and $C_d = 0.0012$ [89]. This would imply an Ekman transport of $|\tau|/(\rho f) = 1.31$ m^2 s^{-1}. Averaged over the top 1000 m, this is equivalent to a DAC of 0.13 cm s^{-1}. In comparison, monthly-average DAC at OSP had a mean magnitude of 2.04 cm s^{-1} (0.47 cm s^{-1} minimum, 4.26 cm s^{-1} maximum). This comparison indicates that, for typical surface wind stresses and depth-average circulation at OSP, the assumption that monthly-average Seaglider-observed DAC is purely geostrophic introduces a small error to the geostrophic velocity calculations.

2.3 Results

2.3.1 Scalar Fields

A dominant feature of the potential temperature record during the Seaglider time series is the large variance shallower than 100 m depth that reflects the annual cycle of surface heating during summer, mixed layer deepening and entrainment of cooler waters in fall, and surface heat loss in late fall and winter (Fig. 2.3a). When viewed versus z and t, a weak periodicity is apparent in the temperature record at all depths greater than the surface layer. These periodic fluctuations are due to repetition of the survey circuit across spatial structure, as indicated by vertical gray lines (which indicate circuit start times at the NW target) in Figure 2.3a. Associated with these temperature striations are similarly periodic

fluctuations in isopycnal depth. There is also an overall increase in the depth of isopycnals located deeper than the surface layer during the time series, and a weakening of stratification (vertical spreading of isopycnals) in the permanent pycnocline (120-170 m depth; Fig. 2.3a).

The pattern-periodic fluctuations in potential temperature are easily seen when the mean vertical temperature stratification is removed and the remaining anomalies normalized by the standard deviation of potential temperature at each depth (denoted $\theta'(z,t)$; Fig. 2.3b). At depths greater than 100 m, the vertically-coherent time striations in the θ' record strongly suggest spatial variability across the survey track that is resolved by the Seaglider surveys. Shallower than 100 m, the striations are less visually distinguishable from the large seasonal anomalies generated by the heating, cooling, and deepening of the surface boundary layer. These features of the θ' record suggest that spatial changes dominate the variance in θ at depths >100 m, while temporal changes dominate the variance shallower than this depth. However, low-frequency time variability is evident deeper than 100 m in the form of a net warming of these waters over the course of the time series; peak temperatures are generally seen at each depth between January-May 2009, coincident with the greatest downward displacement of isopycnals in the main pycnocline and deeper.

The salinity cycle at OSP exhibits weaker seasonality in the surface layer relative to the amplitude of vertical variations than the temperature annual cycle (Fig. 2.4b). Within the surface layer, S is at a minimum in late summer and early fall and a maximum when the surface layer is deepest in late winter. Salinity stratification is greatest in the permanent pycnocline, where salinity is the dominant contributor to density stratification. Vertically-coherent periodicity is also apparent in the S anomaly record at depths >100 m, similar to θ' (Fig. 2.4b). Low-frequency salinity variability on depth surfaces is in the opposite time sense as temperature variability, consistent with downward heaving of isopycnals in the presence of a positive vertical temperature gradient and negative vertical salinity gradient (Figs. 2.3 and 2.4).

The region of high density stratification from 120-170 m in Figures 2.3 and 2.4 – the permanent pycnocline – corresponds to a region of nearly vertically constant temperature,

the subarctic *halocline*. A temperature-salinity-depth diagram constructed from all Seaglider profiles demonstrates that θ-S properties along isopycnals within this zone were not constant throughout the survey time series (Fig. 2.5). Two dominant θ-S modes were observed in the halocline: a cool mode, with halocline temperatures between 4°-4.5°C, and a more prevalent warm mode, with temperatures > 5°C. A profile of this mode, constructed by picking the most common θ/S at each density, would have a weak inversion in temperature, as the warm mode temperatures along $\sigma_\theta = 26.5$ at the base of the halocline are slightly greater than those at the top (Fig. 2.5).

These two water mass modes in the halocline are evident in a histogram of θ along the $\sigma_\theta = 26.5$ isopycnal (Fig. 2.6a), which lies at the base of the permanent pycnocline at a mean depth of 151 m. When separate histograms are constructed individually during seasonal intervals of the Seaglider time series, it is clear that the water mass within the halocline progressed from an expression of the cool mode (June-September 2008) to the warm mode (October 2009-January 2010), with intermediate water masses observed within the interior of the time series (Fig. 2.6b). Some temperatures that exceeded the mean within the warm mode were observed on $\sigma_\theta = 26.5$ in early 2009 as well (Fig. 2.6b). Within the upper halocline, temperature along isopycnals anticorrelates with oxygen concentrations (Fig. 2.7a; $r = -0.67$, which rejects the null hypothesis of zero correlation at 95% confidence [1] if $N = 20$ survey repeats is assumed to be the number of independent samples, a very conservative assumption), and the warm mode was associated with oxygen concentrations 10-15 μmol kg^{-1} lower than those of the cool mode on $\sigma_\theta = 26$. In the middle halocline ($\sigma_\theta = 26.2$), there was no significant correlation between oxygen and temperature along isopycnals (Fig. 2.7b), while in the lower halocline the trend was reversed: oxygen concentrations were 15-20 μmol kg^{-1} higher in the warm mode than cool mode on $\sigma_\theta = 26.5$ (Fig. 2.7c; $r = 0.84$).

[1] The test statistic for the sample correlation coefficient is $t_{\text{samp}} = \frac{r\sqrt{N-2}}{\sqrt{1-r^2}}$ which has a Student's-t distribution with $\nu = N - 2$ degrees of freedom. A two-sided test is used to test the null hypothesis of zero correlation; the test rejects this hypothesis if the sample t score is greater than $F^{-1}(0.975|\nu)$ [variables are positively correlated] or less than $F^{-1}(0.025|\nu)$ [anticorrelated], where $F^{-1}(p|\nu)$ is the inverse of the Student's-t cumulative distribution function having degrees of freedom ν and evaluated at probability level p. In this case, $t_{\text{samp}} = -3.87 < F^{-1}(0.025|18) = -2.1$, which rejects the null hypothesis.

The horizontal θ gradients suggested by the vertical striations in Figure 2.3, quantified using (2.1) and (2.3), were strongest in the permanent pycnocline during the first half of the time series (Fig. 2.8). Horizontal gradients $\nabla\theta$ were primarily eastward within the seasonal thermocline and permanent pycnocline, reaching strengths of 0.25-0.5°C per 50 km (navigation pattern width). Gradients of stronger magnitude than this were occasionally estimated in the upper transition layer. Gradients were weaker at depth and within the surface layer; in the surface layer, gradients were to the south and east in late 2008, and to the south and west in 2009 (Fig. 2.8). Within the permanent pycnocline, $|\nabla\theta|$ weakened considerably after April 2009, and from this month onward, the strongest temperature gradients were in the near-surface transition layer. The eastward temperature gradients observed in the seasonal thermocline and permanent pycnocline until late 2009 are stronger than the climatological southeastward $\nabla\theta$ estimated at OSP in the World Ocean Atlas (WOA) 2013 decadal 1/4° 2005-2012 climatology [14, Fig. 2.8].

Estimated horizontal salinity gradients in monthly intervals were of a different character than $\nabla\theta$ in that there was not a consistent gradient direction within the permanent pycnocline during 2008 and early 2009, despite the fact that like θ, S gradients were of greatest magnitude in the permanent pycnocline (Fig. 2.9). In early 2008, salinity gradients were nearly opposite in direction to those of temperature in the seasonal thermocline and pycnocline, suggestive of pure heaving, though after this period, there is not a clear correspondence between the two. Furthermore, salinity gradients did not weaken in the halocline after April 2009 (Fig. 2.9). Also unlike $\nabla\theta$, ∇S was much weaker in the surface and transition layers relative to its strength in the halocline. Climatological gradients at OSP in the WOA2013 atlas are generally to the northwest, with a maximum strength of 0.0142 per 50 km at 130 m depth, increasing along 287°T (Fig. 2.9). Monthly salinity gradients estimated during the Seaglider surveys were an order of magnitude larger in strength than the climatological gradients and were oriented in the opposite direction for extended periods in the permanent pycnocline/halocline (January-March 2009 in Fig. 2.9).

2.3.2 Geostrophic Circulation

The transition between strong, eastward $\nabla\theta$ in the pycnocline and relatively weak gradients thereafter coincides with a change in character of the estimated geostrophic circulation (Fig. 2.10). Estimated geostrophic velocities were unidirectional in the top 1000 m and weakly vertically sheared; the strongest currents were 5-10 cm s^{-1} in the top 200 m, and <5 cm s^{-1} at greater depths. The sense of shear is aligned with the mean DAC in each monthly interval of the Seaglider time series (Fig. 2.10). Flow was moderate and predominantly poleward during 2008 and early 2009, before "backing" (rotating counterclockwise towards westward flow) and weakening from March-May 2009. Depth-average signals were near-zero from November 2009-onwards. The profile of geostrophic flow estimated from glider-derived horizontal gradients of density and mean DAC is in good qualitative agreement with monthly averages from the depth-mounted ADCP instruments (Fig. 2.10). The ADCP record replicates the estimated backing of flow in March-May 2009 and weakening near the end of 2009, and also estimates the strongest flow in the top 200 m. The glider-derived geostrophic velocity near the surface is also in good agreement with surface geostrophic velocities from the AVISO mapped ADT gridded product (Fig. 2.10).

Also shown in Figure 2.10 are correlations between the ADCP and Seaglider monthly-average velocities evaluated using the square vector correlation statistic ρ_v^2, which was developed by Crosby et al. [27] as a generalization of the univariate correlation coefficient r to vector time series. The maximum value of ρ_v^2 is 2, for two vector time series that are perfectly linearly correlated and can be expressed as linear transformations of one another through scaling and rotation, and the minimum value is $\rho_v^2 = 0$ for uncorrelated vector time series. For a sample size of 20 the null hypothesis that the two time series are independent of one another can be rejected at 95% for a ρ_v^2 score of 0.458. The ρ_v^2 value between Seaglider and ADCP monthly average velocities exceeds this critical value at each of the four depth levels considered in Figure 2.10. This correlation is likely influenced by the low-freqency changes in circulation from poleward to near-neutral captured by both time series. The contribution of

this background circulation was estimated by low-pass filtering each monthly-average vector time series using a triangular filter with three-month half-window width. Vector correlations between anomalies from the low-pass filtered time series were then computed [denoted by $\rho_v(\mathrm{HP})^2$]. Although the values of ρ_v^2 for anomalies to the seasonal-scale circulation were lower, all were still significant at 95% confidence (Fig. 2.10).

Absolute geostrophic velocities estimated from the Seaglider surveys are dependent on both estimates of horizontal gradients and the monthly-average DAC through (2.5) and (2.6). Figure 2.11 shows the vertical geostrophic shear estimated from the Seaglider surveys, which depends only on the gradient of density, in the depth range 250-800 m compared to the vertical shear measured directly by the ADCP. Both instruments showed the strongest vertical shear over this depth range oriented roughly northward during the first three months of the Seaglider time series; strong northward vertical shear was also observed in February 2009. Much like the absolute geostrophic velocities, the vertical shear backed and weakened in March-May 2009, as the sense of vertical shear was aligned with the depth-averaged flow throughout the Seaglider surveys (Fig. 2.10). The agreement between the two platforms' estimates of vertical shear in this depth range confirms that the Seaglider survey estimates of horizontal gradients are sufficient to produce accurate estimates of geostrophic shear. The deep vertical shear was correlated between the two instruments with $\rho_v^2 = 1.54$ for the monthly-average shear values and square vector correlation of the high-passed filtered velocities $\rho_v(\mathrm{HP})^2 = 1.20$; both of these are significant at 95% confidence (Fig. 2.11).

The observed flow strength gives a Rossby number ($Ro = U/fL$) of 0.01, taking $U = 0.05$ m s^{-1} and $L = 50$ km. An alternate formulation of Ro is the vorticity Rossby number, $Ro_\zeta = |\zeta|/f$. Using the estimated vorticity of the depth-average current (ζ_{DAC}; Fig. 2.10) in each month also gives $Ro_\zeta \approx 0.01$. The estimated ζ_{DAC} was predominantly anticyclonic and varied in strength from 0-1.5% of f. The time-record of surface vertical vorticity from the AVISO ADT product in monthly intervals is similar to that of ζ_{DAC}, consistent with the weakly vertically-sheared flow (Fig. 2.10).

2.3.3 Vertical Finestructure

In addition to strong gradients in water mass properties across the navigational track, some individual Seaglider profiles contained evidence of density-compensating variations in θ and S within the lower halocline that are characteristic of horizontal interleaving observed at thermohaline fronts. Temperature-salinity characteristics of two example profiles, one of which displays evidence of interleaving features while the other does not, are shown in Figure 2.12. These profiles were collected during SG144's June-August 2008 deployment.

Within the approximate halocline density range ($26 \leq \sigma_\theta \leq 27$) the warmer of the two profiles appears smooth in a θ-S diagram, while the cooler of the two profiles exhibits small variations in temperature along isopycnals within the lower halocline. Shcherbina et al. [139] propose quantifying the presence of finestructure characteristic of horizontal interleaving between contrasting water masses using the curvature of "spice" π with respect to potential density, $\partial^2\pi/\partial\sigma_\theta^2$. This variable is a useful practical definition of intrusion-like finestructure because when horizontal interleaving does occur, the resulting profiles of θ or π plotted versus σ_θ have characteristic abrupt jumps at the upper and lower interfaces of intrusion features, resulting in large magnitudes of the second derivative at these interfaces. Spice is in general defined as the temperature or salinity anomaly along an isopycnal, though numerous practical definitions exist. Following [139], this study uses the spice variable defined by Flament [55]. Conclusions based on evaluation of the curvature of spice are not sensitive to the choice of definition. Since the spice defined by [55] has the same units as density, its derivative with respect to density is unitless, and its curvature has units of specific volume. Profiles of spice curvature were computed by linearly interpolating π to isopycnal surfaces in each Seaglider cast, computing the curvature with respect to density using a 2nd-order accurate finite-difference approximation to the second derivative, and then filtering the resulting profiles of $\partial^2\pi/\partial\sigma_\theta^2$ with a triangular-weight filter with half-width of 0.05 kg m^{-3} to remove noise with diapycnal scales smaller than that of the observed finestructure features. The spice curvature for the two example profiles is shown in Figure 2.12b. The cooler profile in Figure 2.12 has

more numerous and stronger-magnitude excursions of $\partial^2\pi/\partial\sigma_\theta^2$ (both positive and negative) than the warmer profile.

One possible method of quantifying the net incidence of density-compensating finestructure within a profile would be to integrate the square of the spice curvature in density space; the right-most plot in Figure 2.12 shows the quantity

$$I(\sigma'_\theta) = \int_{26}^{\sigma'_\theta} \left(\frac{\partial^2\pi}{\partial\sigma_\theta^2}\right)^2 \mathrm{d}\sigma_\theta. \tag{2.7}$$

This quantity is positive definite, is zero for a profile that is perfectly isothermal within the halocline, and is large for profiles with either large-magnitude or numerous incidences of thermohaline finestructure. Integrated across the halocline density range to $\sigma_\theta = 27$ $[I(27)]$, this quantity is nearly four times larger for the cool profile than the warm. These results suggest that a comparison of the quantity $I(27)$ between profiles provides a useful indication of their relative "sinuosity" in θ-S space, and thus provides a bulk indicator of vertical finestructure characteristic of thermohaline fronts.

Figure 2.13 shows θ-S detail near the base of the halocline for a series of profiles collected around those shown in the previous figure, where the profiles are colored by the logarithm of their $I(27)$ score. In general, profiles with fewer incidences of finestructure (which appear smoother in θ-S space) have lower I scores. It is also apparent that the profiles with the largest I scores are consistently closer to the cool θ-S mode for this time period. The two example profiles shown in Figure 2.12, indicated by black lines, bound the upper and lower range of θ observed along isopycnals during this period.

The time series of finestructure incidence as quantified by $I(27)$ is consistent with the evolution of water mass properties within the halocline. Peak θ-S finestructure was observed during October 2008-March 2009 (Fig. 2.14). These are months in which temperature along $\sigma_\theta = 26.5$ showed the greatest variability (Fig. 2.5), consistent strong water mass contrasts across the navigational track pattern. This is also in agreement with estimates of $\nabla\theta$ along

σ_θ = 26.5, which were computed using the same ordinary linear regression methods as described in Section 2.2 (Fig. 2.14). Integrated spice curvature began to decrease after March 2009, coincident with backing and weakening of the geostrophic circulation, and a reduction in strength of the isopycnal temperature gradient in the halocline. The weakest $I(27)$ was observed in November-January 2009, when water mass properties along $\sigma_\theta = 26.5$ were most consistent (Fig. 2.6). Integrated spice curvature increased again during SG144's transit inshore along Line P; levels of curvature similar to those in winter 2008-09 at OSP were observed again in February and late March 2010. Horizontal variations of $I(27)$ at OSP were examined within each month; finestructure appeared spatially patchy with no clear horizontal dependence in most months, with the exception of January 2010 when weak finestructure was clearly localized in the SW corner of the navigational pattern (not shown).

2.4 Discussion

Seaglider surveys at OSP observed weak and highly linear geostrophic circulation, which in and of itself is largely consistent with the characterization of the southern GOA as a low-kinetic energy region. The consistency of geostrophic velocity signals obtained independently between the ADCP, AVISO surface dynamic topography, and Seaglider-surface mooring array confirms the ability of the Seaglider surveys in the bowtie pattern to resolve the slowly-evolving mesoscale field with sufficiently low error such that a qualitatively realistic profile of geostrophic velocity can be constructed at monthly intervals. The significant correlation between monthly-average Seaglider and ADCP vertical shear in the lower ADCP instrument zone (250-800 m depth), where the flow is assumed to be entirely geostrophic, indicates that Seagliders can adequately resolve horizontal spatial gradients in density in this zone. Furthermore, the significant correlation between the velocity records, even after high-pass filtering to remove the seasonal-scale flow, indicates that monthly-mean DAC signals from Seagliders are also capturing monthly anomalies in geostrophic circulation. The negative relative vorticity estimated from DAC is also consistent with the surface vorticity estimated from AVISO, and with ADCP observations of internal waves at frequencies below f [2]

during this time at OSP, due to lowering of the effective inertial frequency as a result of these mesoscale motions [82].

However, the pattern of currents observed during the Seaglider surveys – poleward, then westward and weakening – is contrary to the expectation of moderate north-northeastward climatological flow typical of the North Pacific Current at OSP. This circulation occurred in combination with observations of anomalous horizontal water mass gradients, density gradients, and suggestions of thermohaline frontal structure within the permanent pycnocline that run contrary to typical descriptions at OSP. Examination of the moored record and AVISO surface circulation from the time of OCS mooring deployment from 2007-onward indicates that, indeed, the downward heaving of isopycnals, increasing temperature at the base of the permanent pycnocline, and weakened geostrophic velocity was anomalous in comparison to the remainder of the 2007-2015 period covered by the mooring time series (Fig. 2.15). Temperature at 150 m (potential density at 200 m) was at its highest (lowest) during the entire mooring time series in the latter half of 2009, though a second prolonged anomalous period of similar character is evident in early 2014. Two smaller-magnitude downward displacement events were observed in winter 2011-12 and in late 2012. The surface circulation observed during the Seaglider time series in summer and fall of 2008 appears typical of that observed during the remainder of the mooring time series, consistent with north-northeastward flow of the NPC. In contrast, the circulation during the latter portion of the Seaglider time series was anomalously weak, and these conditions appear to have persisted after Seaglider departure from OSP throughout 2011, with even weak southward flow apparent in early 2011 (Fig. 2.15). Examination of daily AVISO surface ADT revealed a local maximum in SSH to the northwest of OSP during some daily images during this period (results not shown).

The potential density at 200 m reached a minimum value near 26.7 during the 2010 anomaly period in the latter half of the Seaglider time series. Whitney et al. [174] examined of trends in temperature and oxygen concentration on isopycnals at OSP during the Weathership and IOS sampling period; from the record of density and temperature anomalies in

the upper ocean over this period (their Fig. 2), it appears there was only one other occasion where the 26.7 isopycnal[2] (normally located at 150-175 m depth) reached 200 m, during the passage of a coastally-generated mesoscale anticyclonic eddy in 1974. Thus, observations of isopycnal displacement from either the OSP mooring time series or the much longer, multi-decade Weathership sampling record suggest an interpretation in which the downward isopycnal displacement and seemingly associated "warm" halocline θ-S mode in the latter half of the time series are the anomalous conditions relative to the mean, rather than the opposite.

Although the temperature along isopycnals during this period was elevated relative to the background conditions – suggestive of warm, saline North American coastal water sometimes transported by to OSP by anticyclonic eddies [174, 23, 97] – the warm mode water also had elevated oxygen concentrations along isopcynals in the lower halocline (Fig. 2.7c). This characteristic rules out a coastal eddy scenario, since Haida and Sitka eddies, and other coastally-generated anticyclones in the Gulf of Alaska, contain oxygen-poor water [8] sourced from the remnant California Undercurrent signature, which persists in diluted form for thousands of kilometers north of the termination of the Undercurrent as a distinct dynamical feature near the north end of Vancouver Island [23, 8, 16, 157]. Proximate to OSP, oxygen concentration along lower halocline isopycnals increases to the south and west, while temperature and salinity increase to the south [8, 16]. The temperature and oxygen concentrations on $\sigma_\theta = 26.5$ during the latter portion of the time series appear similar to the properties of what Aydin et al. [8] term the Western Subpolar Water (WSW), a water mass lying on the northern edge of the subtropical-subarctic frontal zone, intermediate in temperature, salinity, and oxygen characteristics between those of the subtropical North Pacific gyre and the central Alaska Gyre [8, 9]. On $\sigma_\theta = 26.5$, WSW has oxygen concentrations $\sim$225 μmol kg^{-1} and temperatures of 4.5-5.5°C, depending on the longitude and degree of

[2]Whitney et al. [174] report density in σ_t units rather than σ_θ as described in this study; the differences between these variables are small in the upper ocean and do not affect the discussion here. The minimum density value at 200 m during the moored time series is 26.662 in units of σ_t and 26.664 in units of σ_θ on 28 December 2009.

mixing between the WSW and surrounding subarctic water as it travels eastward along the NPC. Aydin et al. [9] attribute the increased oxygen concentrations in the WSW relative to its surroundings to more recent ventilation and modification of these waters in the Kuroshio-Oyashio confluence region in the western subarctic Pacific. The oxygen concentrations and temperatures observed in the cool mode during the Seaglider surveys appear closer to those of central Alaska Gyre (AG) water outlined by [9], which has halocline temperatures near 4°C and oxygen concentrations ∼175 μmol kg^{-1} along $\sigma_\theta = 26.5$. The elevated cool mode θ and [O_2] concentrations relative to AG water observed in the Seaglider surveys are consistent with OSP's location on the southern edge of this gyre. Although the high spatial and vertical resolution of the Seaglider surveys highlights the contrast between these two water masses, neither are particularly anomalous relative to the full range of conditions observed in the halocline during the OSP oceanographic record [*cf.* 174, their Fig. 4].

Thus, one possible explanation for the phenomena observed during the Seaglider time series is the slow passage through OSP of a mesoscale eddy or meander that originated within the WSW region, possibly as a result of baroclinic instability in the interior of the NPC [64, 132, 19]. The downward displacement of isopycnals and negative relative vorticity observed during the Seaglider time series are both consistent with an anticyclonic eddy. The evolution of geostrophic circulation would imply that the eddy began to the east of the array – resulting in moderate northward flow at OSP – then translated to the west and north, moving closer to the array center. A schematic of this scenario is given in Figure 2.16. This idea is consistent with the backing and weakening of geostrophic flow, reduction in strength of water mass gradients within the halocline, and change in orientation of these gradients from eastward to weakly northward (*i.e.*, the gradient of temperature along $\sigma_\theta = 26.5$ remained roughly 90° to the right of the geostrophic circulation, with qualitatively similar time record of strength in the two quantities).

The evolution of the spatial orientation of monthly-average halocline temperature, depth-averaged current, and AVISO sea surface height provides further circumstantial support to the idea of an eddy passing the array site. These quantities are shown in a sequence of

panels covering the duration of the array time series in Figures 2.17 and 2.18. At the onset of the time series, the temperature along $\sigma_\theta = 26.5$ was nearly uniformly cool, though with a persistent eastward isopycnal temperature gradient. The northward depth-averaged current was nearly 90°C to the left of this temperature gradient, in accord with the character of the surface circulation expected from the contours of sea-surface height which increased to the east (Fig. 2.17). The agreement between depth-averaged and surface circulation is to be expected given the weakly vertically sheared and nearly unidirectional geostrophic velocity profiles demonstrated above. In winter 2008-09, increasing temperatures were observed along the eastern side of the navigational track pattern, coincident with closed circular contours of SSH east and northeast of the array, and depth-averaged current vectors that give evidence of weakly anticyclonic circulation across the pattern (*e.g.,* Feb-Mar 2009 in Fig. 2.17).

After April 2009, the weaker isopycnal temperature gradients observed corresponded to weaker surface and depth-averaged circulation. The westward flow during April-October 2009 was consistent with a weak, local high in SSH intermittently apparent surrounding the array location (Fig. 2.18). This supports the idea of the array sampling a horizontally-uniform water mass contained within an eddy interior or core region. In November 2009-January 2010, it appeared that the eddy was nearly centered on OSP: 0-1000 m averaged currents indicate anticyclonic rotation about the center of the array (Fig. 2.18). This is consistent with the reduced incidence of finestructure, weak isopycnal temperature gradients, and near-zero mean circulation during this time.

Examination of AVISO SSH images prior to and following the Seaglider time series (not shown) did not provide conclusive evidence of the origin or ultimate destination of the eddy or anticyclonic meander; indeed, as evidenced by the monthly-average SSH images in Figures 2.17 and 2.18, closed contours of SSH characteristic of an eddy are only intermittently present in the gridded, all-satellite altimeter product. The Chelton et al. [19] eddy dataset identified from the AVISO Reference Series gridded altimetry product (`http://cioss.coas.oregonstate.edu/eddies/`, v3.04, accessed 17 January 2012) was examined to see if the high-pass filtered SSH-based detection algorithm employed by [19]

detected any eddy features corresponding to the phenomena observed during the Seaglider surveys. The Chelton et al. [19] dataset identified anticyclonic features with an approximate correspondence in position and size to the OSP eddy during some periods in 2009: 14-28 January, 13 May-3 June, 17 June-19 August, 16 September-30 September, and 2-9 December 2009. The small size and weak sea surface amplitude of this feature present challenges for its unequivocal detection and diagnosis in gridded altimetry products, due to the horizontal spacing of altimeter ground tracks and the spatial smoothing inherent to the gridded mapping procedure. For eddies characterized by a Gaussian spatial signature, Chelton et al. [19] found that the AVISO Reference Series product filtered out features with e-folding scales of 30 km or less at the latitude of OSP, and only features with radii of $\sim$60 km or larger were fully unattenuated by the mapping procedure. The evolution of horizontal gradients and top 1000 m circulation observed during the Seaglider time series indicates that this feature is of a scale that is at the lower boundary of what is potentially resolvable by a gridded altimeter product. While the all-satellite product used in this study (formerly referred to as the "Up-to-date" product) employs a greater number of altimeters at any given moment than the Reference Series (now referred to as the "two-satellite" product) employed by [19], it is likely that the gridded mapping procedure for the all-satellite product has a similar high-wavenumber cutoff and signal attenuation.

In an analysis of hydrographic data in the GOA from 1955-1958, Tully et al. [161] found similar deep warm anomalies at OSP, and noted that these were coherent with increased temperatures on $\sigma_t = 26.6$ across the eastern portion of the GOA between OSP and Vancouver Island from January 1957 to August 1958. They attributed these anomalies to a shift in the orientation of the NPC, such that flow near OSP was more northward than usual and the latitude of the dividing streamline between the GOA and subtropical gyre was shifted southward. Similarly, a more recent study using an eddy-resolving model of the North Pacific [148] found that anomalous northward advection across the density-compensated subarctic temperature/salinity front, south of which lies relatively warm and saline water along isopycnals [183, 77], can also lead to positive interannual heat content anomalies in the subarctic

region. These studies suggest that interannual changes in NPC location or orientation could bring WSW in closer proximity to OSP, and potentially increase the chances of eddies or meanders carrying WSW to reach the array [37, 9, 133]. Interannual characteristics of surface circulation and subsurface water mass properties in the time period surrounding the Seaglider time series show some evidence that this may have occurred in a fashion similar to that suggested by [161]. Zonal mean surface circulation over the band 150-145°W from the AVISO ADT product was first examined to determine if any noticable changes in latitudinal structure or relative strength between braches of the NPC occurred that may have correlated with increased influence of WSW at OSP. The zonal mean surface eastward flow in this region supports the previous results of Cummins and Freeland [28], in that a latitudinally-banded structure is apparent, with several persistent cores of flow within the more than 1000 km latitudinal extent of eastward circulation in the transition region between subtopics and subarctic (Fig. 2.19). A relatively distinct core of flow is apparent north of 50°N, similar to that found by Cummins and Freeland [28], which supports the distinction that is sometimes made between the main axis of the NPC and the "Subarctic Current" or "Aleutian Current" carrying cooler waters north of 50°N [37, 147]. A difference in these results as compared to those of [28] is that the main axis of the NPC during this time period appears to lie within the latitudes 45-50°N, in contrast to the region south of 45°N prior to 2007 as found in their results, though it should be noted that their results were along 150°W only, as opposed to the zonally-averaged region with 150°E as the western boundary shown here. The strong westward flow north of 55°N represents the Alaska Stream (Fig. 2.19).

There did not seem to be obvious evidence of shifts in strength of the zonal component of the NPC that correlate with water mass anomalies at OSP during the moored record. However, prominent interannual variability was also evident in the meridional component of NPC flow between 150°-145°W (Figure 2.15). The northward component of flow at 50°N was strongest (increasing to >2 cm s^{-1}) during the three periods in which downward isopycnal displacement at 200 m and elevated temperatures at 150 m were observed during the OSP mooring time series. There is only weak vertical temperature stratification in the base of

the halocline at 150 m, hence it is unlikely that the observed change in temperature at that depth is due to downward displacement of isopycnals in the presence of a vertically increasing temperature gradient, and more likely that this reflects water mass changes within the halocline. This is consistent with the hypothesis of Tully et al. [161] that northward flow in the NPC increases the influence of more southerly waters at OSP. To further investigate subsurface water mass characteristics, the spatial structure of potential temperature along $\sigma_\theta = 26.5$ sampled from Argo floats during the full OSP mooring time series was also investigated. Argo profile data interpolated to potential density surfaces were obtained from the Asia-Pacific Data-Research Center (`http://apdrc.soest.hawaii.edu/projects/argo/`). The potential temperature along $\sigma_\theta = 26.5$ in these profiles has a latitudinal structure that is generally consistent with the sustained northward NPC advection from 2008-2010 with a 6-12 month lag, though the number of available profiles in the region to the immediate west of OSP is limited (Fig. 2.20). If 4.75°C is considered the approximate delineation between Alaska Gyre and WSW waters on this isopycnal, the few profiles available suggest that this boundary exhibits interannual changes and was at its northernmost extent in early 2010 (Fig. 2.20).

This northward procession of the AG-WSW boundary is similar to the record of isopycnal displacement and potential temperature increase along isopycnals at the OSP mooring site during the Seaglider surveys, though the coarse resolution of the Argo array as compared to the OSP Seaglider array prevents a rigorous examination of the precise location of the frontal boundary and the timing of its movement – in Figure 2.20, it appears to lag the appearance of WSW waters at OSP as revealed by Seaglider and mooring observations. Nonetheless, Figures 2.19 and 2.20 suggest that, consistent with previous hypotheses [161, 148], northward advection and a shift in orientation in the NPC altered the latitudinal boundary between AG water and WSW, potentially contributing to the observed water mass properties at OSP by bringing WSW in closer proximity such that an eddy generated there could more easily reach the array site.

2.5 Summary and Conclusions

Seagliders augmented the NOAA OCS mooring at OSP from June 2008 to January 2010, providing horizontal spatial sampling proximate to the mooring site, increased sampling depth resolution and extent, and indirect estimation of 0-1000 m depth-averaged current. These surveys are the first of their kind at OSP and provided this information over more than one annual cycle. The circulation and water mass properties observed during this time series were anomalous in comparison to the full OCS mooring time series (2007-present) and, in isopycnal displacement, to the full climatological record at OSP dating to the 1950s. Estimates of horizontal density gradients and mean DAC were used to construct profiles of geostrophic circulation at monthly intervals; these indicated weakly vertically-sheared, unidirectional poleward flow during 2008 that rotated roughly 90° westward and weakened in early 2009. The latter circulation is contrary to the climatological concept of north-northeastward flow at OSP characteristic of the northern margin of the North Pacific Current that forms the boundary between subarctic Gulf of Alaska and subtropical North Pacific gyres.

Corresponding to changes in circulation, strong water mass gradients along isopycnals and evidence of horizontal interleaving were observed in the density range corresponding to the subarctic halocline/permanent pycnocline. The horizontal temperature gradients along isopycnals were roughly 90° to the right of the geostrophic circulation throughout the time series. Within the halocline, two distinct modes of variability were observed, a "cool mode" with temperature and oxygen characteristics consistent with water in the interior of the Alaska Gyre, and a "warm mode" characteristic of Western Subpolar Water carried along the northern margin of the NPC. Monthly averages of surface dynamic topography and observations from the Seaglider time series suggest that the warm mode waters were located within a weak anticyclonic eddy not much larger than the Seaglider navigational pattern, though it is difficult to unequivocally determine this. Downward isopycnal displacements and negative relative vorticity are both consistent with an anticyclone. Large-scale Argo array

and satellite observations of surface circulation and water mass properties in the permanent halocline suggest that the boundary between AG and WSW waters moved northward during the array time series, possibly bringing these waters in close proximity to OSP and making it easier for an eddy or anticyclonic meander to reach the array site. Large-scale changes in subsurface water mass structure have been observed in the Gulf of Alaska previously [161], and may play a role in modulating the pelagic ecosystem through changes in gyre-scale nutrient availability and water temperatures.

Small-scale mesoscale features with weak SSH signatures such as those observed in this study may not be continuously visible or detectable by gridded altimetry products, especially in this low-energy region of the North Pacific Ocean. The results of this study emphasize the capabilities that autonomous *in situ* sensors have in classifying and potentially tracking coherent vortices responsible for transporting heat, salt, energy, and nutrients across the subtropical-subarctic boundary in the North Pacific. Large, kinematically strong features generated along the North American coastal boundary are one possible mechanism by which anomalous waters are brought to OSP, but these observations suggest a viable and lesser-studied alternate pathway, resulting from eddies generated through instabilities in the interior currents. The altimetry-tracked eddy trajectories of Chelton et al. [19] indicate that eddy generation within the ocean interior is indeed common.

Though this chapter did not examine the heat and salt budgets beyond qualitative inspection of the temperature and salinity records, the presence of anomalous circulation features and low-frequency changes in water mass properties at depth suggest that horizontal advection of heat and salt will likely be important in accounting for the balances of these tracers during the period of time covered by the Seaglider surveys. The following chapter investigates these balances and infers the role of vertical advection and mixing using a large-scale least squares problem, while the final chapter uses these transports to diagnose the balance of dissolved oxygen including inference of the net biological contribution.

2.6 Figures

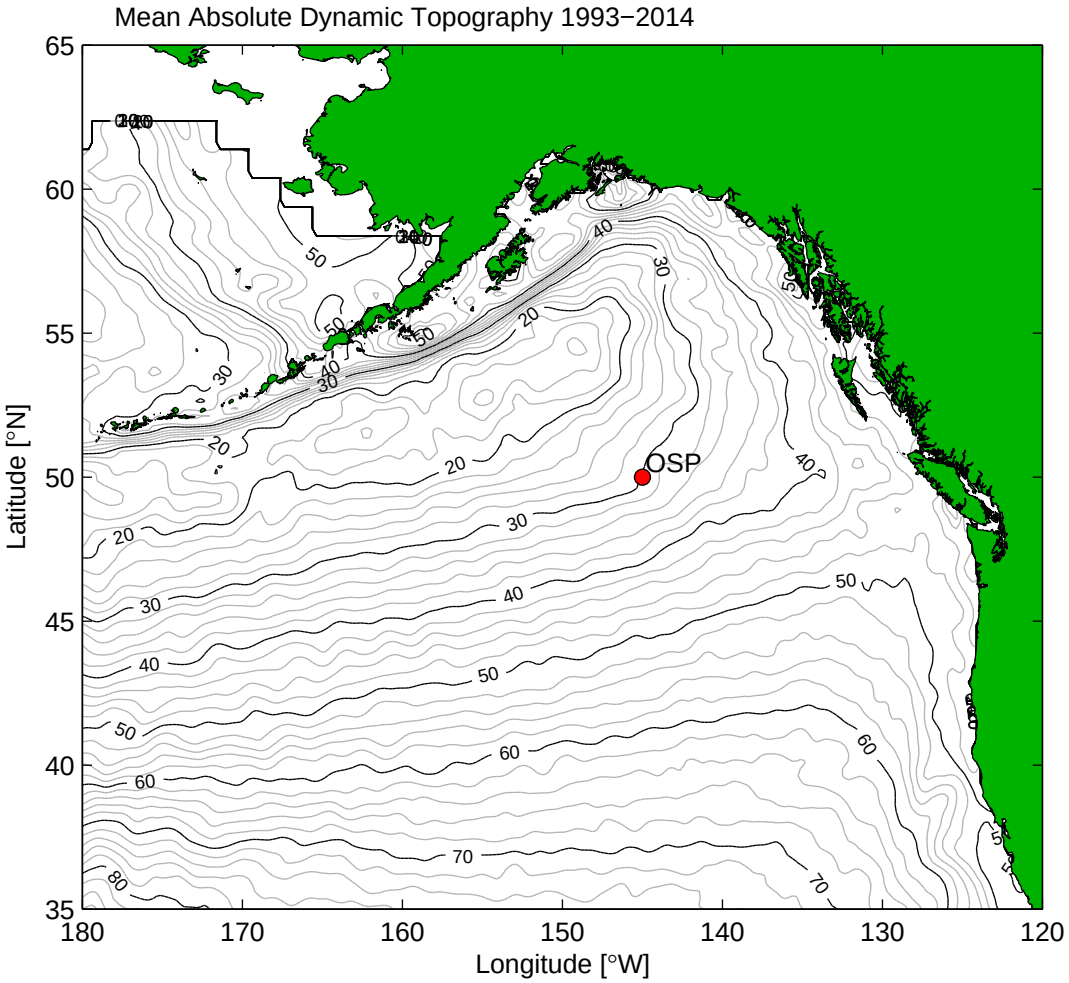

Figure 2.1: AVISO sea surface mean dynamic topography (cm of sea surface height) gridded product for the Northeast Pacific Ocean, 1993-2014. Contour interval is 2 cm. Red marker at 50°N, 145°W indicates Ocean Station Papa (OSP). The center of the Gulf of Alaska gyre is visible as a relative low in sea surface height to the northwest of OSP. The North Pacific Current is evident as a wide swath of east-northeastward flow that intersects the North American coast at latitudes 45°-50°N. OSP lies on the northern edge of this current.

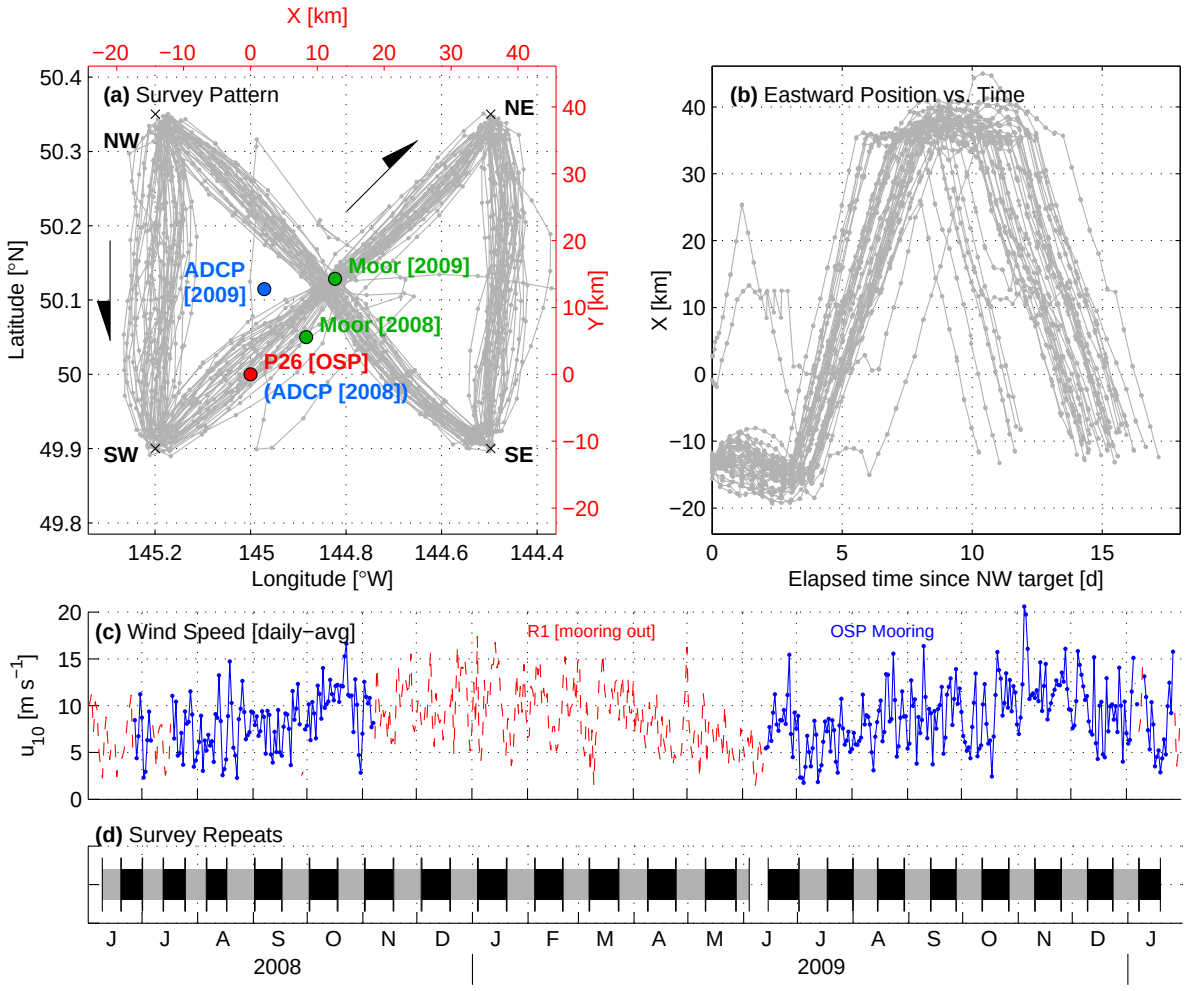

Figure 2.2: Seaglider surveys at Ocean Station Papa (OSP), overview. Panel (a) shows spatial survey pattern; gray curve indicates Seaglider track locations, gray dots give descent-ascent cycle center points. Black arrows indicate direction of survey. Green dots are NOAA surface mooring locations in 2008/2009 deployment years. Blue dot indicates subsurface ADCP mooring location in 2009 deployment year; this mooring was located at OSP in 2008. Panel (b) shows the X-coordinate relative to OSP, as a function of time since the initiation of each repeat of the survey. Panel (c) shows daily-average 10 m wind speed from the OSP mooring (blue curve) or NCEP Reanalysis 1 (R1) product (red dashed curve). Note the mooring was absent from OSP beginning 8 November 2008 until its redeployment in June 2009. Panel (d) shows Seaglider repeat occupation of the survey pattern as a function of time; vertical lines indicate the times at which the glider achieved the northwest (NW) target point, thus beginning a new survey circuit repeat, which are alternately shown in gray and black. Note the 10-d gap in June 2009.

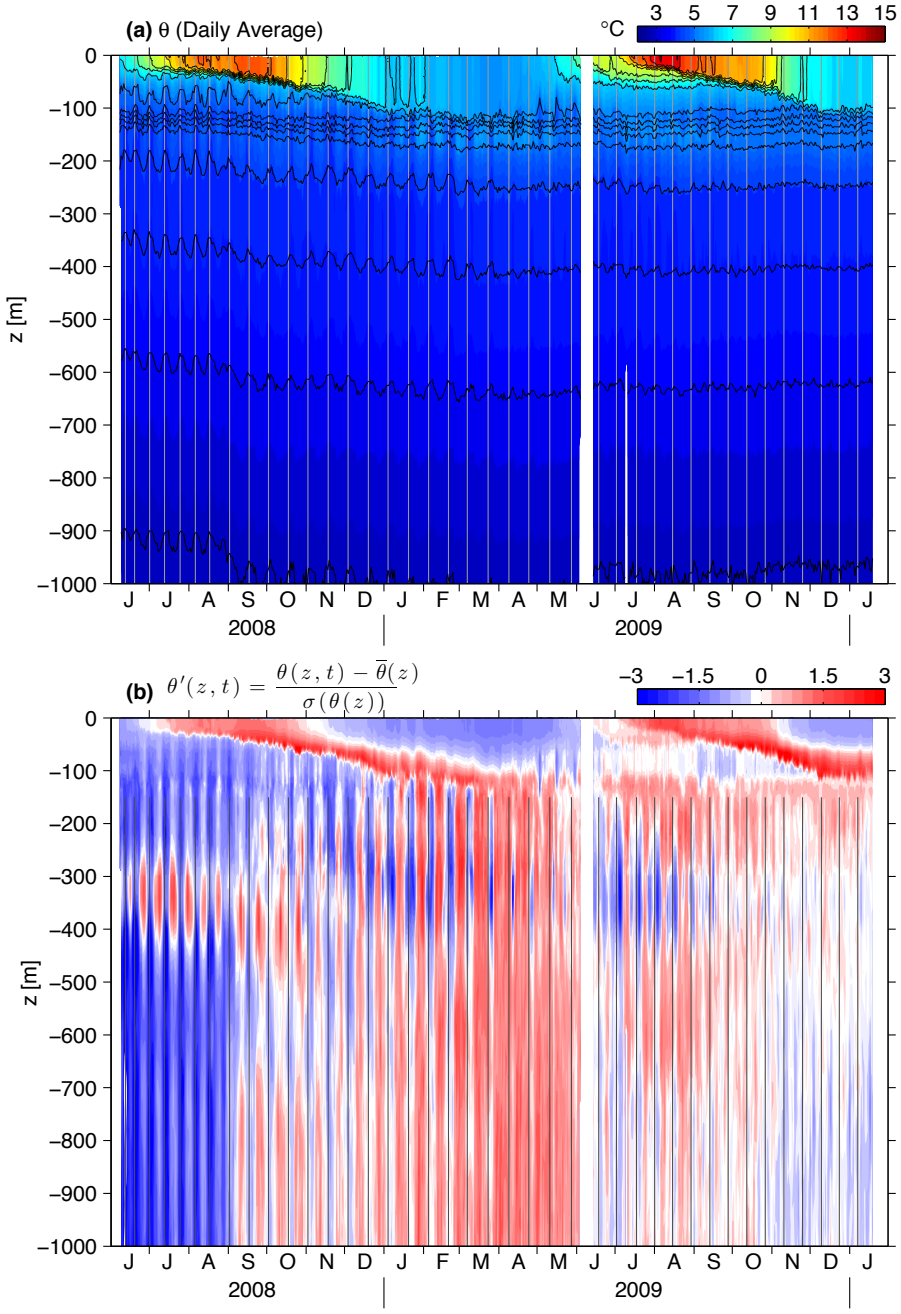

Figure 2.3: Potential temperature θ versus z and t sampled by Seagliders during Ocean Station Papa surveys. In panel (a), background colors indicate θ, while black lines are potential density contours (interval 0.2 kg m^{-3}) and vertical gray lines indicate Seaglider navigational track repeat times – each vertical line indicates when the vehicle achieves the northwest target of the navigational pattern (Fig. 2.2). Panel (b) shows θ anomalies from the time-mean vertical profile, normalized by the depth-dependent standard deviation $\sigma(\theta(z))$.

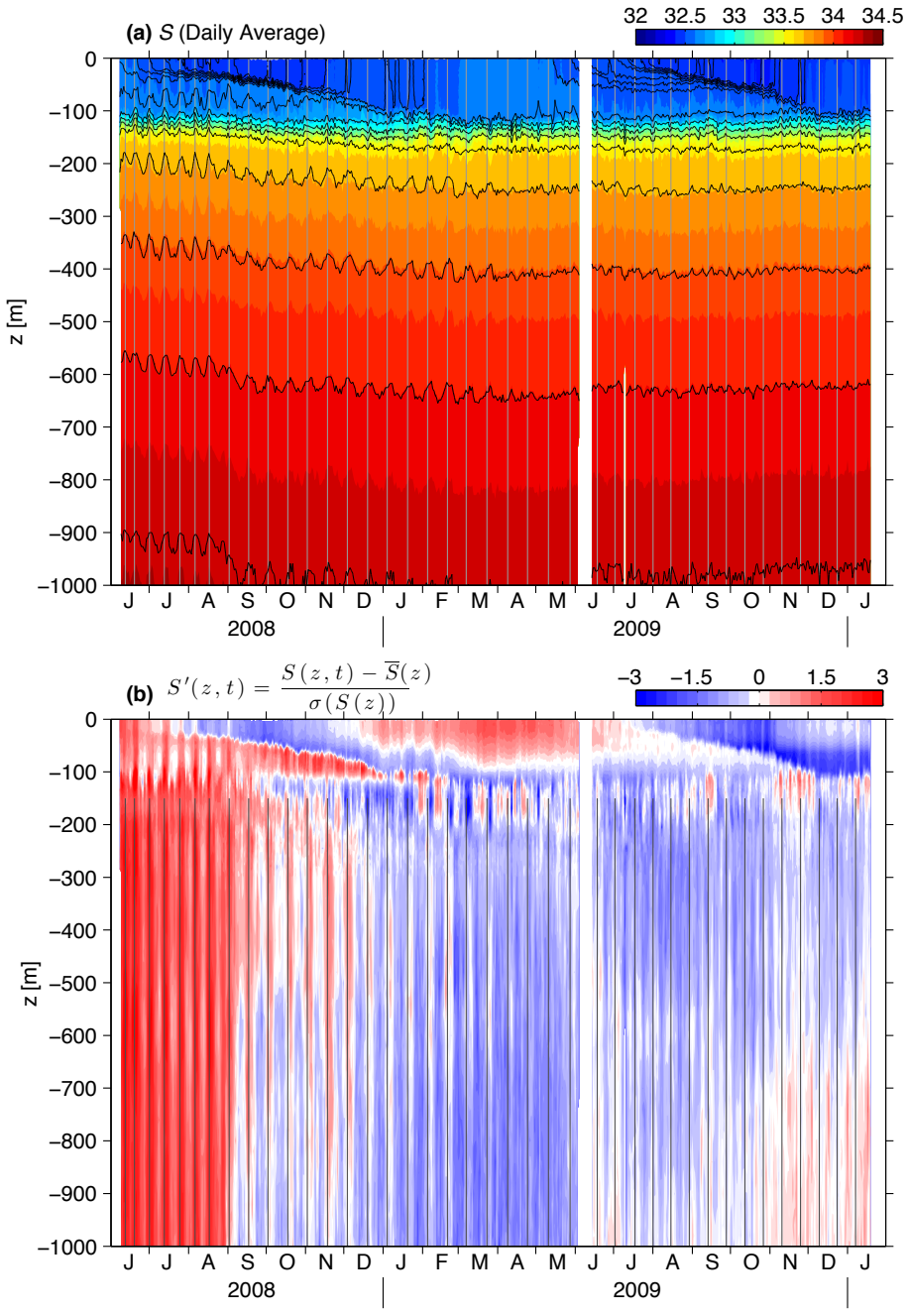

Figure 2.4: Salinity S versus z and t sampled by Seagliders during Ocean Station Papa surveys. In panel (a), background colors indicate S, while black lines are potential density contours (interval 0.2 kg m^{-3}) and vertical gray lines indicate Seaglider navigational track repeat times – each vertical line indicates when the vehicle achieves the northwest target of the navigational pattern (Fig. 2.2). Panel (b) shows S anomalies from the time-mean vertical profile, normalized by the depth-dependent standard deviation $\sigma(S(z))$.

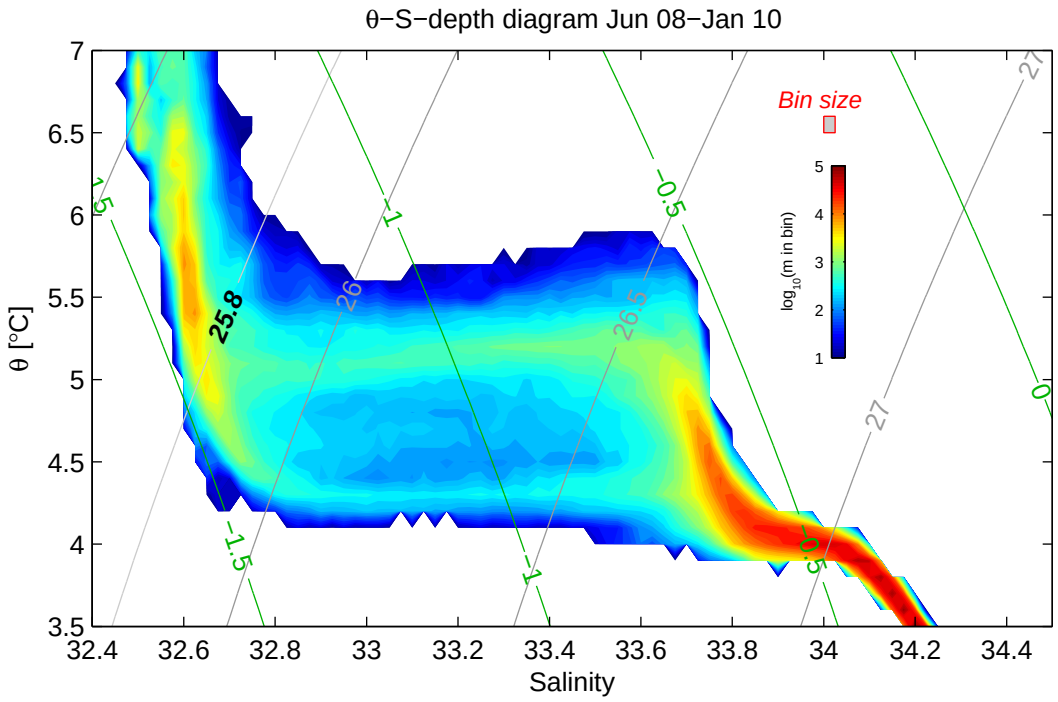

Figure 2.5: Potential temperature (θ)-salinity (S)-depth diagram composed from Seaglider profiles during the array time series. Diagram is constructed by sorting all Seaglider samples into bins in θ-S space, with bin size indicated by shaded square at upper right of diagram. Color contours indicate the sum of the vertical extent of all samples within each bin, in logarithmic scale. This diagram is equivalent to a θ-S-volume diagram if it is assumed that each profile corresponds to an equal horizontal spatial area [123]. Gray lines indicate density contours; σ_θ=25.8 (bold label) is the greatest density of the surface layer observed during the time series and thus forms the top of the halocline or permament pycnocline, which extends at least to σ_θ=26.5. Green lines indicate contours of constant "spice" [55].

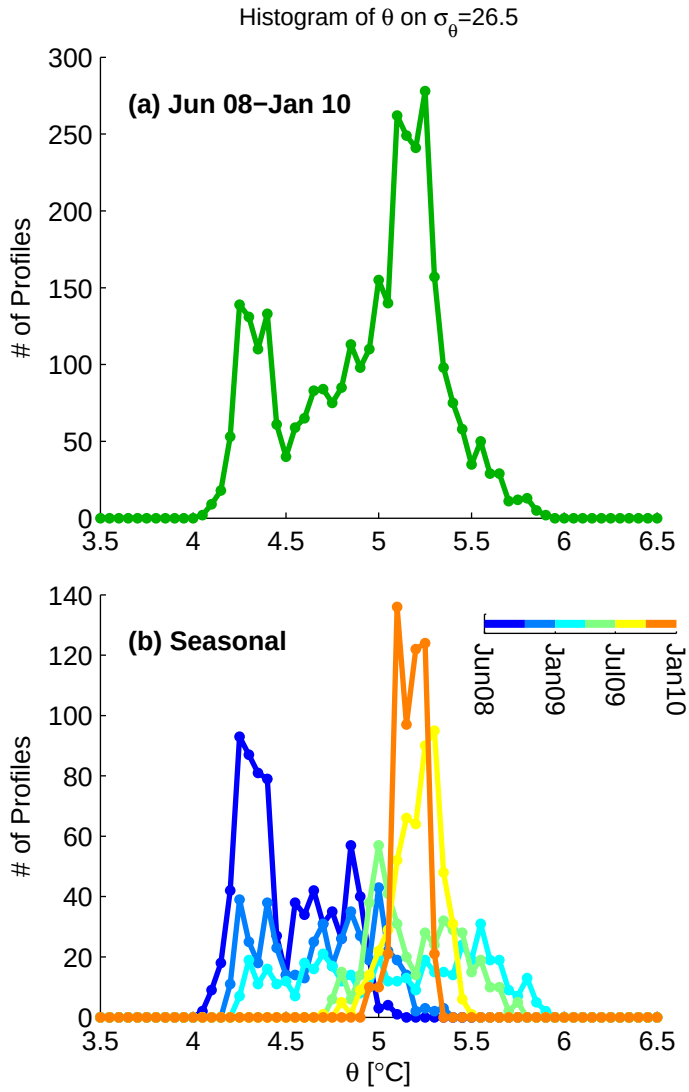

Figure 2.6: Histrogram of potential temperature θ along the σ_θ=26.5 isopycnal, at the base of the halocline/permanent pycnocline. Panel (a) shows histogram constructed from all Seaglider profiles during the array time series; panel (b) shows histograms constructed in quarter-year intervals.

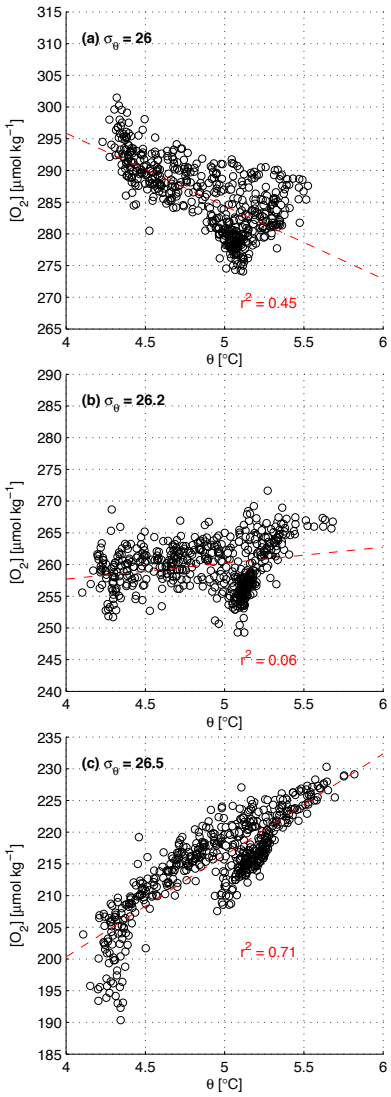

Figure 2.7: Dissolved oxygen concentration [O_2] versus potential temperature θ on three isopycnals within the halocline at OSP during the Seaglider time series: $\sigma_\theta = 26$ (a), $\sigma_\theta = 26.2$ (b), and $\sigma_\theta = 26.5$ (c). Measurements of [O_2] and θ were cycle-averaged, then daily-averaged to reduce errors associated with slow optode response time. The slow response time results in a 10-15 μmol kg^{-1} positive (negative) bias on descent (ascent) profiles in this region of steep vertical oxygen gradients. In each panel, the red dashed curve is a linear trend line fit to [O_2] vs. θ (r^2 value listed in red text). The oxygen concentrations are significantly negatively correlated with θ in (a) and significantly positively correlated with θ in (c).

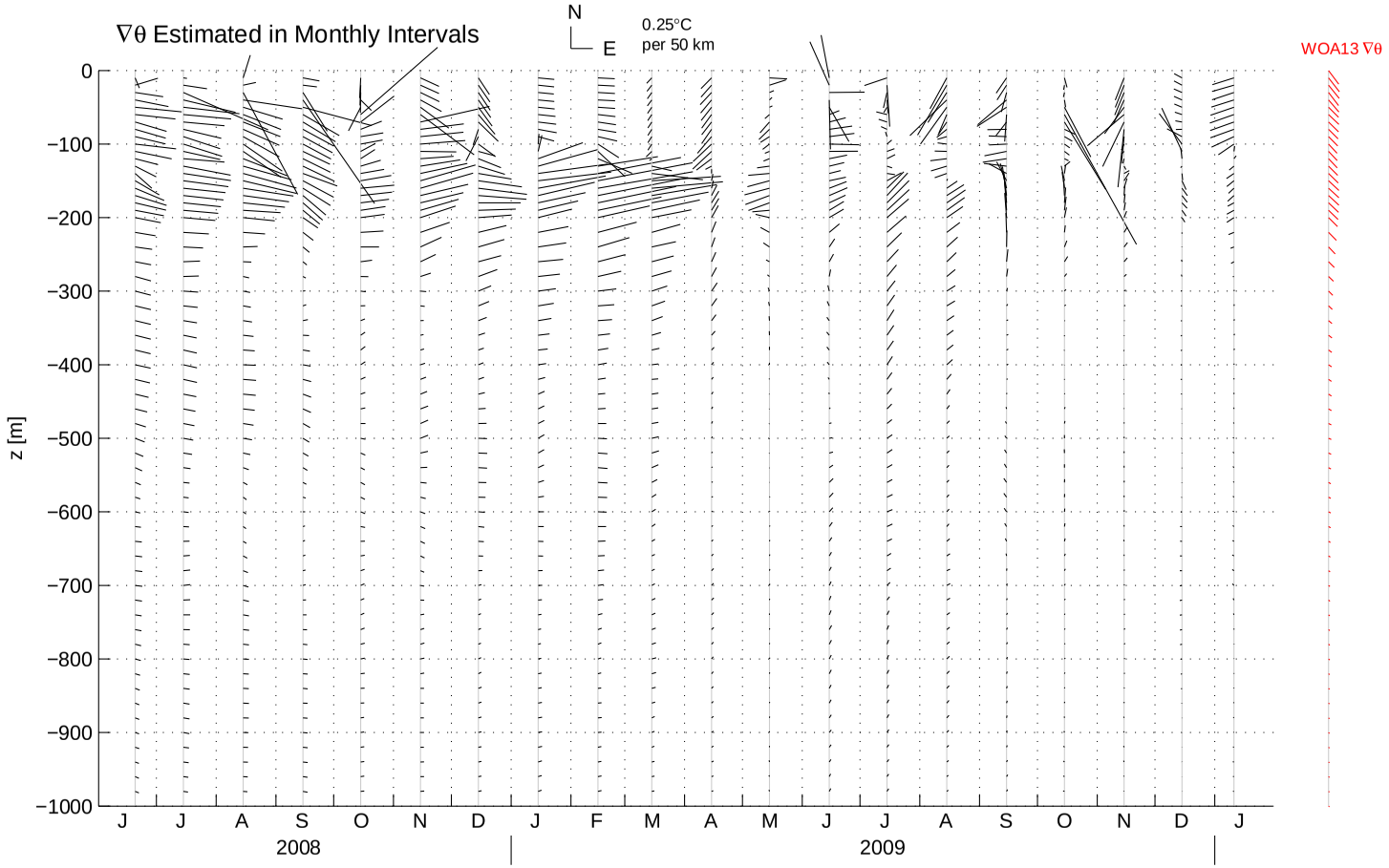

Figure 2.8: Vertical profiles of the horizontal gradient of potential temperature $\nabla\theta$ in monthly intervals estimated from Seaglider surveys at Ocean Station Papa (OSP). Gradient vectors are plotted every 10 m in the upper 200 m and every 20 m from 200 m to 1000 m depth. North and East scale vectors are shown at top. Profile of red vectors at right indicates the $\nabla\theta$ estimated at OSP from the World Ocean Atlas (WOA) 2013 1/4° optimal interpolation decadal climatology for the period 2005-2012.

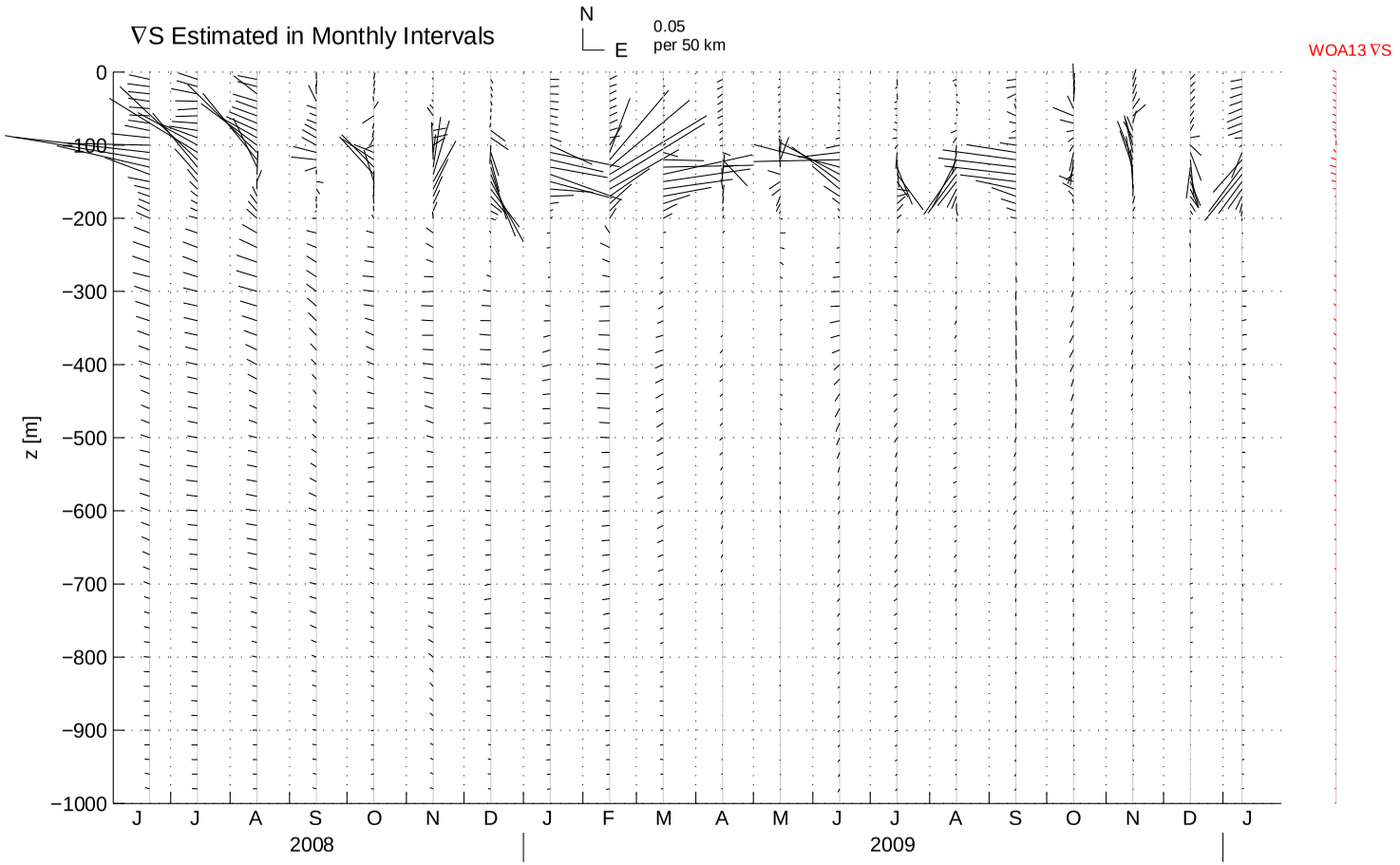

Figure 2.9: Vertical profiles of the horizontal gradient of salinity ∇S in monthly intervals estimated from Seaglider surveys at Ocean Station Papa (OSP). Gradient vectors are plotted every 10 m in the upper 200 m and every 20 m from 200 m to 1000 m depth. North and East scale vectors are shown at top. Profile of red vectors at right indicates the ∇S estimated at OSP from the World Ocean Atlas (WOA) 2013 1/4° optimal interpolation decadal climatology for the period 2005-2012.

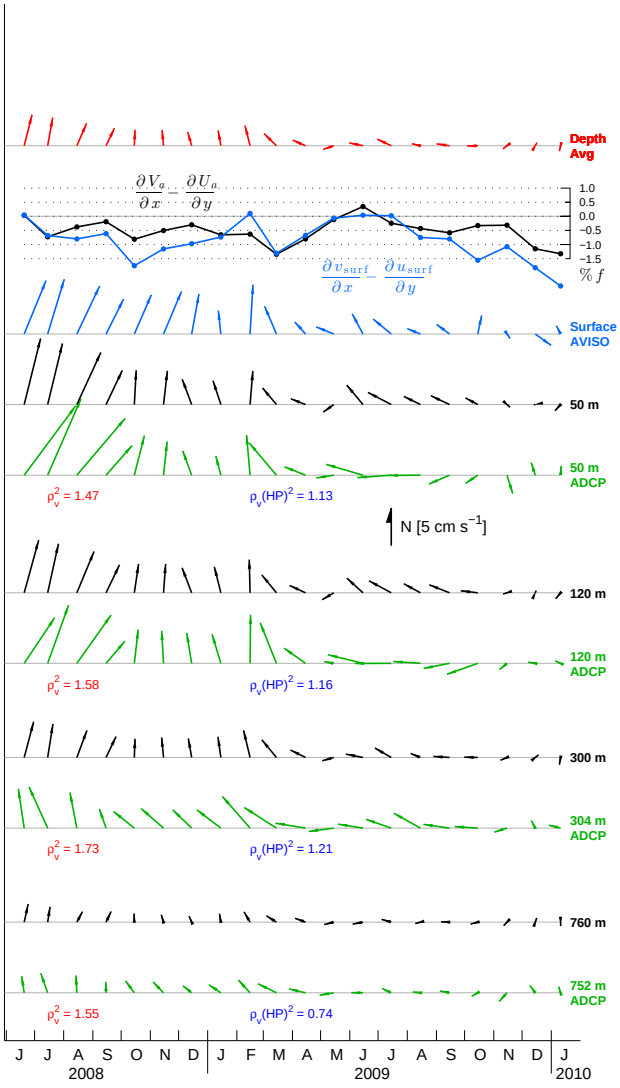

Figure 2.10: Horizontal circulation during the Seaglider time series. Top plot shows 0-1000 m depth-averaged current (red arrows – all quantities are averages in monthly intervals). Second plot from top shows estimated vertical vorticity of depth-averaged flow (black curve) and vertical vorticity of surface flow from AVISO Absolute Dynamic Topography all-satellite gridded product (blue curve). Third plot shows AVISO surface velocity (blue arrows). The remaining plots show monthly mean glider-derived absolute geostrophic velocity at four selected depths (50, 120, 300, and 760 m, black arrows) and mean depth-mounted ADCP velocity in the closest depth bin (green arrows). Text below each depth's plots indicates the square vector correlation coefficient [27] between glider and ADCP velocities at each depth, both for unfiltered (ρ_v^2) and high-pass filtered ($\rho_v(\mathrm{HP})^2$ velocities as described in the text.

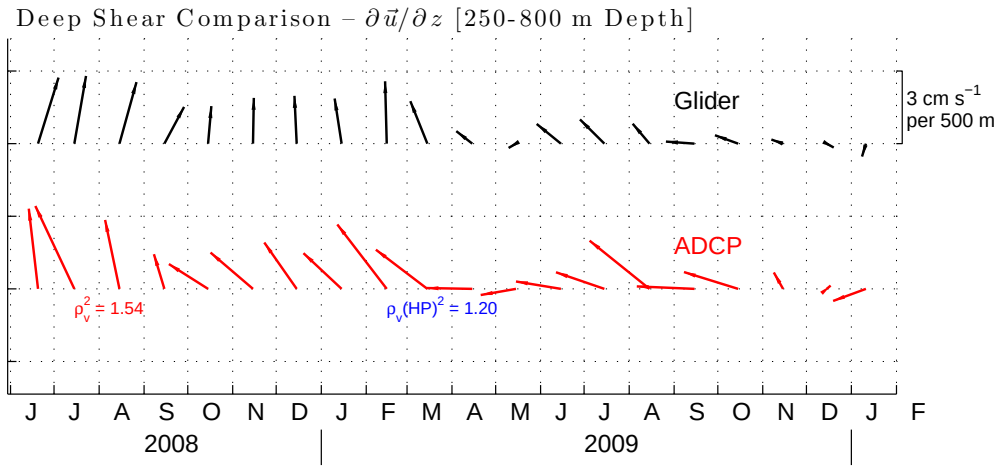

Figure 2.11: Comparison of vertical shear in monthly intervals estimated from Seaglider sampling (black) and moored ADCP (red). Shear is computed over the depth range 250-800 m, which corresponds to the majority of the depth range of the lower instrument in the depth-mounted ADCP mooring, and is a depth range where the flow is expected to be geostrophic. Scale shown at upper right. The strength and direction of the vertical shear is similar to the depth-average current (DAC) signals of Figure 2.10. The square vector correlation coefficient for unfiltered (ρ_v^2) and high-pass filtered ($\rho_v(\mathrm{HP})^2$) shear vectors between the two time series is also shown.

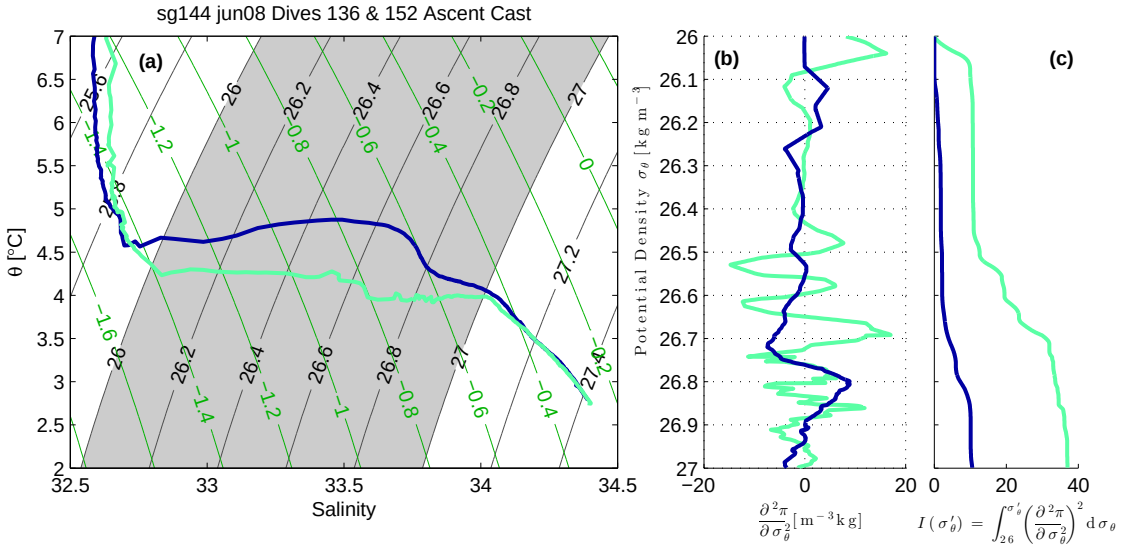

Figure 2.12: Two example profiles from Seaglider (SG) 144's June-August 2008 deployment, one of which (cyan profile) shows evidence of density-compensating θ variations characteristic of horizontal interleaving. Panel (a) shows the potential temperature θ-salinity S characteristics of the two profiles. Black contours indicate potential density σ_θ surfaces and green contours indicate spice surfaces as defined by Flament [55]. Panel (b) shows the curvature of spice π with respect to σ_θ within the range $26 \leq \sigma_\theta \leq 27$ for the two profiles; this density range is also highlighted by gray shading in panel (a). Panel (c) shows the quantity $I(\sigma'_\theta)$ as described in the text; *i.e.*, the integral with respect to density of the square of spice curvature taken from $\sigma_\theta = 26$ to a density σ'_θ.

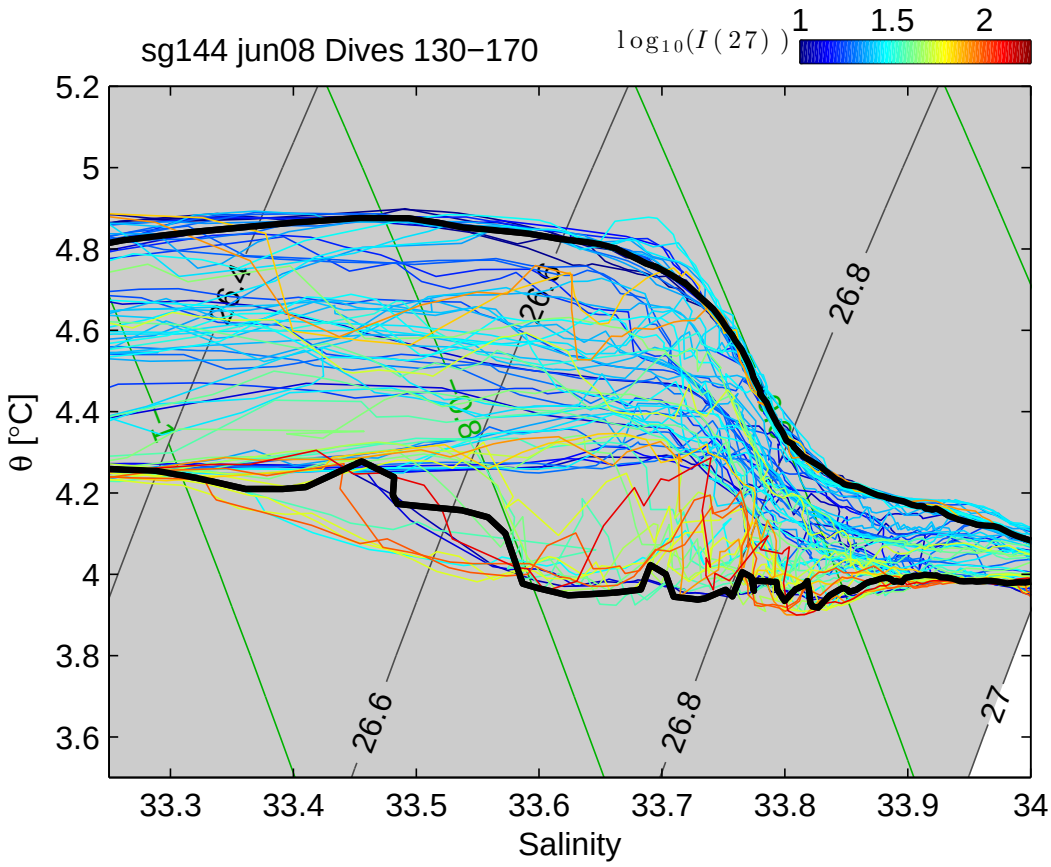

Figure 2.13: Detail of potential temperature θ-salinity S structure in profiles collected during Seaglider (SG) 144 cycles 130-170, 12 July-24 July 2008. Plot is centered on the lower portion of the permanent halocline. Profiles are plotted with color corresponding to the logarithm of theiir integrated square spice curvature in the halocline ($I(27)$), with color scale at right. Example profiles from Figure 2.12 are plotted as solid black lines.

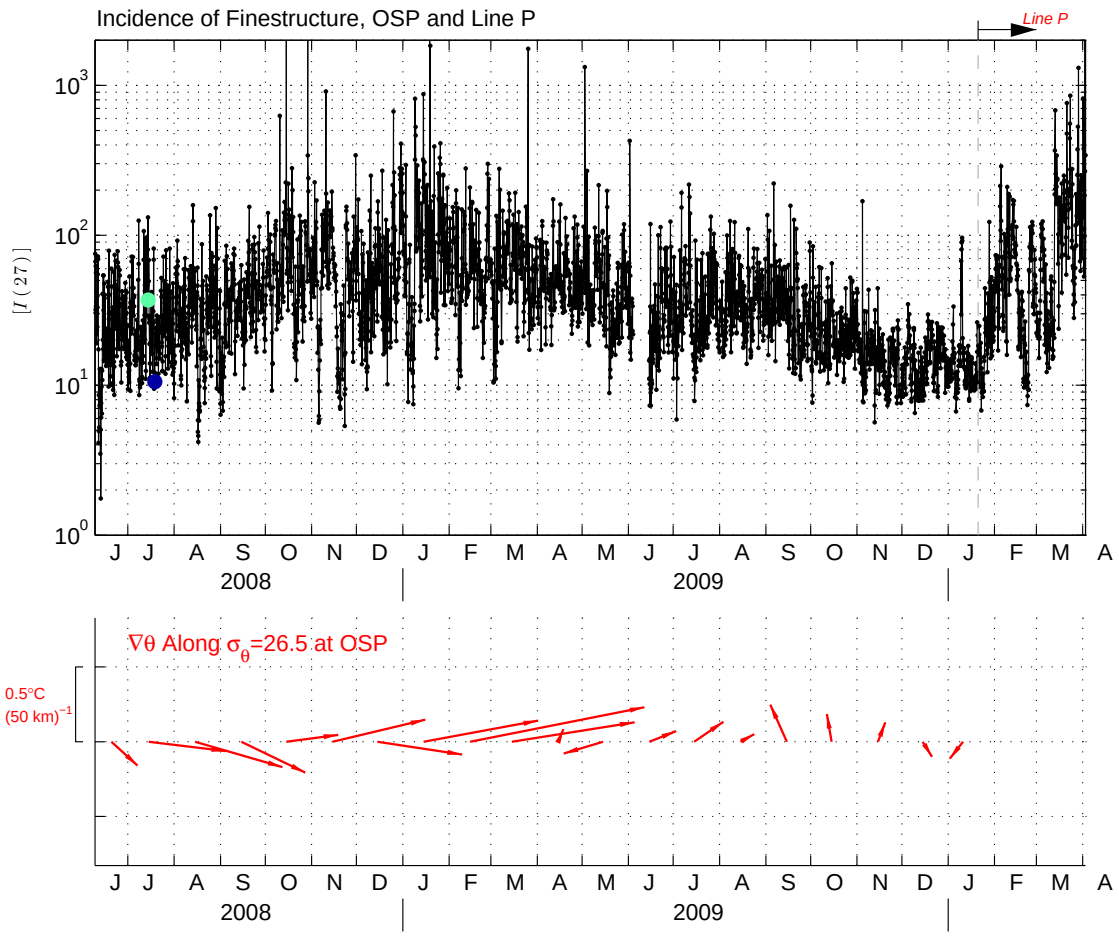

Figure 2.14: Upper panel shows time series of integrated square spice curvature $I(27)$, indicative of the presence of vertical θ-S finestructure within individual Seaglider profiles. Cyan and blue dots in the upper panel correspond to the two example profiles shown in Figure 2.12. The time period shown corresponds to the full extent of Seaglider surveys at Ocean Station Papa (OSP) in addition to Seaglider 144's transit inshore along Line P. Lower panel shows the time series of the horizontal gradient of potential temperature on $\sigma_\theta = 26.5$ (scale at left).

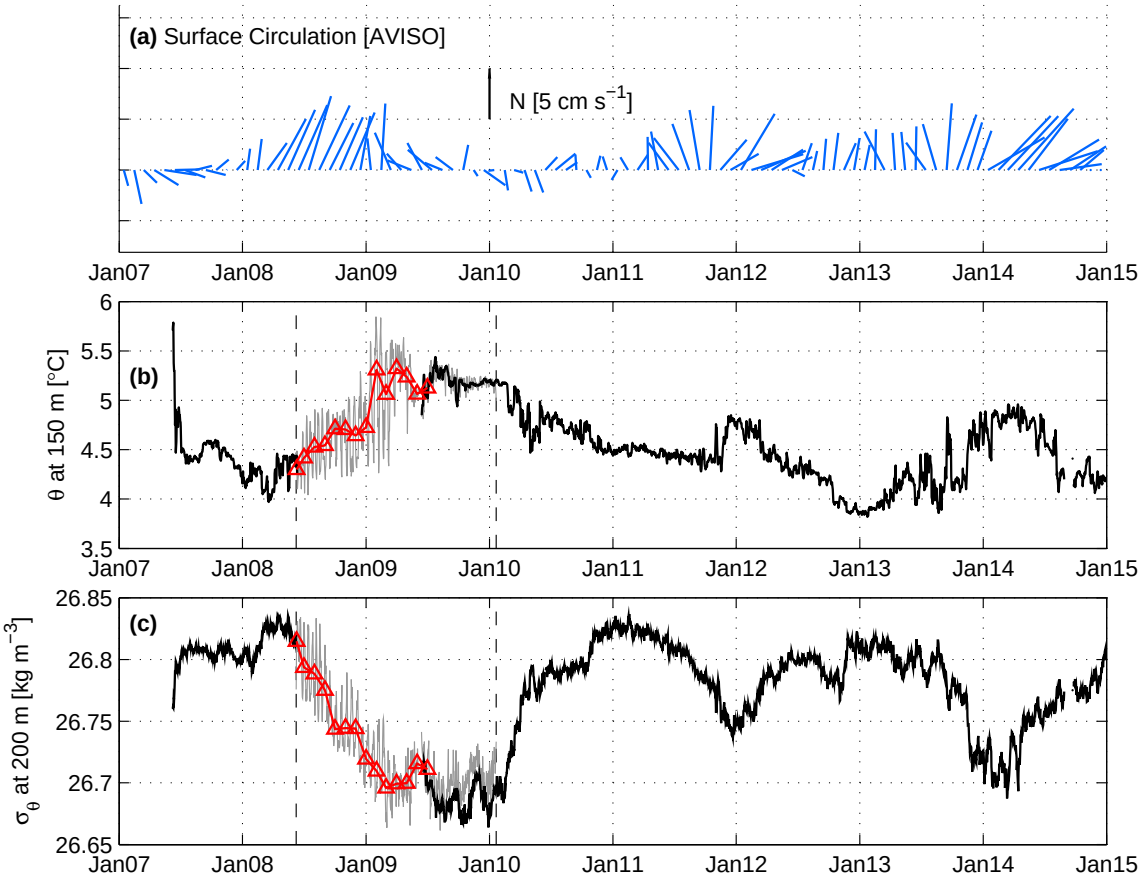

Figure 2.15: Records of (a) surface circulation, (b) potential temperature θ at 150 m, and (c) potential density σ_θ at 200 m during the OSP mooring time series, a subset of which is covered by the Seaglider+mooring array described here (8 June 2008 to 21 January 2010). Vertical dashed lines in panels (b) and (c) indicate the time bounds of the Seaglider surveys at OSP. The black curves in (b) and (c) indicate the mooring record. Gray curves in (b) and (c) indicate Seaglider samples – periodicity in these records is due to spatial variability not sampled by the mooring. The red curves in (b) and (c) indicate monthly estimates of θ or σ_θ at the mooring location (*i.e.*, the center of the Seaglider survey pattern). These curves are plotted only for times at which the mooring was absent from OSP.

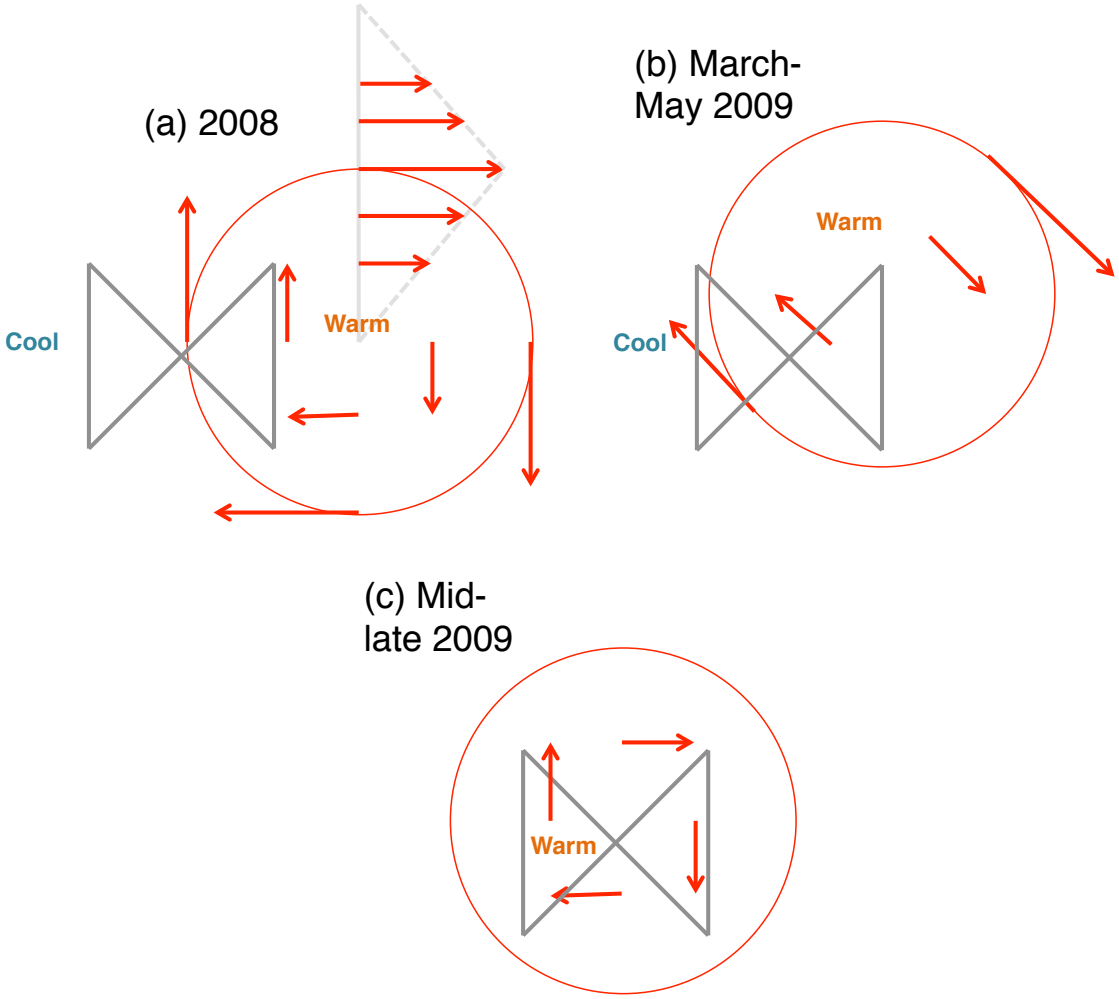

Figure 2.16: Schematic configuration of hypothesized eddy circulation observed during the Seaglider surveys at Ocean Station Papa: (a) 2008, (b) early 2009, and (c) mid- to late-2009. Gray lines show Seaglider survey pattern, red circle indicates eddy maximum velocity radial station, red arrows indicate eddy currents. In (a), the profile of currents as a function of radius is also sketched. 'Warm' and 'Cool' annotations refer to temperatures in the halocline within the interior and exterior of the eddy, respectively.

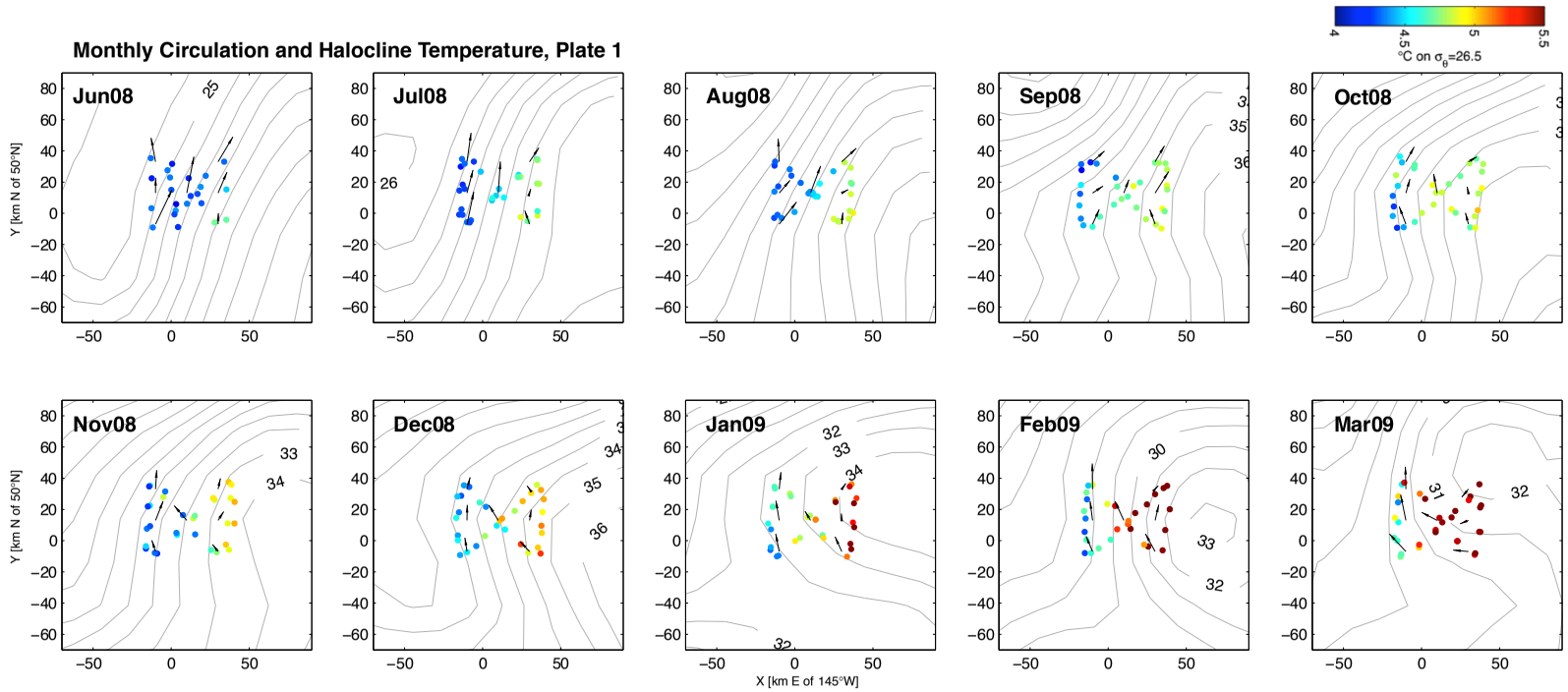

Figure 2.17: Evolution of sea surface height, halocline water mass properties, and depth-averaged current at monthly intervals during Seaglider surveys at Ocean Station Papa, plate 1 of 2 (June 2008 to March 2009). Blue dots in each panel indicate daily-averaged potential temperature along the $\sigma_\theta = 26.5$ isopycnal (scale at upper right). Black vectors indicate Seaglider 0-1000 m depth-averaged currents, averaged in nine discrete zones covering the navigational pattern. Gray contours indicate monthly-average AVISO Absolute Dynamic Topography sea surface height (1 cm contour interval).

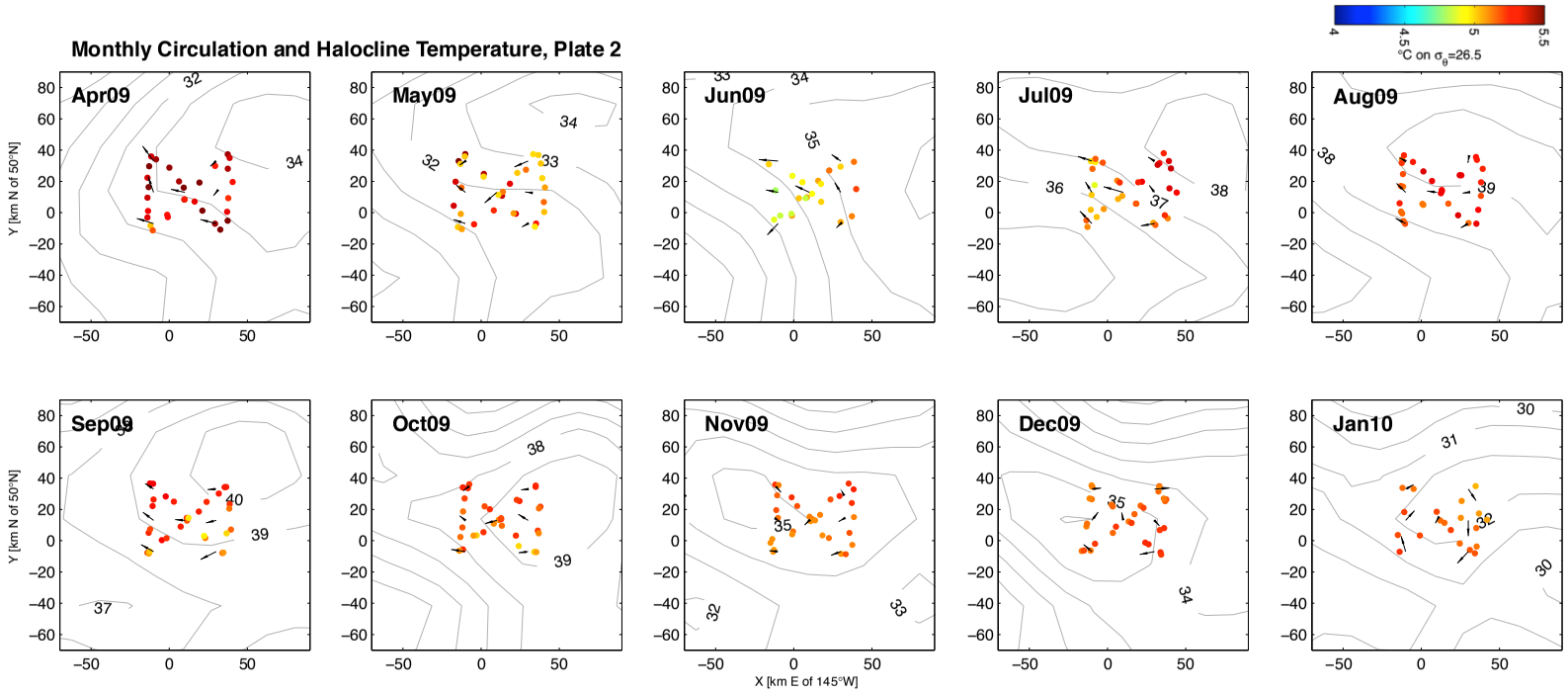

Figure 2.18: Evolution of sea surface height, halocline water mass properties, and depth-averaged current during Seaglider surveys at Ocean Station Papa, plate 2 of 2 (April 2009 to January 2010). Blue dots in each panel indicate daily-averaged potential temperature along the $\sigma_\theta = 26.5$ isopycnal (scale at upper right). Black vectors indicate Seaglider 0-1000 m depth-averaged currents, averaged in nine discrete zones covering the navigational pattern. Gray contours indicate monthly-average AVISO Absolute Dynamic Topography sea surface height (1 cm contour interval).

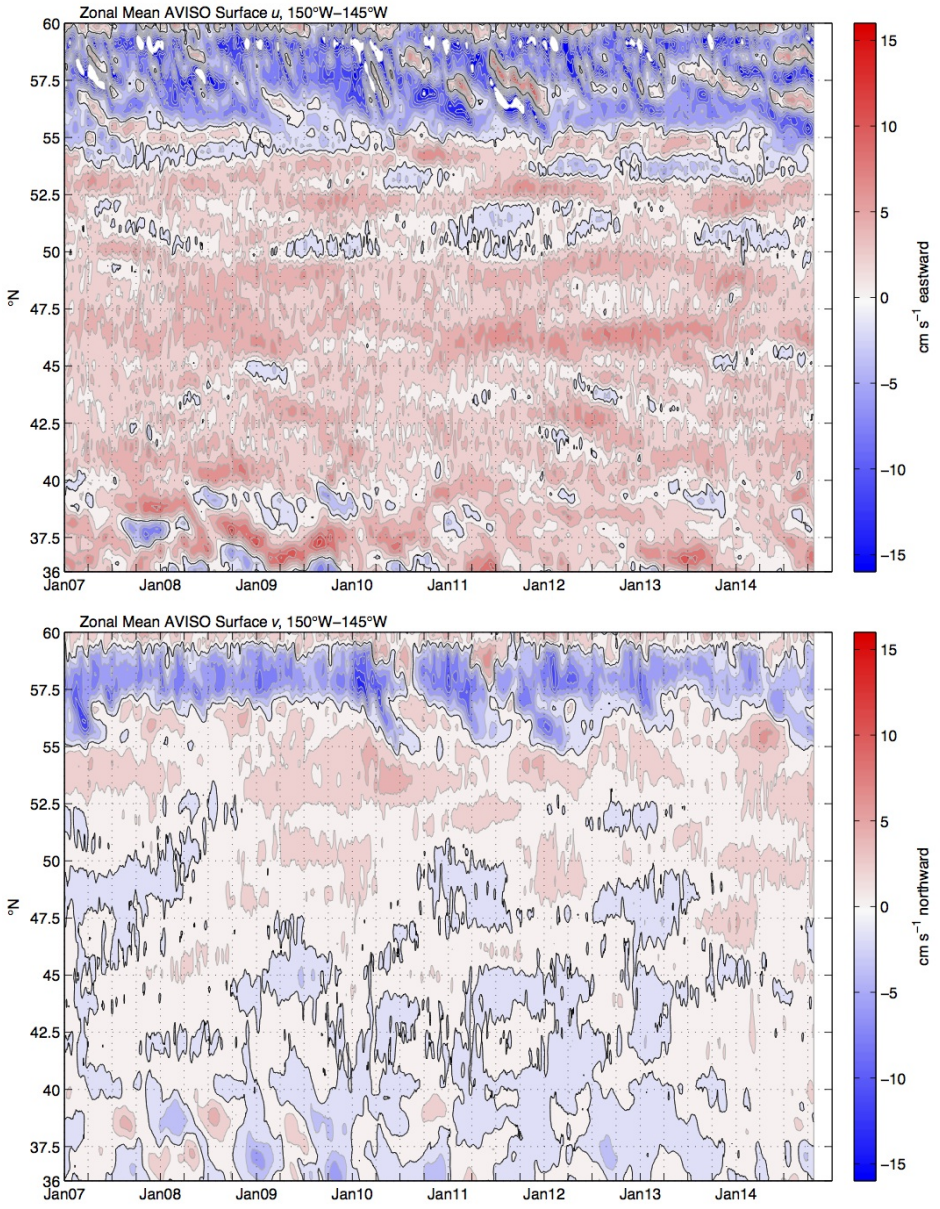

Figure 2.19: Time series of zonal mean eastward (upper panel) and northward (lower panel) flow between longitudes 150°-145°W, from the AVISO all-satellite Absolute Dynamic Topography product.

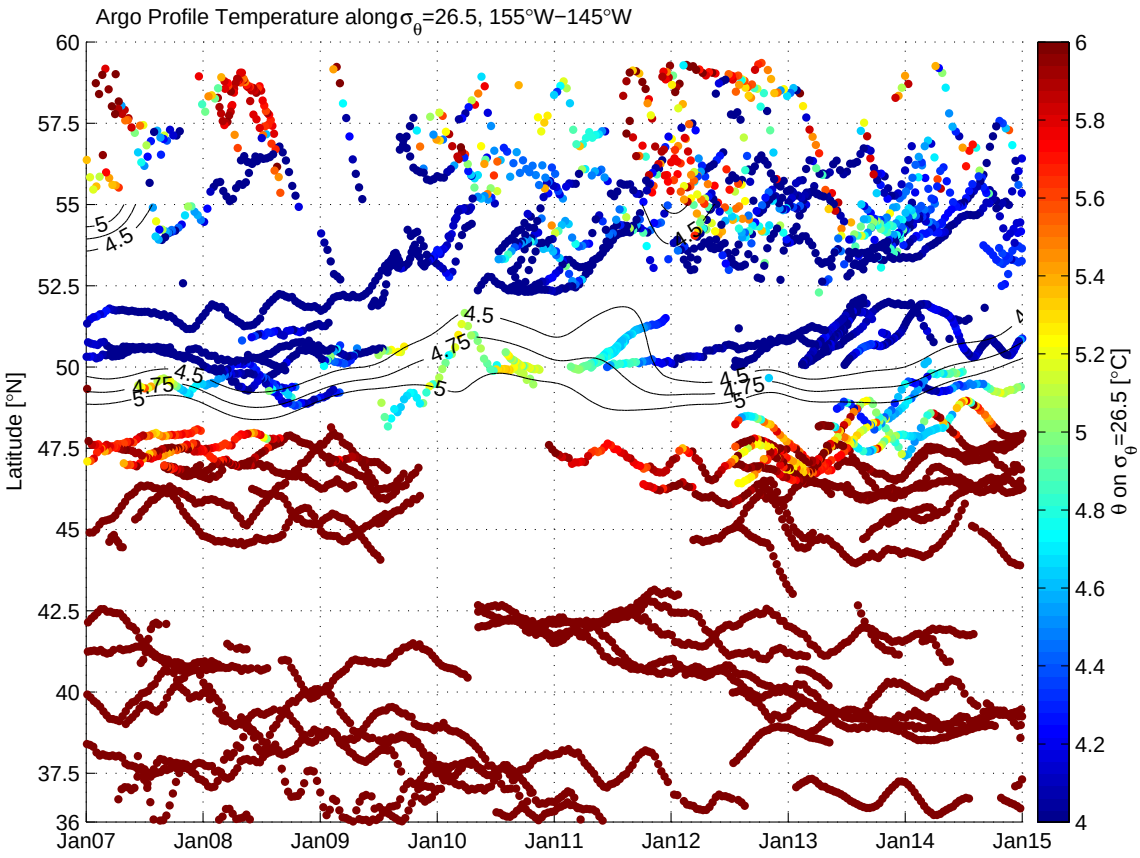

Figure 2.20: Time series of potential temperature θ on $\sigma_\theta = 26.5$ between longitudes 155°-145°W, obtained from Argo profile data. The 4.5°C, 4.75°C, and 5°C contours, approximately representing the boundary between Alaska Gyre and Western Subpolar Water, are also shown. These are obtained using Gaussian smoothing of the profiles shown here to a regular time and latitudinal grid with a three-month time scale and 2° latitudinal scale. The few profiles obtained at latitudes of OSP suggest an increase in θ near 50°N and corresponding northward movement of the AG-WSW boundary from mid-2009 through early 2011, which lags the northward (surface) flow observed in Figure 2.19 by 6-12 months.

Chapter 3

DIAGNOSIS OF HEAT AND SALT BALANCES USING LEAST-SQUARES METHODS WITH INEQUALITY CONSTRAINTS

with Charles C. Eriksen and Meghan F. Cronin

3.1 Introduction

At Ocean Station Papa, (OSP; 50°N, 145°W), in the southern Gulf of Alaska, the dominant features of vertical density stratification in the upper ocean are the permanent halocline and seasonal thermocline [37, 147]. The halocline is a region of strong salinity stratification below the maximum depth of winter mixing, while the shallower seasonal thermocline is formed from solar heating during spring, summer, and fall. During summer and fall the seasonal thermocline is dominated by a vertically narrow, more intense, but ephemeral region of temperature stratification below the surface mixed layer known as the *transition layer*. The latter layer is located at shallow depths (20-40 m) in summer and is steadily eroded and shifted downward by fall and winter mixing driven by wind, surface waves, and heat loss. The halocline, by contrast, is a permanent feature throughout the subarctic North Pacific Ocean resulting from an excess of precipitation over evaporation, in combination with weak exchange between subarctic and subtropical gyres [168, 46]. This layering of fresh near-surface waters above saline intermediate waters reduces the vertical exchange of nutrients between the deep and surface ocean [69] and inhibits the formation of deep water at high latitudes in the North Pacific, such as is observed in the North Atlantic [168]. Lower halocline water is ventilated in the western Pacific and Sea of Okhotsk, while upper halocline water is

ventilated in the central and western Gulf of Alaska [8, 9, 22, 174]. Eastward flow at latitudes 35°N-50°N in the North Pacific Ocean links these ventilation sites with the North American coast [37].

The southern Gulf of Alaska including OSP is a region of net transfer of heat and freshwater from the atmosphere to the ocean [84, 136]. The presence of the permanent halocline underlying a seasonal thermocline has a fundamental influence on the nature of the oceanic mechanisms available to offset these atmospheric inputs at steady state. Over long time scales, due to the strong halocline salinity stratification, any upwelling of cool, deep water that would be large enough to offset the surface heat input would also result in an excessive input of saline water to the surface ocean [147, 84]. This led Large [84] and Tabata [147] to conclude that only weak vertical advection occurs, sufficient to offset the surface freshwater input, while the net heat input is instead mainly removed by horizontal advection. This climatological advective removal of heat is likely due to seasonal flow acting on seasonal horizontal gradients in the upper ocean near OSP, a process that has been observationally confirmed to occur during individual fall seasons [147, 87, 118, 119, 160]. However, as yet, there has not been a systematic observational study of the fate of heat input to the Gulf of Alaska waters over several years. At shorter time scales, horizontal and vertical advection in combination are inferred to be responsible for monthly and interannual anomalies in SST and heat and freshwater content at OSP, which are not correlated with anomalies in surface inputs [84, 75]. Within individual seasons, vertical mixing is important for the redistribution of heat and freshwater input to the upper ocean, transferring heat to the thermocline where it is presumably removed by horizontal advection, and freshwater to the top of the halocline where it strengthens the salinity stratification and maintains the existing vertical structure [84].

Continued observational monitoring of the heat and freshwater cycling at OSP is critical for the understanding of these balances in a climatically- and ecologically-important region. This is especially true in light of recent prominent interannual anomalies in SST in the subarctic North Pacific [171, 12], and evidence of long-term enhancement in stratification,

alterations to the annual cycle of winter mixing, and possible reduction in the availability of nutrients to the surface ocean at OSP ([57, 59, 92], though see [155] for an alternate view). As the above observational and numerical studies indicate, despite the weak horizontal currents and gradients near OSP, horizontal advection plays a fundamental role in the balances at monthly and longer time scales in this region, and its measurement is important to properly resolving the heat and freshwater balances there. Estimating horizontal advection at OSP, especially deeper than the well-mixed surface layer where satellite observations are incapable of measuring circulation or horizontal gradients, requires persistent *in situ* monitoring not available to previous studies that generally spanned a single season. Measurement of horizontal gradients allows the direct computation of advection and geostrophic shear, increasing the number of terms that can be estimated in the heat and salinity balances – which in turn strengthens any inference of the unresolved vertical terms, vertical advection and mixing. The first of these is not currently directly measurable while the second, absent persistent temperature or velocity microstructure measurements, must also be inferred indirectly.

To strengthen the understanding of the above processes in the southern Gulf of Alaska, Seaglider autonomous underwater vehicles were deployed in three missions at OSP from June 2008-January 2010, measuring mesoscale spatial gradients surrounding the site of a NOAA Ocean Climate Stations (OCS) surface fluxes mooring (Chapter 2). The goals of these deployments were to describe the circulation and water mass characteristics surrounding the OCS mooring (Chapter 2), diagnose the balances of heat and freshwater including the influence of horizontal advection and the unresolved vertical terms, and use the physical transports estimated from these balances to evaluate net community production or respiration of oxygen (Chapter 4). This chapter describes the application of Seaglider measurements to the second of these goals, using least-squares methods to determine the most likely combination of three-dimensional advective terms and vertical mixing.

Seagliders provide persistent autonomous measurements of temperature and salinity at high vertical resolution. As a result, the halocline and transition layer are clearly evident in the daily-average stratification observed during Seaglider surveys at OSP (Fig. 3.1a). In

these plots, the square of the buoyancy frequency N^2 is shown, which represents the vertical density stratification absent the effects of seawater compressibility [63, 106]. At OSP, the halocline is a region of enhanced N^2 from 100-175 m depth, with a peak in strength at 125-145 m (Fig. 3.1a). During the OSP Seaglider surveys, the halocline depth range exhibited seasonal and interannual variations, which can be caused by variations in wind-stress curl [29, 30] or passing mesoscale eddies [174, Chapter 2]. The transition layer is evident as a band of high N^2 below the near-zero stratification of the surface layer in summer and fall. The individual contributions to density stratification from temperature (Fig. 3.1b) and salinity (Fig. 3.1c) indicate that the transition layer stratification is almost entirely due to temperature, though has an increasing contribution from salinity as the fall season progresses. Within the halocline, temperature stratification is near-neutral or sometimes unstable (cool water overlying warm, Fig. 3.1b).

Tabata [147] examined changes in heat and freshwater content (through its complement, seawater salinity, as will be done throughout this chapter) during 1956-61 in comparison to those that would be expected based on the estimated surface inputs. Engaging in a similar exercise over the duration of the Seaglider surveys at OSP offers the first suggestion that horizontal advection of heat or freshwater likely played an important role. The surface input of heat during the Seaglider survey time series is estimated to be $1.65\pm0.33\times10^9$ J m^{-2}, which would be sufficient to raise the mean potential temperature of the top 200 m by 2.02°C (Fig. 3.2). This heat input is estimated from a combination of surface fluxes observed by the NOAA OCS mooring at OSP, and other sources during gaps in the mooring time record – this procedure will be described below in Section 3.2. The heat content at OSP instead increased by only $0.58\pm0.11\times10^9$ J m^{-2} (mean temperature increase of 0.71°C), implying a net cooling, likely due to either horizontal or vertical advection. In contrast, the mean salinity change in the top 200 m of -0.136±0.048 is nearly equal to the -0.124±0.066 expected due to dilution from the surface moisture flux (Fig. 3.3). This suggests little net storage of salt due to horizontal and vertical advection (Fig. 3.3).

A simple calculation based on these results illustrates the effect of the differential temper-

ature and salinity stratification at OSP. If the top 200 m heat balance during the Seaglider surveys were closed by constant vertical advection below the surface layer, and corresponding divergent horizontal flow within the surface layer, a mean vertical velocity w of 36±12 m yr^{-1} would be required (if a vertical diffusivity of 10^{-5} m^2 s^{-1} is assumed at 200 m). In contrast, a mean w of -2±7 m yr^{-1} would be required to close the salinity budget. The upwelling required to close the heat budget is significantly larger than that required to close the salt budget. Stated another way, much like the results of Tabata [147], if the observed net removal of heat is to be accounted for by mean vertical advection alone, the resulting import of salt across the halocline would be too large relative to what was observed. While advective processes were likely not steady in time during the Seaglider surveys, this simple exercise demonstrates that if vertical processes alone are to be invoked to close the heat and salinity budgets simultaneously, they at least must be time-varying. As will be shown below, horizontal advection was indeed active in the top 200 m during the Seaglider survey time period, though in a manner contrary to the climatological conventions described above, importing fresh water from the south and east without importing a significant amount of heat. This violation of climatological balances reflects the anomalous, eddy-like circulation observed at OSP during the Seaglider surveys (Chapter 2).

In this chapter, the goal is to accurately determine the time-varying horizontal and vertical velocity components and turbulent diffusivities within the top 200 m during Seaglider surveys at OSP (the *unknowns*). The method employed here is to form a large set of equations governing the unknowns, and solve these equations using least-squares methods, with inequality constraints acting on the unknown turbulent diffusivities such that they must be at least as large as an assumed, weak interior diffusivity – known as linear least-squares with inequality constraints ("problem LSI;" [90]). This method has been employed by several investigators to determine unknown velocity and diffusivity components from tracer data in oceanographic or limnologic problems [*e.g.,* 115, 163, 5], including in the OSP area by Matear [104]. Unlike the problem posed by [104], the unknowns in this case are time-dependent. In this work, an extension of the typical application of problem LSI is proposed, in which the

problem is formulated such that the unknowns satisfy the time-integrated budgets of temperature and salinity, and the solution for all unknowns throughout the time series is obtained simultaneously. In addition to allowing tracer observations at a time t to provide information about unknowns at all times prior to t, minimizing the time-integral of error in the physical balances is also advantageous for diagnosing the balance of dissolved oxygen, which will be addressed in Chapter 4.

Other approaches to time-dependent inverse problems exist, such as assimilating observations into a dynamical model using the Kalman filter, 4D-variational assimilation, or the method of Lagrange multipliers. Like this study, these methods seek to estimate a "state vector" or solution that can include unknown horizontal velocities and diffusivities, and potentially also horizontal and vertical gradients (such that products of multiple elements of the state vector are considered, creating a nonlinear problem), by minimizing an objective function that takes into account observational and model uncertainty [180]. This study uses the least-squares method with inequality constraints because of its precedent of use in the OSP area, the transparency of the formulation and scaling of the objective function, and the linear relationship between the unknowns to be considered and the observations. After a solution is obtained, the structure of the corresponding advective and turbulent transports is investigated, and the results applied to the balances of temperature and salinity in the top 200 m. In what follows, Section 3.2 provides details of the measurements and the formulation of the least-squares problem. Section 3.3 describes the results, while a discussion follows in Section 3.4. Section 3.5 provides a summary and conclusions.

3.2 Methods

3.2.1 Measurements and Surface Fluxes

Seagliders surveyed at OSP from 8 June 2008 to 21 January 2010 in a series of three deployments. Sampling strategy and processing methods are described in detail in Chapter 2 and are briefly summarized here. Seagliders performed 1700 dive-climb cycles, collecting 3400 ver-

tical profiles, while sampling temperature, salinity, pressure, dissolved oxygen, fluorescence, and optical backscatter from the surface to 1000 m depth along a 1:3 (vertical:horizontal) glide slope. Seagliders sampled within a 50×50 km box around the NOAA OCS mooring site, repeating a "butterfly"-shaped navigational track every 14.5 days on average. Each repeat consisted of 36-59 dive-climb cycles, with a median number of 43. After each dive-climb cycle, comparison of Seaglider dead-reckoned surface position to the observed surface position also gives an estimate of 0-1000 m depth-averaged current (DAC).

Seaglider samples of potential temperature θ, salinity S, dissolved oxygen $[O_2]$, and density ρ in the top 200 m were bin-averaged in depth for each profile. Depth bins will be referred to with depth index i. Depth bin spacing is 2 m vertically in the top 150 m, and 5 m vertically below, yielding $n_i = 86$ depth grid points in the top 200 m. Horizontal gradients of scalar variables in each bin are estimated in monthly time intervals using least-squares fits as described in Chapter 2. The monthly time interval corresponds to roughly the time required for a glider to make two complete occupations of the transect pattern, and is the finest time scale on which it can be reasonably expected that the Seaglider surveys provide robust information about the horizontal gradients in the 50×50 km box around OSP. Time intervals are indicated by the index j, and the duration of the time series yields $n_j = 20$ intervals. Mean vertical profiles of all scalar variables are estimated by time-averaging the binned samples within each monthly interval. These profiles are used to evaluate the stratification and vertical derivatives of θ and S within each monthly interval. The n_j time intervals and n_i depth bins between the surface and 200 m depth define the temporal and vertical domain in which the unknown physical transports are to be estimated.

Vertical profiles of each variable are also estimated center of the Seaglider track pattern at the preceding and following edges of each monthly time interval. These profiles are used to evaluate the time derivatives of θ and S in the regression problem attempted here, and are correspondingly given time indices with partial notation (*e.g.,* $\theta_{i,0.5}, \theta_{i,1.5}, \ldots, \theta_{i,n_j-0.5}, \theta_{i,n_j+0.5}$, such that $\theta_{i,12.5}$ indicates potential temperature estimated at depth i and at the time boundary between intervals $j = 12$ and $j = 13$). These profiles are estimated using a uniform-

weighting local regression procedure. Denote $t_{n+0.5}$ as the time at the following edge of the monthly interval n at which a vertical profile is to be estimated. At each depth level i, all samples collected within ± 15 d of $t_{n+0.5}$ are selected and fit with a regression equation of the form (*e.g.,* for salinity)

$$\hat{S} = a_1(x - x_0) + a_2(y - y_0) + a_3(t - t_{n+0.5}) + a_4(t - t_{n+0.5})^2 + a_5 \tag{3.1}$$

where $a_{1,2,\ldots,5}$ are regression coefficients, $x - x_0$ and $y - y_0$ are the zonal and meridional distances relative to the center of the Seaglider navigational track pattern, and $\hat{S}$ indicates salinity predicted by the regression fit. The choice of predictors in this regression equation is discussed in Chapter 2. The coefficient a_5 is the estimate of S at depth i and time $t_{n+0.5}$ at the center of the Seaglider survey pattern, denoted by $S_{i,n+0.5}$.

Uncertainty in these profiles, and thus the uncertainty on net storage of heat or salt in the top 200 m during Seaglider surveys quoted in Section 3.1, was assessed using a noise perturbation scheme to the estimated regression fit (3.1). In each depth bin i, after the fit (3.1) was estimated, 100 further iterations were performed. In each iteration, random noise was added to the fit at each sample, with variance and time autocorrelation of the noise prescribed to be similar to that of the residuals between observations and the original fit. Following the addition of noise, another fit was performed to the noise-perturbed data from that iteration. The standard deviation of the coefficient a_5 across 100 noise-perturbed fits gives an estimate of its root-mean square (RMS) uncertainty. For estimating the corresponding uncertainty in the vertical integral of each profile, it was assumed that the vertical correlation of errors in a_5 between depths was similar to the correlation of residuals to the fit (3.1) at different depths. The uncertainty in the vertical integrals at the first and last time points were used to produce the uncertainties in net heat and salinity changes during the Seaglider surveys described in Section 3.1.

When available, this study uses daily-averaged net surface heat and moisture fluxes estimated by Cronin et al. (M.F. Cronin, N.A. Pelland, S.R. Emerson, and W.R. Crawford,

Estimating diffusivity from the mixed layer heat and salt balances in the North Pacific, manuscript submitted to Journal of Geophysical Research-Oceans) from observations collected by the NOAA OCS mooring deployed at OSP from June 2007-present. The OCS mooring samples wind speed and direction, air temperature, relative humidity, downwelling short- and long-wave radiation, rain rate, and barometric pressure; the sampling strategies for these instruments are described by Cronin et al. [24] and Cronin et al. (submitted manuscript), while measurement errors are discussed in Kubota et al. [81]. Latent and sensible heat fluxes were computed using the Coupled Ocean-Atmosphere Response Experiment (COARE) 3.0 algorithm [49] with warm layer and coolskin corrections, while net solar and longwave radiation was estimated using the measured downwelling values and a seasonal cycle for surface albedo based on the International Satellite Cloud Climatology Project (ISCCP; `http://isccp.giss.nasa.gov/`). Rain gauge measurements were corrected for wind effects following [137], while evaporation was estimated using estimated latent heat flux and buoy-measured sea surface temperature.

During Seaglider surveys at OSP, a mooring line failure occurred on 11 November 2008, and mooring surface fluxes were unavailable from that date until redeployment on 14 June 2009. During this period, and any other gaps in surface fluxes due to buoy hardware failures, daily-average latent and sensible heat fluxes were obtained from the Objectively Analyzed air-sea Fluxes for the Global Oceans (OAFLUX) dataset [182, `http://oaflux.whoi.edu/heatflux.html`]. Data provided by the International Satellite Cloud Climatology Project [184], also hosted at the OAFLUX webiste, were used to estimate surface radiative fluxes. These data were provided on a 1° grid at daily resolution. Comparison of the ISCCP estimates of net upward longwave flux to daily-average OCS buoy-based measurements during periods of overlap in 2007-2009 indicated a bias of -11.0±6.5 W m^{-2} (ISCCP minus buoy). The confidence interval on this bias is 95% based on a Student's-t distribution with 24 degrees of freedom, which is the number of months of overlap between ISCCP and OCS mooring estimates. Similarly, OAFLUX sensible heat flux estimates were found to have a bias of -6.4±2.6 W m^{-2} relative to buoy-based estimates. After correcting the ISCCP outgoing

longwave and OAFLUX sensible heat fluxes for these biases, the resulting monthly-average net heat flux from OAFLUX+ISCCP had a bias relative to the buoy of 0.8 W m^{-2} and RMS difference of 18.3 W m^{-2} during periods of overlap. In comparison, RMS monthly-average net surface heat flux measured from the mooring was 108 W m^{-2} during the period 2007-2009. Latent heat fluxes from OAFLUX and ISCCP net shortwave radiation were not found to have significant biases (2.1±3.6 W m^2 and -1.6±11.0 W m^2, respectively) within the period of overlap with the OCS buoy, and these components of the net surface heat flux were not altered.

The uncertainty on the total surface heat flux during the Seaglider surveys listed in Section 3.1 was computed as follows. For the OCS mooring-based fluxes, an uncertainty in the time-series mean sensible and latent heat fluxes of ±5.7 W m^{-2} was assumed. The mean radiative fluxes were assumed to have an uncertainty of 1%. These bias levels follow those used in uncertainty analyses of Cronin et al. [24], and correspond to uncertainties associated with the mean heat flux during the time period covered by the mooring only. An additional uncertainty of 3 W m^{-2} was assumed for the period of time covered by the OAFLUX+ISCCP fluxes, which represents the mean bias in heating rate associated with selecting an arbitrary portion of time from the OAFLUX record equal in length to the mooring data gap during the Seaglider time series. This gives a total uncertainty of 6.5 W m^{-2} in the mean heating rate 8 June 2008-21 January 2010.

Net moisture flux during mooring absence was estimated as the difference between OAFLUX net surface evaporation and Global Precipitation Climatology Project (GPCP) 1DD V1.2 daily precipitation estimates [73, `http://precip.gsfc.nasa.gov/gpcp_daily_comb.html`]. Monthly-average precipitation estimates from the GPCP product were compared to those of the OCS mooring during periods of overlap between the instruments in the years 2007-2013. The monthly-average GPCP product P_{GPCP} was found to overestimate the precipitation relative to the OCS mooring; estimates of P_{GPCP} (units of cm d^{-1}) were corrected according to

$$P_{\mathrm{GPCP,cor}} = 0.6643 P_{\mathrm{GPCP}} + 0.0375 \tag{3.2}$$

which was determined from a linear least-squares fit to mooring monthly-average precipitation versus that from GPCP. Similarly, OAFLUX evaporation E_{OA} (units of cm d^{-1}) was corrected according to

$$E_{\mathrm{OA,cor}} = 1.0125 E_{\mathrm{OA}} - 0.0168. \tag{3.3}$$

Following these corrections, the RMS disagreement between monthly-average $E - P$ estimated from the OCS mooring and from the OAFLUX and GPCP products was 0.077 cm d^{-1}. In comparison, RMS monthly-average net moisture flux measured from the mooring was 0.156 cm d^{-1} during 2007-2009. For estimates of uncertainty in the net moisture flux across the entire time series used in Section 3.1, a 25% uncertainty was assumed in mooring estimates of evaporation minus precipitation. An additional uncertainty of ± 0.06 cm d^{-1} was assumed for net moisture flux from the OAFLUX+GPCP products. Similar to the heat flux uncertainties described above, this was the level of error associated with selecting an arbitrary portion of the OAFLUX record equal in length to the mooring gap during the time series.

Wind stress curl estimates used in this study were derived from the Cross-Calibrated Multi-Platform (CCMP) L3.0 6-hourly 0.25° gridded winds obtained from the Physical Oceanography Distributed Active Archive Center (PODAAC; `http://podaac.jpl.nasa.gov`). The CCMP product produces a high-resolution gridded product that incorporates cross-calibrated measurements from satellite microwave radiometers and scatterometers and combines these with *in situ* measurements and a first guess of the gridded wind field based on ECMWF reanalysis. This product was chosen because of its incorporation of multiple data sources, high temporal and spatial resolution, and temporal duration that spanned the Seaglider time series at OSP. Winds in the CCMP product were converted to wind stresses using the drag coefficient dependence on wind speed of Large and Pond [89] and wind stress curl was computed using centered first-differences of the 6-hourly gridded stress field and interpolated to the latitude and longitude of OSP.

3.2.2 Principle

The velocity components and turbulent diffusivities during the Seaglider surveys at OSP compose a set of unknowns, and a conventional approach is to use the balances of temperature and salinity to form a set of equations that governs them. The problem solution is taken to be the set of unknowns that best satisfies the equations in a least-squares sense. This study will consider the role of both horizontal and vertical advection, as well as vertical turbulent diffusion, in equations for temperature and salinity, as will be described below. However, to first illustrate the conceptual framework that is used to pose the least-squares problem, this section considers a simplified example of this technique. Consider formulating a set of equations for the one-dimensional (vertical) balances of potential temperature θ and salinity S at a single depth and time interval, in which the effects of only vertical advection and turbulent diffusion are included:

$$\frac{\partial \theta}{\partial t} = -w\frac{\partial \theta}{\partial z} + \kappa\frac{\partial^2 \theta}{\partial z^2} + \epsilon_\theta \tag{3.4}$$

$$\frac{\partial S}{\partial t} = -w\frac{\partial S}{\partial z} + \kappa\frac{\partial^2 S}{\partial z^2} + \epsilon_S, \tag{3.5}$$

where w is the unknown vertical velocity, and κ is an unknown vertical turbulent diffusion coefficient, which in this case is assumed to be invariant in the vertical. The vertical and temporal derivatives in (3.4) and (3.5) are the observed quantities, and $\epsilon_{\theta,S}$ are residual terms that account for errors in these observed quantities, or unresolved processes. Recasting this problem in matrix form yields

$$\mathbf{C}\vec{w} = \vec{p} + \vec{\epsilon}, \tag{3.6}$$

where

$$\mathbf{C} = \begin{bmatrix} -\frac{\partial \theta}{\partial z} & \frac{\partial^2 \theta}{\partial z^2} \\ -\frac{\partial S}{\partial z} & \frac{\partial^2 S}{\partial z^2} \end{bmatrix} \tag{3.7}$$

and $\vec{w} = [w\ \kappa]^T$, $\vec{p} = [\partial\theta/\partial t\ \partial S/\partial t]^T$, $\vec{\epsilon} = [\epsilon_\theta\ \epsilon_S]^T$, and superscript T indicates a transpose. The least-squares solution is then a vector $\vec{w}$ that minimizes $|\mathbf{C}\vec{w} - \vec{p}|^2 = |\vec{\epsilon}|^2$; *i.e.,* one that

minimizes the sum of squares of the residual of the θ and S balances, $\epsilon_\theta^2 + \epsilon_S^2$.

Consider now an extension to the above problem, in which there are observations of vertical and temporal gradients at a second time interval subsequent to the first. In this problem there are four unknowns, w and κ at times 1 and 2. One approach is to form another system of equations comparable to (3.6) at time 2, and solve this second system for the second set of unknowns. Solutions obtained in this way would minimize the total sum of square errors in $\partial\theta/\partial t$ and $\partial S/\partial t$ across times 1 and 2.

Alternately, a single system of four equations could be formed, where these equations govern not the local rate-of-change of θ or S, but instead the total change from the time series onset:

$$\Delta t \times \begin{bmatrix} -\frac{\partial\theta}{\partial z}\big|_1 & \frac{\partial^2\theta}{\partial z^2}\big|_1 & 0 & 0 \\ -\frac{\partial S}{\partial z}\big|_1 & \frac{\partial^2 S}{\partial z^2}\big|_1 & 0 & 0 \\ -\frac{\partial\theta}{\partial z}\big|_1 & \frac{\partial^2\theta}{\partial z^2}\big|_1 & -\frac{\partial\theta}{\partial z}\big|_2 & \frac{\partial^2\theta}{\partial z^2}\big|_2 \\ -\frac{\partial\theta}{\partial z}\big|_1 & \frac{\partial^2\theta}{\partial z^2}\big|_1 & -\frac{\partial\theta}{\partial z}\big|_2 & \frac{\partial^2\theta}{\partial z^2}\big|_2 \end{bmatrix} \begin{bmatrix} w_1 \\ \kappa_1 \\ w_2 \\ \kappa_2 \end{bmatrix} = \Delta t \times \begin{bmatrix} \frac{\partial\theta}{\partial t}\big|_1 \\ \frac{\partial S}{\partial t}\big|_1 \\ \frac{\partial\theta}{\partial t}\big|_1 + \frac{\partial\theta}{\partial t}\big|_2 \\ \frac{\partial S}{\partial t}\big|_1 + \frac{\partial S}{\partial t}\big|_2 \end{bmatrix} + \begin{bmatrix} \epsilon_{\Delta\theta_1} \\ \epsilon_{\Delta S_1} \\ \epsilon_{\Delta\theta_{1:2}} \\ \epsilon_{\Delta S_{1:2}} \end{bmatrix}, \qquad (3.8)$$

where subscripts indicate the unknowns or observed quantities at time 1 or 2, and Δt is the duration of the time interval corresponding to each set of observations. An important point is that the $\mathbf{C}$ matrix in this system is block lower-triangular, rather than block-diagonal, as would be the case if the balances were formed in terms of local rate-of-change. As a result, the equations governing the unknowns at time 2 are not independent from those at time 1, and later observations can provide information about the unknowns in an earlier time.

Solutions to this system minimize the sum of square errors $\sum_{n=1}^{2} \epsilon_{\Delta\theta_{1:n}}^2 + \sum_{n=1}^{2} \epsilon_{\Delta S_{1:n}}^2$, where for θ,

$$\epsilon_{\Delta\theta_{1:n}} = \Delta\theta_{1:n} - \sum_{j=1}^{n} \Delta t \left[-w_j \left.\frac{\partial\theta}{\partial z}\right|_j + \kappa_j \left.\frac{\partial^2\theta}{\partial z^2}\right|_j \right] \qquad (3.9)$$

and $\Delta\theta_{1:n} = \sum_{j=1}^{n} \Delta t \left.\frac{\partial\theta}{\partial t}\right|_j$ is the total change in θ from times 1 through n. The second term can also be expressed as the total change in θ predicted by the solution, denoted by $\Delta\hat{\theta}_{1:n}$.

In this way, the solution minimizes the sum of square errors in the integral of $\frac{\partial\theta}{\partial t}$, $\frac{\partial S}{\partial t}$ rather than minimizing errors in $\frac{\partial\theta}{\partial t}$, $\frac{\partial S}{\partial t}$ at each time interval.

Denote the temperature before or after interval n as $\theta_{n-0.5}$ and $\theta_{n+0.5}$, respectively. Then the estimate of temperature at $n+0.5$ given by the solution $\hat{\theta}_{n+0.5}$ is

$$\hat{\theta}_{n+0.5} = \theta_{0.5} + \epsilon_{\theta_{0.5}} + \Delta\hat{\theta}_{1:n} + \epsilon_{\Delta\theta_{1:n}} \tag{3.10}$$

where $\epsilon_{\Delta\theta_{1:n}}$ is the error in temperature change predicted by the least-squares solution, and $\epsilon_{\theta_{0.5}}$ is the error in observed temperature at the start of the time series. In the limit $\epsilon_{\theta_{0.5}} \to 0$, the error in $\hat{\theta}_{n+0.5}$ is equal to $\epsilon_{\Delta\theta_{1:n}}$. In other words, if the observed temperature prior to time 1 is known exactly, minimizing error in the system (3.8) is equivalent to minimizing the square error between the observed $\theta(t)$, $S(t)$ and that predicted by the solution, $\hat{\theta}(t)$, $\hat{S}(t)$.

This formulation of the residuals of the least-squares problem is also motivated by Chapter 4, in which the velocities and turbulent diffusivity coefficients obtained here are to be applied to estimation of the biological net community production (NCP) of dissolved oxygen. This quantity is of interest because, if integrated vertically to the maximum depth of winter mixing and over a sufficient period of time, the NCP of dissolved oxygen is roughly proportional to the amount of organic carbon exported from the upper ocean. The net biological production (or respiration) of oxygen appears as an additional source (or sink) term in the conservation equation for dissolved oxygen; *e.g.,* in the one-dimensional example here,

$$\frac{\partial[\mathrm{O_2}]}{\partial t} = -w\frac{\partial[\mathrm{O_2}]}{\partial z} + \kappa\frac{\partial^2[\mathrm{O_2}]}{\partial z^2} + J^{\mathrm{bio}} \tag{3.11}$$

where $[\mathrm{O_2}]$ is the dissolved oxygen concentration per unit mass (units of μmol $\mathrm{O_2}$ kg^{-1}), and J^{bio} is its rate of biological production. The latter quantity can be esimated simply as a residual between the left-hand side of equation (3.11) and the first two terms on the right-hand side. Thus, in this simple example, the NCP per unit mass of seawater integrated

over times 1 and 2 would be estimated as

$$\mathrm{NCP}_{1-2} = \sum_{j=1}^{2} \Delta t \times J_j^{\mathrm{bio}} = ([\mathrm{O_2}]_{2.5} - [\mathrm{O_2}]_{0.5}) - \sum_{j=1}^{2} \Delta t \left[-w_j \left. \frac{\partial [\mathrm{O_2}]}{\partial z} \right|_j + \kappa_j \left. \frac{\partial^2 [\mathrm{O_2}]}{\partial z^2} \right|_j \right], . \quad (3.12)$$

It is clear that the right-hand side of (3.12) has the same form as the right-hand side of (3.9) – that is, the calculation of NCP depends on a time-integral of the balance of physical transports of oxygen. In order to determine these transports, a reasonable approach is to formulate the least-squares problem in a way that penalizes errors in the time-integrated θ and S balances, since it is this error that is most relevant to NCP. This chapter uses the above principle to estimate the unknown transports during the during Seaglider surveys at OSP using a large-scale, overconstrained least-squares problem.

3.2.3 Problem Formulation

Tracer Equations

The core of the problem consists of simplified versions of the heat and salt conservation equations, *e.g.* for heat

$$\frac{D\theta}{Dt} \left(\equiv \frac{\partial \theta}{\partial t} + \vec{u} \cdot \nabla \theta \equiv \frac{\partial \theta}{\partial t} + u \frac{\partial \theta}{\partial x} + v \frac{\partial \theta}{\partial y} + w \frac{\partial \theta}{\partial z} \right) = -\frac{\partial}{\partial z} \left(\overline{w'\theta'} + \frac{I}{\rho_0 c_p} \right), \quad (3.13)$$

where (u, v, w) are respectively the velocity components in the zonal, meridional, and vertical directions, $\overline{w'\theta'}$ is the turbulent vertical transport of temperature, and I is the vertical profile of penetrative solar radiation, all of which are functions of z and t. Horizontal turbulent transport has been neglected, and the volumetric heat capacity $\rho_0 c_p$ has been assumed constant at 4.092 $\times 10^6$ J $^\circ\mathrm{C}^{-1}$ m^{-3}. Later sections will investigate further simplification

of (3.13). Integrating (3.13) between a starting time t_s and final time t_f yields

$$\theta(z,t_f)-\theta(z,t_s)=-\int_{t_s}^{t_f}\left[u(z,\tau)\frac{\partial\theta(z,\tau)}{\partial x}+v(z,\tau)\frac{\partial\theta(z,\tau)}{\partial y}+w(z,\tau)\frac{\partial\theta(z,\tau)}{\partial z}\right]\mathrm{d}\tau- \int_{t_s}^{t_f}\frac{\partial}{\partial z}\left(\overline{w'\theta'}(z,\tau)+\frac{I(z,\tau)}{\rho_0 c_p}\right)\mathrm{d}\tau, \quad (3.14)$$

where τ represents a dummy variable of integration with respect to time.

If the time integral in (3.14) spans the first M time intervals, such that $t_s = t_{0.5}$ and $t_f = t_{M+0.5}$, then (3.14) becomes, in discrete form, for any depth bin i

$$\theta_{i,M+0.5}-\theta_{i,0.5}=-\sum_{j=1}^{M}\Delta t_j\left[u_{ij}\left.\frac{\partial\theta}{\partial x}\right|_{ij}+v_{ij}\left.\frac{\partial\theta}{\partial y}\right|_{ij}+w_{ij}\left.\frac{\partial\theta}{\partial z}\right|_{ij}\right]- \sum_{j=1}^{M}\frac{\Delta t_j}{\Delta z_i}\left[\left.\overline{w'\theta'}\right|_{i+0.5,j}-\left.\overline{w'\theta'}\right|_{i-0.5,j}+(\rho_0 c_p)^{-1}\left(I_{i+0.5,j}-I_{i-0.5,j}\right)\right], \quad (3.15)$$

in which summations over the first M time intervals approximate the time integrals of advection, turbulent diffusive convergence, and radiative absorption. M can be any positive integer from 1 to n_j. For the convergence of turbulent transport and radiative absorption – the second term on the right-hand side of (3.15) – a centered finite-difference scheme around the vertical grid level i approximates the vertical derivative $\frac{\partial}{\partial z}$. The difference has been taken between the layer interfaces at the top and bottom of depth bin i, denoted by indices $i+0.5$ and $i-0.5$ respectively, which are separated by a vertical distance Δz_i. Equation (3.15) represents a more general version of the one-dimensional vertical balance (3.9) described in the prevoius section. Note that in (3.15), the error term has been omitted for simplicity, as will be the case for all equations that follow.

The discrete, time-integrated balance (3.15) forms the bulk of the equations that compose the least-squares problem described here. Using (3.15), for each time interval j one can write n_i temperature balance equations that govern the change in temperature at depth i

betwen the beginning of the time series and time $j + 0.5$. This yields $n_i \times n_j$ total equations for temperature during the time series, and one can write a comparable number for salinity. In principle, these equations can then be solved for the unknown u_{ij}, v_{ij}, w_{ij}, and turbulent transports, though such a system has more unknowns than equations, as currently constructed. The following describes in increments the formulation of a time-series-wide system of equations, starting with the balance (3.15), and continuing to add simplifications that reduce the number of unknowns or further adds equations that serve to overconstrain the solution.

The simplest discrete form of the balance (3.15) governs the evolution of temperature as a function of the unknowns within only a single time interval, *e.g.*, if the summations in equation(3.15) are taken only over the first $M = 1$ interval. In this case, equation (3.15) becomes

$$\theta_{i,1.5} - \theta_{i,0.5} = -\Delta t_1 \left[u_{i1} \left.\frac{\partial \theta}{\partial x}\right|_{i1} + v_{i1} \left.\frac{\partial \theta}{\partial y}\right|_{i1} + w_{i1} \left.\frac{\partial \theta}{\partial z}\right|_{i1} \right] - \frac{\Delta t_1}{\Delta z_i} \left[\left.\overline{w'\theta'}\right|_{i+0.5,1} - \left.\overline{w'\theta'}\right|_{i-0.5,1} + (\rho_0 c_p)^{-1} \left(I_{i+0.5,1} - I_{i-0.5,1}\right) \right]. \quad (3.16)$$

Equation (3.16) expresses the temperature balance for each of the n_i depth bins at time $j = 1$, as a function of the unknown velocity components at each depth bin (u_{i1}, v_{i1}, w_{i1}) and the unknown turbulent transports $\overline{w'\theta'}$. At this stage there are $4n_i$ unknowns in the n_i temperature equations in the first time interval: n_i unknowns for each of the three velocity components, and n_i unknown turbulent fluxes (if it is assumed that the surface turbulent fluxes are known). The radiative flux can be specified separately from the measured solar heating and empirically-determined functional forms of $I(z)$.

Simplifying the Unknowns

The number of unknowns can be reduced by parameterizing the turbulent transport, which is assumed to take one of three forms depending on vertical location. At each time interval

j, the observed stratification is used to delineate three separate vertical regions of the upper 200 m, which are, from top to bottom, a well-mixed surface layer (hereafter abbreviated "SL"), a stratified transition layer (TL), and the interior region (INT). These regions are defined based on the profile of N^2 defined from the monthly-average temperature and salinity stratification. Searching downward from the surface, the first depth bin in which N^2 reaches 10% of its peak value in the top 200 m in its respective monthly time interval is defined as the uppermost depth bin in the TL. The time-varying depth of this uppermost TL bin is denoted h_j. The SL in each time interval is composed of all depth bins with $-h_j < z_i \leq 0$. Depth bins with $-H_j \leq z_i \leq -h_j$ are within the TL, where H_j is the depth of the first bin with depth greater than or equal to $h_j + 50$ m. All remaining bins are within the INT. Figure 3.4 illustrates the arrangement of these three layers relative to the observed stratification during an example summer time interval (August 2008, $j = 3$). Note that the vertical boundaries of the TL are based on N^2 observed in each time interval, and thus the vertical boundaries of each region change during each time interval as well. The number of depth bins within the TL was 26 in all time intervals with the exception of March 2009, when the bottom of the TL was deep enough to be within the region of reduced vertical depth bin spacing deeper than 150 m, thus reducing the number of bins in the TL to 24.

Away from the SL, where "nonlocal" or countergradient turbulent fluxes are sometimes observed – such as in strong oceanic heat loss and free convection, where upward heat fluxes can persist despite neutral stratification [86] – the turbulent fluxes of scalar quantities are parameterized as being proportional to their vertical gradient and a vertical turbulent diffusivity κ, *e.g.* for temperature,

$$\overline{w'\theta'} = -\kappa \frac{\partial \theta}{\partial z}. \tag{3.17}$$

Observational studies show that in the upper ocean, surface-generated turbulence drives elevated dissipation of turbulent kinetic energy and high κ values in the surface mixing layer, which are 2-3 orders of magnitude larger than the weak and uniform values observed in the relatively quiescent interior [96, 146]. The highly sheared and stratified transition

layer at the base of the mixed layer forms the boundary between these two regions, over which diffusivity varies rapidly in the vertical. Thus, previous studies suggest κ that is weak in the INT region, but potentially elevated by 1-2 orders of magnitude in the TL. The 50 m vertical extent of the TL in this study is chosen based on the typical maximum extent of layers of elevated stratification, shear, dissipation of kinetic energy, and vertical mixing observed below the surface mixed layer in microstructure measurements [146].

The vertical diffusivites κ are estimated at the upper and lower interfaces of each TL bin [91]. For a depth bin within the TL, the convergence of turbulent transport in (3.15) is discretized as

$$-\frac{\Delta t}{\Delta z_i}\left[\overline{w'\theta'}_{i+0.5,j} - \overline{w'\theta'}_{i-0.5,j}\right] = \frac{\Delta t}{\Delta z_i}\left[\kappa_{i+0.5,j}\left.\frac{\partial\theta}{\partial z}\right|_{i+0.5,j} - \kappa_{i-0.5,j}\left.\frac{\partial\theta}{\partial z}\right|_{i-0.5,j}\right]. \tag{3.18}$$

A vertical profile of κ in each time interval is anticipated to decay with depth in the 50 m-thick TL region. The small magnitude of the diffusive signal in the interior relative to the strength of horizontal and vertical advection presents difficulties for the ability of this array to resolve vertical diffusivities as a residual deeper than the TL. For the purposes of this problem, it is assumed that the diffusivity is constant value of $\kappa_{\mathrm{INT}} = 10^{-5}$ m^2 s^{-1} in the INT region, in accord with with interior values of κ observed or inferred below the surface layer in other studies [170, 146, 54]. Thus for INT depth bins, with the exception of the uppermost bin, the convergence of turbulent transport is discretized as

$$-\frac{\Delta t}{\Delta z_i}\left[\overline{w'\theta'}_{i+0.5,j} - \overline{w'\theta'}_{i-0.5,j}\right] = \kappa_{\mathrm{INT}}\frac{\Delta t}{\Delta z_i}\left[\left.\frac{\partial\theta}{\partial z}\right|_{i+0.5,j} - \left.\frac{\partial\theta}{\partial z}\right|_{i-0.5,j}\right]. \tag{3.19}$$

The uppermost INT bin is unique because turbulent transport on its upper interface is given by the unknown diffusivity at the lower boundary of the TL, while diffusivity on its lower interface is given by the assumed κ_{INT}. Thus in the uppermost INT bin, turbulent

convergence takes the form

$$-\frac{\Delta t}{\Delta z_i}\left[\overline{w'\theta'}_{i+0.5,j} - \overline{w'\theta'}_{i-0.5,j}\right] = \frac{\Delta t}{\Delta z_i}\left[\kappa_{i+0.5,j}\left.\frac{\partial\theta}{\partial z}\right|_{i+0.5,j} - \kappa_{\mathrm{INT}}\left.\frac{\partial\theta}{\partial z}\right|_{i-0.5,j}\right]. \tag{3.20}$$

On the right-hand side of (3.20), the diffusivity on the upper interface $\kappa_{i+0.5,j}$ is an unknown, while the remaining terms are known or assumed in the case of κ_{INT}. These known or assumed terms form one element of the vector of "observed quantities" in this problem [vector $\vec{b}_1^{\theta}$ in (3.27), below], comparable to the vector $\vec{p}$ in equation (3.7).

Within the SL, the turbulent flux is assumed to vary linearly between the value given by the diffusivity at the interface above the uppermost TL depth bin and the surface value $\overline{w'\theta'}_{0,j}$. Following Large [84], the turbulent flux at the surface is set equal to the sum of the non-solar kinematic fluxes of heat:

$$\overline{w'\theta'}_{0,j} = [Q_j^L + Q_j^E + Q_j^H](\rho_0 c_p)^{-1}, \tag{3.21}$$

where Q_j^L, Q_j^E, Q_j^H are respectively the outgoing longwave, latent, and sensible heat fluxes averaged over time interval j [84]. Turbulent convergence in SL depth bins is discretized as

$$-\frac{\Delta t}{\Delta z_i}\left[\overline{w'\theta'}_{i+0.5,j} - \overline{w'\theta'}_{i-0.5,j}\right] = -\frac{\Delta t}{(h_j - 1\,\mathrm{m})}\left[\overline{w'\theta'}_{0,j} + \kappa_{h+0.5,j}\left.\frac{\partial\theta}{\partial z}\right|_{h+0.5,j}\right], \tag{3.22}$$

where $\kappa_{h+0.5,j}$ is the unknown diffusivity at the interface above the uppermost TL grid point (recall that depth bin indices increase upwards), which has vertical coordinate $z = -h_j + 1$ m. All other terms on the right-hand side of (3.22) are known.

These assumptions complete the parameterization of the turbulent vertical flux of temperature in the top 200 m; the convergence of this flux in the TL, INT, and SL is given by (3.18), (3.19), and (3.22), respectively. Turbulent convergence at the uppermost INT point is given by (3.20). Note that κ_{INT} and $\overline{w'\theta'}_{0,j}$ are specified, so there are only the $n_j^{\kappa} = n_j^H + 1$ unknown diffusivities, where n_j^H is the number of TL bins, in each time interval

j. Figure 3.4 illustrates the vertical grid on which the diffusivities are discretized for August 2008.

Consistent with the above parameterization, it is assumed that in each time interval the absorption of surface solar radiation occurs linearly within the SL; *i.e.,* that

$$-\frac{\partial}{\partial z} I_j(z) = -\left[Q_j^S - I_j(-h_j)\right]/h_j;\ -h_j < z_i \leq 0, \tag{3.23}$$

where Q_j^S is the mean shortwave surface heat flux in bin j, and

$$I_j(z) = Q_j^S \left[R_1 e^{z/\zeta_1} + (1 - R_1) e^{z/\zeta_2}\right], \tag{3.24}$$

where $R_1 = 0.62$, $\zeta_1 = 0.6$ m, and $\zeta_2 = 20$ m, consistent with Jerlov Type IA water [120]. Below the SL, attenuation of surface solar radiation at each depth grid point is given by the vertical derivative of (3.24). The above approximations mean that the convergence of turbulence and radiative absorption are both uniform across all grid points in the SL, even though the modeled temperature may not be.

The number of unknown w_{ij} in any time interval can also be reduced by imposing a "rigid lid" boundary condition of $w = 0$ at the surface, and assuming that within the SL, divergence is constant and w varies linearly between the surface and its value at the top of the TL:

$$w_{ij}(z_i > -h_j) = \left[-(z_i + h_j)/h_j + 1\right] w_{h,j}. \tag{3.25}$$

As a result, in each time interval, the number of unknown vertical velocities are $n_j^w = n_i - n_j^h$, where n_j^h is the number of depth grid points within the SL in interval j.

The number of unknown horizontal velocities remains constant in each time interval at $n_j^{uv} = 2n_i$, since u and v are estimated at each one of the n_i depth grid points. Thus, the overall number of unknowns at any time j is

$$n_j^U = n^{uv} + n_j^w + n_j^\kappa = 2n_i + (n_i - n_j^h) + (n_j^H + 1). \tag{3.26}$$

System of Tracer Equations

Using (3.16), (3.25), and the above parameterizations of turbulent convergence, it is possible to construct a linear system of n_i equations for potential temperature at time $j = 1$:

$$\mathbf{A}_1^\theta \vec{x}_1 = \vec{b}_1^\theta, \tag{3.27}$$

where the vector $\vec{x}_1$ is a $n_1^U \times 1$ vector of the unknown velocity components and turbulent diffusivities, $\mathbf{A}_1^\theta$ is an $n_i \times n_1^U$ matrix of coefficients of the vector of unknowns, and $\vec{b}_1^\theta$ is an $n_i \times 1$ vector of right-hand side terms in each equation – which include the temperature changes at each depth level $(\theta_{i,1.5} - \theta_{i,0.5})$, and for rows outside the TL, terms involving the surface flux or deep diffusivities, as given by (3.22), (3.19), and (3.20). Figure 3.5 gives a schematic arrangement of the elements in $\mathbf{A}_1^\theta$.

To this point, for $j = 1$ there are n_i equations and n_1^U unknowns. As shown in (3.26), the number of unknowns in any time interval is always at least $2n_i$, since this is the number of u and v unknowns. There are additional $n_i - n_j^h$ vertical velocity unknowns in the TL region and INT regions. The number of vertical velocity unknowns varies between 32 (March 2009) and 81 (June 2008 and July 2009) depending on the thickness of the SL – in the winter months, when the SL is thick, there are fewer depth bins in the TL and INT regions and hence fewer vertical velocity unknowns. There are also $n_j^H + 1$ diffusivity unknowns surrounding the TL depth grid points. The number of diffusivity unknowns is always 27 with the exception of March 2009, when the TL extends below 150 m depth, where the vertical grid spacing is decreased from every 2 m to every 5 m and there are only 25 diffusivity unknowns. Due to these effects of varying SL thickness, the number of total unknowns at each time interval varies between $2n_i + 57$ and $2n_i + 108$ ($2n_i$ horizontal velocity components, plus vertical velocity and diffusivity).

At $j = 1$ (June 2008), there are the maximum of $2n_i + 108$ unknowns, due to a very thin SL, for only n_i equations. The system is underdetermined without the addition of further equations or constraints. However, using the principles outlined above, it is possible

to discretize a second system of n_i equations using the salinity budget at each depth level:

$$\mathbf{A}_1^S \vec{x}_1 = \vec{b}_1^S. \tag{3.28}$$

In the the salinity balance equations, the turbulent flux of salt at the sea surface is parameterized using a "virtual salt flux" defined by

$$\overline{w'S'}_{0,j} = -S_{0,j}(E_j - P_j) \tag{3.29}$$

where $S_{0,j}$ is the sea surface salinity in time interval j, and $E_j - P_j$ the net moisture flux out of the surface ocean [25, 53, 175].

Two additional equations can be written that govern the vertically-integrated temperature and salinity balances by summing (3.16) over the top 200 m. For the temperature balance at $j = 1$ this takes the form

$$\sum_{i=1}^{n_i} \Delta z_i \theta_{i,1.5} - \sum_{i=1}^{n_i} \Delta z_i \theta_{i,0.5} = -\Delta t_1 \Bigg[\sum_{i=1}^{n_i} \Delta z_i \left(u_{i,1} \left.\frac{\partial \theta}{\partial x}\right|_{i,1} + v_{i,1} \left.\frac{\partial \theta}{\partial y}\right|_{i,1} + w_{i,1} \left.\frac{\partial \theta}{\partial z}\right|_{i,1} \right) - \overline{w'\theta'}_{0,j} - (\rho_0 c_p)^{-1} Q_j^S - \kappa_{\mathrm{INT}} \left.\frac{\partial \theta}{\partial z}\right|_{-200\mathrm{m}} \Bigg]. \tag{3.30}$$

The subsystems for θ and S can be combined to yield a larger system of $2n_i + 2$ equations

$$\mathbf{A}_1^{tr} \vec{x}_1 = \begin{bmatrix} \mathbf{A}_1^\theta \\ \mathbf{A}_1^S \\ \mathbf{A}_1^{\int \theta} \\ \mathbf{A}_1^{\int S} \end{bmatrix} \vec{x}_1 = \vec{b}_1^{tr} = \begin{bmatrix} \vec{b}_1^\theta \\ \vec{b}_1^S \\ \vec{b}_1^{\int \theta} \\ \vec{b}_1^{\int S} \end{bmatrix} \tag{3.31}$$

where the superscript tr indicates the system for the combined *tracer* equations.

System of Dynamical Equations

Although the salinity budget and vertically-integrated balances add equations, the system is still underdetermined, and at $j = 1$ there remain 106 more unknowns ($2n_i + 108$) than tracer equations ($2n_i + 2$). To constrain the problem, further equations must be specified expressing that, in addition to satisfying the temperature and salinity balances at each depth level and integrated throughout the top 200 m, the unknowns should have characteristics that are close to those expected for the weak and highly linear flow observed in the interior region at OSP. During the array time series, using the observed geostrophic flow speed as a velocity scale U and the array size as a length scale L gives a Rossby number ($Ro = U/fL$) of $\mathcal{O}(\sim 0.01) \ll 1$ (*see* Chapter 2). Under these conditions, the interior vorticity equation is approximately a balance between advection of planetary vorticity and vortex stretching [130]

$$\beta v = f\frac{\partial w}{\partial z}, \tag{3.32}$$

where f is the Corilois parameter, and here β is its meridional gradient. For a depth bin within the TL or INT regions, (3.32) can be discretized as

$$\beta v_{i,j} = f\frac{1}{\Delta z_i}\left[w_{i+1,j} - w_{i-1,j}\right], \tag{3.33}$$

where the vertical derivative of w has been replaced by a centered-difference approximation. (For the uppermost TL point, or lowermost INT point, backward- or forward-difference approximations are made instead.) Including the expression (3.33) within the system of equations adds a relationship between the unknown vertical and meridional velocities that the solution will attempt to satisfy, and provides an additional n_j^w constraints.

The above equations provide a constraint on the slope of the vertical profile of w in each time interval. An additional constraint is applied to the intercept of this profile based on CCMP estimates of wind stress curl. This constraint is formulated based on the linearized,

steady vorticity equation within the Ekman layer:

$$\beta v = f\frac{\partial w}{\partial z} + \frac{\partial}{\partial z}\left(\frac{\partial\overline{w'v'}}{\partial x} - \frac{\partial\overline{w'u'}}{\partial y}\right), \tag{3.34}$$

where $-\rho_0(\overline{w'u'}, \overline{w'v'})$ are the zonal and meridional components of turbulent stress. Integrating this balance vertically from the surface, where w is assumed to vanish, to the base of the Ekman layer $z = -H^{Ek}$, where stresses are assumed to vanish, yields

$$w(-H^{Ek}) + \frac{\beta}{f}\int_{-H^{Ek}}^{0} v\mathrm{d}z = \frac{1}{\rho_0 f}\nabla\times\vec{\tau}, \tag{3.35}$$

where $\vec{\tau}$ is the wind stress vector at the ocean surface. Following observations of significant Ekman transport penetrating below the surface mixed layer [21, 135], H_j^{Ek} is taken to be the depth of the SL plus 25 m in each monthly interval j, and the balance (3.35) is discretized as

$$w_{E,j} + \frac{\beta}{f}\sum_{i=E}^{n_i}\Delta z_i v_{ij} = \frac{1}{\rho_0 f}\langle\nabla\times\vec{\tau}\rangle_j, \tag{3.36}$$

where $z_E = -H_j^{Ek}$, and $\langle\nabla\times\vec{\tau}\rangle_j$ is the average CCMP wind stress curl in monthly interval j. Equation (3.36) provides an additional $n_j = 20$ rows to the system.

For geostrophic flow, vertical shear obeys the thermal wind balance

$$\frac{\partial u}{\partial z} = \frac{g}{\rho_0 f}\frac{\partial\rho}{\partial y} \tag{3.37}$$

$$\frac{\partial v}{\partial z} = -\frac{g}{\rho_0 f}\frac{\partial\rho}{\partial x}, \tag{3.38}$$

or, in discrete form,

$$\frac{1}{\Delta z_i}\left[u_{i+1,j} - u_{i-1,j}\right] = \left.\frac{g}{\rho_0 f}\frac{\partial\rho}{\partial y}\right|_{ij} \tag{3.39}$$

$$\frac{1}{\Delta z_i}\left[v_{i+1,j} - v_{i-1,j}\right] = -\left.\frac{g}{\rho_0 f}\frac{\partial\rho}{\partial x}\right|_{ij}. \tag{3.40}$$

Equations (3.39) and (3.40) provide a relationship between the unknown velocity components u_{ij} and v_{ij} and the estimated horizontal density gradients in each time interval that the solution will attempt to satisfy. These constraints also provide a further $2n_i$ equations.

Finally, two equations in each time interval govern the vertically-integrated volume transport over the top 200 m:

$$\sum_{i=1}^{n_i} \Delta z_i u_{i,j} = \sum_{i=1}^{n_i} \Delta z_i u^g_{i,j} \tag{3.41}$$

$$\sum_{i=1}^{n_i} \Delta z_i v_{i,j} = \sum_{i=1}^{n_i} \Delta z_i v^g_{i,j} \tag{3.42}$$

where (u^g, v^g) are the geostrophic velocity components estimated in Chapter 2. Equations (3.41) and (3.42) state that the integrated transport in the top 200 m from the least-squares solution should be equal to the sum of the geostrophic transports. Adding equations that penalize the solution vector for deviations from the geostrophic velocities estimated in Chapter 2 incorporates information about the reference level velocity provided by glider estimates of DAC in the top 1000 m.

Note that, given the above constraints on the vertical shear and integrated transport of the solution u and v, the problem is posed to solve for only the geostrophic component of horizontal tracer advection. The time scales of ageostrophic wind-driven flow, and the horizontal gradients over which these flows act, are in all likelihood much shorter than can be resolved by the two-week survey repeat time of Seagliders in this study (*see* [35, 87, 118, 119, 160]). The net advective effects of these flows in the monthly balances, if any, will become apparent as residuals in the global system of equations or errors in the solution vector. The inclusion of specified monthly-average Ekman flows will also be explored in Section 3.4, and it will be shown that the solution properties are not qualitatively altered by these flows. Note that, since the solution velocities are implicitly geostrophic, in applying the constraint (3.36) it is assumed that $v_{ij} = v^g_{ij}$; *i.e.,* that the meridional geostrophic velocity dominates the total meridional velocity (Chapter 2).

The combination of (3.32), (3.36), (3.39), (3.40), (3.41), and (3.42) gives a set of equations at $j = 1$ termed the *dynamical* equations, denoted with the superscript *dyn*:

$$\mathbf{A}_1^{dyn}\vec{x}_1 = \begin{bmatrix} \mathbf{A}_1^{w} \\ \mathbf{A}_1^{wE} \\ \mathbf{A}_1^{u} \\ \mathbf{A}_1^{v} \\ \mathbf{A}_1^{\int u} \\ \mathbf{A}_1^{\int v} \end{bmatrix} \vec{x}_1 = \vec{b}_1^{dyn} = \begin{bmatrix} \vec{b}_1^{w} \\ \vec{b}_1^{wE} \\ \vec{b}_1^{u} \\ \vec{b}_1^{v} \\ \vec{b}_1^{\int u} \\ \vec{b}_1^{\int v} \end{bmatrix}. \tag{3.43}$$

where the superscripts w, wE, u, v, $\int u$, and $\int v$, and refer to systems constructed using equations (3.32), (3.36), (3.39), (3.40), (3.41), and (3.42), respectively.

Local and Global Systems of Equations

Combining the tracer and dynamical equations for $j = 1$ forms an overconstrained "local" system

$$\mathbf{A}_1\vec{x}_1 = \begin{bmatrix} \mathbf{A}_1^{tr} \\ \mathbf{A}_1^{dyn} \end{bmatrix} \vec{x}_1 = \vec{b}_1 = \begin{bmatrix} \vec{b}_1^{tr} \\ \vec{b}_1^{dyn} \end{bmatrix}. \tag{3.44}$$

To see that the system is overconstrained, consider that, at every depth bin in this monthly interval, there are two unknown horizontal components (u_{i1}, v_{i1}), but there are also two equations corresponding to the θ and S balances – hence there are at least as many equations as u and v unknowns. Furthermore, there is always one vorticity equation (3.33) for each vertical velocity unknown, which guarantees that there are at least as many equations as unknown velocity components. There are 27 additional unknown vertical diffusivities, but these are exceeded by the additional $2n_i = 172$ equations governing the vertical shear of horizontal velocity, (3.39) and (3.40), 4 equations governing the vertically integrated θ, S, u, and v, and one equation governing the vertical velocity at $z = -H_1^{Ek}$. Thus, at $j = 1$, there are 430 equations (rows of matrix $\mathbf{A}_1$) and 280 unknowns (columns), and the system

is overconstrained. This argument would similarly apply to any other monthly interval, hence the local system for any j would be overconstrained. Figure 3.7 shows the schematic configuration of matrix $\mathbf{A}_1$ and the composition of equations and unknowns for this system.

Another set of equations could be constructed that corresponds to tracer balances that are integrated across the first two time intervals [summation taken over the first 2 time intervals in equation (3.15)]. The matrix equation corresponding to this system is

$$\begin{bmatrix} \mathbf{A}_1^{tr} & \mathbf{A}_2^{tr} \\ \mathbf{A}_1^{dyn} & \mathbf{0}_{1,2}^{dyn} \\ \mathbf{0}_{2,1}^{dyn} & \mathbf{A}_2^{dyn} \end{bmatrix} \begin{bmatrix} \vec{x}_1 \\ \vec{x}_2 \end{bmatrix} = \begin{bmatrix} \vec{b}_2^{tr} \\ \vec{b}_1^{dyn} \\ \vec{b}_2^{dyn} \end{bmatrix} \tag{3.45}$$

where $\vec{x}_2$ is the vector of unknowns at time $j = 2$, and $\mathbf{A}_2^{tr}$ indicates the matrix of coefficients of these unknowns $\left(-\Delta t_2 \frac{\partial \theta}{\partial x}\Big|_{i,2}, -\Delta t_2 \frac{\partial \theta}{\partial y}\Big|_{i,2}, \ etc. \right)$. $\vec{b}_2^{tr}$ represents the vector of temperature and salinity changes between $j = 0.5$ and $j = 2.5$ that the unknowns in bins $j = 1$ and $j = 2$ are attempting to satisfy, in addition to the sum of any residual turbulent and radiative transport terms in bins 1 and 2 that are specified *a priori* (surface fluxes and deep diffusive fluxes) and not included in the vector of unknowns, as discussed in section 3.2.3. $\mathbf{0}_{l,m}^{dyn}$ is a zero matrix with number of rows equal to the number of dynamical equations at time $j = l$ and number of columns equal to the number of unknowns at time $j = m$. In what follows, the notation surrounding these zero matrices will be dropped for clarity.

As in the example problem (3.8), if the system for $j = 2$ is appended to that of $j = 1$, and duplicate rows are removed, this yields

$$\begin{bmatrix} \mathbf{A}_1^{tr} & \mathbf{0} \\ \mathbf{A}_1^{tr} & \mathbf{A}_2^{tr} \\ \mathbf{A}_1^{dyn} & \mathbf{0} \\ \mathbf{0} & \mathbf{A}_2^{dyn} \end{bmatrix} \begin{bmatrix} \vec{x}_1 \\ \vec{x}_2 \end{bmatrix} = \begin{bmatrix} \vec{b}_1^{tr} \\ \vec{b}_2^{tr} \\ \vec{b}_1^{dyn} \\ \vec{b}_2^{dyn} \end{bmatrix}. \tag{3.46}$$

Relative to (3.44), this system has a greater number of unknowns, but remains overcon-

strained – the number of rows added is equal to that which would be present in a local system for $j = 2$, and following the argument described above, this is greater than the number of unknowns at $j = 2$. Hence, if extended in this way to an arbitrary number of time intervals, the system is guaranteed to have more equations than unknowns.

In this manner, it is possible to construct a "global" rather than local system for temperature and salinity balances integrated from the starting time of the Seaglider surveys to the end time of each of the $n_j = 20$ monthly intervals. This system is a function of a vector of all of the unknowns $\vec{x}$ during the time series:

$$\mathbf{A}\vec{x} = \vec{b}, \tag{3.47}$$

where

$$\mathbf{A} = \begin{bmatrix} \mathbf{A}_1^{tr} & \mathbf{0} & & \dots & \mathbf{0} \\ \mathbf{A}_1^{tr} & \mathbf{A}_2^{tr} & \mathbf{0} & & \vdots \\ \vdots & & \ddots & & \\ & & & & \mathbf{0} \\ \mathbf{A}_1^{tr} & \mathbf{A}_2^{tr} & \dots & & \mathbf{A}_{n_j}^{tr} \\ \mathbf{A}_1^{dyn} & \mathbf{0} & \dots & & \mathbf{0} \\ \mathbf{0} & \mathbf{A}_2^{dyn} & \ddots & & \vdots \\ \vdots & \ddots & \ddots & & \\ & & & & \mathbf{0} \\ \mathbf{0} & \dots & & \mathbf{0} & \mathbf{A}_{n_j}^{dyn} \end{bmatrix}, \quad \vec{x} = \begin{bmatrix} \vec{x}_1 \\ \vec{x}_2 \\ \vdots \\ \vec{x}_{n_j} \end{bmatrix}, \quad \text{and } \vec{b} = \begin{bmatrix} \vec{b}_1^{tr} \\ \vec{b}_2^{tr} \\ \vdots \\ \vec{b}_{n_j}^{tr} \\ \vec{b}_1^{dyn} \\ \vec{b}_2^{dyn} \\ \vdots \\ \vec{b}_{n_j}^{dyn} \end{bmatrix}. \tag{3.48}$$

The global system has 5201 unknowns in 8203 equations.

Scaling the Global Cost Function

Solutions to the system (3.47) are in general obtained by finding the vector $\hat{x}$ that minimizes the inner product of the vector of residuals $\vec{r} = \mathbf{A}\hat{x} - \vec{b}$; *i.e.,* the solution that minimizes the

scalar q where

$$q = \vec{r}^T \vec{r} = \sum_{k=1}^{n^{eq}} r_k^2 \tag{3.49}$$

and $n^{eq} = \sum_{j=1}^{n_j} \left(n_j^{tr} + n_j^{dyn} \right)$. In practice, obtaining the solution by minimizing q is undesirable, principally because the residuals r_k are composed of different dimensions depending on the equation to which they correspond. As an example, an acceptable residual in a temperature equation near the surface might be on the order of 1°C, while for a salinity equation, it might instead be 0.1 (parts per thousand). Thus the temperature residual would increase the cost function value q by $(1°\text{C})^2$, while the salinity equation would increase q by only 0.01 – even though the error in each equation is subjectively comparable and ideally should contribute equally to the cost function q. With no scaling or transformation of the residual vector, the temperature residuals of r_k^2 would be of a much greater magnitude, and it might be expected that the solution obtained by minimizing (3.49) would satisfy the temperature equations, relative to their variance or their uncertainty, to a much greater degree than the salinity equations. This approach would neglect the information added by the alternate vertical and horizontal structure of salinity at OSP in comparison to temperature.

The goal instead is to seek solutions to a modified version of (3.47),

$$\mathbf{WA}\vec{x} = \mathbf{W}\vec{b}, \tag{3.50}$$

where the matrix $\mathbf{W} = \mathbf{I}\vec{s}$, $\mathbf{I}$ is the $n^{eq} \times n^{eq}$ identity matrix, and $\vec{s}$ is a $n^{eq} \times 1$ vector of scaling factors. The solution is then the vector $\hat{x}$ that minimizes the inner product q^s of the scaled residuals $\vec{r}^s = \mathbf{WA}\hat{x} - \mathbf{W}\vec{b}$,

$$q^s = \vec{r}^{sT}\vec{r}^s = \left(\mathbf{WA}\hat{x} - \mathbf{W}\vec{b}\right)^T \left(\mathbf{WA}\hat{x} - \mathbf{W}\vec{b}\right) = (\mathbf{W}\vec{r})^T(\mathbf{W}\vec{r}) = \vec{r}^T\mathbf{W}^T\mathbf{W}\vec{r} \tag{3.51}$$

$$= \sum_{k=1}^{n^{eq}} r_k^2 s_k^2. \tag{3.52}$$

Each r_k^2 corresponds to the square residual from one row of the system (3.47), and the scaling factors for each row s_k are based on the equation type and depth level corresponding to that row. The cost function q^s is a summation of the inner products of each of the subsystems composed of unique equation types:

$$
\begin{aligned}
q^s = \sum_{k=1}^{n^{eq}} r_k^2 s_k^2 = & \sum_{i=1}^{n_i}\sum_{j=1}^{n_j} \left(s_{ij}^{\theta}\right)^2 \left(\Delta\hat{\theta}_{ij} - \Delta\theta_{ij}\right)^2 + \sum_{i=1}^{n_i}\sum_{j=1}^{n_j} \left(s_{ij}^{S}\right)^2 \left(\Delta\hat{S}_{ij} - \Delta S_{ij}\right)^2 + \\
& \sum_{j=1}^{n_j} \left(s_j^{\int\theta}\right)^2 \left(\Delta\int\hat{\theta}_j - \Delta\int\theta_j\right)^2 + \sum_{j=1}^{n_j} \left(s_j^{\int S}\right)^2 \left(\Delta\int\hat{S}_j - \Delta\int S_j\right)^2 \\
& + \sum_{j=1}^{n_j}\sum_{i=1}^{h(j)} \left(s_{ij}^{w}\right)^2 \left(\left.\frac{\partial\hat{w}}{\partial z}\right|_{ij} - \frac{\beta}{f}\hat{v}_{ij}\right)^2 + \sum_{i=1}^{n_i}\sum_{j=1}^{n_j} \left(s_{ij}^{u}\right)^2 \left(\left.\frac{\partial\hat{u}}{\partial z}\right|_{ij} - \frac{g}{\rho f}\left.\frac{\partial\rho}{\partial y}\right|_{ij}\right)^2 \\
& + \sum_{i=1}^{n_i}\sum_{j=1}^{n_j} \left(s_{ij}^{u}\right)^2 \left(\left.\frac{\partial\hat{v}}{\partial z}\right|_{ij} + \frac{g}{\rho f}\left.\frac{\partial\rho}{\partial x}\right|_{ij}\right)^2 + \sum_{j=1}^{n_j} \left(s_{ij}^{\int u}\right)^2 \left(\int\hat{u}_j - \int u_j^g\right)^2 \\
& + \sum_{j=1}^{n_j} \left(s_{ij}^{\int u}\right)^2 \left(\int\hat{v}_j - \int v_j^g\right)^2 + \sum_{j=1}^{n_j} (s_j^{wE})^2 \left(w_{E,j} + \frac{\beta}{f}\sum_{i=E}^{n_i} \Delta z_i v_{ij} - \frac{1}{\rho_0 f}\langle\nabla\times\vec{\tau}\rangle_j\right)^2,
\end{aligned}
\tag{3.53}
$$

where hatted variables indicate model variables, either tracers or solution vector elements. The following describes the choice of scaling factors s_k for the problem attempted here. These are based on the desired properties of the solution, relative dimensions of the temperature and salinity equations, and the estimated uncertainties in the dynamical equations. The choice of scaling factors is not unique and is a subjective element of all similarly-formulated least-squares problems [115].

The first two summations of equation (3.53) state that the cost function increases if the model-predicted changes in temperature and salinity from the time series onset ($\Delta\hat{\theta}_{ij} = \hat{\theta}_{i,j+0.5} - \theta_{i,0.5}$, $\Delta\hat{S}_{ij} = \hat{S}_{i,j+0.5} - S_{i,0.5}$) differ from those observed ($\Delta\theta_{ij}$, ΔS_{ij}). A reasonable choice of scaling factor for these equations is one that normalizes the square residuals by some fraction of the (time) variance at each depth level. In addition, the scaling factor for each equation should also take into account the variable grid spacing of the vertical mesh in

the top 200 m (Figure 3.4). Thus, s_{ij}^{θ} and s_{ij}^{S} are formulated such that the square residuals are thickness-weighted and normalized by 20% of the variance at each depth level:

$$\left(s_{ij}^{\theta}\right)^2 = \left(\frac{\Delta z_i}{200\mathrm{m}}\right)\frac{1}{0.2\sigma^2(\theta_i)}, \quad \left(s_{ij}^{S}\right)^2 = \left(\frac{\Delta z_i}{200\mathrm{m}}\right)\frac{1}{0.2\sigma^2(S_i)}, \tag{3.54}$$

where $\sigma^2(\theta_i)$ indicates the variance of temperature at depth i. Similarly, residuals in the equations for vertically-integrated temperature and salinity are normalized by 20% of the variance in these quantities:

$$\left(s_{j}^{\int\theta}\right)^2 = \frac{1}{0.2\sigma^2(\int\theta_i)}, \quad \left(s_{j}^{\int S}\right)^2 = \frac{1}{0.2\sigma^2(\int S_i)}. \tag{3.55}$$

The scale factors for residuals in the modeled vorticity equation (s_{ij}^{w}) are chosen based on the size of neglected terms in the interior Sverdrup balance (3.32). This balance is obtained from a linearized, steady version of the vertical vorticity equation for a Boussinesq stratified fluid. If the assumption of steady flow is relaxed, away from the Ekman layer the vorticity equation reads,

$$\frac{1}{f}\frac{\partial\zeta}{\partial t} + \frac{\beta}{f}v = \frac{\partial w}{\partial z}, \tag{3.56}$$

where $\zeta = \frac{\partial v}{\partial x} - \frac{\partial u}{\partial y}$ is the vertical relative vorticity. While depth-resolved estimates of ζ and its time derivative are not available, the glider estimates of DAC described in Chapter 2 provide an indication of the relative size of the terms in (3.56) when integrated across the top 1000 m, and thus provide an indication of the size of the terms neglected in (3.32). Figure 3.6 shows an estimate of $f^{-1}\partial\langle\zeta\rangle\partial t$ in each time interval. Although the observed vorticity is weak (only 1% of f), the results of Figure 3.6 suggest that, in a depth-average of (3.56), deviations from a purely steady vorticity balance can be as large as the βv term. The mean value of $|f^{-1}\partial\langle\zeta\rangle/\partial t| \,/\, |f^{-1}\beta\langle v\rangle|$ from July 2008-March 2009 is 0.24, and 2.9 thereafter. The RMS value of the estimated depth-average $f^{-1}\partial\zeta/\partial t$ is 1.7×10^{-9} s^{-1}, and this value is used as a measure of the possible deviation of $\partial w/\partial z$ from the steady balance (3.32) for the region below the Ekman layer when constructing the scaling factors s_{ij}^{w}. Note that, in (3.56), the

ratio ζ/f is an alternate formulation of the Rossby number; the omitted, unsteady term thus scales as $|f^{-1}\partial\zeta/\partial t| \sim Ro/T$, where T is a time scale. Choosing $|f^{-1}\partial\zeta/\partial t| \sim 1.7\times10^{-9}$ s^{-1} is equivalent to choosing $T = 68$ d. This is intermediate between two other possible choices of T based on phenomena observed during the Seaglider surveys at OSP: it is longer than the advective time scale L/U, which is equal to 11.6 d ($L = 50$ km, $U = 0.05$ m s^{-1}), but shorter than the ∼180 d time scale associated with circulation changes resulting from the passage of an eddy-like feature near OSP (Chapter 2).

Within the Ekman layer, where turbulent transport of momentum becomes a leading order term, it is assumed that deviations from the balance (3.32) should scale as $\sim |W_{Ek}|/H_{Ek}$, where $|W_{Ek}| = |\nabla\times\vec{\tau}|/(\rho f) = 0.088$ m d^{-1} is a characteristic Ekman velocity magnitude based on RMS monthly-average wind stress curl from the CCMP product, and H_{Ek} is the Ekman layer thickness. The latter scaling is applied in upper half of the TL, and the former scaling in the lower half of the TL and INT (the vertical velocity only being resolved in the TL and INT). Thus, the scaling factors for vertical velocity divergence residuals are then given by:

$$\left(s_{ij}^{w}\right)^2 = \begin{cases} \frac{\Delta z_i}{(200\mathrm{m}-h_j)}\frac{1}{(1.7\times10^{-9}s^{-1})^2} & \text{if } -H_j^{Ek} < z_i \\ \frac{\Delta z_i}{(200\mathrm{m}-h_j)}\left(\frac{\rho f H_j^{Ek}}{|\nabla\times\vec{\tau}|}\right)^2 & \text{if } -H_j^{Ek} \geq z_i \end{cases}, \tag{3.57}$$

where H_j^{Ek} is taken to be h_j+25 m, as described above. Note that in (3.57), the denominator in the thickness-weighting term is equal to the model vertical extent minus the SL thickness. This reflects the vertical domain of the unknown w_{ij}, since w within the surface layer is assumed to be proportional to w at its base (*cf.* Equation (3.25)).

As discussed above, the horizontal velocities in the solution are assumed to be in geostrophic and thermal wind balance, to within the errors of estimating the horizontal density gradient, and by (3.39) and (3.40), the vertical geostrophic shear. The uncertainty in the magnitude of vertical shear follows from a similar iterative procedure to that described in Section 3.2 for estimating uncertainty in the vertical profiles at the beginning and end of each time interval. During an iteration, the procedure computes the vertical shear at i, j using the ob-

served density gradient, plus random noise added independently to each component, where the noise is drawn from a normal distribution with whose variance is given by the estimated error variance in each component. The magnitude of the error in vertical shear is then

$$\left|\delta_l\left(\frac{\partial \vec{u_{ij}}}{\partial z}\right)\right| = \left(\left[\delta_l\left(\frac{\partial u_{ij}}{\partial z}\right)\right]^2 + \left[\delta_l\left(\frac{\partial v_{ij}}{\partial z}\right)\right]^2\right)^{1/2}, \tag{3.58}$$

where $\delta_l\left(\frac{\partial u_{ij}}{\partial z}\right) = \frac{g}{\rho f}\delta_l\left(\frac{\partial \rho}{\partial y}|_{ij}\right)$ is the noise-induced perturbation in vertical shear in the u component at i, j on iteration l. Repeating this procedure over 500 iterations gives an estimate of the probability density of the magnitude of the shear error, $f_{ij}\left(\left|\delta\left(\frac{\partial \vec{u}}{\partial z}\right)\right|\right)$, and its cumulative distribution, $F_{ij}\left(\left|\delta\left(\frac{\partial \vec{u}}{\partial z}\right)\right|\right)$. These distributions are one-sided since the magnitude of the shear error is positive definite. The 95% upper bound of $F_{ij}\left(\left|\delta\left(\frac{\partial \vec{u}}{\partial z}\right)\right|\right)$ is used to normalize deviation of $\frac{\partial \vec{u}}{\partial z}$ from the thermal wind balance given by (3.39) and (3.40). The scaling factors for vertical shear residuals from thermal wind are then given by:

$$\left(s_{ij}^{u}\right)^2 = \frac{\Delta z_i}{200\text{m}} \frac{1}{\left[F_{ij}^{-1}(0.95)\right]^2}. \tag{3.59}$$

The residuals in the volume transport equations are scaled by an assumed glider DAC uncertainty of $\sim$1 cm s^{-1}:

$$\left(s_j^{(\int u)}\right)^2 = \frac{1}{\left(200\text{m} \times 0.01\text{m s}^{-1}\right)^2}. \tag{3.60}$$

Finally, the residuals in the equations constraining the magnitude of vertical velocity at $z = -H_j^{Ek}$ are scaled by an estimated uncertainty in the CCMP wind stress curl, $er(\langle \nabla \times \vec{\tau} \rangle)$:

$$er(\langle \nabla \times \vec{\tau} \rangle) = \sqrt{\left[er\left(\frac{\partial \langle \tau^y \rangle}{\partial x}\right)\right]^2 + \left[er\left(\frac{\partial \langle \tau^x \rangle}{\partial y}\right)\right]^2}, \tag{3.61}$$

where errors in the spatial derivatives of each component of surface wind stress have been assumed to be independent. The uncertainty in the spatial derivative in each component is

given by

$$er\left(\frac{\partial \tau^y}{\partial x}\right) = \frac{\sqrt{2\left[er(\langle \tau^y \rangle)\right]^2}}{2\Delta x_{\mathrm{CCMP}}}, \tag{3.62}$$

where $\Delta x_{\mathrm{CCMP}} = 25$ km is the grid resolution of the CCMP product, and $er(\langle \tau^y \rangle) = 0.0099$ N m^{-2} is the RMS disagreement between monthly-average meridional surface stress estimated from the mooring and CCMP product during the Seaglider time series. Similarly, $er(\langle \tau^x \rangle) = 0.0214$ N m^{-2}; the corresponding uncertainty on the wind stress curl in each monthly interval is $er(\langle \nabla \times \vec{\tau} \rangle) = 6.7 \times 10^{-7}$ N m^{-3}. Scale factors for residuals in the balance (3.36) are then given by

$$\left(s_j^{wE}\right)^2 = \left(\frac{\rho f}{er(\langle \nabla \times \vec{\tau} \rangle)}\right)^2. \tag{3.63}$$

Inequality Constraints

In addition to the above "soft" constraints, the problem should take into account known realistic bound or inequality "hard" constraints that the solution $\vec{x}$ must satisfy. A reasonable constraint is to require that the solution must have $\kappa > 0$ since the turbulent diffusivities should be positive [*e.g.,* 104]. Furthermore, upper ocean microstructure studies suggest the diffusivities in the trasition layer are elevated relative to diffusivities measured away from the surface boundary layer [96, 146]. Since this formulation of the problem only resolves diffusivities within the 50 m thickness of the TL, a realistic condition to impose on the solution is that it must include diffusivity that is at least as strong as the assumed deep diffusivity κ_{INT}. In matrix form, this is accomplished by imposing the constraint

$$\mathbf{H}\vec{x} \geq \vec{e}, \tag{3.64}$$

where $\mathbf{H}$ and $\vec{e}$ are defined to satisfy the condition that the solution vector should have $\kappa \geq \kappa_{\mathrm{INT}} = 10^{-5}$ m^2 s^{-1}. A solution that minimizes the sum of scaled residuals (3.52) subject to the constraints (3.64) was obtained using an 'active set' quadratic programming algorithm implemented by the function *lsqlin* in MATLAB (The Mathworks, Inc.).

3.3 Results

3.3.1 Solution Accuracy

Once a solution is obtained, using the governing equations, *e.g.,* (3.15) for θ, the circulation and diffusivity in the solution $\vec{x}$ give an estimate of the change in potential temperature or salinity from the time series onset to any later time. Adding this estimate to the observed θ or S at the time series onset, similar to the example (3.10), gives the solution's estimate of the time record of a scalar variable at monthly time resolution during the Seaglider surveys. For θ, this estimate is formulated as:

$$\hat{\theta}_{i,M+0.5} = -\sum_{j=1}^{M} \Delta t_j \left[u_{ij} \left.\frac{\partial \theta}{\partial x}\right|_{ij} + v_{ij} \left.\frac{\partial \theta}{\partial y}\right|_{ij} + w_{ij} \left.\frac{\partial \theta}{\partial z}\right|_{ij} \right] - \sum_{j=1}^{M} \frac{\Delta t_j}{\Delta z_i} \left[\overline{w'\theta'}_{i+0.5,j} - \overline{w'\theta'}_{i-0.5,j} \right] - \sum_{j=1}^{M} \frac{\Delta t_j}{\rho_0 c_p} \left.\frac{\partial I}{\partial z}\right|_{ij} + \theta_{i,0.5}, \quad (3.65)$$

where $\theta_{i,0.5}$ is the estimated vertical profile of potential temperature at the start of the time series on 8 June 2008. The variable $\hat{\theta}_{i,M+0.5}$, $M = 1, 2, \ldots, n_j$ will be referred to as "solution potential temperature," and likewise for salinity $\hat{S}$.

Figure 3.8 shows the time record of $\hat{\theta}$ at $z = -20$ m. The time-integrated addition or removal of heat by advection, turbulent diffusion, and specified solar radiation are also shown. At this depth, the estimated balance of terms is primarily between the absorption of solar radiation and the divergence of turbulent transport. Horizontal and vertical advection are secondary terms at 20 m. The largest errors between solution and observed potential temperature – presumably due to errors in the input data, or due to unresolved terms not included in (3.13) – occur in July 2008, and May and August 2009. A useful metric by which to judge the accuracy of the solution is the ratio of error variance to observed variance, which

is termed the "normalized mean square error" (NMSE):

$$\text{NMSE} = [n_j^{-1} \sum_{j=1}^{n_j} (\hat{\theta}_{i,j+0.5} - \theta_{i,j+0.5})^2] / \sigma_i^2(\theta), \tag{3.66}$$

where $\sigma_i^2(\theta)$ is the variance in observed θ at depth i. At this depth, $\hat{\theta}$ has a NMSE of 12.1%. At the end of the time series, the temperature predicted by the solution differs from observed by 0.46°C, corresponding to a mean error in heat storage rate at 20 m of 0.04 W m^{-3}. This compares to an estimated 1.52 W m^{-3} mean radiative absorption at 20 m. Results for this depth are encouraging in that the solution has largely succeeded in reproducing the seasonal cycle in potential temperature and in balancing the integrated temperature change over the 20 month time series with error of less than a degree.

Figure 3.9 shows profiles of error in solution potential temperature at the end of each of the $n_j = 20$ time intervals. These results indicate that the errors at 20 m are fairly well-representative of those in the SL, and that solution errors in general decrease vertically in accord with the time-variance of potential temperature, which follows from the formulation of the scaling factors as discussed in section 3.2.3. The majority (91.0%) of errors are of magnitude of a degree or less, and the largest are found in the TL in Fall 2008 and throughout the TL and SL in the 1 July 2009 model profile. The NMSE is 0.2 or less at 44 of 86 depth levels, and its vertical average is 0.206 if the varying thicknesses of each depth level are accounted for (0.221 without accounting for thickness; Fig. 3.9).

The structure of solution salinity errors ($\hat{S} - S$) is more vertically uniform than that of potential temperature (Fig. 3.10). The greatest magnitude salinity errors are in the INT region, where salinity variance is also greatest, and in the TL region when the the SL is deep enough that the TL extends vertically into the halocline (*e.g.,* Winter 2009). Salinity NMSE is less than 0.2 at 42 of 86 depth grid points and thickness-averaged NMSE = 0.233. It is also apparent from Figure 3.10 that there is some vertical structure in normalized salinity error – NMSE is generally elevated in the top 70 m in comparison to temperature.

Figure 3.11 shows the solution temperature and salinity in comparison to the observations

when averaged over four zones in the top 200 m. The first two zones (SL, TL) follow from the definitions described above. The lower two zones are a partition of the INT region above and below 120 m – the upper of these two is referred to as the remnant thermocline (abbreviated RemTherm in this figure) and the lower of the two is denoted halocline (HaloCln). Note that there are times during the winter when the upper boundary of INT is deeper than 120 m and thus the remnant thermocline zone is undefined during these months. This accounts for the discontinuities in the remnant thermocline record displayed in Figure 3.11. The results of Figure 3.11 show that the model effectively reproduces the seasonal variability in the SL and TL zones in both temperature and salinity, and accounts for the secular variability observed in the halocline for both variables as well. When averaged over this vertical scale, the model also correctly reproduces the observed vertical stratification in temperature and salinity for all time interval edge profiles except one: the remnant thermocline is cooler than the halocline by 0.12°C at 1 December 2008, which is an error in magnitude from the observed difference in temperature by 0.25°C. As can be seen in Figure 3.11, the observed stratification is weak at this time, and the thickness of the remnant thermocline zone is also small (it vanishes in the following time interval).

The MSE and NMSE for each zone are shown in Table 3.2, where in this case NMSE is normalized by the variance of mean temperature or salinity in each zone. The maximum NMSE for either variable in any zone is 0.26 for potential temperature in the remnant thermocline, while the maximum NMSE for salinity is 0.22 in the SL. The remaining zones for each variable have NMSE ≤ 0.11.

3.3.2 Physical Transports

Three-Dimensional Circulation

Results of the previous section demonstrate that the transports estimated by the solution reasonably reproduce seasonal and low-frequency variability of θ and S across the array time series, and do so without accumulation of errors, as was the intended goal. However, in an

overconstrained proble, this is by construction; the scaling of the residuals could be used to force arbitrarily small errors in the temperature and salinity balances. It remains to be seen if the solution elements themselves – the estimated horizontal and vertical velocities, and vertical turbulent diffusivities – are within realistic bounds or, in the case of horizontal velocities, are close to initial estimates. Horizontal velocities estimated by the solution are shown in Figure 3.12. These are compared to the geostrophic velocities estimated in Chapter 2, which used relative velocity profiles obtained from observed horizontal density gradients and reference velocities inferred from the glider DAC observations. As described in Chapter 2, the horizontal velocities are weakly vertically sheared throughout the observed water column, and this holds for the top 200 m as well, as the velocity is nearly unidirectional in the top 200 m in each month (Fig. 3.12). Solution horizontal velocities (black lines) replicate the observed progression of moderate poleward flow during the first 9 months of the time series that "backs" (rotates counterclockwise) and weakens over the remaining months. Root-mean-square differences in velocity magnitude between the solution and estimates from Chapter 2 vary from 1.0-1.1 cm s^{-1} at each of the four depths considered in Figure 3.12. The RMS magnitude of the offset in 0-200 m depth average velocity between the solution and the estimates from Chapter 2 is 0.88 cm s^{-1}.

Profiles of vertical velocity estimated by the solution are shown in Figure 3.13. The profiles are plotted in two distinct periods – the first (left panel in Fig. 3.13) corresponds to June 2008-February 2009, when estimated horizontal velocities were predominantly poleward, and vertical velocities would be expected to be divergent upward based on the linear vorticity balance (3.32). Profiles in the left panel exhibit a consistent upward increase, while those in the right panel (March 2009-on) appear nearly nondivergent. The contrast in the shape of the profiles between the left and right panel indicates that, despite the scaling factors allowing for a divergence that deviates from the steady balance (3.32), the solution vertical velocities do reflect some influence of the meridional velocity and advection of planetary vorticity. In both cases, the divergence within the interior is weak relative to the offset of each profile, and profiles of w are relatively uniform across the top 200 m with the exception of the SL.

Dashed lines extending across the SL in Figure 3.13 reflect the interpolated vertical velocity within this zone, which is assumed to vary linearly from the uppermost estimated value in the TL.

Upwelling at $z = -H_j^{Ek}$ in the least-squares solution varies by as much as 0.61 m d^{-1} month-to-month (Fig. 3.14). These variations in w profile offset correlate with those obtained if the geostrophic velocities from Chapter 2 are used to compute horizontal advection in the halocline, and it is then assumed that 1) divergence is given by (3.32), and 2) w must as close as possible balance the halocline advection and time rate-of-change of density (*i.e.,* if it is assumed that halocline flow is adiabatic). Vertical velocities obtained with this latter assumption are denoted w_β in Figure 3.14. Figure 3.14 also shows the solution upwelling at the Ekman layer base minus the effects of vortex stretching of the meridional velocity shallower than $z = -H_j^{Ek}$, which is the quantity that is most comparable to the estimated wind stress curl-driven upwelling (Eq. 3.36). In general, accounting for the upwelling due to meridional flow shallower than $z = -H_j^{Ek}$ results in a negligible correction to $w(-H_j^{Ek})$. The month-to-month variations in corrected $w(-H_j^{Ek})$ correlate with Ekman upwelling calculated from CCMP monthly-average wind stress curl, though with gain and net offset of > 1 (Fig. 3.15). w_{LS} and w_β track the oscillating pattern observed over the first 9 months of the time series, but are of a larger amplitude than predicted CCMP wind stress curl. Mean estimated upwelling at $z = -H_j^{Ek}$ during the time series is 0.121 m d^{-1}, or 44.1 m yr^{-1}, while the mean estimated upwelling due to wind stress curl is 0.013 m d^{-1} (4.7 m yr^{-1}).

Diffusivity and TL Structure

Vertical turbulent flux of scalar variables within the TL and INT regions is assumed proportional to the local vertical gradient through an eddy diffusivity κ. In the INT region, $\kappa_{\mathrm{INT}} = 10^{-5}$ m^2 s^{-1} is assumed. In the TL – which spans 50 m vertically, and extends downward from the base of the SL – diffusivity is depth-dependent and estimated by the least-squares solution at the vertical interfaces surrounding TL depth bins. In the SL, turbulent transport is assumed to vary linearly between that estimated at the top of the TL

and the specified surface value.

The estimated diffusivity profiles in the TL exhibit consistent shape and amplitude throughout the array time series (Fig. 3.16). Diffusivity κ approaches 10^{-3} m^2 s^{-1} at the top of the TL and quenches rapidly with depth in the seasonal thermocline or halocline. In most profiles, the diffusivity decays by about a decade between the TL top and the depth of peak stratification in the TL (indicated by background shaded curves in Fig. 3.16). When viewed as a composite versus height referenced to the depth of peak stratification, the monthly profiles show a consistency in the slope of $\log_{10}(\kappa)$ versus depth in the upper TL (Fig. 3.17), which is about a decade per 10 m. The upward increase of κ at this slope appears to initiate near the depth peak stratification in most months.

The decay of diffusivity from the peak value at the top of the TL to the assumed deep value has a remarkably consistent structure in each month, if variations in profile amplitude are taken into account. Figure 3.18(a) displays a composite of diffusivity profiles, in which each profile has been normalized ($\kappa_{\rm norm}$) by subtracting the assumed $\kappa_{\rm INT}$ and dividing by the "residual amplitude," or the peak value of the residual between the estimated profile and the interior diffusivity:

$$\kappa_{\rm norm} = \frac{\kappa - \kappa_{\rm INT}}{\kappa_h - \kappa_{\rm INT}} \tag{3.67}$$

The vertical coordinate is the height above the TL top ($z_{TL} \equiv z + h_j$), which aligns all 20 months. When normalized in this way, the profiles exhibit an approximately exponential decrease from the peak values at the base of the SL. Fitting an exponential to the profile for each month gives e-folding scales that vary from 2.4 m to 10.3 m, with a mean value of 4.5 m. If a mean profile is first constructed, and an exponential fit to this profile, the e-folding scale is 4.4 m. Deeper than $\sim$ 20 m below the SL, the profiles do not decay quite as quickly as an exponential function (Fig. 3.18), but above 15 m the exponential is a very good approximation. A power-law curve with form $\hat{\kappa} = c_1 \times [-(z+h)]^{-c_2}$ gave better results when fitted to the mean profile for $z_{TL} \leq -10$ m. The best-fit power-law curve had coefficients $c_1 = 2.05$ and $c_2 = 1.27$.

The vertical structure of stratification in the TL changes seasonally as the sharp thermocline below the summer SL erodes and is replaced by weaker, vertically broader stratification in the winter and spring months (Fig. 3.18(b)). The buoyancy frequency and κ_{norm} profiles in Figure 3.18(b,c) are divided into two corresponding seasonal groupings, based on visual inspection. High stratification profiles (red lines in Fig. 3.18(b,c)) correspond to July-November 2008 and July-October 2009 (labeled "summer/fall"). The summer/fall diffusivity profiles estimated by the solution decay more rapidly with depth than the profiles from other months (Fig. 3.18(c)). The composite summer/fall profile has an e-folding scale of 3.3 m versus 5.3 m for the winter/spring profiles.

The estimated diffusivity profiles exhibit monthly and seasonal variability within the upper TL. Figure 3.19 shows the diffusivity estimated at three locations within the TL: at the level of peak N^2 within the TL, 50% of peak N^2, and 10% of peak N^2 (top of the TL/base of the SL). As noted previously, there is a ten-fold variation in the diffusivity over this range. The weakest diffusivities are estimated during the spring restratification period (April and May of 2009) and during September 2008, while the highest diffusivities are estimated in October-December 2008, and August-November 2009.

3.3.3 Balance of Terms

The least-squares solution to the problem (3.50) accounts for a majority of the variance in θ and S during the array time series, has circulation that is not very different from *a priori* estimates, and has diffusive transports qualitatively similar to general expectations. This suggests that the solution elements are an accurate representation of the monthly balances of θ and S and are not overly compensating for unobserved processes or errors. The advective and diffusive transports estimated by the solution provide useful information about the balance of terms in the temperature and salinity equations and their vertical structure throughout the annual cycle at OSP. Estimated advection and diffusion terms in the θ and S balances are shown in Figure 3.20. These terms are of a fundamentally different character in each of the tracer equations, which reflects the differences in stratification above and below

the permanent halocline in the Gulf of Alaska near OSP. The profiles of estimated turbulent flux given by the least-squares solution are also shown in Figure 3.21.

In the θ balance, the largest terms and local rate of change are found shallower than 120 m, where vertical gradients in temperature dominate the stratification (Fig. 3.20a). The heat balance in the SL is primarily between local storage, convergence of turbulence, and absorption of solar radiation. Convergent downward diffusive and radiative fluxes of heat are apparent within the SL and upper TL during the summer months (June-August 2008, May-July 2009; Fig. 3.21a, b), which is the primary agent for the observed heating and increase in temperature stratification in these zones (overlap of blue and black curves in summer in Fig. 3.20a). Figure 3.21b indicates that, under the assumption of type IA water (Section 3.2), a significant penetration of solar radiative flux to the TL occurs in the months May-August. In October-December 2008 and August-November 2009, the divergence of turbulent heat flux cools the SL, while convergent downward turbulent flux in the upper TL warms this layer (Fig. 3.21a, Fig. 3.20a). This process exports heat from the SL to progressively deeper depths as the SL deepens and is responsible for the maximum in the annual temperature cycle occurring at progressively later times as depth increases (*see* Fig. 2.3b). Horizontal advection increases in importance in the TL, reflecting strong horizontal gradients there (*see* Chapter 2), though the vertical terms remain dominant. Horizontal advection is proportionally more important in summer and fall 2008 than in the following year. Vertical advection is also at times estimated to be an important term in the TL, in particular during the first summer (July and September 2008; Fig. 3.20a).

In contrast to θ, the S balance terms are greatest in magnitude deeper than 100 m, where salinity dominates the density stratification (Fig. 3.20b). Convergence of turbulent transport is secondary in this zone, with the exception of winter 2009 when the boundary layer deepens and extends to the top of the halocline. In these winter months, an upward divergent diffusive flux of salt removes salt from the upper halocline (alternately, imports freshwater; Fig. 3.21c), which acts to maintain the vertical salinity stratification within this zone [84]. In most months, horizontal and vertical advection balance one another in the

halocline, though occasionally horizontal or vertical advection balances a local change in salinity (Fig. 3.20b). Salinity budget terms are generally small in the SL though are larger in the TL and increase in magnitude as the summer and fall progress, reflecting an increase in the contribution of salinity to the stratification in the TL (Figs. 3.20b, 3.21c).

An alternate metric by which to judge the balances in each zone is to consider the average magnitude of budget terms irrespective of their sign. Figure 3.22 displays the mean absolute value of terms averaged across each of the four zones defined in Section 3.3.1 and then time-averaged throughout the time series duration; *e.g.,* for horizontal advection in the SL, Figure 3.22 shows

$$\langle A_h \rangle = \frac{1}{n_j} \sum_{j=1}^{n_j} \left| \frac{1}{h_j} \int_{-h_j}^{0} u_{ij} \left. \frac{\partial \theta}{\partial x} \right|_{ij} + v_{ij} \left. \frac{\partial \theta}{\partial y} \right|_{ij} \mathrm{d}z \right|, \tag{3.68}$$

where in this case angle brackets denote a time series- rather than monthly-average. Figure 3.22 also displays the mean size of unresolved terms in the θ and S budgets. The results for θ confirm that in the SL, the largest terms are the local change in temperature, the divergence of turbulent transport, and absorption of solar radiation. Vertical advection is near-zero, as would be expected for a zone defined to have $N^2 < 10\%$ of the peak value in each month. Mean horizontal advection in the SL is a secondary term, accounting on average for a change in temperature of 1°C over 100 d.

Horizontal and vertical advection are proportionally more important in the temperature budget below the TL, though as specified previously, the vertical terms (advection and diffusion) remain the largest in this layer (Fig. 3.22a). Horizontal advection becomes a leading term in the remnant thermocline and halocline, where the effects of eddy diffusion are secondary – note the change of vertical scale for the remnant thermocline (base of TL to 120 m depth), and halocline (120 m depth or TL base to 200 m) plots compared to the TL or SL for θ. The unresolved terms increase in magnitude relative to the estimated advection/diffusion in the remnant thermocline and halocline, and are of the same order as the observed rate of change, though as shown in section 3.3.1, their time integral is small

compared to the other terms.

In the SL, the mean magnitude of horizontal advection in the S budget is larger relative to turbulence and local storage than in the θ budget, though the latter terms dominate (Fig. 3.22b). The unresolved salinity terms in the SL are also of a proportionally greater magnitude than those for θ. In contrast to the θ budget, in which the average size of $\left|\frac{\partial\theta}{\partial t}\right|$ decreases by an order of magnitude with distance from the surface, $\left|\frac{\partial S}{\partial t}\right|$ is largest in the TL and almost as large in the halocline. Similar to θ, however, horizontal and vertical advection become dominant terms and exceed turbulent diffusion in size in the S budget below the SL and TL (Fig. 3.22b).

The 120 m depth boundary is approximately the mean depth of winter mixing at OSP (Fig. 3.1a), forming the delineation between the permanent halocline and the temperature-stratified upper ocean. It is also a natural depth of integration when evaluating annual NCP of dissolved oxygen, as will be discussed in Chapter 4. Figure 3.23a shows the top 120 m heat balance, integrated in time from the start of the Seaglider surveys (t_0). This balance takes the form

$$\underbrace{\rho_0 c_p \int_{-120\,\mathrm{m}}^{0} \theta(z,t)\mathrm{d}z}_{H_{120}(t)} = \underbrace{\rho_0 c_p \int_{t_0}^{t}\int_{-120\,\mathrm{m}}^{0} \left[-u(z,\tau)\frac{\partial\theta}{\partial x}(z,\tau) - v(z,\tau)\frac{\partial\theta}{\partial y}(z,\tau)\right]\mathrm{d}z\mathrm{d}\tau}_{A_h}$$
$$+ \underbrace{\rho_0 c_p \int_{t_0}^{t}\int_{-120\,\mathrm{m}}^{0} \left[-w\frac{\partial\theta}{\partial z}(z,\tau)\right]\mathrm{d}z\mathrm{d}\tau}_{A_v} + \underbrace{\int_{t_0}^{t}\left[-\overline{w'\theta'}_0(\tau) - Q^S(\tau)\right]\mathrm{d}\tau}_{Q_0}$$
$$+ \underbrace{\rho_0 c_p \int_{t_0}^{t}\left[-\kappa(-120\,\mathrm{m},\tau)\frac{\partial\theta}{\partial z}(-120\,\mathrm{m},\tau)\right]\mathrm{d}\tau}_{\mathrm{Kz}_{120}} + \rho_0 c_p \int_{-120\,\mathrm{m}}^{0} \theta(z,t_0)\mathrm{d}z, \quad (3.69)$$

where underbraces indicate the labels applied to each term in Figure 3.23a. The observed top 120 m heat content [$H_{120}(t)$, left-hand side of (3.69)] at the beginning and end of each

monthly time interval is indicated by the black line in Figure 3.23a. On the right-hand side of (3.69), the least-squares solution allows estimation of the horizontal and vertical advective terms (A_h, A_v) and turbulent diffusion at 120 m (κ_{120}), while the net surface heat flux (Q_0) is specified. The balance (3.69) assumes that absorption of solar radiation below 120 m is negligible. The sum of these terms, plus the heat content at the time series onset [final term on the right-hand side of (3.69)], is the least-squares solution estimate of the top 120 m heat content time evolution. This term is shown in red in Figure 3.23a; other curves show the individual components A_h, A_v, κ_{120}, and Q_0.

The solution results show that the top 120 m heat balance is between surface fluxes, local storage, and vertical advection during the array time series (Fig. 3.23a). Note that these terms are simply vertical and temporal integrals of the monthly, depth-resolved budget terms shown in Figure 3.20a; the surface fluxes Q_0 reflect the net absorption of solar radiation and convergence of turbulent transport integrated vertically across the water column in each month. As expected from Figure 3.20a, these are significant in the top 120 m heat balance, as is local heat storage or loss. In the least-squares solution estimate, the offset between surface fluxes and the observed storage of heat is mainly closed by upwelling of cool water (Fig. 3.23a).

This vertical advection plays a greater role than might be expected from the monthly profiles of Figure 3.20a. This is due to two factors – first, vertical advection in any month is nearly guaranteed to be entirely of one sign throughout the top 120 m, since the vertical temperature gradient is increasing upward or near-zero, while vertical velocity is only weakly divergent; see Figure 3.13. This means that there is little cancellation that occurs when vertically integrating the $w\frac{\partial\theta}{\partial z}$ term in Figure 3.20a. In addition, the net cooling during the time series appears to result from the covariance of strong upwelling with strong vertical gradients in temperature in summer and fall: the strongest cooling due to A_v occurs in July-August 2008, and August-October 2009 (Fig. 3.23a). In nearly all other months, vertical advection has much less impact. Horizontal advection adds heat during the first half of the time series, then removes heat, such that the net effect over the duration of the time series

is nearly zero. Overall, the solution estimate of top 120 m heat content (red line) effectively reproduces the observed variability in heat content, with NMSE [equation (3.66)] of 0.041.

Figure 3.23b shows the results for a similar heat balance, vertically-integrated between 120 m and 200 m depth. In this region, horizontal advection of heat from the east (Chapter 2) accounts for nearly all of the observed temperature changes in the halocline (Fig. 3.23b). Upwelling removes some heat but is much less effective at cooling this portion of the water column per unit vertical velocity because of weak vertical temperature gradients in the salinity-stratified halocline (Fig. 3.1b, *see also* Fig. 2.3). Downward flux of heat into this zone from diffusion at 120 m (mainly in winter 2009, when boundary layer turbulence penetrates to the top of the halocline) is a secondary term. Turbulent diffusion at 200 m is very small, though this is a byproduct of the assumed $\kappa_{\mathrm{INT}} = 10^{-5}$ m^2 s^{-1} there. The solution advective and diffusive fluxes in the halocline reproduce the observed integrated heat content wth NMSE 0.055.

In the top 120 m S budget, both horizontal and vertical advection are important – horizontal advection of fresh water from the south and east (Chapter 2) nearly cancels with upwelling of saline water and the upward diffusion of salt across the 120 m boundary, meaning the observed changes in top 120 m salinity are approximately those given by the surface fluxes (Fig. 3.24a). As noted by previous investigators, the removal of heat from the upper 120 m by vertical import of cool water must also result in a large import of salt, due to the mean stratification of the halocline. Deeper than 120 m, vertical advection also acts to increase the mean salinity, while horizontal advection and diffusive transport at 120 m add freshwater during the time series (Fig. 3.24b). Diffusion of salt at 200 m is a negligible term under the assumed κ_{INT}. The solution transports give an NMSE in top 120 m salinity of 0.089 and in 120-200 m salinity of 0.032.

3.4 Discussion

Formulating the balances of temperature and salinity at monthly time steps smears over many storms and abrupt changes in SL temperature or thickness that occur on time scales

of 1-2 days [*e.g.,* 35, 87, 118, 85, 38]. Despite this, a model of flow including monthly-mean circulation, surface heat and freshwater inputs, and vertical diffusivity accounts for a majority of the variance in each scalar quantity in each physical zone of the upper ocean at OSP. At individual depth levels, the mean square error of the temperature and salinity records predicted by the solution vector was on average ∼20% of the variance. There was some weak vertical structure of the errors, with normalized salinity errors elevated near the surface and temperature errors elevated in the transition layer, especially in summer and fall 2008 (Figs. 3.9, 3.10). The increase in normalized $\hat{S}$ error near the surface to some degree reflects a greater proportional uncertainty in the surface freshwater fluxes compared to the surface heat flux (Section 3.2). In addition, salinity variance is weaker relative to the accuracy in the Seaglider sensor package in the surface layer in comparison to temperature. The salinity variance at 20 m is 0.0046, and ratio of salinity variance to instrument error variance is $(0.0046/(0.01^2)) = 46$ where 0.01 represents the assumed accuracy in Seaglider salinity measurements. In comparison, the ratio of temperature variance to instrument error variance at 20 m is 6.7×10^5, if an accuracy of 0.003°C for temperature measurements is assumed.

Profiles of $\hat{\theta}$ had large errors for 1 July 2009 (Fig. 3.9), which may be due to two factors related to sampling within the month prior. The array was incompletely occupied during June 2009 – battery depletion forced the early suspension of sampling from SG120, which completed its final dive on 3 June at 2244UTC. Its replacement SG144 did not initiate sampling until 14 June at 1536UTC, resulting in a 10+ d gap in sampling (*see* Chapter 2). Compounding this problem, the SL abruptly deepened over a period of several days following the passage of two strong storms in late June (Fig. 3.1a). When spatially uniform temporal changes occur across the Seaglider transect pattern over time scales shorter than those required to complete one circuit, time variability is "smeared" onto the spatial domain in the sampling record. As a consequence of these events, the horizontal gradients (and hence the elements of matrix $\mathbf{A}$) are likely poorly resolved in the June 2009 time interval. To test whether the poor resolution of the horizontal gradients in June 2009 unduly influenced the

results, an alternate form of the problem was posed, in which the June 2009 time interval was omitted. In this alternate form, for budget equations corresponding to months after June 2009, the observed temperature changes 1 June - 1 July 2009 replaced the advective and diffusive fluxes in (3.15) and moved to the right-hand side of (3.50), with corresponding changes in the salinity budget equations. The solution without June 2009 (results not shown) resulted in a slight reduction in the salinity errors in the three months prior to June 2009, and a slight increase in the errors of temperature and salinity in the two months following. Depth-averaged horizontal velocities differed by < 1 cm s^{-1} from the base solution in every month; the largest differences were in July and August 2009, in which the solution with June 2009 omitted estimated a greater southward component of flow, with differences from the base solution of $\sim$0.85 cm s^{-1}. Upwelling at $z = -H_j^{Ek}$ increased by 0.13 m d^{-1} in July 2009 in the solution with June 2009 omitted, and was not significantly altered otherwise. Vertical profiles of diffusivity were negligibly different between the two solutions. The small overall changes in the solution accuracy and solution vector elements between the problem with and without June 2009 indicates that the results are not particularly sensitive to the inclusion of this month.

The $\mathcal{O}(\sim 0.1°C)$ errors in $\hat{\theta}$ in fall 2008 are persistent through several months (1 August-1 November) and over a depth range of 20-80 m as the TL deepens (Fig. 3.9). The improved closure of the depth-resolved heat budget in the TL in fall of 2009 in comparison to 2008 may reflect the presence of the mooring after June 2009 and its role in the array sampling. Recall from Chapter 2 that, when the mooring is present, the moored time record of θ and S at each depth is subtracted from Seaglider observations at that same depth prior to performing regression fits that estimate the spatial gradients in these variables (Section 2.2.3). In the boundary layer, this helps to alleviate the effect of smearing low-wavenumber, high-frequency variability in the SL and TL onto the glider spatial record, provided that the time variability observed at the mooring is coherent across the 50×50 km array. The improved performance of the least-squares solution in fall 2009 suggests that this is a valid assumption and that the removal of the mooring time record from the glider sampling record improves the accuracy

of the estimated horizontal spatial gradients of temperature.

As described in Section 3.2, the choices made in the problem setup and residual scaling imply that the solution estimates only the geostrophic component of monthly-average horizontal velocity. Any net horizontal advection due to ageostrophic, wind-driven Ekman flow and gradients in the surface boundary layer at a less-than-monthly time scale is not resolvable by the Seaglider survey configuration due to the limitation of the vehicle transit speed. However, an additional configuration of the problem was posed to test the sensitivity of the solution to the inclusion of monthly-average Ekman flows acting on monthly gradients. For this configuration, in each monthly interval, a profile of Ekman velocity obeying [*e.g.,* 20]

$$if\mathbf{u}_E = \frac{1}{\rho_0}\frac{\partial}{\partial z}\mathbf{X}, \tag{3.70}$$

where $i = \sqrt{-1}$, $\mathbf{u}_E = u_E + iv_E$ is the complex-valued Ekman velocity and $\mathbf{X} = -\rho_0(\overline{w'u'} + i\overline{w'v'})$ is the turbulent stress, was constructed using a vertical functional form for $\mathbf{X}$ suggested by Niiler and Paduan [113] based on analysis of near-surface drifter motions near OSP. One model of stress depth-dependence consistent with their results is

$$\mathbf{X} = \mathbf{X}_0 + \gamma(e^{\lambda z} - 1), \tag{3.71}$$

where γ and λ are complex-valued constants, and the stress at the surface $\mathbf{X}_0$ is set equal in this case to the monthly-average surface wind stress determined from the buoy wind speed or CCMP product when the buoy was not available. The constant λ is determined from

$$\frac{1}{h_{NP}} = \frac{-\lambda e^{-\lambda h_{0,NP}}}{e^{-\lambda H_{NP}} - 1} \tag{3.72}$$

where h_{NP} is a complex-valued momentum mixing depth determined by Niiler and Paduan [113], $h_{0,NP}$ is the drogue depth of 15 m in their measurements, and H_{NP} is the depth at which stress goes to zero, taken to be H_j^{Ek}. The parameter λ was then determined iteratively from (3.72) in each monthly interval. The parameter γ follows from the constraint that $\mathbf{X}$

must go to zero at $z = -H_j^{Ek}$, $\gamma = -\mathbf{X}_0/(e^{-\lambda H_j^{Ek}} - 1)$. The ageostrophic flow in each monthly interval then follows from (3.70),

$$\mathbf{u}_E = \frac{\gamma\lambda}{if\rho_0} e^{\lambda z}; \quad z \geq -H_j^{Ek}. \tag{3.73}$$

The dot product of the ageostrophic velocity given by (3.73) and monthly-average horizontal gradients of temperature and salinity was computed in each interval and added to the right-hand side of (3.50). The profiles estimated here assume that either the wind stress is constant throughout each monthly interval, or that the functional form of stress dependence and the constants γ and λ are independent of wind stress magnitude. This ignores any effect of rectification of the time-varying Ekman velocity spiral in a monthly average due to nonlinear dependence of the boundary layer eddy momentum diffusivity on wind stress [109].

In a solution obtained with mean Ekman advection added to the right-hand side, root-mean square differences in upper 200 m mean velocity from the base solution were 0.13 cm s^{-1} and the maximum difference was 0.31 cm s^{-1} in October 2009. Root-mean square differences in vertical velocity at $z = -H_j^{Ek}$ from the Ekman and base solution were 0.02 m d^{-1}. These differences are small in comparison to the size of horizontal and vertical velocities in the base solution; the TL diffusivity profiles were similarly not substantially altered (results not shown). Figures 3.26 and 3.27 show the potential temperature and salinity anomalies, respectively, for the solution with specified Ekman flow, overlaid on those of the base configuration (*cf.* Figs. 3.9 and 3.10). Consistent with the vertical extent of the specified Ekman flow, the solution that includes the latter quantity has accuracy that is only noticeably different within the SL and upper TL. Close inspection of these plots reveals that the change in solution accuracy is not uniformly an improvement; in fact, averaged over the uppermost 74 m (the mean value of H_j^{Ek}), the NMSE in the Ekman flow configuration for θ (S) is 0.248 (0.463), in comparison to 0.232 (0.349) in the base configuration. The small change in solution accuracy and solution elements in the configuration with specified monthly-average Ekman flow indicates that the problem is not particularly sensitive to its

inclusion; its absence from the base configuration is furthermore justified based on the lack of any significant improvement in solution accuracy with Ekman flow included.

In the base solution, RMS errors between the estimated horizontal velocities and the geostrophic velocities estimated in Chapter 2 ($\sim$1 cms^{-1}) are within the previously-quoted, though quantitatively untested, theoretical uncertainty in glider DAC. Sampling error also likely increases the uncertainty in the estimate of mean DAC in each month, and even if DAC were 100% accurate, uncertainty in vertical shear in the profiles from Chapter 2 could contribute to error in transport averaged over a subset of the water column. Considering these factors, the RMS error obtained here between solution elements and initial estimates indicate good agreement between the solution and observations from Chapter 2.

The vertical structure of κ in the transition layer estimated in this study is in good agreement with microstructure measurements that span the upper-ocean boundary layer (*e.g.,* Sun et al. [146], their Figs. 4, 6, and 9; Lozovatsky et al. [96], their Fig. 7; Fernandez-Castro et al. [54], their Fig. 10; Raymond et al. [128], their Fig. 10). The variation in κ of 1-2 decades over a region 10-20 m thick above the transition layer stratification peak emphasizes that there is a rapid transition between surface layer turbulence and the weak, internal-wave driven values of κ in the stratified interior ocean. The monthly averaging vertically blurs the effect of diffusion by considering the turbulent flux as proportional to κ and the mean monthly vertical profile of each property; it is likely that the vertical structure of κ in instantaneous profiles or those averaged over a shorter period would exhibit transitions that are at least as sharp. Indeed, results from microstructure sampling in June 2007 at OSP described in Rousseau et al. [134] support this idea, while also demonstrating further consistency with the bulk vertical structure of κ found here. Rousseau et al. [134] estimated vertical profiles of turbulent dissipation and diapycnal diffusivity from microstructure profiling at OSP during 7-11 June 2007. The mean profile of diapycnal diffusivity (roughly equivalent to the vertical diffusion estimated in this study, given the nearly-vertical gradient of density in the upper ocean) shown in their Figure 1 exhibits a rapid increase above the maximum transition layer stratification at 60 m, increasing by approximately four decades over 25 m, a rate of vertical

increase nearly twice that observed in this study.

Pearson et al. [122] conclude that, in the stratified turbulence characteristic of the TL, the vertical eddy diffusivity should scale as

$$\kappa \sim \frac{\sigma_w^2}{N}, \tag{3.74}$$

where σ_w^2 is the variance of turbulent vertical velocity fluctuations, or vertical turbulent kinetic energy per unit mass (VKE). Observations in the atmospheric boundary layer [112, 74] and large-eddy simulations (LES) of atmospheric [117] and oceanic [65] boundary layer flows support this scaling, with $\kappa N/\sigma_w^2$ varying from 0.17-0.35 [65]. If this scaling holds throughout the transition layer, it follows that the observed increases in N with depth, independent of any changes in VKE, should correspond to decreases in κ (Fig. 3.18b). This is consistent with the winter/spring profiles having a greater depth scale of decay than summer/fall in Figure 3.18. In summer/fall, the mean profile of N^{-1} is minimum (N is maximum) at 12 m below the top of the TL. Over this distance N^{-1} decreases by a factor of 0.35 over the top 12 m of the TL. Over the same distance the mean profile of κ decreases by a factor of 0.07. Similarly, in winter/spring, the mean profile of N^{-1} decreases by a factor of 0.37 over the top 20 m, while mean κ decreases by 0.08. These calculations imply that the increase in N alone in the transition layer is not sufficient to explain the decrease in κ, and that a decrease in VKE must be invoked as well.

The diffusivity in the upper transition layer exhibited some weak seasonal variability (Fig. 3.19). The mean κ at the top of the TL in October-December during Seaglider surveys was estimated to be a factor of 1.68 larger than during June-August. During these same months, N^{-1} at the top of the TL increases by a factor of 1.27. The temporal variations in κ estimated by the least-squares solution (Fig. 3.19) are at least qualitatively consistent with increased turbulence in winter due to convective heat loss, enhanced surface wind stress, and shear due to storm-generated near-inertial oscillations, along with decreased turbulence in summer due to downward buoyancy flux and reduced wind speeds. The relative roles of each

of these processes in modulating seasonal variations in turbulence intensity and diffusivity in the stratified TL are not well-understood and warrant continued study.

An increase in the diffusivity near the top of the TL from summer to fall is also qualitatively consistent with the results of Cronin et al. (submitted manuscript), who evaluated diffusivity and heat flux at the base of the SL as a residual in a budget of SL-average temperature, and found an increase in climatological diffusivity at the SL base from $\sim 1 \times 10^{-4}$ m^2 s^{-1} in summer to $\sim 3 \times 10^{-4}$ m^2 s^{-1} in the fall. It is difficult to directly compare the magnitude of these estimates to this study because of the varying definitions of SL thickness between the two – the $0.1N^2$ criterion in a monthly-average profile of N^2 used for the definition of SL thickness here was chosen purely for practical considerations, as it represents approximately the shallowest limit at which Seaglider profiles reliably estimate vertical gradients of temperature and salinity in the monthly-average sense. The SL depth defined in this study was on average 9.7 m shallower than the monthly average of SL depth determined from Seaglider profiles using the definition from Cronin et al. (submitted manuscript), which is the depth at which there is a density increase of 0.03 kg m^{-3} from the 10 m density value. The SL depth in this study was less than the monthly-average of the 0.03 kg m^{-3} increment in every month except April 2009.

More comparable between the two studies are the heat fluxes near the SL base, since the vertical profile fo heat flux does not vary as rapidly in the vertical as diffusivity, and the entrainment heat fluxes in Cronin et al. are small, and thus the two studies are measuring approximately the same quantity. The summer and fall values of heat flux at the SL base are in good agreement between the two studies, with values $<$100 W m^{-2} of downward flux in summer increasing to $\sim$100 W m^{-2} or greater in September-November. Like this study, the Cronin et al. climatological downward heat fluxes in December-February are estimated to be weaker than those in the fall, though the amplitude of the seasonal variations are much larger here. It is possible that removal of errors that result in upward heat flux during these months biases the Cronin et al. results downwards. The greatest disagreement between the Cronin et al. results and those shown here is in April, where their climatology shows the

largest heat flux and diffusivity, in contrast to weak heat flux and diffusivity estimated here, though the uncertainties are largest in that month in their analysis as well.

The monthly-mean vertical velocity w profiles are weakly divergent and have month-to-month variations that are larger than the depth variability within the top 200 m (Fig. 3.14). It is difficult to diagnose from the observations available in this study what process sets the value of w at the SL base and thus accounts for the large profile offsets relative to one another. Though upwelling in the least-squares solution (w_{LS}) correlates with Ekman upwelling computed from CCMP wind stress curl (w_{Ek}) at the mid-depth point of the TL (at which it is assumed that turbulent stresses vanish), which is to be expected given that the solution objective function is penalized for deviations from estimated wind stress curl, though there is a net offset and an apparent gain of 1.48:1 (w_{LS}:w_{Ek}; Fig. 3.15). These month-to-month variations are also apparent in estimates formed without use of the least-squares problem (w_β in Fig. 3.14). It is possible that the algorithms used to map scatterometer stress on a regular grid smooth the true wind stress field such that curl is underestimated at OSP.

The estimated large variations in w exceeding those predicted from wind stress curl may be related to the presence of a small anticyclonic eddy or meander at OSP as described in Chapter 2. Previous studies have shown that the mesoscale circulation associated with such a feature can result in large oscillations in vertical velocity surrounding the feature edge due to vortex waves or perturbation to eddy circular symmetry. For example, in an idealized model of three-dimensional circulation in a North Atlantic eddy, perturbations to eddy circular symmetry resulted in ageostrophic vertical velocity excursions of ± 10 m d^{-1} [101]. These oscillations are an order of magnitude stronger than those estimated in w_{LS}, though the eddy considered in the study [101] was considerably stronger than the currents observed during the OSP array time series. In simulations of an anticyclonic Agulhas ring using the inviscid, adiabatic semigeostrophic omega equation, Nardelli [110] found large oscillations in vertical velocity near the eddy rim consistent with vortex Rossby waves, which are due to potential vorticity (PV) anomalies propagating along the radial gradient of PV present in an eddy. These studies suggest that vertical motion of the mesoscale field, independent of directly

wind-driven velocities, is capable of generating oscillations in vertical velocity of the type estimated in this study.

Furthermore, Nudds and Shore [114] find that, in a numerical simulation of eddies in the Gulf of Alaska, uplift of subsurface isopycnals within the core of anticyclonic eddies induced upwelling velocities of 0.2-0.7 m d^{-1}, comparable in magnitude to those estimated here. This would not necessarily explain the large oscillations in w_{LS}, unless the core of the eddy was moving back and forth across the array extent, which cannot be ruled out. However, upwelling within the core of an anticyclonic eddy is consistent with the mean positive offset of w^{LS} from w^{Ek}. The vertical vorticity values of $\sim |0.01f|$ observed in this study are an order of magnitude too small to produce the estimated Ekman pumping velocities through differential surface stress [*e.g.,* 107]. Horizontal voriticity variations could also produce vertical velocities at the base of the Ekman layer different from those estimated using wind stress curl [98], but there is a lack information about second derivatives of the surface velocity field at the scale of the array during the time series and it is not feasible to assess this possibility. Freeland [58] uses the Argo array to estimate upwelling at 700 dbar averaged across the central Gulf of Alaska that ranges from 0.02-0.12 m d^{-1} from 2003-2010. As pointed out by [58], the effect of averaging over such a large scale removes the influence of eddy features such as those likely observed in this study.

As described in Section 3.2.3, the system (3.50) allows deviations of vertical shear of the horizontal velocities from the estimated thermal-wind shear, and allows divergence that differs from the internal Sverdrup balance. It is of interest whether a solution of comparable accuracy could have been obtained without these allowances, that is, by assuming that 1) the geostrophic velocities from Chapter 2 were well-known enough that they could be excluded from the vector of unknowns, and the horizontal advective terms moved to the right-hand side of (3.50), and 2) the divergence – and thus relative profile of w – would be given exactly by the internal Sverdrup balance. Such a system would involve fewer unknowns, and considerably less complexity and computational time. To explore this possibility an alternate problem was formed in which the above two assumptions were made, with the vector of unknowns

consisting only of κ and the vertical velocity at 200 m in each month, $w_{200,j}$. The problem was solved using the same algorithm, scalings, and inequality constraints as described in Section 3.2, though without any constraint on the intercept of the vertical velocity profile given by (3.36).

Normalized MSE (3.66) for $\hat{\theta}$ and $\hat{S}$ given by the least-squares solution to this problem is considerably higher than for the original configuration in which u, v and depth-dependent w are included as unknowns (Fig. 3.25). In Figure 3.25, the NMSE of the original configuration is denoted by the abbreviation "DIV_UV," while the solution obtained by the alternate model is denoted by "BETA_UV_G." In particular, NMSE for configuration BETA_UV_G in the θ budget exceeds 1 everywhere below 100 m, and exceeds 1 at most depths in the S budget below 50 m. This result validates the model configuration used in DIV_UV, and indicates that if horizontal velocities are to be included, a minimum-error solution is obtained only if u, v are included in the vector of unknowns.

These results, along with those from Chapter 2, suggest that the horizontal gradients are known well enough that they can be used to construct a qualitatively realistic profile of geostrophic velocity at monthly intervals, but that these profiles are not known well enough to compute the dot product between horizontal velocity and the horizontal gradients of temperature and salinity. In Chapter 2, it was shown that estimates of geostrophic velocity and deep vertical geostrophic shear made from the ADCP and Seaglider surveys are correlated, even when considering anomalies relative to the low-frequency backing and weakening observed during the survey time series. However, construction of estimates of advection – the dot product of this geostrophic velocity profile and the gradients – is error-prone because the velocity profile vertically accumulates errors in gradients at individual depth bins; *i.e.*, even if errors in the horizontal gradients are uncorrelated in the vertical (white noise, an optimistic assumption), their integral is vertically correlated (red noise). Additionally, small errors in the velocity profile and horizontal gradients can result in large errors in heat/salt advection when the gradients are nearly orthogonal to the geostrophic velocity profile. This is the case for θ for much of the halocline and seasonal thermocline during the first half of

the Seaglider surveys series (*see* Figs. 2.8 and 2.10), hence the dot product between these two quantities is very sensitive to small changes in their relative angle.

Figure 3.25 shows two additional least-squares solutions in which horizontal velocities are excluded from the problem entirely. In one model of flow, vertical velocities are assumed nondivergent in the TL and INT region, and the unknowns include the constant vertical velocity and profile of κ in each month. This model is denoted "NONDIV." In another model, the unknowns include depth-dependent w in each month, where divergence of w is allowed to vary from zero but with the same scaling penalties as for the DIV_UV case. This model is denoted "DIV." Neither model includes constraints on the intercept of the vertical profiles of w. The NMSE for these solutions is generally intermediate between that of the DIV_UV and BETA_UV_G cases (Fig. 3.25). The solutions with only vertical velocity have NMSE nearly as low as the DIV_UV solution at some depths, in particular in the S budget above 80 m. This emphasizes the dominance of the vertical terms in the near-surface budgets of θ and S at OSP throughout the annual cycle. The greatest incremental improvement of DIV_UV relative to the vertical-only solutions (DIV, NONDIV) is in the halocline, in particular for θ, where the DIV_UV solution is the only one able to replicate the observed variability. The DIV and NONDIV solutions generally give NMSE < 1 above 80 m but horizontal velocities must be invoked below this depth to explain the observed variability.

During the Seaglider surveys at OSP, estimated horizontal advection plays a large role in the θ budget deeper than 120 m, importing warm water from east of OSP, and in the S budget both in the halocline and top 120 m where northward and westward flow brought relatively fresh water to OSP. The un-measured vertical terms (vertical advection and diffusion) dominate the temperature budget within the top 120m, and a model of flow with only vertical velocity does nearly as well in this zone. Horizontal and vertical advection of salinity nearly cancel one another in both the top 120 m and halocline, while vertical advection cools the top 120 m and is the primary agent offsetting the excess surface input of heat observed in the time series. This balance of terms is contrary to the conventional balance at OSP, in which weak upwelling balances the surface freshwater input, and seasonal horizontal

flows in the boundary layer import cool water from the northwest of OSP to balance the annual surface input of heat [147, 84]. As noted in Section 3.1, the latter phenomenon has been observed during the fall season by several previous studies [87, 119, 160, §3]. However, analyses of the Weathership era record [84] and heat advection in the Gulf of Alaska from the Argo autonomous float array from 2003-on [75] have demonstrated substantial variance around this balance on monthly or interannual time scales. Tabata [147] found that monthly anomalies from the annual cycle of temperature during the early Weathership record were substantially explained by horizontal geostrophic advection. It is clear from the observations described in Chapter 2 that the phenomena observed during the Seaglider surveys at OSP do not represent mean North Pacific Current flow, as evidenced by the weakly westward circulation, downward isopycnal displacement, and vertical thermohaline finestructure below the surface. It is therefore unsurprising that the transport estimates of the least-squares solution give advective balances of θ and S that differ from those observed over decadal scales at OSP. While it remains an open question what fraction of time at OSP heat and freshwater budgets are well-characterized by mean conditions and what fraction is dominated by eddy conditions, the results of this study provide further confirmation that the latter conditions can exert influence over the upper-ocean heat and freshwater balances for periods of a year or more. The results of Chapter 2 (Fig. 2.15) show that downward isopycnal displacement characteristic of the anticyclonic mesoscale feature observed in the Seaglider surveys was present for $\sim$1.5 yr of the 7.5 yr (to January 2015, and continuing) OCS mooring time series.

The climatological balance of terms quoted in previous studies is based on observations of a near-steady state in heat and freshwater content throughout the Weathership observation period, while it is clear from the results of this study (Figs. 3.23 and 3.24) that heat content increased and mean salinity decreased through the duration of the Seaglider surveys. While these observations are consistent with the sign of the long-term trend in the upper ocean at OSP [57, 59, 76, 155], they are at much larger rates than have been observed over recent decades. The available evidence is consistent with the passing of a weak anticyclonic eddy carrying water from the southwest of OSP, and that horizontal import of warm and relatively

fresh water relative to the background along depth surfaces associated with this feature is responsible for the violation of the climatological balance of terms. Large [84] found multiple periods of interannual heat and freshwater content fluctuation in the Weathership era that were uncorrelated with anomalies in surface forcing, and the observations of this study demonstrate one mechanism by which this can occur.

The balances observed during Seaglider surveys are in any case illustrative of the effect of the differential temperature and salinity stratification in the Gulf of Alaska: if salinity does not significantly increase, or decreases as observed during the Seaglider surveys, then any vertical advection that is large enough to offset the surface annual cycle heat input in the top 120 m cannot occur in isolation. This is because the corresponding import of salt across the halocline is too large (see A_v term in Fig. 3.24), and must be offset by another process that removes salt. In this case, the horizontal gradients in the top 120 m are such that horizontal advection acts to freshen the top 200 m without significantly adding or removing heat from the surface layer, thus balancing the input of saline water from upwelling.

3.5 Summary and Conclusions

Tracer and vertically-integrated velocity data from a combined Seaglider-Moored array deployed at OSP were used to solve for unknown, time-dependent, monthly-average three-dimensional circulation and vertical diffusivity values in the upper ocean. The methodology involved formulating a single large-scale system of equations for all of the time series unknowns, based on simplified budgets of heat and salt at monthly time steps. The problem was formulated such that the solution sought to minimize differences between the observed θ/S record and that predicted by the solution vector elements, motivated by the prospective use of the unknowns in the balance of dissolved oxygen (to be addressed in Chapter 4). Additional equations governing the unknowns or relationships between the unknowns, based on assumptions about the dynamics of horizontal and vertical flow, augmented the system and overconstrained the problem. The solution was also required to satisfy hard inequality constraints on the turbulent diffusivities which required them to meet or exceed the weak

values assumed in the stratified interior.

The duration of the monthly intervals in which the balances were formulated was chosen in order to match the time scale of the least-squares problem with the time required for Seagliders to effectively survey the spatial domain surrounding the OSP mooring. Though Seagliders provide a high vertical resolution picture of upper ocean stratification, they move slowly, and suffer from aliasing of internal wave motions – as a result, the minimum scale at which they likely provide information about the spatial structure surrounding this array is about a month. This means that storm-scale advection and diffusion is not resolved in the problem considered here, which contributes significantly to the errors observed at individual depth levels at single time intervals. However, when averaging over distinct vertical zones, such as the surface layer, transition layer, and halocline, the noise is significantly reduced and a clear picture emerges, in which the solution is able to successfully account for the observed bulk stratification, seasonal variability in the upper layers, and secular variability in the halocline.

It is important to note that the scaling factors used to penalize solution residuals in this method are inherently subjective, and could be used to force arbitrarily small errors in the temperature and salinity budgets, at the potential expense of departure of the estimated horizontal velocities and diffusivities from initial estimates as they attempt to compensate for errors or unresolved processes. However, the horizontal velocities obtained in the solution vector were in good qualitative agreement with the geostrophic velocities estimated in Chapter 2, with differences of the order expected due to uncertainty in Seaglider DAC calculations and sampling error. Profiles of vertical velocity largely obeyed the steady internal Sverdrup balance, with weak vertical divergence expected of low Rossby number flow. In addition, the estimated vertical diffusivities were in excellent agreement with previous observational studies of diffusion in the stratified turbulence characteristic of the lower boundary layer. The shape of the vertical profile of diffusivity exhibited a rapid upward increase characteristic of an exponential function above the depth of peak stratification in each month. Monthly averaging vertically smears the profile of diffusivity to some degree, and the transitions observed

in instantaneous profiles or those averaged over a shorter time span may be even sharper. A scaling for diffusivity in stratified turbulence suggests that much of the vertical structure of diffusivity can be explained by changes in the buoyancy frequency, but that a decrease with depth in the vertical component of turbulent kinetic energy must also be invoked. Diffusivity amplitude was coherent across the upper transition layer in each month, and showed monthly variability, with weakest values estimated during the restratification months when the mixed layer shoals in April and May. Diffusivity in the upper TL increased in the fall months relative to the summer months, qualitatively consistent with the results of Cronin et al. (submitted manuscript) for diffusivity at the base of the mixed layer. The summer-to-fall changes appear to be modulated by both changes in vertical kinetic energy and stratification.

The diagnosed balances of temperature and salinity were of fundamentally different character, reflecting the stark differences in surface forcing and climatological upper-ocean stratification of the two variables in the Gulf of Alaska. Temperature budget terms were largest in the top 120 m, while salinity budget terms were greatest in the halocline region (120 m - 200 m). The unresolved vertical terms – turbulence, advection, and radiative absorption – were dominant in the temperature budget above 120 m, while horizontal advection was a leading term below 120 m. The salinity budget is not closed as well as the temperature budget by the least-squares solution, probably reflecting weaker variance relative to sampling uncertainty, as well as greater errors in the surface freshwater flux. Horizontal and vertical advection in the salinity budget were important everywhere below the SL, and upwelling was estimated to import cool water to offset the surface input of heat, with horizontal advection of fresh water counteracting the corresponding vertical import of deep, salty water across the halocline. This balance is contrary to the climatological concept of circulation at OSP, likely due to the presence of a mesoscale eddy or meander near the surveys during 2008-2010 (Chapter 2). Previous investigators found similar prolonged periods at OSP where upper ocean heat and freshwater content anomalies were uncorrelated with estimated surface fluxes – the results of these surveys illustrate in detail one process by which this may occur.

The Seaglider component to the OSP NOAA moored array adds depth resolution, depth

extent, and information about horizontal gradients, along with estimation of depth-averaged current. One compromise of the array configuration is the slow speed with which the glider occupies the transit pattern, and thus gathers horizontal spatial information, relative to rapid changes that occur in the boundary layer. Despite this drawback, this work demonstrates that with application of modern estimation methods, and simple assumptions about the dynamics of the background flow, a combined single Seaglider and mooring array can capably resolve monthly-scale upper-ocean variability in this weakly advective location. The principal limitation in its application is uncertainty in the estimated horizontal gradients, in particular due to low-horizontal wavenumber, high-frequency variability in surface and transition layers. Estimation of horizontal gradients is further complicated by an energetic internal wave field relative to the mesoscale circulation at OSP, which adds noise to measurements collected along a depth surface, even if true gradients along that surface are stationary.

Seaglider surveys at OSP represented the first instance of continuous measurement of depth-resolved mesoscale horizontal gradients *in situ* at OSP for duration longer than a year. These surveys resolved horizontal gradients at temporal resolution finer than the annual and seasonal scale, but coarser than the storm scale. The successor to the array described in this study, the NSF Ocean Observatories Initiative (OOI) Station Papa node, has been deployed since summer 2013 and features multiple autonomous vehicles and moorings. Given the presence of continuous moored and autonomous observations with spatial separation comparable to the survey extent in this work, the OOI array could potentially extend the results of this study by resolving the heat and freshwater budgets at much finer temporal scales, provided the observations are taken with sufficient care. An inverse method such as that described here could be easily adapted to the problem of determining three-dimensional circulation and vertical mixing using higher time resolution OOI data. If deployed for a sufficient period of time the OOI array may be able to offer insight regarding outstanding questions in the southern Gulf of Alaska such as the role of high-frequency advection in the annual balances of heat and freshwater and the nature of climatological seasonal cooling.

3.6 Tables

Term	Definition
$\mathbf{A}_j^S$, $\mathbf{A}_j^\theta$	Matrix of coefficients for unknowns in salinity/potential temperature equations for all depths in time interval j (*see* Fig. 3.5)
$\mathbf{A}_j^{dyn}$, $\mathbf{A}_j^{tr}$	Matrix of coefficients for dynamical/tracer equations in time interval j
$\mathbf{A}_j$	Matrix of coefficients for all unknowns in interval j in "local" system of equations (*see* Fig. 3.7)
$\mathbf{A}$	Matrix of coefficients for unknowns in "global" system of equations
$\vec{b}_j^S$, $\vec{b}_j^\theta$	Vector of right-hand side terms in salinity/potential temperature equations in time interval j
$\vec{b}_j^{dyn}$, $\vec{b}_j^{tr}$	Vector of right-hand side terms in dynamical/tracer equations in time interval j
$\vec{b}_j$	Vector of right-hand side terms in "local" system of all equations in time interval j
$\vec{b}$	Vector of right-hand side terms in "global" system of equations
Δt_j	Length of time interval j
Δz_i	Thickness of depth bin i
h_j	Thickness of the surface layer in time interval j
H_j	Thickness of the surface and transition layers in time interval j
H_j^{Ek}	Assumed thickness of the Ekman layer in time interval j ($= h_j + 25$ m)
i	Depth bin index
$I(z)$	Penetrative solar radiation profile
j	Time interval index
κ	Vertical turbulent diffusivity
n_j^{eq}	Number of equations in time interval j
n_i	Number of depth bins ($n_i = 86$) used to estimate vertical profiles in the top 200 m

n_j	Number of time intervals ($n_j = 20$) at which gradients are estimated in array time series
n_j^h, n_j^H	Number of points in the surface layer/transition layer in time interval j
n_j^U	Number of unknowns in time interval j
n^{uv}	Number of u, v unknowns in each time interval ($= 2n_i$)
n_j^w	Number of w unknowns in time interval j ($= n_i - n_j^h$)
N^2	Squared buoyancy frequency ($\approx -\frac{g}{\rho}\frac{\partial \rho}{\partial z}$, where σ_θ is potential density and g gravitation acceleration)
q	Cost function to be minimized for the solution to the un-scaled, global system of equations
q^s	Cost function to be minimized for the scaled global system
$\vec{r}$	Vector of residuals for the un-scaled global system of equations ($= \mathbf{A}\vec{x} - \vec{b}$)
$\vec{r}^s$	Vector of scaled residuals ($= \mathbf{W}\vec{r}$)
$\vec{s}$	Vector of scaling factors applied to residuals $\vec{r}$ in scaled cost function
S_{ij}	Salinity at depth i and time j
σ_w^2	Vertical component of turbulent kinetic energy per unit mass
$\vec{\tau}$	Surface wind stress vector, with zonal τ^x and meridional τ^y components
θ_{ij}	Potential temperature at depth i and time j
u^g, v^g	Zonal and meridional geostrophic velocity components, estimated in Chapter 2
u_{ij}, v_{ij}	Zonal and meridional velocity components at depth i and time j
$\mathbf{u}_E$	Complex-valued Ekman velocity ($= u_E + iv_E$)
w_{ij}	Vertical velocity at depth i and time j
$\mathbf{W}$	Diagonal matrix of scaling factors applied to least-squares problem residuals ($= \mathbf{I}\vec{s}$, where $\mathbf{I}$ is the identity matrix)
$\vec{x}_j$	Vector of unknowns at time j
$\vec{x}$	Vector of problem unknowns, containing all u_{ij}, v_{ij}, w_{ij}, and κ
$\mathbf{X}$	Complex-valued turbulent stress ($= -\rho_0(\overline{w'u'} + i\overline{w'v'})$)

Table 3.1: Commonly-used symbols, mathematical terms, and abbreviations used in this chapter.

Zone	MSE(θ) [°C^2]	NMSE(θ)	MSE(S) [(ppt)^2 $\times 10^{-3}$]	NMSE(S)
SL	0.427	0.06	0.989	0.22
TL	0.095	0.08	0.524	0.01
RemTherm	0.036	0.26	0.390	0.11
HaloCln	0.004	0.07	0.124	0.02

Table 3.2: Errors in vertical-mean solution temperature and salinity in four distinct zones.

3.7 Figures

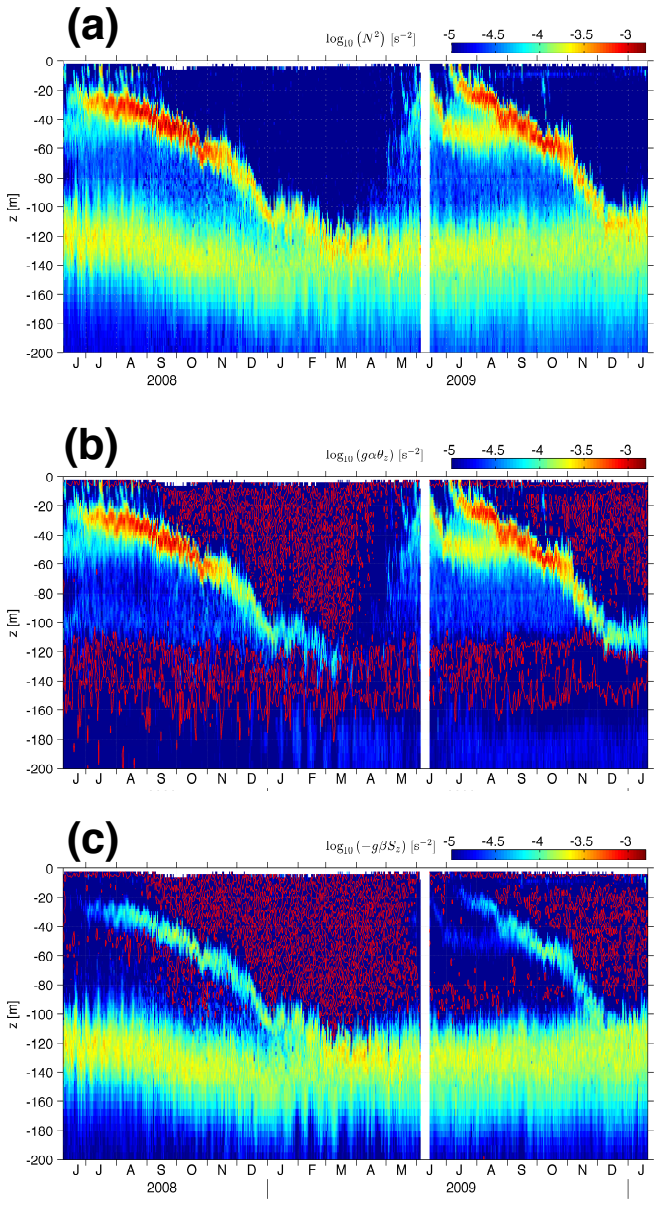

Figure 3.1: (a) Square buoyancy frequency ($N^2 = g\alpha\partial\theta/\partial z - g\beta\partial S/\partial z$, where α and β are the thermal expansion and haline contraction coefficients as defined in [106]) and its contribution from (b) thermal stratification and (c) salinity stratification, calculated from daily-average data collected during Seaglider surveys at Ocean Station Papa, 8 June 2008-21 January 2010. In (b) and (c), zero-contours are shown in red. Within these regions, the contribution to density stratification due to the respective scalar variable is unstable.

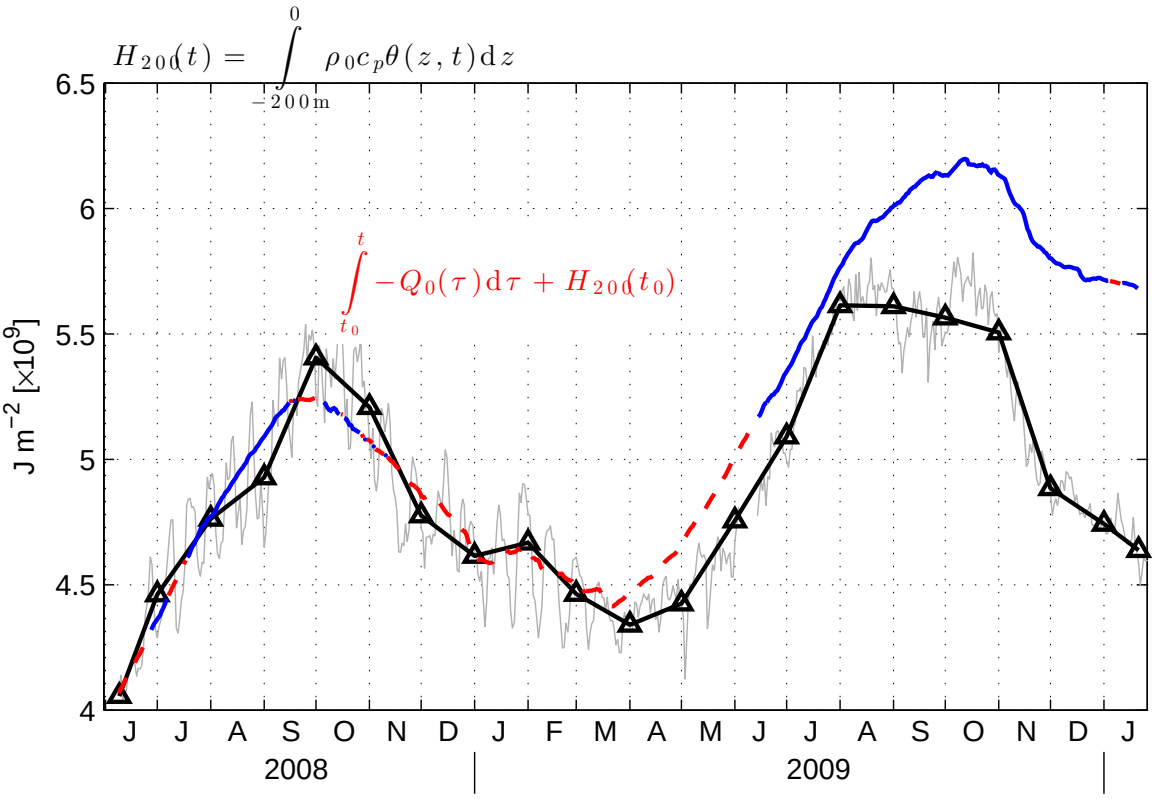

Figure 3.2: Heat content in the top 200 m during Seaglider surveys at OSP (gray and black curves), in comparison to heat content evolution expected from surface flux of heat alone (blue/red curve). Gray curve represents vertically-integrated heat content from daily-average Seaglider survey data. Black curve represents an estimate of heat content at the center of the glider navigational track (Chapter 2, Fig. 2.2) at the beginning and end of each month of the time series. In these curves, a constant volumetric heat capacity of 4.0923×10^6 J $(^\circ\mathrm{C})^{-1}$ m^{-3} has been assumed. The blue/red curve represents the time-integral of the estimated downward surface flux of heat, offset from the heat content at the time series onset. Blue portions of the curve represent estimates of net heat flux from the NOAA Ocean Station Papa mooring, while red curves represent estimates made from remote sensing products due to mooring data gaps. Estimated surface fluxes are described in Section 3.2.

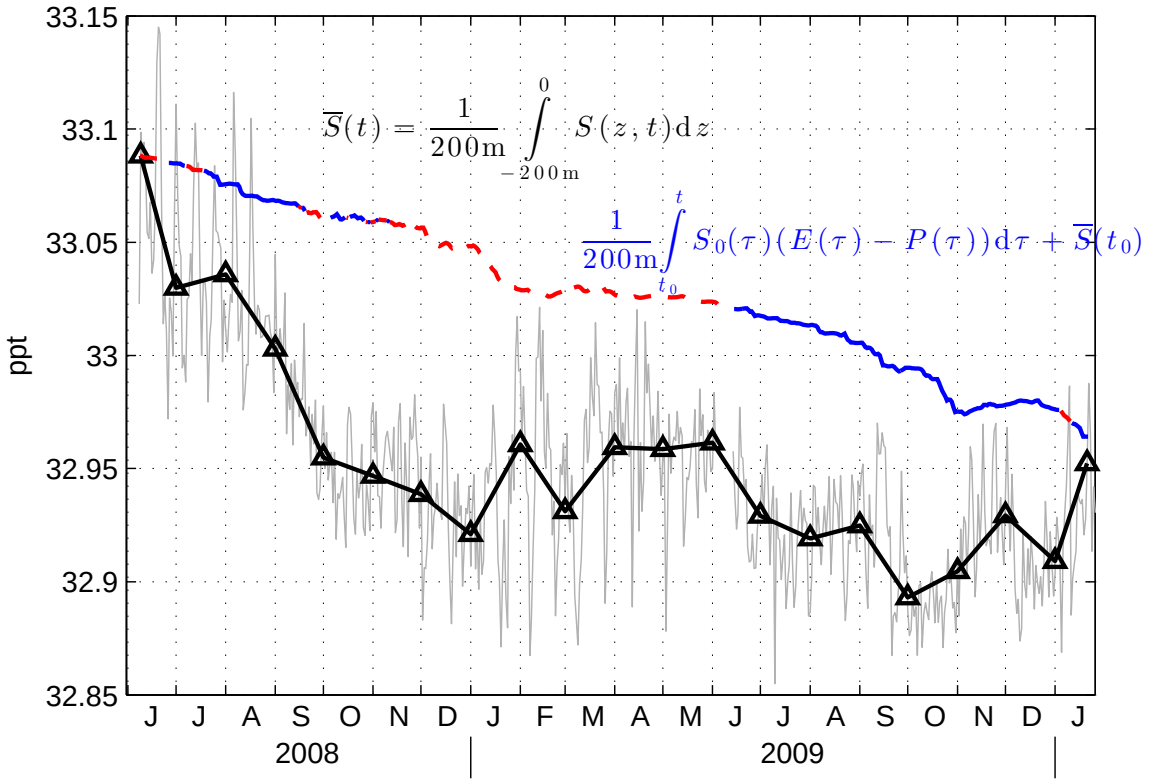

Figure 3.3: Mean salinity in the top 200 m during Seaglider surveys at OSP (gray and black curves), in comparison to mean salinity evolution expected from surface flux of heat alone (red/blue curve). Gray curve represents mean salinity from daily-average Seaglider survey data. Black curve represents an estimate of mean salinity at the center of the glider navigational track (Chapter 2, Fig. 2.2) at the beginning and end of each month of the time series. The blue/red curve represents the time-integral of the estimated dilution due to net moisture flux at the surface, offset from the mean salinity at the time series onset. Blue portions of the curve represent estimates of net moisture flux from the NOAA Ocean Station Papa mooring, while red curves represent estimates made from remote sensing products due to mooring data gaps. Estimated surface fluxes are described in Section 3.2.

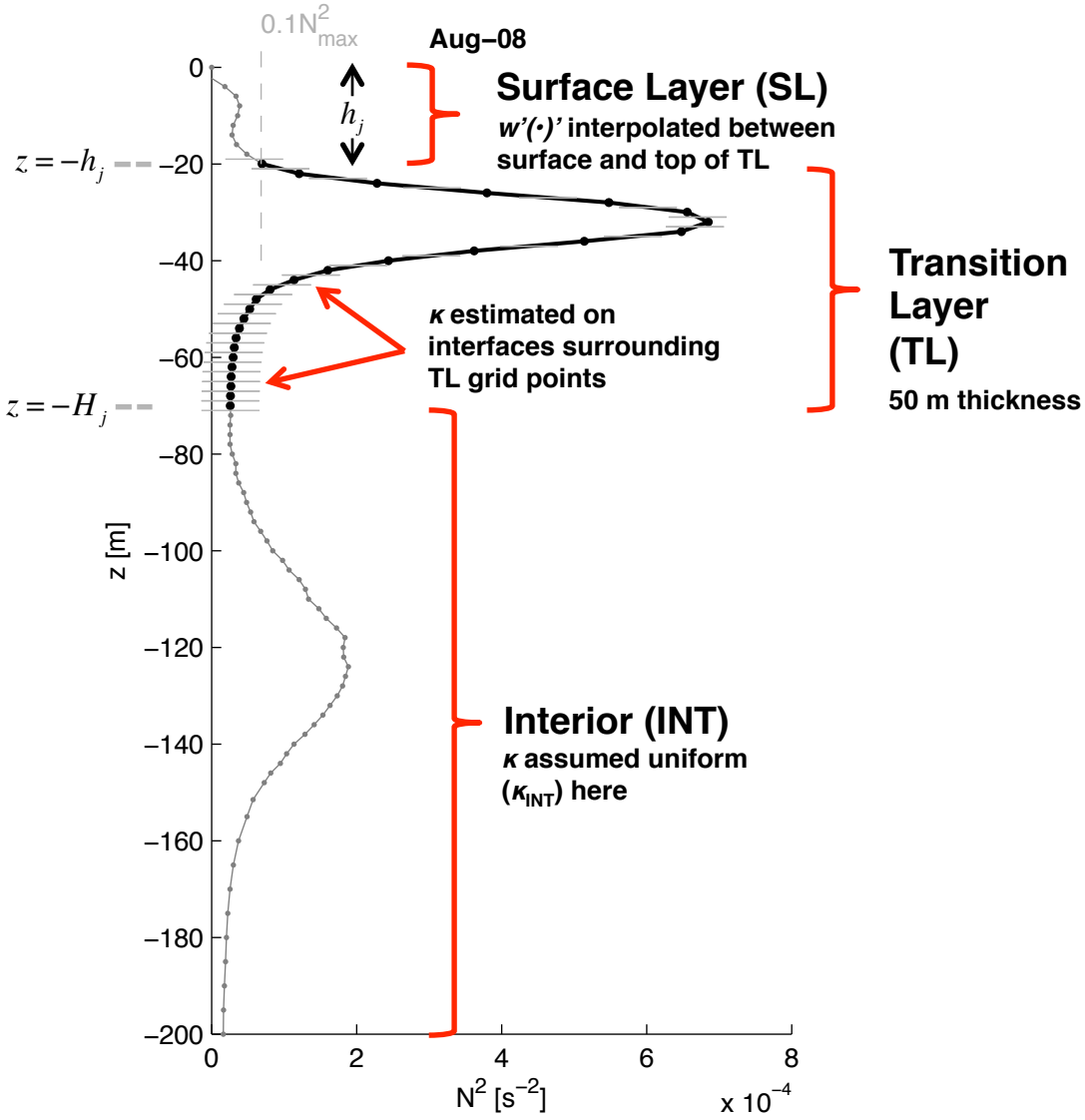

Figure 3.4: Monthly-mean stratification in August 2008 (time interval $j = 3$) and arrangement of vertical model layers for this month, as defined in section 3.2.3. Dot markers denote depth grid points in the top 200 m. The Transition Layer (TL) is bracketed by depths $z = -h_j$ and $z = -H_j$ for time interval j, as shown at left. Diffusivites at the interfaces above and below transition layer depth grid points (indicated by solid black lines/points) are included in the vector of unknowns. The peak in stratification centered at $z = -30$ m is the top of the seasonal thermocline, which is present in summer at Ocean Station Papa. The weaker peak at $z = -125$ m represents the salinity-stratified permanent halocline, which is present in all months (Fig. 3.1).

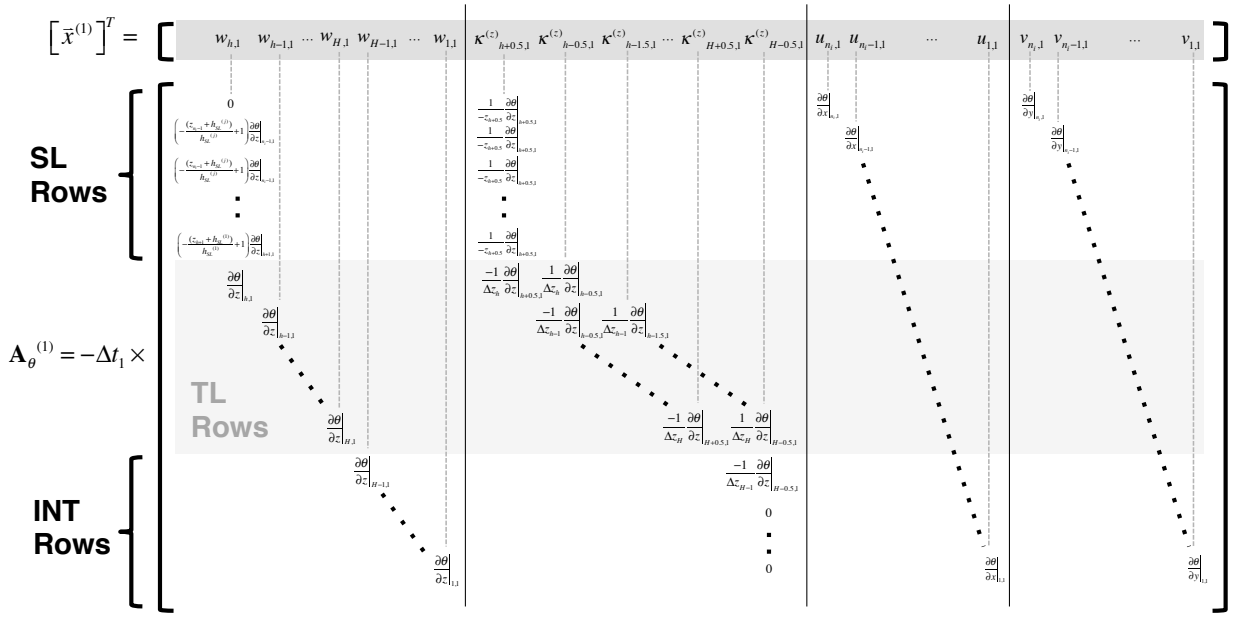

Figure 3.5: Elements of matrix $\mathbf{A}_1^\theta$ and vector $\vec{x}_1$ within the system of equations described by (3.27). Each row of $\mathbf{A}_1^\theta$ corresponds to the equation governing the change in temperature during $j = 1$ at one vertical grid point. Each column corresponds to the coefficients for one of the unknowns within the vector $\vec{x}_1$.

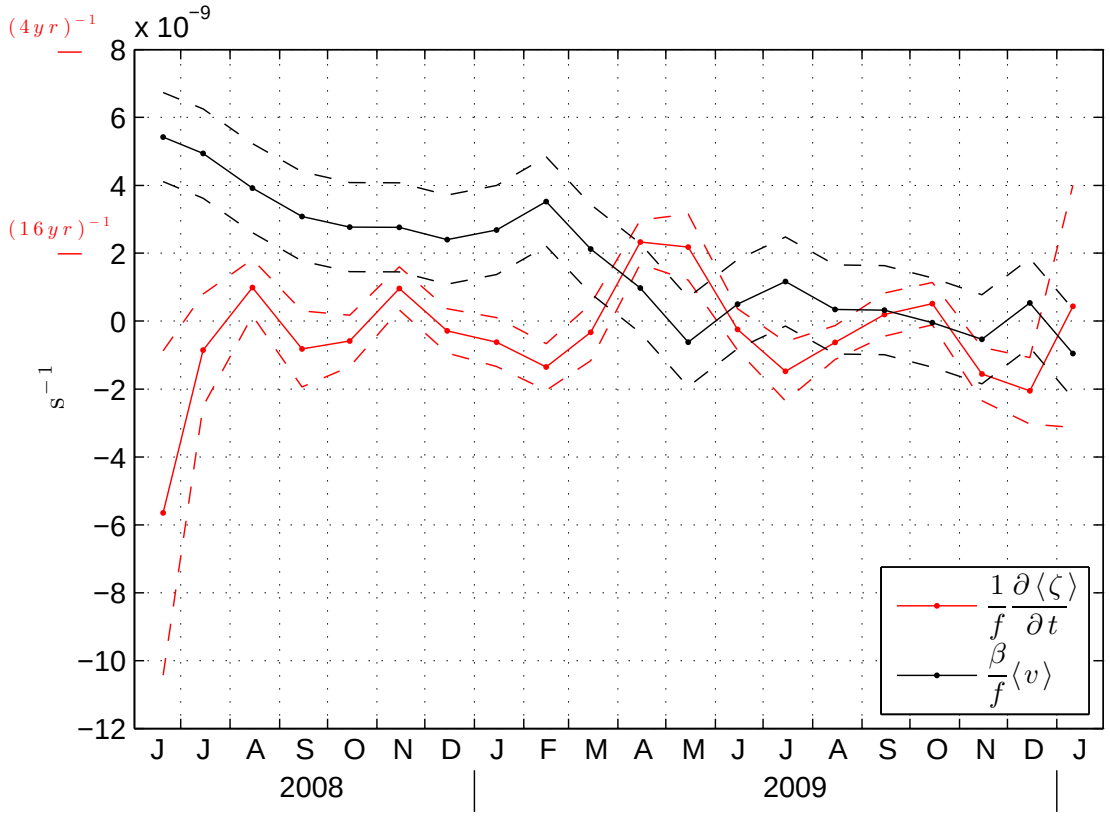

Figure 3.6: Comparison of terms in linear, unsteady, depth-averaged vorticity balance, computed from Seaglider 0-1000 m depth-averaged current (DAC) estimates in each monthly time interval. Angle brackets in legend indicate averaging over top 1000 m. Confidence bounds for $\partial\langle\zeta\rangle/\partial t$ are based on the uncertainty of $\langle\zeta\rangle$ estimates and the associated uncertainty in a centered-difference approximation of the derivative around each bin, assuming errors in bins are independent. Confidence bounds for $\frac{\beta}{f}\langle v\rangle$ are based on an assumed ± 1 cm s^{-1} error.

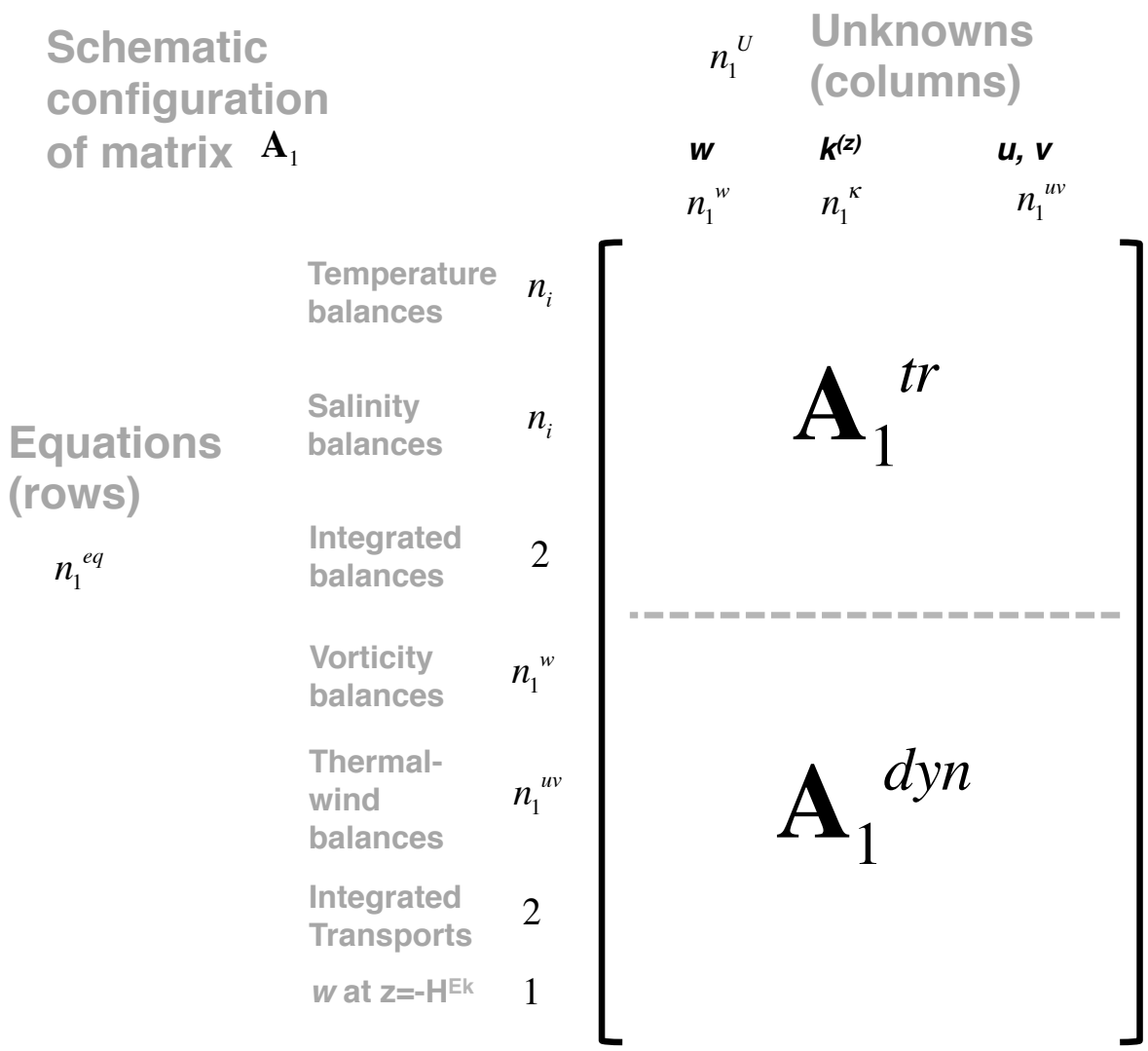

Figure 3.7: Schematic configuration of matrix $\mathbf{A}_1$. This matrix is composed of two sub-matrices, $\mathbf{A}_1^{tr}$ and $\mathbf{A}_1^{dyn}$, each of which have n_1^U columns, corresponding to the number of unknown w, κ, u, and v at time interval $j = 1$. $\mathbf{A}_1^{tr}$ has $2n_i + 2$ rows, corresponding to to the temperature and salinity balances at each of n_i depth grid points, and a vertically-integrated balance for each variable. $\mathbf{A}_1^{dyn}$ has n_1^w rows corresponding to vorticity balance equations, n_1^{uv} thermal-wind balance rows, 2 rows for the vertically-integrated zonal and meridional volume transports in the top 200 m, and one row for the integrated vorticity balance shallower than $z = -H_1^{Ek}$. The detailed configuration of the portion of $\mathbf{A}_1^{tr}$ corresponding to the temperature equations is shown in Figure 3.5.

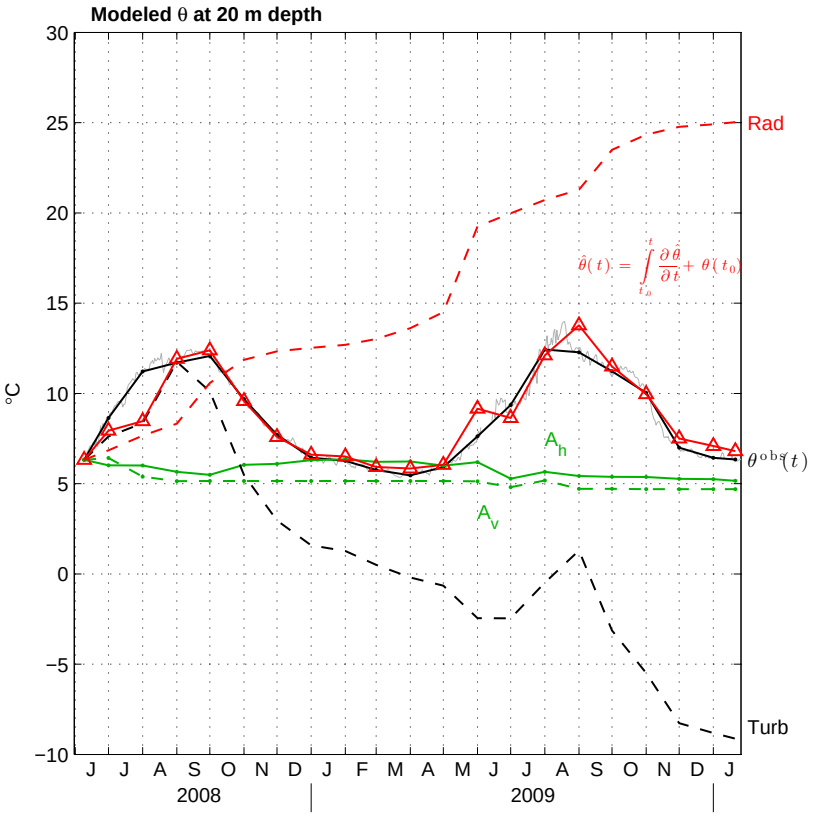

Figure 3.8: Record of observed [$\theta^{\mathrm{obs}}(t)$, black dots] and solution [$\hat{\theta}(t)$, red triangles] potential temperature θ at monthly intervals at 20 m depth. Solution θ is the sum of time-integrals of absorption of solar radiation (labeled "Rad," red dashed curve), convergence of turbulent transport ("Turb," black dashed), horizontal advection ("A_h," green solid), and vertical advection ("A_v," green dashed), as described in the text. Radiative absorption is specified; all other terms are estimated by the least-squares solution. Gray line shows daily-average θ at 20 m from Seaglider surveys.

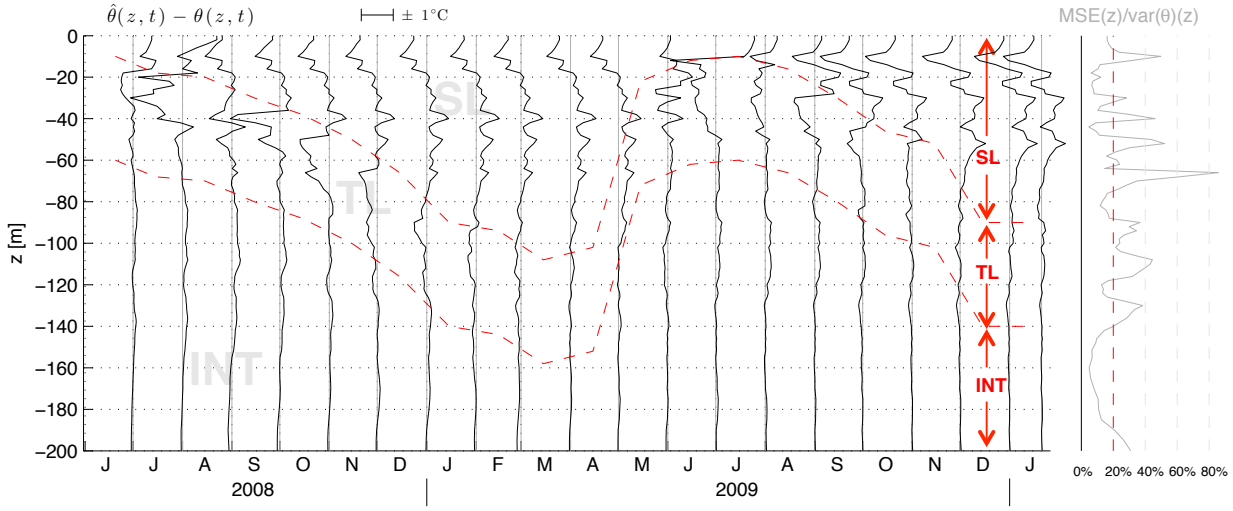

Figure 3.9: Differences between potential temperature predicted by the least-squares solution $\hat{\theta}$ and observed potential temperature θ. Black lines show profiles of temperature anomaly at the end of each monthly time interval (scale at upper left; 10 d = 1°C). Red dashed lines indicate boundaries between vertical domains: SL = surface layer, TL = transition layer, INT = interior region (see section 3.2.3). Gray profile plotted at right shows the mean square error (MSE) of solution potential temperature normalized by the time variance, as a function of depth. Red dashed vertical line indicates the an MSE level of 20% of variance.

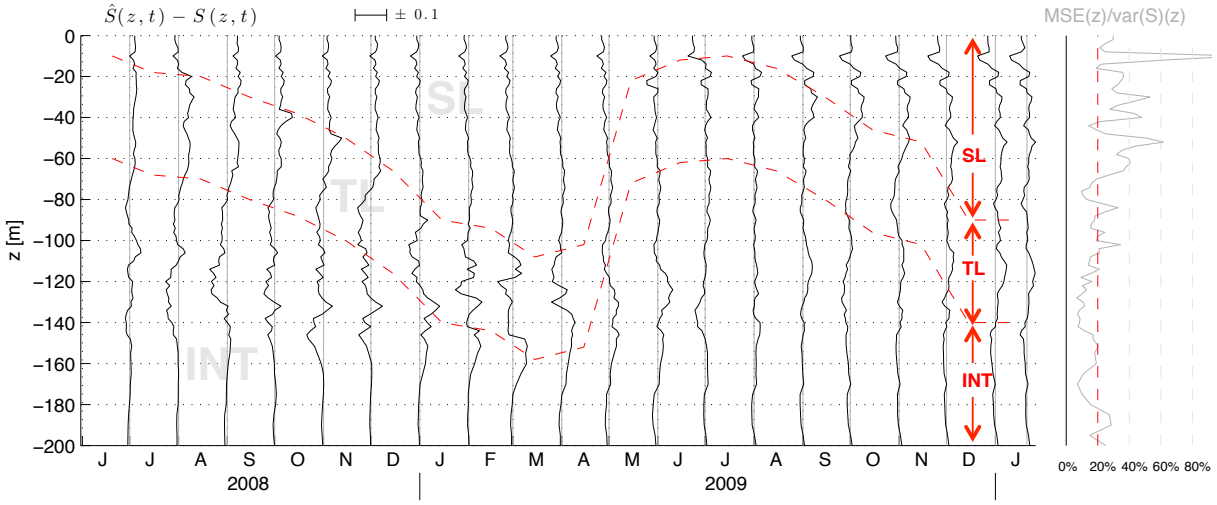

Figure 3.10: Differences between solution salinity $\hat{S}$ and observed salinity S. Black lines show profiles of salinity anomaly at the end of each monthly time interval (scale at upper left; 10 d = 0.1 parts per thousand). Red dashed lines indicate boundaries between vertical domains: SL = surface layer, TL = transition layer, INT = interior region (see section 3.2.3). Gray profile plotted at right shows the mean square error (MSE) of solution salinity normalized by the time variance, as a function of depth. Red dashed vertical line indicates an MSE level of 20% of variance.

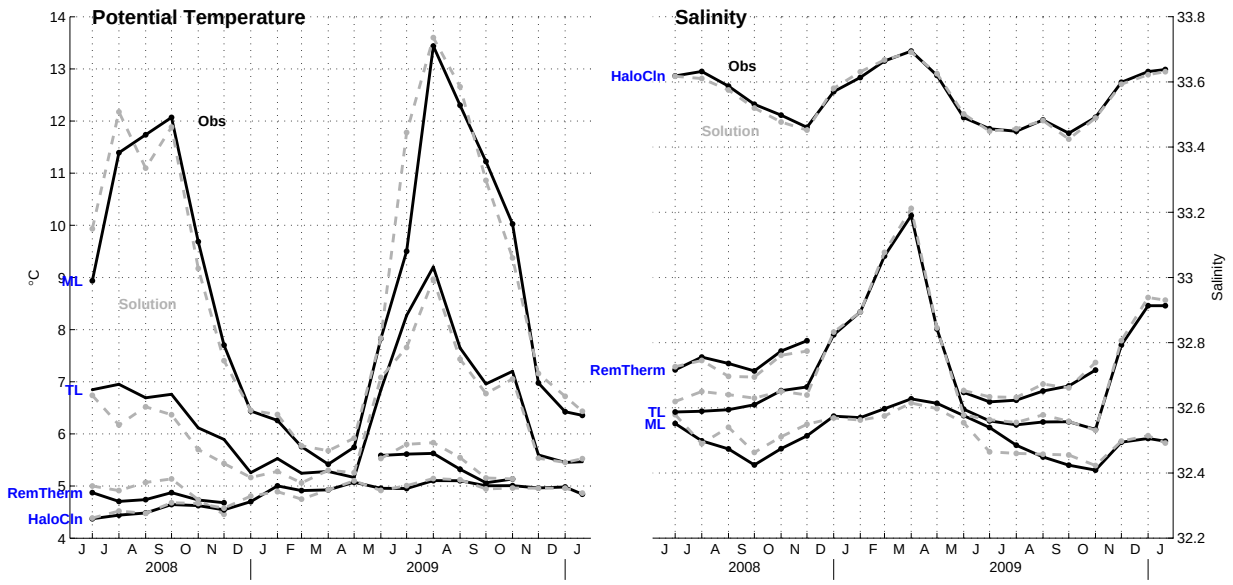

Figure 3.11: Temperature and salinity, averaged vertically in distinct zones. Black lines show observed values and dashed gray lines show those obtained from observed surface fluxes and transports from the solution to the system (3.50). Vertical averages are taken over four zones: the first two correspond to the surface layer (SL) and transition layer (TL) as defined in the text. The remnant thermocline ("RemTherm") is defined as the base of the TL to 120 m depth. Note that this depth range does not always exist, as the TL base is sometimes deeper than 120 m. The halocline ("HaloCln") is defined as the range from 120 m or the TL base, whichever is shallower, to 200 m.

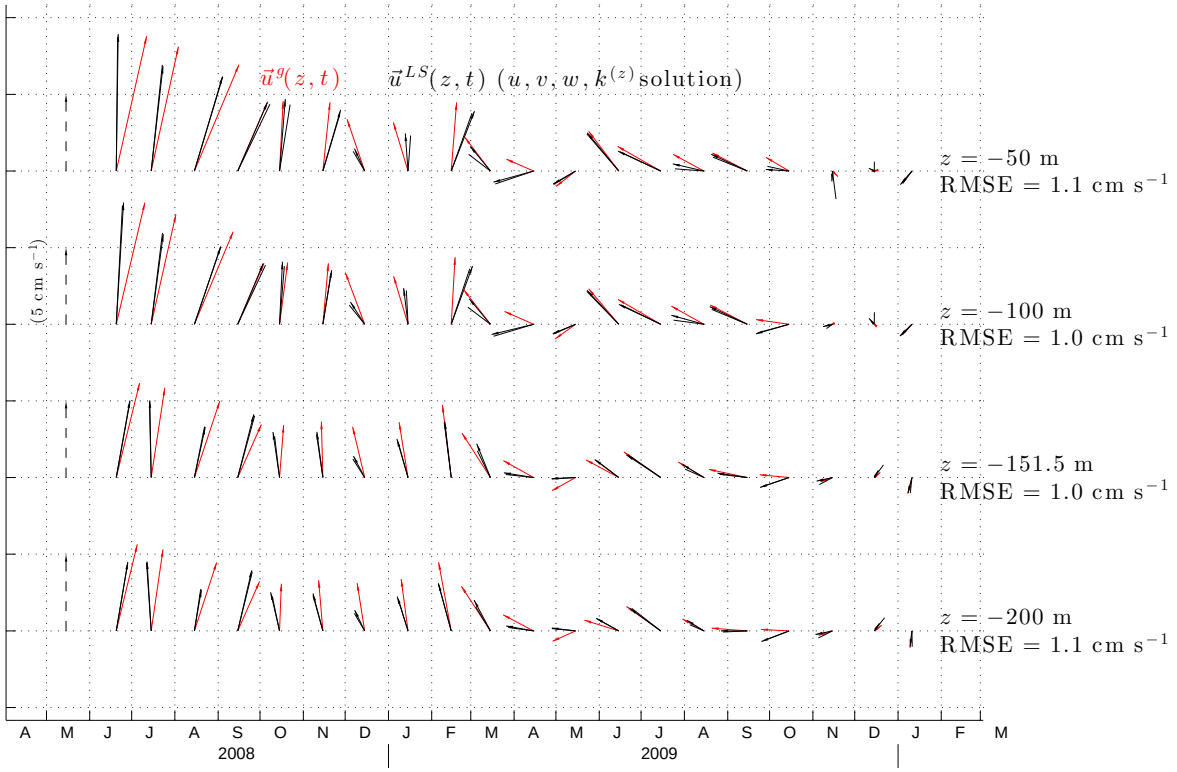

Figure 3.12: Horizontal velocities estimated by the least-squares solution ($\vec{u}^{LS}$, black) and geostrophic velocities reference to observed 0-1000 m depth-averaged current ($\vec{u}^g$, gray; see Chapter 2) at four selected depths. Scale vector (dashed black) at far left for each row – scale is 1 cm s^{-1} = 10 d. Text at right of each row indicates the depth of velocity estimates and the root-mean-square magnitude of the velocity error (RMSE) between observed and solution velocities.

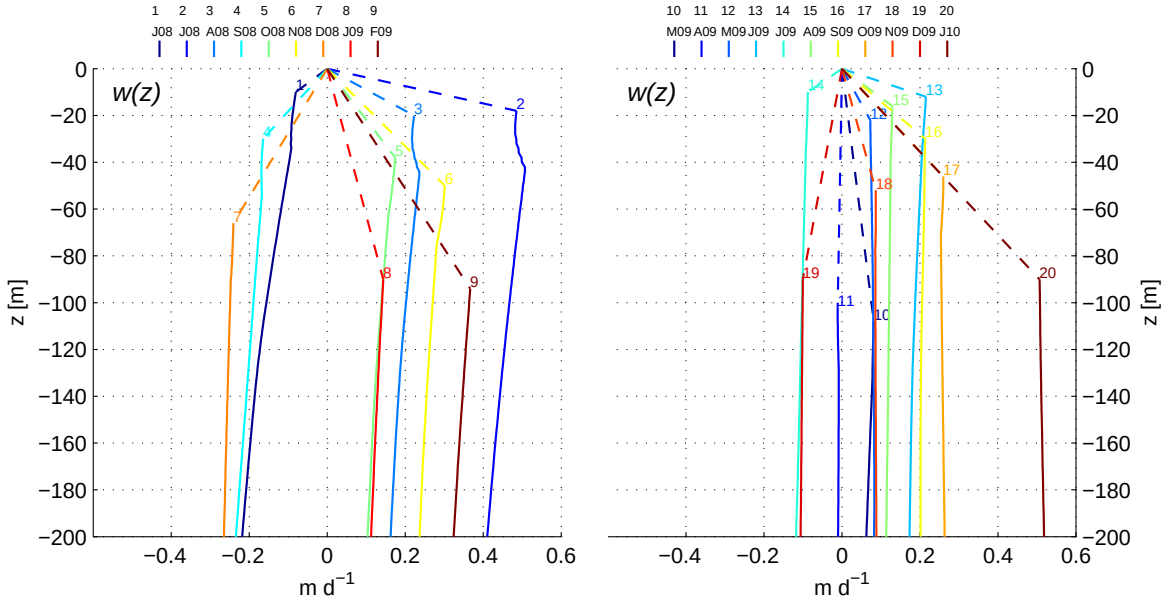

Figure 3.13: Profiles of vertical velocity w estimated by the least-squares solution, June 2008–February 2009 (left) and March 2009–January 2010 (right). Profiles in the left panel are from time intervals during which estimated flow is uniformly poleward and the vertical velocity would be expected to be divergent upward by the linear, steady balance (3.32). The right panel covers months when the estimated meridional flow is near-neutral. Colors and numbers at the base of the surface layer indicate the time interval to which each profile corresponds (labels at top in each panel).

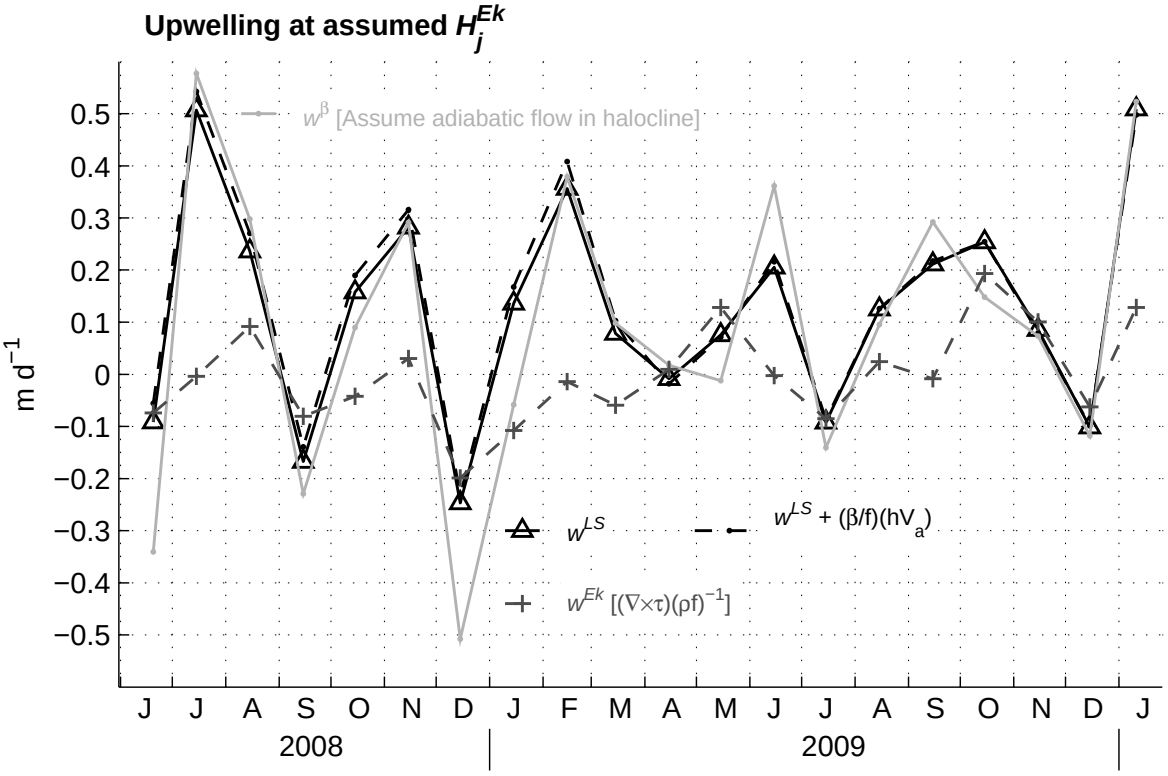

Figure 3.14: Vertical velocity at $z = -H_j^{Ek}$ estimated from the least-squares solution ("w^{LS}," black) and from geostrophic velocity from Chapter 2 under the assumption of adiabatic flow in the halocline ("w^{β}," gray). Monthly Ekman upwelling estimated from Cross-Calibrated Multi-Platform monthly-average wind stress curl is also shown ("w^{Ek}," gray crosses). Black dashed line shows solution upwelling at $z = -H_j^{Ek}$ minus the effects of vortex stretching of the meridional velocity shallower than $z = -H_j^{Ek}$ ("$w^{LS} + (\beta/f)(hv_a)$," where v_a is the vertically-average meridional velocity shallower than $z = -H_j^{Ek}$.

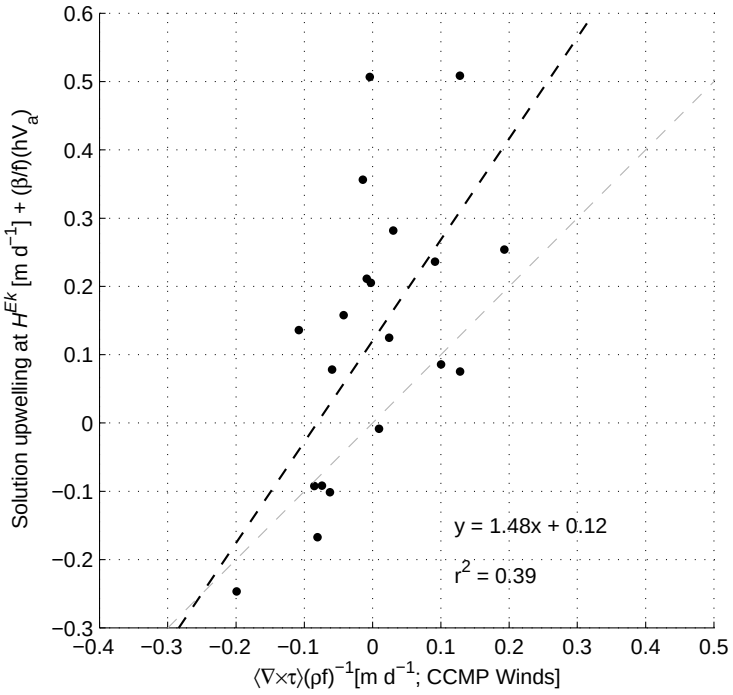

Figure 3.15: Scatter plot of upwelling estimated by the least-squares solution at $z = -H_j^{Ek}$, minus the effects of vortex stretching of the meridional velocity shallower than $z = -H_j^{Ek}$ (y-axis) versus Ekman upwelling based on monthly-average scatterometer wind stress curl (x-axis). The dashed black line shows a y-vs.-x regression line. The correlation coefficient r between the two variables is 0.63 (t-value of 3.41), which rejects the null hypothesis of no correlation at 95% confidence ($t > t_{0.975} = 2.09$ for $\nu = 19$ using a two-sided Student's-t test). Gray dashed line shows the 1-1 line.

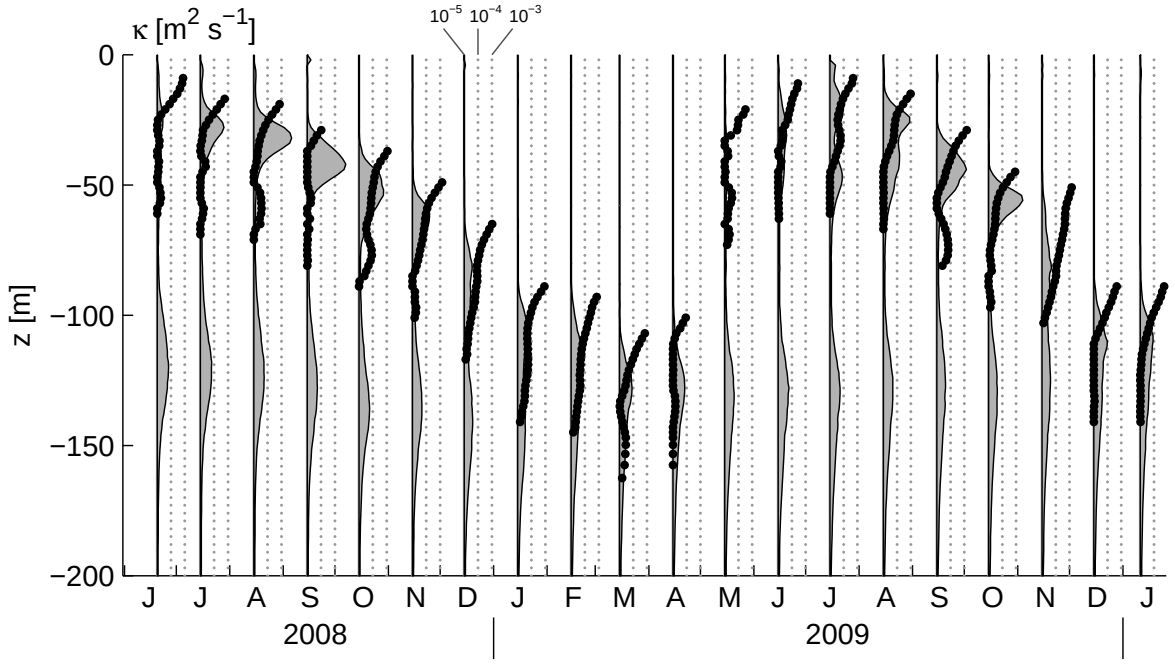

Figure 3.16: Vertical eddy diffusivity κ estimated in the TL by the least-squares solution. Black dots indicate profiles of κ, which are plotted on a logarithmic scale in a coordinate system relative to the center of each time interval. Diffusivity is not displayed in the INT region where it is assumed constant. The center time (solid vertical line in each bin) indicates a value of 10^{-5} m^2 s^{-1}, which is also the assumed deep diffusivity value. Two gray dotted lines offset horizontally from each center time indicate diffusivity increases of 1 and 2 decades respectively (this scale is also labeled at top for December 2008). Background shaded profiles indicate the stratification (buoyancy frequency squared; N^2) in each month. The profiles of N^2 are scaled such that the first dotted line in each month corresponds to an N^2 value of $2.5{\times}10^{-4}$ s^{-2}.

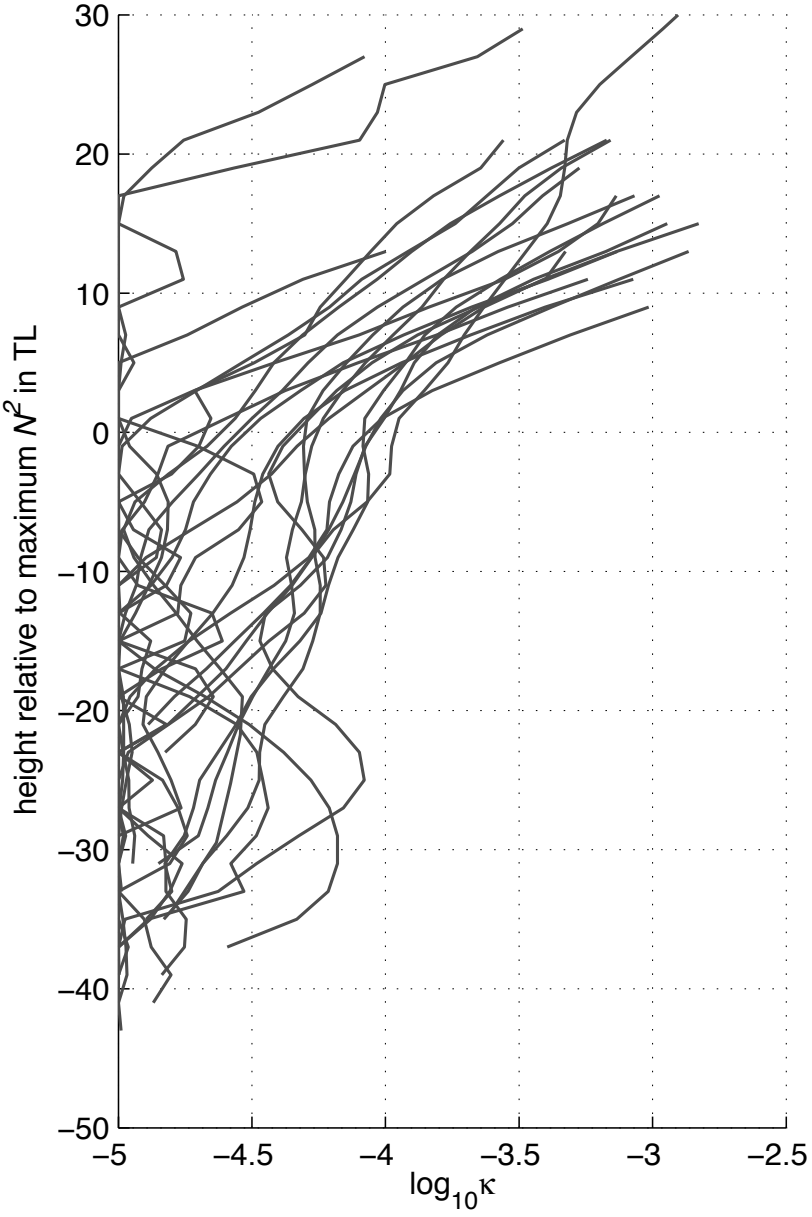

Figure 3.17: Monthly profiles of $\log_{10}\kappa$, plotted versus height above the depth of peak stratification (buoyancy frequency squared; N^2) in the TL.

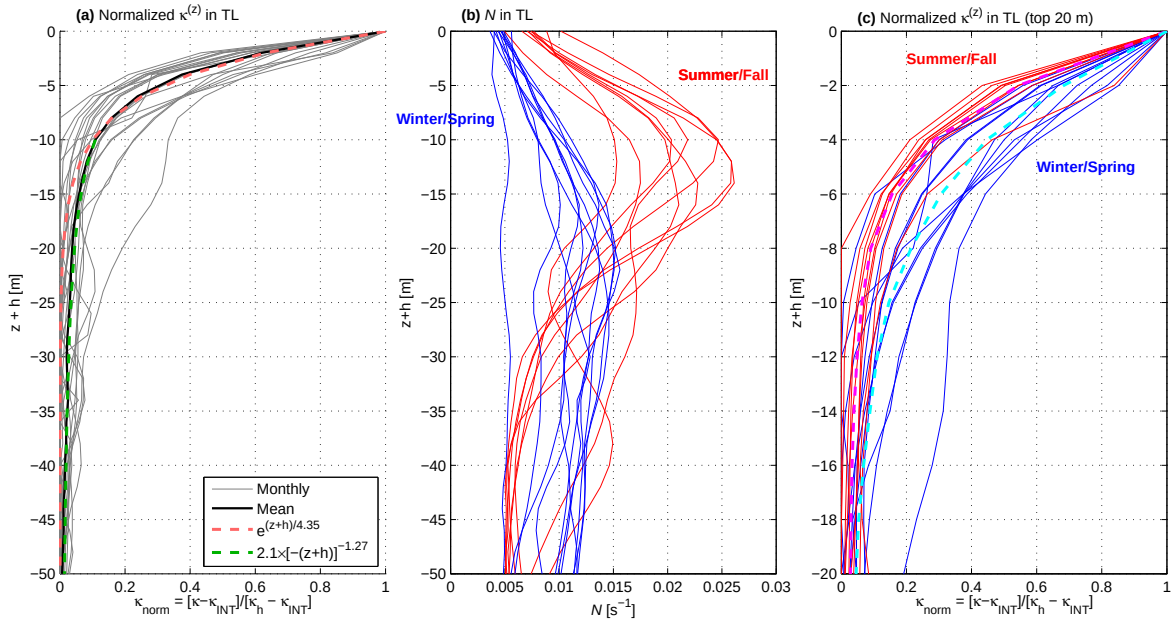

Figure 3.18: Profiles of normalized κ (panels a,c) and buoyancy frequency (N; panel b) in the transition layer (TL). Profiles plotted versus height above the TL upper boundary. Profiles in (a,c) are normalized by subtracting the assumed deep diffusivity $\kappa_{\rm INT}$, and dividing by the residual amplitude (peak value of the profile after $\kappa_{\rm INT}$ is removed). In (a), the solid black curve is a mean profile and the dashed red curve is an exponential fit to the mean profile, which has an e-folding depth of 4.42 m. The green dashed curve is a power-law fit to the mean profile below 10 m. In (b) and (c), red profiles indicate high-stratification profiles (July-November 2008, July-October 2009). Blue profiles indicate low-stratification profiles from other months. Note that panel (c) displays the upper 20 m of the transition layer only. In (c), the thick cyan dashed line (thick magenta dashed line) is the mean of the low-stratification (high-stratification) profiles in the top 20 m.

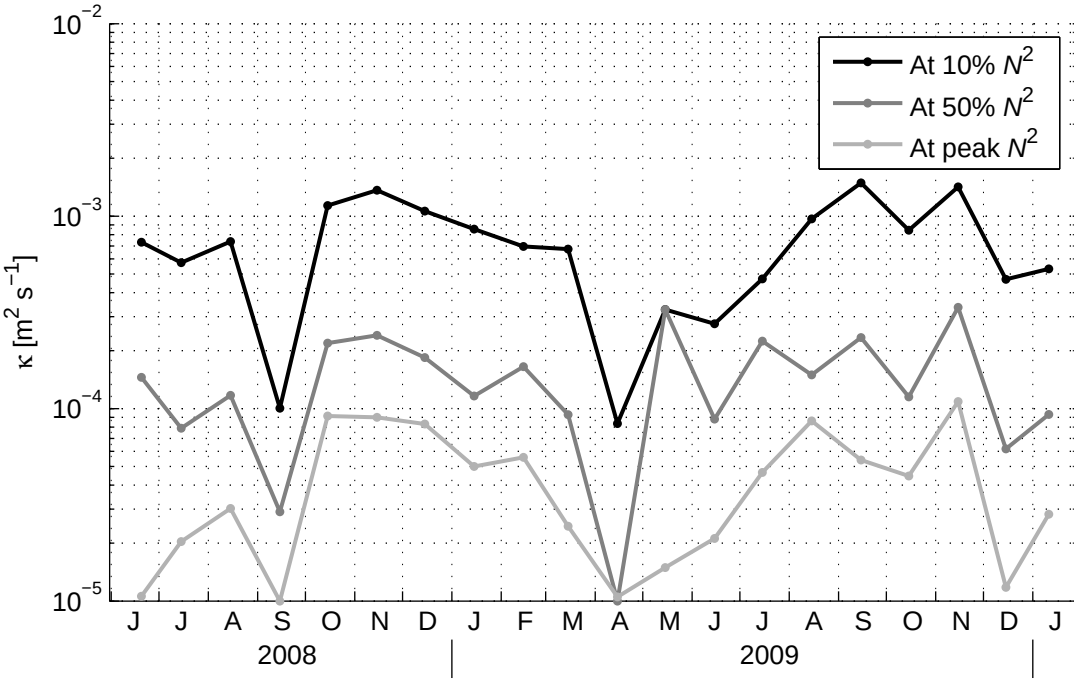

Figure 3.19: Diffusivity estimated from the least-squares solution at three locations within the transition layer (TL). The black line shows diffusivities at the top of the TL (defined as the uppermost depth bin at which stratification is at least 10% of its peak value in the TL in each month). The dark gray line shows diffusivities at the depth where stratification is 50% of the peak value. The light gray line shows diffusivities at the depth of peak stratification.

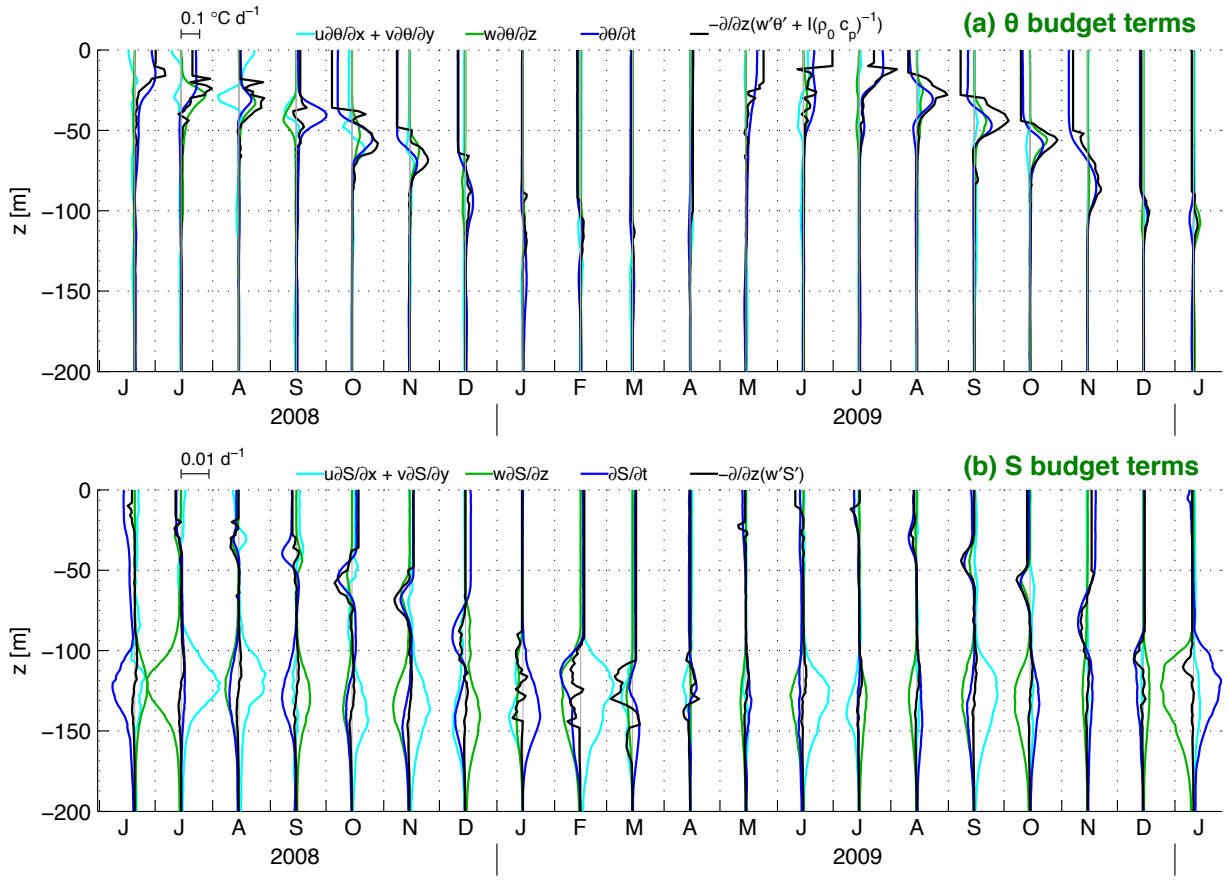

Figure 3.20: Terms in monthly potential temperature [θ; panel (a)] and salinity [S; panel (b)] budgets estimated by the least-squares solution. In each month, vertical profiles of resolved terms in the balances of each variable are plotted in an x-coordinate system with origin at the center of each month. Scale is shown at upper left in each panel. Cyan lines indicate horizontal advection, green lines vertical advection, blue lines the local rate-of-change, and black lines the convergence of turbulent transport in (b), or turbulent transport plus absorption of solar radiation in (a).

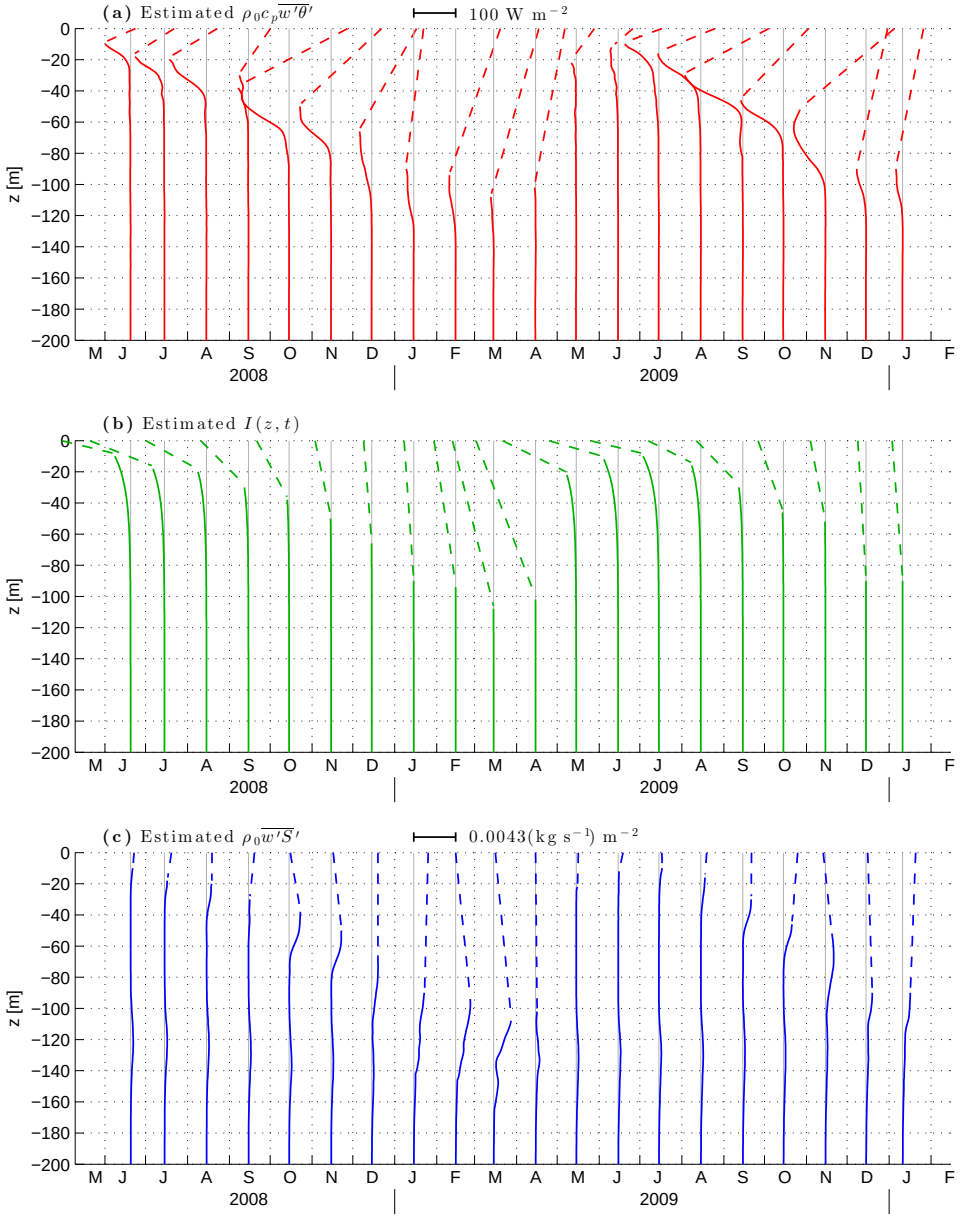

Figure 3.21: Monthly profiles of vertical turbulent and radiative flux of heat and salt during the Seaglider time series. Profiles of heat flux (a) and salt flux (c) are estimated by the least-squares solution. Dashed portions of the profiles are those within the surface layer (SL), where turbulent flux is interpolated between the surface value and the value estimated by the solution at the top of the transition layer (TL). The scales in panels (a) and (c) are such that two profiles that appear similar in size are equal in their contribution to the turbulent buoyancy flux, $\overline{w'b'} = g(\alpha\overline{w'\theta'} - \beta\overline{w'S'})$. Panel (b) shows for comparison the specified solar radiative flux profiles. Similar to (a) and (c), dashed portions of profiles indicate where they are interpolated within the SL.

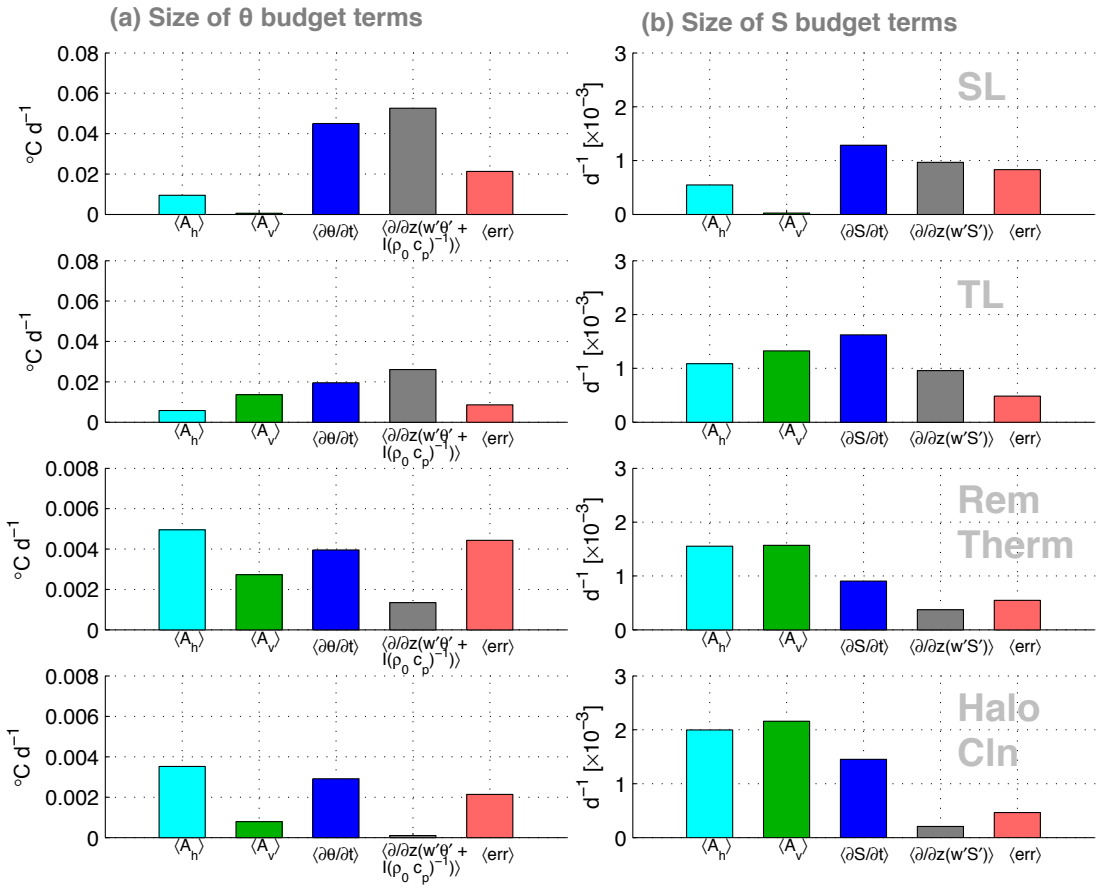

Figure 3.22: Mean absolute value of θ (panel a, left) and S (panel b, right) budget terms in the surface layer (SL, top row), transition layer (TL, second row), remnant thermocline (RemTherm, third row), and halocline (HaloCln, fourth row) during the array time series. Remnant thermocline and halocline zones are defined in the text. Cyan bars are horizontal advection (A_h), green bars vertical advection (A_v), blue bars local rate-of-change ($\partial(\cdot)/\partial t$), and gray bars the divergence of turbulent transport ($\partial/\partial z(\overline{w'(\cdot)'})$) in (b) or turbulent transport plus radiative absorption in (a). Red bars are unresolved terms. For θ, note the change in y-scale for the SL and TL plots relative to the lower three zones.

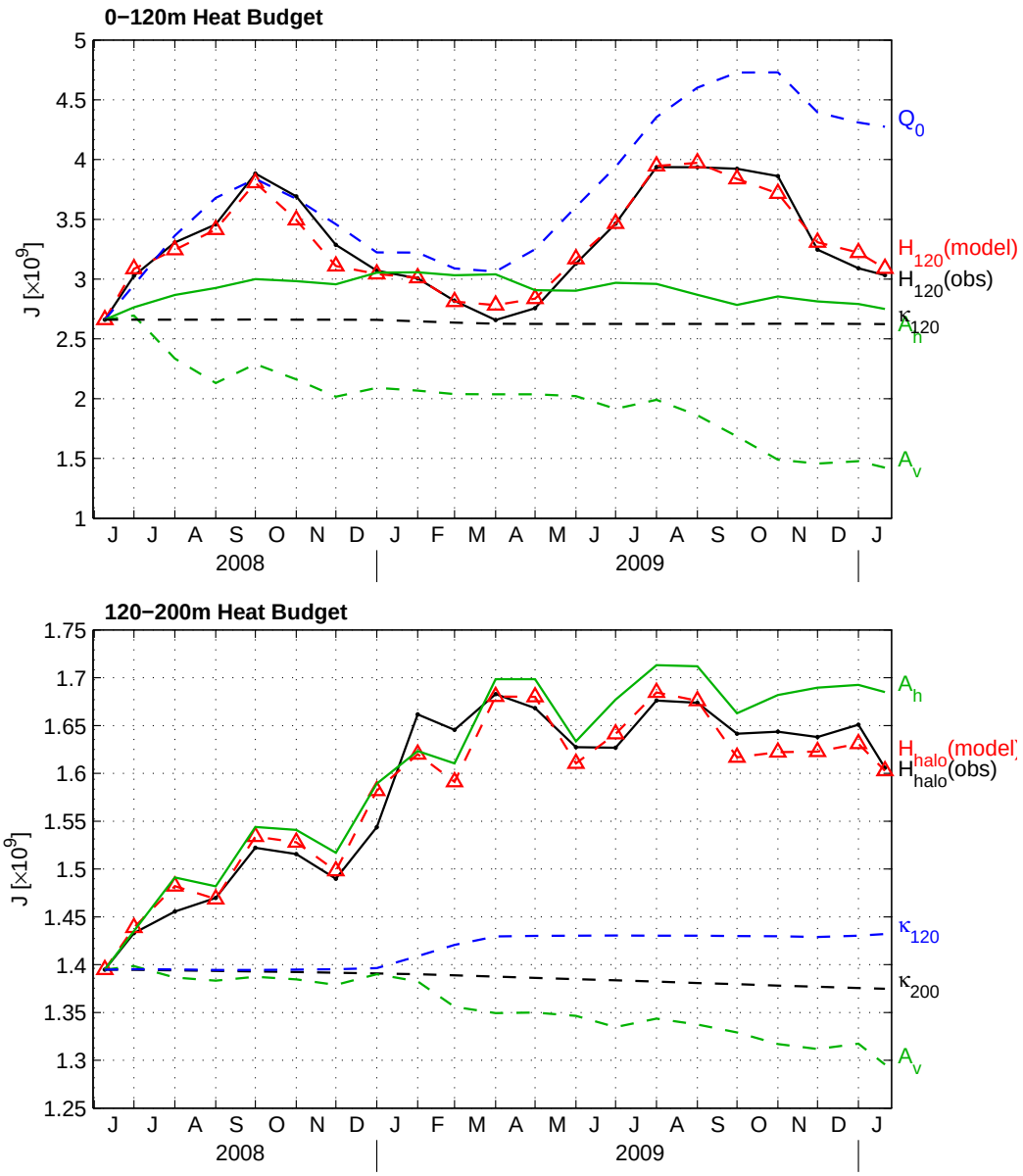

Figure 3.23: Time-integrated balances of heat during the array time series for the top 120 m (a) and halocline region (b). Black lines indicate the record of observed heat content in each region [H(obs)]. Red dashed lines indicate solution heat content [H(model)]. Terms composing H(model) are also shown: blue lines indicate heat flux crossing the upper boundary of each zone [surface heat flux Q_0 in (a), diffusion at 120 m κ_{120} in (b)]. Black dashed lines show lower boundary heat flux [κ_{120} in (a), κ_{200} in (b)]. Solid green lines indicate horizontal advection (A_h), dashed green lines indicate vertical advection (A_v). These terms are defined for the top 120 m balance by (3.69).

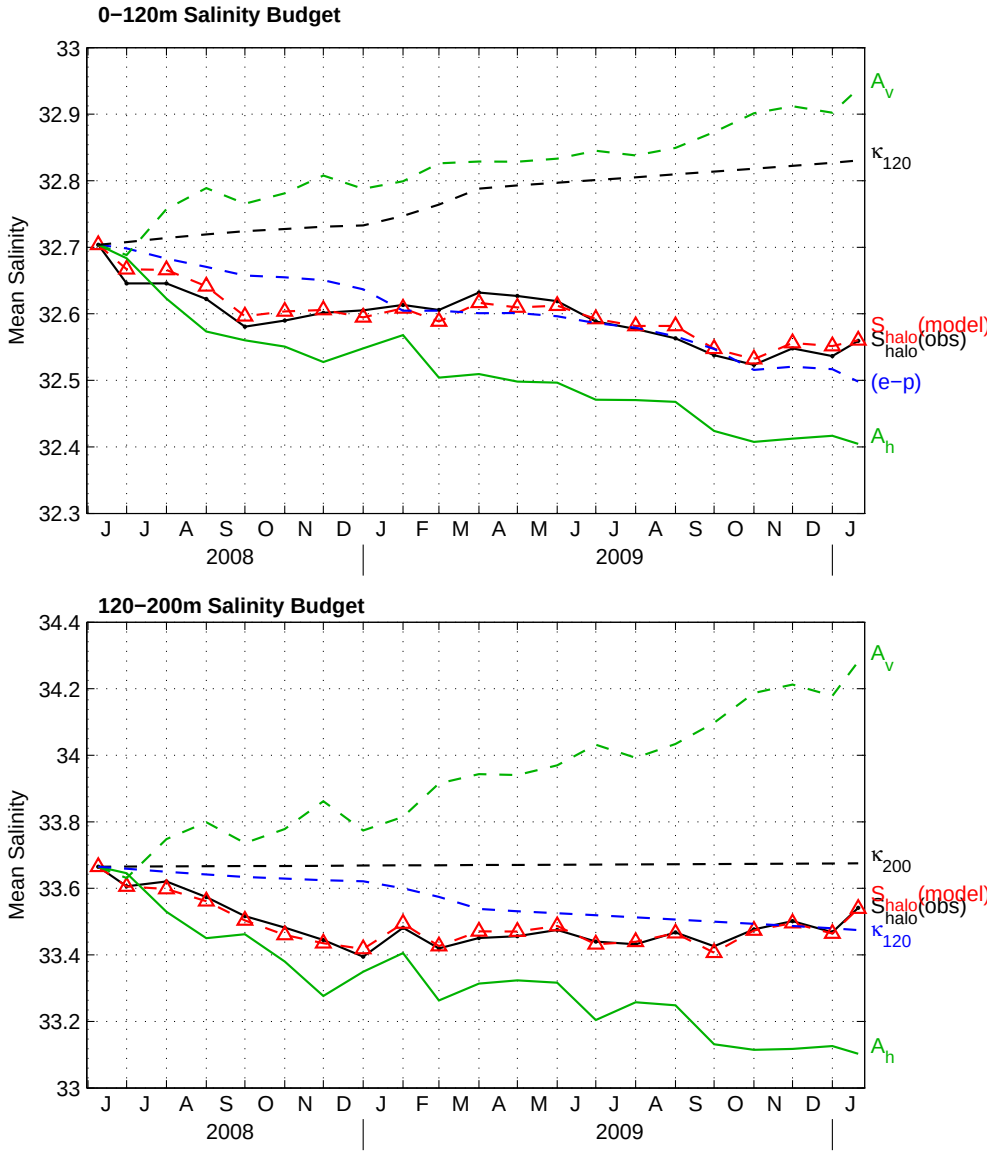

Figure 3.24: Time-integrated balances of salinity during the array time series for the top 120 m (a) and halocline region (b). In each panel, black lines indicate the record of observed mean salinity in each region [S(obs)]. Red dashed lines indicate solution mean salinity [S(model)]. Terms composing S(model) are also shown: blue lines indicate change in mean salinity due to salt flux crossing the upper boundary of each zone [surface moisture flux (e-p) in (a), diffusion at 120 m κ_{120} in (b)]. Black dashed lines show change in mean salinity due to lower boundary salt flux [κ_{120} in (a), κ_{200} in (b)]. Solid green lines indicate horizontal advection (A_h), dashed green lines indicate vertical advection (A_v).

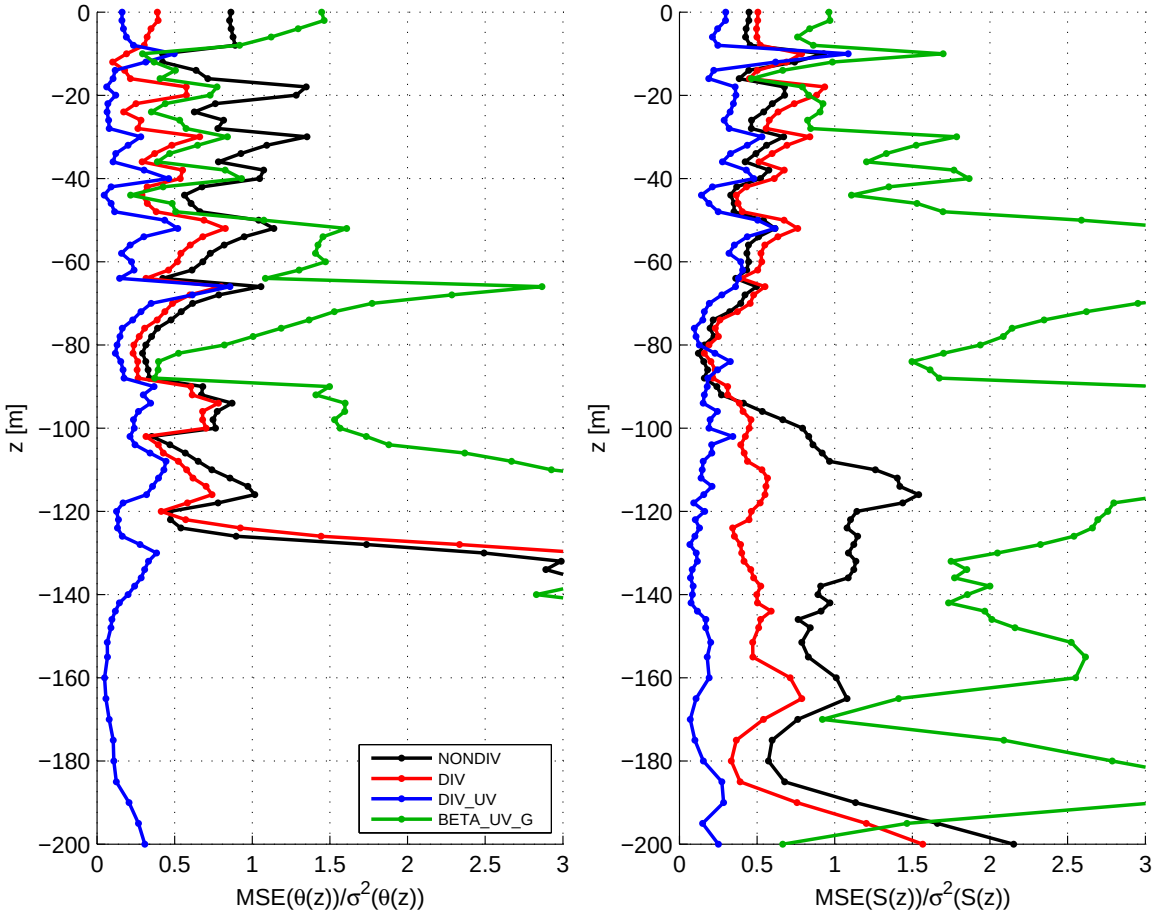

Figure 3.25: Mean-square error (MSE) as a fraction of variance in the time-integrated potential temperature (left) and salinity (right) budgets for four configurations of the least-squares problem. The main configuration described in Section 3.2, from which all main results are derived, is labeled "DIV_UV" and shown in blue. Black and red lines indicate alternate formulations in which horizontal advection is omitted and transports are limited to vertical velocities and diffusivities only; "NONDIV" indicates nondivergent vertical velocity below the surface layer in each month, "DIV" indicates a configuration with depth-dependent vertical velocity. "BETA_UV_G" (green line) indicates a configuration of the problem in which the original estimates of geostrophic velocity and vertical divergence due to the internal Sverdrup balance are considered exact, and the least-squares problem solves for only an offset to the vertical velocity profile w_0 and vertical profile of diffusion.

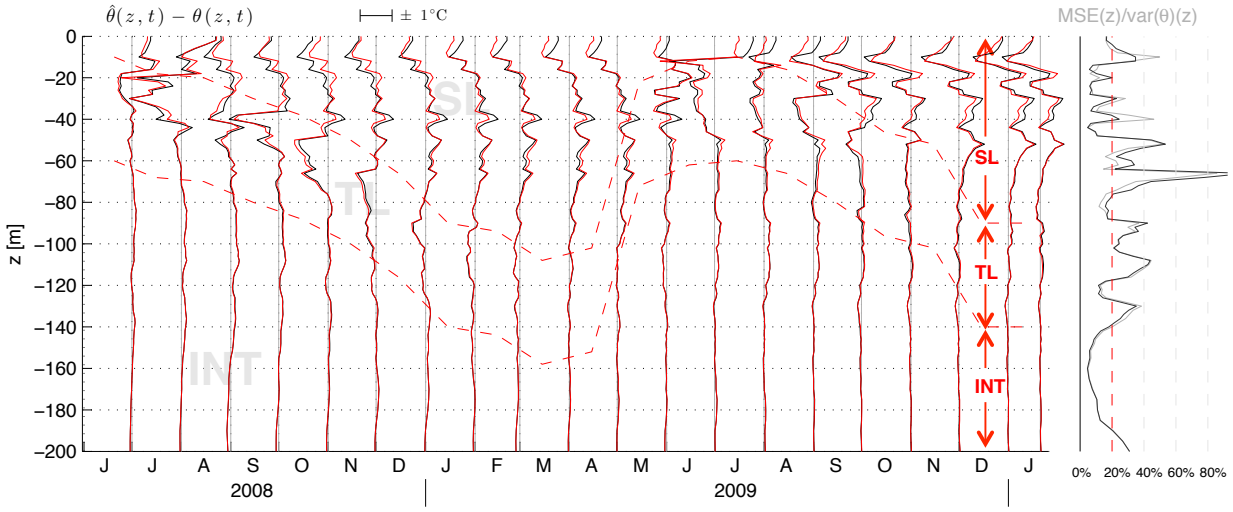

Figure 3.26: Differences between potential temperature predicted by the least-squares solution $\hat{\theta}$ and observed potential temperature θ, as in Figure 3.9, but with results overlaid from solution with specified Ekman flow as described in Section 3.4. Black lines show profiles of temperature anomaly at the end of each monthly time interval from the base configuration; red solid lines show results from solution with Ekman flow. Gray profile plotted at right shows the mean square error (MSE) of solution potential temperature normalized by the time variance, as a function of depth; black profile in this plot shows the same quantity for the Ekman flow solution.

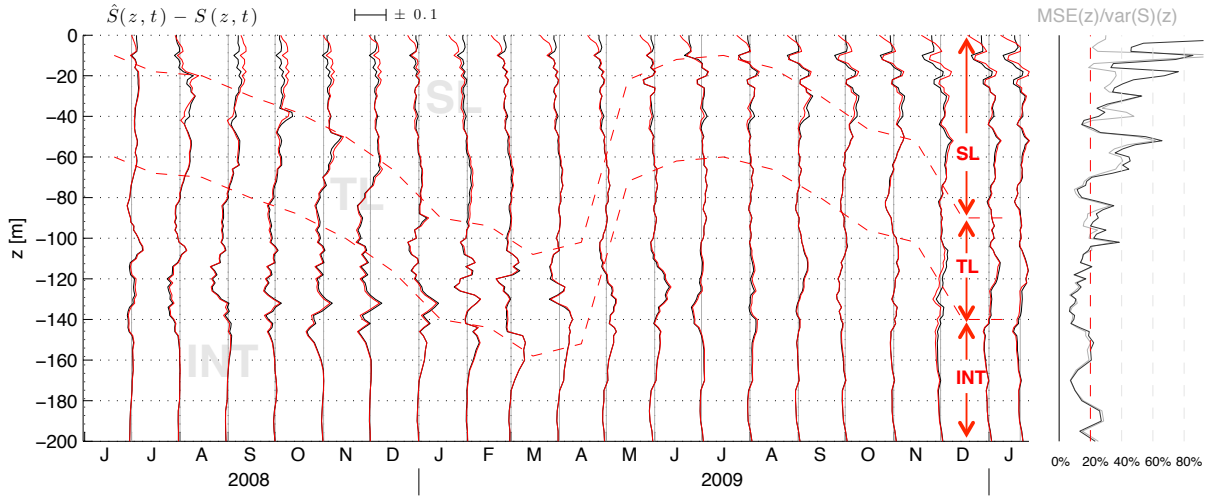

Figure 3.27: Differences between salinity predicted by the least-squares solution $\hat{S}$ and observed potential temperature S, as in Figure 3.9, but with results overlaid from solution with specified Ekman flow as described in Section 3.4. Black lines show profiles of salinity anomaly at the end of each monthly time interval from the base configuration; red solid lines show results from solution with Ekman flow. Gray profile plotted at right shows the mean square error (MSE) of solution salinity normalized by the time variance, as a function of depth; black profile in this plot shows the same quantity for the Ekman flow solution.

Chapter 4

KINEMATICS OF DISSOLVED OXYGEN AND ESTIMATES OF OCEAN METABOLISM

with Charles C. Eriksen, Steven R. Emerson, Meghan F. Cronin

4.1 Introduction

For several decades, Ocean Station Papa (OSP; 50°N, 145°W) has been the site of extensive development of methods surrounding one of the fundamental questions of chemical oceanography and the ocean's role in the earth climate system – the measurement of *net community production* (NCP). Net community production is defined as the net fixation of organic carbon by autotrophic organisms (phytoplankton) in the surface ocean, minus respiration due to autotrophs and heterotrophs [zooplankton and higher-trophic level organisms; 44]. This quantity has fundamental importance for the climate system since, at annual time scales or longer, NCP is in approximate equilibrium with *export production* (EP), the flux of organic carbon in particulate or dissolved form from the surface ocean to the interior [15]. This downward flux of carbon due to the oceanic ecosystem – the ocean's "biological pump" – regulates, in part, the exchange of carbon between the ocean and atmospheric systems and exerts a fundamental control on the atmospheric concentration of carbon dioxide [50]. Though a variety of methods have been used to measure rates of NCP in the surface ocean, or estimate global-average NCP by proxy measurements such as satellite ocean color images, there is a lack of substantial information about the seasonality of NCP, its relative magnitude in a variety of oceanic ecosystems, and its interannual variability, in large part due to a scarcity of locations with sufficiently detailed and persistent measurements to allow its estimation [95, 44]. This hampers the validation of estimates of NCP from ocean ecosystem models or

satellites, and inhibits the ability to simulate, diagnose, and assess the climate system as a whole. Further understanding of NCP, its variability, and factors affecting its estimation are thus important priorities for the broader understanding of ocean biogeochemistry.

Since the vertical export of carbon from the surface ocean due to particulate flux, subduction, vertical mixing, or vertical zooplankton migration is very difficult to measure directly, an alternate approach is to attempt to measure the mass balances of other metabolic tracers influenced by photosynthesis and respiration in the surface ocean, infer the net biological contribution to these balances, and equate this to the net export of organic carbon using the (approximately) known stoichiometry of NCP – the ratio in which nutrients or dissolved gases are consumed or produced relative to carbon during photosynthesis and respiration. A commonly-used tracer in this approach is dissolved oxygen, which through advances in instrumentation can now be measured from sensors mounted on moorings or autonomous platforms [103, 111, 42]. When NCP is positive and net autotrophic conditions persist (*i.e.,* production overcomes respiration), the oxygen concentration following a fluid element increases in the absence of any mixing. Thus, in the upper ocean, a Boussinesq, Reynolds-averaged conservation equation for dissolved oxygen reads

$$\frac{D[\mathrm{O}_2]}{Dt} = -\frac{\partial}{\partial z}\overline{w'[\mathrm{O}_2]'} + J^{\mathrm{bio}}, \tag{4.1}$$

where $[\mathrm{O}_2]$ is the concentration of dissolved oxygen per unit mass of seawater (μmol kg^{-1}), $D/Dt\,(\equiv \partial/\partial t + \vec{u}\cdot\nabla)$ is the derivative following a fluid element, $\vec{u}$ is the velocity, $\overline{w'[\mathrm{O}_2]'}$ is the vertical turbulent transport of oxygen, and J^{bio} is the rate of change of $[\mathrm{O}_2]$ due to the net biological production or respiration of oxygen. In principle, (4.1) can be used to estimate J^{bio} as the difference between the rate of change of $[\mathrm{O}_2]$ following a fluid element (left-hand side) and the convergence of turbulent transport (first term on right-hand side), if these terms are known.

In many cases it is possible to simplify the balance (4.1) to reduce the number of terms that must be estimated. Since persistent measurements of $[\mathrm{O}_2]$ and other dissolved gases are

most commonly obtained as point samples in the surface mixed layer (SL), a typical approach is to integrate (4.1) vertically within the SL, and estimate integrated J^{bio} within the SL as the residual between observed oxygen concentration changes and those expected due to surface gas exchange, horizontal advection, entrainment of waters deeper than the SL, and turbulent diffusion at the SL base, or some combination thereof [*e.g.,* 42]. This approach has the advantage that the SL generally encompasses the majority of the upper-ocean euphotic zone, within which any positive NCP is confined (though see [111]). Thus an integral of J^{bio} over the mixed layer, and a further integral of this quantity over an annual cycle or growing season can be roughly equated to annual NCP (ANCP). Since detailed measurements of the physical transports are not available, often simultaneous observations of biologically inert gases (*e.g.,* nitrogen or argon) approximate what the net effects of physical transport would be in the oxygen budget. The SL-integrated dissolved oxygen mass balance has been utilized extensively during the summer months in the subarctic North Pacific [39, 40, 42, 72, 78, 62] and elsewhere [*e.g.,* 45, 66, 43, 3].

At OSP, the above estimates of NCP from dissolved gas balances give a clear picture of the positive NCP that occurs within the SL during the summer growing season (May-October), when biological oxygen signals are strong, with typical summertime rates of organic carbon production in the euphotic zone of 8-18 mmol C m^{-2} d^{-1}. This is in agreement with measurements of nitrate drawdown [178], particulate flux from thorium-uranium disequilibrium [17], and rates of primary productivity obtained from bottle incubations of 67 mmol C m^{-2} d^{-1} [13] if an f-ratio (new production:total production, equal to the export ratio at steady state) of 0.25 is assumed [167]. However, some important questions surrounding the application of the oxygen mass balance method to an estimate of ANCP are still outstanding. One potential limitation of the SL-integral method is the fact that any net respiration deeper than the SL but shallower than the depth of annual ventilation represents organic carbon that temporarily leaves the surface ocean but is remineralized and converted back to inorganic form before crossing the maximum depth of winter mixing. When the mixed layer re-entrains this zone in the following winter, this inorganic carbon will then be re-exposed

to the atmosphere [116, 80]; hence, it is not exported from the upper ocean on a time period longer than a year and does not represent ANCP. As a result, if an estimate of ANCP is formed as a residual in a mass balance that is vertically integrated over only the SL, it will be an overestimate of the true ANCP by an amout equal to the net shallow respiration [80]. Since few estimates of the oxygen mass balance extend into the thermocline at OSP, it remains an open question how large this correction should be. Respiration within the zone deeper than the SL and shallower than the maximum mixing depth will hereafter be referred to as "shallow respiration," and in this study the lower boundary of this zone is taken to be 120 m, the typical maximum thickenss of the SL at OSP (though see discussion of the appropriateness of this depth boundary in Section 4.4).

In addition, the kinematics of oxygen are poorly resolved deeper than the SL at OSP, and it is not well-understood what combination of physical transports (such as horizontal advection, vertical advection, or vertical diffusion) would need to be measured with sufficient accuracy in order to isolate the shallow respiration signal or any deep euphotic zone production there. Within the SL itself, in previous studies the horizontal advection of oxygen has been either neglected [*e.g.,* 39, 40] or inferred indirectly [42]. Although order-of-magnitude estimates in Giesbrecht et al. [62] and Emerson [39] suggest that horizontal advection of oxygen should be a small term in the SL, further measurements at the scales relevant to local advection are needed to confirm the validity of this assumption.

This study investigates the above questions surrounding the application of the oxygen mass balance method at OSP using observations from Seaglider surveys there from June 2008 to January 2010. Individual Seagliders were deployed in three nearly-continuous missions during this time, in a similar configuration to previously-conducted surveys at the Hawaii Ocean Time Series (HOT) site [111, 43, Chapter 2]. Seagliders sampled in the area around the NOAA Ocean Climate Stations mooring at OSP [42, 67, 41], providing increased coverage and resolution in both depth and horizontal spatial structure of the physical and dissolved oxygen field. They did so for nearly 20 months, spanning most of two summer seasons in which biological oxygen signals are most prominent (hereafter, "growing seasons"). The horizontal

and vertical advection and vertical turbulent transport of dissolved oxygen are estimated using velocity and diffusivity obtained from a least-squares solution designed to minimize the time-integrated error in balances of temperature and salinity during the Seaglider time series (Chapter 3). Net community production or respiration of O_2 is then inferred as a residual between convergences of oxygen transport and observed rates of change.

As will be shown, the Seaglider observations at OSP allow a rigorous estimate of the amount of respiration deeper than the surface layer but shallower than the depth of winter mixing. These results also confirm that the kinematic balance of oxygen in the SL is primarily vertical, as previously assumed, and that horizontal advection is secondary. However, horizontal advection was significant in a vertically-integrated budget of oxygen shallower than the maximum depth of winter mixing, and within the permanent pycnocline. Respiration rates were resolved deeper than 120 m but were indistinguishable from noise deeper than 150 m. Some deep euphotic zone productivity was apparent, though much weaker than deep euphotic zone productivity observed in the subtropics. In what follows, Section 4.2 describes the oxygen data used in this analysis and the methods for calcuation of metabolic rates at monthly intervals throughout the top 200 m, and section 4.3 gives the results of these calculations. Section 4.4 discusses the results in the context of previous measurements of the oxygen mass balance at OSP and considers implications for the concept of ANCP in the subarctic North Pacific, while section 4.5 provides a summary and conclusions.

4.2 Methods

4.2.1 Oxygen Data

Three individual Seaglider deployments collected measurements of temperature T, salinity S, pressure, and $[O_2]$ from 8 June 2008 to 21 January 2010 while repeating a bowtie survey pattern inscribed within a 50×50 km box around the NOAA Ocean Climate Stations OSP mooring (*see* Chapter 2, Fig. 2.2). Seagliders repeated the navigational pattern on average once every 14.5 days, collecting a median 86 vertical profiles along a 1:3 vertical:horizontal

glide slope (Chapter 2). Seaglider SG120 operated from 8 June 2008 to 30 August 2008, SG144 from 30 August 2008 to 4 June 2009, and SG120 from 14 June 2009 to 21 January 2010 prior to departing OSP and proceeding inshore while sampling along Line P. Each vehicle sampled $[O_2]$ using two sensors: a SeaBird Electronics SBE-43 Clark-type electrode sensor, and an Aanderaa Instruments 3830 oxygen optode sensor.

The SBE-43 sensor is unpumped to save power and is naturally aspirated by the flow relative to the vehicle as it ascends or descends. This induces a low bias in these sensors that depends on the speed and possibly pitch of the vehicle [111, 125, 1] and whose form is not well-constrained. As a result, this study uses results from the optode sensor only. With the exception of September 2008, Seagliders collected samples from all instruments every 10 seconds while profiling from the surface to 80 m, every 20 seconds from 80 m to 150 m, every 30 seconds from 150 m to 300 m, and every minute when profiling between 300 m and 1000 m. During September 2008 the sampling interval for the optode was reduced to every 40 seconds between 80 m and 150 m, every 150 seconds between 150 m and 300 m, and the optode was not sampled deeper than 300 m depth during this time.

Optode dissolved oxygen is calculated using a third-degree polynomial in the calibrated optode phase measurement ("DPHASE"), which has four temperature-dependent coefficients; Seaglider measurements of *in situ* temperature were used to evaluate these coefficients. Dissolved oxygen concentrations were corrected for salinity and pressure effects following [164] and [151]. Four research vessels visited OSP during the array time series and performed bottle casts and Winkler titration measurements of dissolved oxygen: the CCGS *John P. Tully* as part of its regularly scheduled occupations of Line P in June 2008, June 2009, and August 2009, and the R/V *Thomas G. Thompson* in August 2008 as part of a University of Washington student cruise. The salinity- and pressure-corrected optode data were converted to saturation fraction $s = [O_2]/[O_2]_{\mathrm{sat}}$, where $[O_2]_{\mathrm{sat}}$ is the oxygen concentration at saturation equilibrium and standard temperature and pressure computed from Garcia and Gordon [60], and compared to estimates of s from Winkler titration measurements in the surface mixed layer from the available shipboard cruises, following D'Asaro and McNeil [33].

For each SG deployment, all instruments were corrected for an initial offset in s from comparison casts available at the initiation of the deployment. After this initial correction was applied, comparison to subsequent shipboard casts later in each deployment revealed an apparent downward drift in the measurements from each instrument, though the inferred rates of drift were not equal among the three. A second correction for drift in the measured s was applied to each instrument to bring it into agreement with the shipboard casts, assuming a linear drift with time. For the second deployment (SG120, August 2008 to June 2009), which ceased sampling 10 days prior to visitation by the Tully, drift was evaluated using a comparison of $[O_2]$ to measurements from SG144, which sampled from 14 June 2009 onward. This comparison was performed on the 6°C isotherm within the seasonal thermocline, where oxygen exhibits a relatively stable decline following the shoaling of the SL in late spring. Appendix D gives further details regarding postcalibration of the optode oxygen measurements.

Post-calibrated oxygen samples for vertical profile were bin-averaged in depth to create a profile on a vertical depth grid with spacing every 2 m from 0 to 150 m depth and every 5 m thereafter to 200 m. This study uses optode data from only the top 200 m, where pressure effects on the optode response are small [33]. The subscript notation i denotes the depth bin index (there are $n_i = 86$ depth bins). Horizontal gradients of $[O_2]$ were computed in each depth bin i using least-squares fits in monthly time intervals, in the same manner as T and S as described in Chapter 2; index j denotes the time interval ($n_j = 20$). The monthly time intervals reflect the minimum time scale at which the glider and moored array provides reliable information about the spatial gradients across the survey pattern. A mean monthly profile was also computed in each interval, which is used to compute vertical derivatives of oxygen; $[O_2]_{ij}$ refers to monthly mean oxygen concentration at depth bin i and in time interval j. In addition, a profile of oxygen was estimated at the center of the glider track pattern (50.13°N, 144.83°W) beginning and end of each month using uniform-weighting local least-squares regression estimation (LOESS), as described in Chapter 3 and in Appendix D.

These profiles are used to approximate the time derivatives in each monthly bin:

$$\left.\frac{\partial[\mathrm{O_2}]}{\partial t}\right|_{ij} = \frac{[\mathrm{O_2}]_{i,j+0.5} - [\mathrm{O_2}]_{i,j-0.5}}{\Delta t_j}, \tag{4.2}$$

where $[\mathrm{O_2}]_{i,j+0.5}$ ($[\mathrm{O_2}]_{i,j-0.5}$) indicates the LOESS vertical profile at the center of the track pattern at the end (beginning) of time interval j, and Δt_j is the time interval duration.

4.2.2 Calculation of NCP

Governing Equations

Before describing the method used in this study, it is informative to review some aspects of the most common method of estimating NCP from the dissolved oxygen mass balance, which is to form a budget equation for the SL-average oxygen concentration. Vertically integrating the balance (4.1) from the surface to the base of the SL, which has thickness h, yields

$$\int_{-h}^{0} J^{\mathrm{bio}} \mathrm{d}z = \int_{-h}^{0} \frac{D[\mathrm{O_2}]}{Dt} \mathrm{d}z + \left[\overline{w'[\mathrm{O_2}]'}_0 - \overline{w'[\mathrm{O_2}]'}_{-h}\right], \tag{4.3}$$

where $\overline{w'[\mathrm{O_2}]'}_0$ is the turbulent flux at the ocean surface, which is set equal to the estimated surface gas exchange. The term $\overline{w'[\mathrm{O_2}]'}_{-h}$ represents the turbulent flux of oxygen at the base of the SL, which is parameterized in a diffusive, down-gradient form (*i.e.,* $\overline{w'[\mathrm{O_2}]'}_{-h} = -\kappa \partial[\mathrm{O_2}]/\partial z|_{-h}$). Consider for simplicity an idealized case in which there are no horizontal or vertical mean currents ($\vec{u} \equiv 0$), and thus $D[\mathrm{O_2}]/Dt = \partial[\mathrm{O_2}]/\partial t$. Since

$$\int_{-h}^{0} \frac{\partial[\mathrm{O_2}]}{\partial t} \mathrm{d}z = \frac{\partial}{\partial t} \int_{-h}^{0} [\mathrm{O_2}] \mathrm{d}z + \frac{\partial(-h)}{\partial t} [\mathrm{O_2}]_{-h}, \tag{4.4}$$

and $\partial/\partial t \int_{-h}^{0} [\mathrm{O_2}]\mathrm{d}z = \partial/\partial t \left(h[\mathrm{O_2}]_\mathrm{a}\right)$, where $[\mathrm{O_2}]_\mathrm{a}$ is the SL-average oxygen concentration, (4.3) becomes

$$\int_{-h}^{0} J^{\mathrm{bio}}\mathrm{d}z = h\frac{\partial}{\partial t}[\mathrm{O_2}]_\mathrm{a} - \frac{\partial h}{\partial t}\left([\mathrm{O_2}]_{-h} - [\mathrm{O_2}]_\mathrm{a}\right) + \left[\overline{w'[\mathrm{O_2}]'}_0 - \overline{w'[\mathrm{O_2}]'}_{-h}\right], \tag{4.5}$$

where the SL-integrated NCP is now written in terms of the vertical-average oxygen concentration within the SL. Equation (4.5) is similar to the form used by, for example, Emerson [39] in a SL budget of dissolved oxygen at OSP. The second term on the right-hand side of (4.5) is the familiar "entrainment" term common to most SL-average budgets[1]. Physically, this term is invoked to model a change in average oxygen concentration due to convective deepening of the SL at a rate $\partial h/\partial t > 0$ and entrainment of water with oxygen concentration $[\mathrm{O_2}]_{-h}$. In practice, the SL is not perfectly well-mixed, its thickness h must be defined using some finite increment of stratification, and consequently vertical motion of h does not always reflect "entrainment." Hence it is more precise to refer to this term as accounting for a change in average oxygen concentration in the SL due to fluid motion relative to $z = -h$.

From an observational standpoint, the principal advantage of writing the budget in the SL-average form is that measurements at a single depth anywhere within this region are usually similar to the average concentration within the SL, $[\mathrm{O_2}]_\mathrm{a}$. As a result, given point measurements such as moored observations near the ocean surface, and observations of or assumptions about the strength of turbulent flux at the SL base and the oxygen concentration of entrained waters, it is possible to estimate biological productivity. A disadvantage of this approach is that both entrainment mixing and diffusive transport at the mixed layer base ($\overline{w'[\mathrm{O_2}]'}_{-h}$) are turbulent processes [162, 86, 85], and as a result, the addition of entrainment to the SL-average budget represents a partition of the effects of vertical turbulent flux between two terms that depends on the rate of change of h [87, 160]. In real situations

[1]Note that typically the entrainment term also contains a contribution from the vertical velocity at the SL base $w(-h)$, *e.g.,* [87], their eq. 5.6. This term arises due to the integral of the continuity equation across the SL, and is not present in the simple example here with $\vec{u} = 0$.

both entrainment and diffusive mixing are active to varying degrees, depending on a number of factors including the time evolution of surface buoyancy and momentum fluxes [38]. If depth-resolved measurements of the terms in (4.1) are available, then the balance could be evaluated at each depth, avoiding the need for an entrainment term that, as the previous example shows, arises when one has observations only of the mean oxygen concentration within a zone whose lower boundary $z = -h(t)$ changes with time. In this study, estimates of vertical and horizontal advection, and vertical turbulent flux, are available in depth-resolved form at monthly intervals from the results of Chapter 3, in addition to estimates of the vertical profile of $[O_2]$ and $\partial[O_2]/\partial t$ as described above. As a result, it is not necessary to evaluate productivity using a SL-average budget, and there is no dedicated entrainment term. Consistent with the diagnosis of the balances of potential temperature and salinity in Chapter 3, this study estimates J^{bio} using the balance (4.1) in pointwise fashion (in each depth bin i and monthly interval j) as described below. Vertical and temporal integrals of NCP are then obtained by summing J^{bio} over depth bins and monthly intervals.

In this study the rate of change of $[O_2]$ due to net community production or respiration J^{bio}_{ij} at depth i and time interval j is estimated by

$$J^{\mathrm{bio}}_{ij} = \left.\frac{\partial[O_2]}{\partial t}\right|_{ij} + u_{ij}\left.\frac{\partial[O_2]}{\partial x}\right|_{ij} + v_{ij}\left.\frac{\partial[O_2]}{\partial y}\right|_{ij} + w_{ij}\left.\frac{\partial[O_2]}{\partial z}\right|_{ij} + \frac{\partial}{\partial z}\left(\overline{w'[O_2]'}_{ij}\right) + \epsilon^{[O_2]}_{ij}, \quad (4.6)$$

where u_{ij}, v_{ij}, w_{ij} are zonal, meridional, and vertical velocity components and $\overline{w'[O_2]'}_{ij}$ is the vertical turbulent transport of oxygen. The first term on the right-hand side is denoted the local rate-of change. The negative of the sum of the second through fifth terms on the right-hand side is the *physical tendency*. Thus the estimate of J^{bio}_{ij} is formed as a difference between the local rate-of-change and the physical tendency. ϵ_{ij} is an error term and will be discussed below. The balance is evaluated in each of the 86 depth bins in the top 200 m, and in each of the 20 calendar months occupied by Seaglider surveys at OSP. The local rate-of-change, horizontal, and vertical gradients of dissolved oxygen are evaluated as described in Section 4.2.1. To evaluate the physical tendency, the velocity components are obtained from

the least-squares solution designed to account for balances of temperature and salinity as described in Chapter 3. As will be shown below, the vertical profile of turbulent transport between the surface and 200 m depth is also obtained from the least-squares solution, but with surface boundary condition given by the estimated surface gas exchange, and deep boundary condition given by the transport resulting from an assumed weak interior diffusivity at 200 m.

The turbulent transport of oxygen in (4.6) is parameterized one of three ways, depending on the vertical location of the depth bin in consideration. Recall from Chapter 3 that in each monthly time interval, the top 200 m of the water column is partitioned vertically into three zones, the SL, transition layer (TL), and interior (INT). The SL is defined to be the region from the surface to the bin just shallower than the bin at which the stratification reaches 10% of the peak value in that monthly time interval. The TL extends from this bin to 50 m deeper. The INT spans the region between the base of the TL and 200 m. Note that though the TL thickness remains constant, the depth bin delineating its upper boundary changes monthly, hence also the depths spanned by the TL, along with the extents of the SL and INT.

In the INT region, turbulent transport of oxygen is given by

$$\overline{w'[\mathrm{O_2}]'}_{ij}(-200\,\mathrm{m} \le z_i < -H_j) = -\kappa_{\mathrm{INT}} \left.\frac{\partial[\mathrm{O_2}]}{\partial z}\right|_{ij}, \tag{4.7}$$

where κ_{INT} is an assumed deep vertical diffusivity of 10^{-5} m^2 s^{-1}, and H_j is the depth of the deepest bin within the TL in time interval j. Within the TL region the turbulent transport is

$$\overline{w'[\mathrm{O_2}]'}_{ij}(-H_j \le z_i \le -h_j) = -\kappa_{ij} \left.\frac{\partial[\mathrm{O_2}]}{\partial z}\right|_{ij}, \tag{4.8}$$

where κ_{ij} is a depth-dependent diffusivity given by the least-squares solution in Chapter 3, and h_j is the depth of the uppermost TL bin in time interval j.

In the SL, the turbulent transport of oxygen is assumed to vary linearly between the

value given by the diffusivity at the top of the TL $\overline{w'[\mathrm{O_2}]'}_{h+0.5,j}$ from (4.8) and the surface value

$$\overline{w'[\mathrm{O_2}]'}_{ij}(-h_j < z_i < 0) = \left(\overline{w'[\mathrm{O_2}]'}_{0,j} - \overline{w'[\mathrm{O_2}]'}_{h+0.5,j}\right)\left[\frac{z+h_j}{h_j}\right] + \overline{w'[\mathrm{O_2}]'}_{h+0.5,j}, \qquad (4.9)$$

where the surface value is set such that the surface flux of $\mathrm{O_2}$ per square meter, $\rho_0\overline{w'[\mathrm{O_2}]'}_{0,j}$ where $\rho_0 = 1024$ kg m^{-3} is a reference density, is equal to the mean surface exchange of $[\mathrm{O_2}]$ in time interval j. This exchange is estimated based on various parameterizations of air-sea gas transfer as described in the following section.

Recall that it is the divergence (convergence) of vertical turbulent transport, $\partial/\partial z(\overline{w'[\mathrm{O_2}]'}) > 0$ (< 0), that removes oxygen from (adds oxygen to) a depth bin. Hence, in the SL, the assumption of a linear flux profile means the rate of removal or addition of oxygen within all depth bins in the SL is vertically constant within each month. This assumption was made in Chapter 3 for the balances of potential temperature and salinity to avoid explicitly modeling the turbulent fluxes in regions where they may be "nonlocally" driven [86], such as the weakly stratified surface layer in autumn and winter, where upward vertical heat flux persists despite near-zero stratification. The turbulent fluxes are in this case not well-modeled by a simple downgradient diffusion as in (4.7) and (4.8). The assumption of linear or nearly-linear flux profiles in the unstratified SL under a variety of conditions is supported by observations, theory, and numerical modeling of the oceanic [86, 140, 38, 65] and atmospheric [112, 181] boundary layers, and by laboratory simulations [*e.g.,* 177]. The assumption of a linear flux may affect the details of J^{bio} estimated at individual depths within the SL but will not affect the integral across this zone, since by (4.3) the estimate of integrated biological productivity within the SL depends only on the turbulent flux at the top and bottom of the SL.

Surface Gas Exchange

Surface gas exchange was calculated using four different parameterizations in order to assess the sensitivity of estimated NCP in the SL to the choice of parameterization. The first two

of these were Liang et al. [93] (hereafter LEA13) and Stanley et al. [143] (hereafter SEA09). The third was a combined Liss and Merlivat [94] diffusive exchange plus Woolf and Thorpe [179] bubble formulation as suggested by Steiner et al. [144] (hereafter LM86+WT91). The fourth, as suggested by Vagle et al. [165], used the LM86+WT91 formulation for wind speeds less than 12 m s^{-1}, and the McNeil and D'Asaro [108] parameterization for greater wind speeds (hereafter MD07). These parameterizations were chosen because all of them at least implicitly include parameterizations of the major physical processes affecting gas exchange: diffusive exchange, exchange due to partially collapsing bubbles, and injection of gas from the atmosphere into the ocean due to fully collapsing bubbles. Additionally, all four of these have been used at OSP. Bushinsky and Emerson (Marine Biological Production from Remote In Situ Oxygen Measurements, manuscript submitted to Global Biogeochemical Cycles) have used LEA13 to successfully simulate surface nitrogen supersaturation at OSP using a one-dimensional upper-ocean model. Emerson and Stump [42] employed SEA09 in an upper-ocean nitrogen and oxygen mass balance in summer. The LM86+WT91 formulation, and MD07 modification at higher wind speeds, have been tested by [144] and [165].

Surface gas exchange was computed using daily-average values of oceanic properties (s, T, and S at 10 m depth) obtained from the Seaglider time series, independent of their position within the survey pattern, and hourly-average values of atmospheric variables (sea-level pressure, wind speed, air temperature, pressure, downwelling solar and longwave radiation, rain rate) obtained from the NOAA OSP mooring (`http://www.pmel.noaa.gov/ocs/data/disdel_v2/disdel_v2.html`), when available. For times when the NOAA mooring was inoperative (11 November 2008 to 14 June 2009), 6-hourly values from the NOAA National Centers for Environmental Prediction/National Center for Atmospheric Research Reanalysis 1 dataset [R1; 79] product were used. These data were provided by the NOAA/OAR/ESRL Physical Sciences Division, Boulder, Colorado, USA (`http://www.esrl.noaa.gov/psd/`). From the available atmospheric data, the COARE v3.0 algorithm was used to estimate the surface stress τ along with the "warm layer" and "cool skin" temperature corrections [48]. These represent the difference between ocean surface temperature and bulk temperature

measured at 10 m depth due to penetrative solar radiation and surface heat loss. These corrections are important because it is the air-water gas concentration difference at the ocean surface that drives the diffusive flux of gas through the ocean surface [68, 66]. Thus, the 10 m temperature adjusted for warm layer and cool skin corrections was used to compute temperature-dependent quantities at the ocean surface (concentration at saturation equilibrium $[O_2]_{sat}$, Schmidt number, and surface density). Salinity and oxygen concentrations at 10 m depth were assumed to be equal to those at the surface. Gas exchange was computed at the time scale of the highest-time resolution platform available (either mooring or R1), then averaged in monthly time intervals.

A bias in sea-level pressure of 1.83 mbar was observed in the R1 dataset relative to the OSP buoy measurements. After removal of this bias, monthly-average gas exchange rates computed independently from R1 and buoy data in the months of overlap between these datasets (July-October 2008, July-January 2009) were in good agreement; mean±standard deviation of differences between monthly-averages values were -1.86±5.33 mmol O_2 m^{-2} d^{-1} for the LEA13 parameterization. This mean difference is 6.2% as large as typical rates of summer outgassing of ∼30 mmol O_2 m^{-2} d^{-1}.

Uncertainty

The term $\epsilon_{ij}^{[O_2]}$ represents errors due to unresolved terms, errors in spatial gradients or time derivatives, or errors in the estimated advective/diffusive transports in the balance of dissolved oxygen (4.6). The average magnitude of this term relative to the observed local rates-of-change can be assessed for the non-biologically active tracers temperature and salinity using the results from Chapter 3. Figure 4.1 shows the vertical profile of mean square error in the estimated temperature and salinity rate-of-change (for S, $\langle(\epsilon_{ij}^{S})^2\rangle_j$, where angle brackets denote a time-average), divided by the variance in the observed local rate-of-change $[\sigma_j^2(\partial S_{ij}/\partial t)$, where $\sigma_j^2(\cdot_{ij})$ indicates the variance of a quantity at depth i across the n_j time intervals]. Note that this differs from the normalized mean-square error presented in Chapter 3, which instead quantified the error in the integral of $\partial S/\partial t$.

Mean square error in ϵ^θ as a fraction of variance in the local rate-of-change had a minimum (maximum) of 0.082 (1.214) and a vertical mean of 0.404 (Fig. 4.1). Comparable numbers for ϵ^S were 0.102, 1.243, and 0.420. Some vertical structure was apparent in the salinity balance errors, with a reduction in error in the halocline deeper than 100 m depth. As will be shown below, the oxygen budget is similar in character to the temperature budget shallower than 100 m depth, and similar to the salinity budget deeper than 100 m. As such, it is assumed that the oxygen balance given by the least-squares solution in Chapter 3 will have normalized error similar in magnitude to the salinity (temperature) balance deeper (shallower) than 100 m depth. The mean value of $\langle(\epsilon^S_{ij})^2\rangle_j/\sigma_j^2(\partial S_{ij}/\partial t)$ deeper than 100 m and shallower than 200 m depth was 0.213 (black dashed line in Fig. 4.1); mean $\langle(\epsilon^\theta_{ij})^2\rangle_j/\sigma_j^2(\partial \theta_{ij}/\partial t)$ shallower than 100 m depth was 0.355. Thus the uncertainty in the oxygen budget in each depth bin and time interval is given by

$$\epsilon^{[\mathrm{O_2}]}_{ij} = \sqrt{\gamma_i \sigma_j^2(\partial[\mathrm{O_2}]_{ij}/\partial t)}, \tag{4.10}$$

where γ_i is 0.355 if -100 m $\leq z_i$ and 0.213 if -200 m $\leq z_i < -100$ m. For vertical or temporal integrals of J^{bio}, it is assumed that the errors $\epsilon^{[\mathrm{O_2}]}_{ij}$ are independent within each depth bin and time interval, such that uncertainty on the sum increases as the root of sum of squares of the individual uncertainties (*e.g.,* [129]). For bins within the SL, there is additional uncertainty associated with the surface gas exchange. Errors in surface gas exchange associated with optode accuracy are assessed using a Monte Carlo Scheme described in Appendix E. Additional sources of uncertainty, such as possible biases in buoy wind speed at high winds, and the form of drift in the oxygen optode, are not considered. As a result, these uncertainties on estimates of ANCP derived from surface gas exchange should be considered lower bounds.

4.3 Results

4.3.1 Oxygen Vertical and Temporal Structure

Dissolved oxygen concentrations in the surface layer decrease throughout the summer months at OSP as the surface ocean warms and solubility decreases; during Seaglider surveys, surface [O_2] was at a minimum in late September/early October 2008 and August/September 2009. Surface concentrations increase as the mixed layer cools and deepens, reaching a maximum winter concentration in April 2009 (Fig. 4.3). Oxygen concentrations were significantly above those expected at saturation equilibrium in the surface layer throughout the summer during Seaglider surveys. During the winter, weak undersaturation or near-neutral saturation states were observed (Fig. 4.3).

Figure 4.4 shows daily-average [O_2] as a function of depth and time in the upper 200 m. In the the seasonal thermocline zone (deeper than the surface layer and shallower than the maximum depth of winter mixing; depths ∼25-120 m in June and disappearing ∼January), weakly supersaturated waters are left behind following mixed layer shoaling in both summers. The oxygen concentration steadily declines in this zone thereafter, suggestive of respiration. This is evident in Figure 4.4a by decreasing [O_2] from 50-100 m depth in the months May-October. This decline can also be seen in the shoaling of the 0% supersaturation horizon within the seasonal thermocline as the summer season progresses (Fig. 4.4).

The amplitude in the annual cycle in the seasonal thermocline is reduced in comparison to the surface layer, and the minimum in oxygen concentrations occurs later in the year (November-December) immediately prior to re-entrainment of these waters by the surface mixed layer. Small regions of supersaturation are also apparent in the deep euphotic zone (*i.e.,* in the 10-20 m deeper than the SL) in summers 2008 and 2009, though it is unclear whether this is due to biological production or from heat addition due to vertical mixing (Chapter 3). Oxygen concentration and saturation state decline with depth deeper than the maximum depth of winter mixing (∼120 m) in the permanent pycnocline (Fig. 4.4).

Temporal periodicity apparent in [O_2] and density records in summer 2008 in Figure 4.4

arises from the glider's repeated encounters of spatial variations across its repeat track. Strong gradients across the track pattern during this time period were due to survey of the western portion of a weak mesoscale eddy impinging on OSP (*see* Chapters 2 and 3). Horizontal gradients in dissolved oxygen concentration $\nabla[O_2]$, estimated using the least-squares procedure described in Chapter 2, were strongest in the permanent pycnocline from June 2008 to March 2009 (Fig. 4.2). The gradients were primarily eastward in the lower halocline ($\sim$175 m depth) during this period, reflecting downward displacement of isopycnals to the east in the presence of an upward-increasing oxygen gradient. Horizontal gradients were weakest in the SL, and in the 40-80 m depth range in both summers (Fig. 4.2).

4.3.2 Kinematics

The least-squares solution of Chapter 3, in combination with the estimated surface gas exchange, gives profiles of turbulent vertical flux of oxygen $\rho_0\overline{w'[O_2]'}$ that illustrate the primary mechanism behind the large seasonal variability in surface $[O_2]$ identified above (Fig. 4.5). Recall that, within the SL, turbulent flux is linearly interpolated between the resolved value at the base of the SL/top of the TL and the estimated surface gas exchange. The difference between these two values divided by the thickness of the SL – and thus, the slope of the turbulent flux profile – determines the net addition or removal of oxygen from the SL due to turbulence. These profiles were constructed using the LEA13 formulation for surface gas exchange, though other formulations alter the fluxes only in the SL and do not differ qualitatively in the annual cycle.

In summer, divergent upward turbulent fluxes reduce oxygen in both the SL (June-September 2008, March-August 2009) and the 25 m immediately deeper than the SL (June-October 2008, July-October 2009). The upwardly divergent fluxes in the upper TL are a consequence of the stratification of $[O_2]$ in the summer months at OSP, where the warming mixed layer overlies cool, relatively oxygenated water. Due to this negative vertical gradient the turbulent flux of oxygen at the top of the thermocline is upward (bringing oxygen into the mixed layer; Fig. 4.4). In fall and winter, a convergent downward flux of oxygen is

present, which adds oxygen to the mixed layer, an effect that is most apparent in October 2008-February 2009 (Fig. 4.5). Everywhere deeper than the upper 25 m of the TL the turbulent fluxes are small in comparison to those in the SL, with the exception of the halocline (oxycline) region near $z = -125$ m, where there are strong vertical gradients of oxygen which can result in moderate vertical fluxes of oxygen despite the assumed weak diffusivity there ($z = -125$ m in Fig. 4.5).

The turbulent flux shown in Figure 4.5 plays a dominant role in the budget of $[O_2]$ in the SL and TL. Figure 4.6 shows vertical profiles of all resolved terms in the oxygen budget, which include the convergence of the turbulent flux shown in Figure 4.5, horizontal/vertical advection, and the estimated local rate-of-change. These plots exclude biological productivity and residuals due to errors or unresolved terms, thus the sum of the advection and diffusion is not expected to equal the local rate-of-change. The composition of terms in the oxygen budget, and the overall size of individual terms, is of markedly different character depending on the vertical zone. Within the SL, the divergence of the turbulent transport (gas exchange minus diffusion at SL base) and local rate-of-change dominate the resolved portion of the budget (red and blue curves resemble one another in Fig 4.6). Horizontal and vertical advection become more important immediately deeper than the SL, as with temperature (cyan and green curves, Fig. 4.6). All budget terms are small in magnitude in the lower seasonal thermocline (40 m to 80 m depth in 2008, 40 m to 100 m depth in 2009). Horizontal and vertical advection terms are large and nearly offset one another in the halocline, especially in 2008, a consequence of strong spatial gradients of oxygen observed in this zone (Fig. 4.2). Overall, the nature of the dissolved oxygen balance has characteristics similar to both the temperature and salinity budgets. Unlike both of these variables, budget terms for the $[O_2]$ balance are large in both the permanent pycnocline (as with salinity) and the SL and TL (as with temperature). The balance between local change and convergence of turbulent flux in the SL, weak horizontal advection there, and increasing importance of advection with depth in the TL is similar to θ. In the halocline, the offsetting horizontal and vertical advection (*e.g.*, July 2008, February 2009) or advection offsetting local change (June 2008, January

2010) are similar to (and opposite in sign of) the corresponding terms in the S balance (Fig. 3.20).

One way to judge the significance of terms to the balance of dissolved oxygen (4.6) is to compute their time-average magnitude irrespective of sign, as was done for potential temperature and salinity in Chapter 3. Figure 4.7 displays the mean absolute value of budget terms – horizontal advection A_h, vertical advection A_v, local rate-of-change $\partial[\mathrm{O_2}]/\partial t$, the divergence of turbulent transport $\partial/\partial z(\overline{w'[\mathrm{O_2}]'})$, and unresolved terms due to productivity J^{bio} and errors – averaged across each of four vertical zones and then time-averaged throughout the time series duration. As an example, for horizontal advection in the SL, Figure 4.7 shows

$$\langle A_h \rangle = \frac{1}{n_j} \sum_{j=1}^{n_j} \left| \frac{1}{h_j} \int_{-h_j}^{0} u_{ij} \left. \frac{\partial[\mathrm{O_2}]}{\partial x} \right|_{ij} + v_{ij} \left. \frac{\partial[\mathrm{O_2}]}{\partial y} \right|_{ij} \mathrm{d}z \right|, \tag{4.11}$$

where h_j is the thickness of the surface layer in time interval j. The zones include the SL and TL, as defined in Section 4.2.2, and two portions of the INT region, which are the remnant thermocline ("RemTherm," the region deeper than the TL and shallower than 120 m) and halocline ("HaloCln," shallower than 200 m and deeper than 120 m or the TL base, whichever is deeper). In the SL, the largest terms are convergence of turbulent flux, local storage, and residual productivity plus errors. Advection increases in importance with depth (note the change in scale for the lower 3 plots relative to the top one) and is at least as strong as biological terms in the TL (Fig. 4.7b). Horizontal and vertical advection become the largest terms in the halocline. Local storage terms also increase in size in this zone, influenced by water mass changes associated with a passing mesoscale feature (*see* Chapters 2 and 3).

4.3.3 Rates of Production or Respiration

TL and INT Regions

The unresolved terms in the balance of dissolved oxygen can be equated to the rate of change of $[\mathrm{O_2}]_{ij}$ due to biological processes J_{ij}^{bio} and errors. In this section, J_{ij}^{bio} is examined in the

TL and INT regions, where the estimated convergence of turbulent transport is independent of gas exchange. A primary question is whether the observed drawdown in $[O_2]$ deeper than the TL but shallower than the halocline in both summers is due to biological or physical processes. Figure 4.8 shows the observed record of $[O_2]$ within this region at 74 m depth. This figure also shows the integrated physical tendency of oxygen during periods when this depth exceeds the SL depth. These periods are when a steady oxygen decline is observed throughout this zone in the daily-averaged concentrations of Figure 4.4. If the integrated physical tendency overlies the observed concentrations, within the uncertainty bars, then no net biological activity is inferred. If the observed concentrations lie below the integrated physical tendency, respiration is inferred.

The results of Figure 4.8 strongly suggest that the estimated physical transports cannot account for the observed decline in oxygen. The difference between the integrated physical tendency and observed decline falls well outside uncertainty bounds when integrated over the periods for which the SL is shallower than 74 m. The integrated physical tendency is indistinguishible from zero during both 2008 and 2009. In contrast, $[O_2]$ decreases by 13.91 μmol kg^{-1} over summer 2008 and 15.70 μmol kg^{-1} in summer 2009. These differences give an estimated oxygen utilization rate (OUR) at this depth in the mid-seasonal thermocline of -0.072$\pm$0.029 μmol kg^{-1} d^{-1} in 2008 and -0.061$\pm$0.029 μmol kg^{-1} d^{-1} in 2009.

In addition to evaluating concentration at a single depth, the oxygen concentration per unit volume $\rho_0[O_2]$ can be integrated vertically as well as temporally across seasons, and compared with integrated physical tendency. Figure 4.9 shows the results of this calculation for the 50-100 m depth range. This corresponds to the depth range in which the bulk of the shallow oxygen decline was observed in Figure 4.4. Figure 4.9 compares the vertical integral of oxygen concentration per unit volume in this region, $\int_{-100\,\mathrm{m}}^{-50\,\mathrm{m}} \rho_0[O_2](z,t)\mathrm{d}z$, to the vertically- and temporally-integrated physical tendency during summer 2008 and 2009. The time bounds span May-October, which is the periods for which the SL is shallower than 50 m depth. Similar to the results at $z = -74$ m, the observed drawdown in oxygen content in this zone exceeds the integrated physical tendency beyond the uncertainties. A net respiration

of 0.79±0.07 (0.83±0.09) mol O_2 m^{-2} is inferred during summer 2008 (2009). Integrating J_{ij}^{bio} across all time intervals and all depths greater than the SL but shallower than 120 m, taken to be the average maximum depth of winter mixing at OSP, yields 1.89±0.24 mol O_2 m^{-2} total shallow respiration. The observed net respiration corresponds to a mean rate of 1.17±0.15 mol O_2 m^{-2} yr^{-1}. This rate is not overly sensitive to choices of the lower boundary of integration (1.03 mol O_2 respired m^{-2} yr^{-1} for 110 m, 1.29 mol O_2 respired m^{-2} yr^{-1} for 130 m).

Figure 4.10 shows the time-mean profile of J^{bio} estimated in all bins deeper than the SL (where estimates to not depend on the surface gas exchange). Prior to constructing this profile, in each time interval estimates of J^{bio} in the top 25 m of the TL were replaced with their average over this zone, to reduce the effect of small errors in the vertical profile of diffusivity which can create large spikes of productivity or respiration over short vertical intervals. Since the SL depth changes seasonally, the time-averages in this profile are not over a uniform time span, and are seasonally biased shallower than ∼110 m (shallower depths are only included in this profile during the summer months, when the SL is comparatively thin; Fig. 4.4). The profile indicates a mean compensation depth, where net respiration and production are roughly equal, of approximately 35 m during the months in which the SL is shallower than this depth. The presence of the largest rates of net respiration between 60 m and 80 m depth, along with an ultimately weakening respiration rate with depth, is broadly consistent with other observational evidence of the depth-dependence of open-ocean respiration [*e.g.,* 103]. This profile indicates that the rates of OUR estimated at 74 m depth (Fig. 4.8) are characteristic of those throughout the seasonal thermocline (40-120 m depth). Some deep euphotic zone productivity is indicated shallower than 35 m depth, consistent with [O_2] supersaturation observed immediately deeper than the mixed layer (Fig. 4.4).

In Figure 4.10, some net respiration is estimated deeper than 120 m, the depth of annual winter mixing. If respiration can be measured deeper than the maximum extent of winter mixing, this represents a direct estimate of EP, which is the respiration of organic carbon exported due to ANCP in the surface ocean. Figure 4.11 shows the observed oxygen content

and integrated physical tendency for the 120-200 m depth range. The integrated tendency can be decomposed into terms including horizontal advection A_h, vertical advection A_v, diffusive flux at 120 m κ_{120}, and diffusive flux at 200 m κ_{200} as follows:

$$\underbrace{\rho_0 \int_{-200\,\mathrm{m}}^{-120\,\mathrm{m}} [\mathrm{O_2}](z,t)\mathrm{d}z}_{\int_{\mathrm{halo}}[\mathrm{O_2}](t)} = \underbrace{\rho_0 \int_{t_0}^{t} \int_{-200\,\mathrm{m}}^{-120\,\mathrm{m}} \left[-u(z,\tau)\frac{\partial[\mathrm{O_2}]}{\partial x}(z,\tau) - v(z,\tau)\frac{\partial[\mathrm{O_2}]}{\partial y}(z,\tau)\right] \mathrm{d}z\mathrm{d}\tau}_{A_h}$$
$$+ \underbrace{\rho_0 \int_{t_0}^{t} \int_{-200\,\mathrm{m}}^{-120\,\mathrm{m}} \left[-w\frac{\partial[\mathrm{O_2}]}{\partial z}(z,\tau)\right] \mathrm{d}z\mathrm{d}\tau}_{A_v} + \underbrace{\rho_0 \int_{t_0}^{t} \left[\kappa(-120\,\mathrm{m},\tau)\frac{\partial[\mathrm{O_2}]}{\partial z}(-120\,\mathrm{m},\tau)\right] \mathrm{d}\tau}_{\kappa_{120}}$$
$$+ \underbrace{\rho_0 \int_{t_0}^{t} \left[-\kappa(-200\,\mathrm{m},\tau)\frac{\partial[\mathrm{O_2}]}{\partial z}(-200\,\mathrm{m},\tau)\right] \mathrm{d}\tau}_{\kappa_{120}} + \underbrace{\rho_0 \int_{t_0}^{t} \int_{-200\,\mathrm{m}}^{-120\,\mathrm{m}} J^{\mathrm{bio}}(z,\tau)\mathrm{d}z\mathrm{d}\tau}_{\int J}$$
$$+ \underbrace{\rho_0 \int_{-200\,\mathrm{m}}^{-120\,\mathrm{m}} [\mathrm{O_2}](z,t_0)\mathrm{d}z}_{\int_{120}[\mathrm{O_2}](t_0)}. \quad (4.12)$$

As in the budgets of heat and salinity in the halocline, horizontal and vertical advection play dominant roles; for oxygen, horizontal advection imports oxygen while vertical advection removes it (Fig. 4.11). The net addition of oxygen by physical terms exceeds the observed mean concentration after autumn 2008, hence integrated respiration is inferred. This mean respiration rate estimated during the array time series in this zone is 4.4 μmol $\mathrm{O_2}$ $\mathrm{kg^{-1}}$ $\mathrm{yr^{-1}}$. However, it is clear from Figure 4.11 that this respiration rate is a small difference between large physical terms. The estimated respiration across the time series is comparable to the root-mean square (RMS) uncertainty level associated with the errors (4.10), and also to the error that would be expected by the closure of the heat budget ($\pm$3.3 μmol $\mathrm{O_2}$ $\mathrm{kg^{-1}}$ $\mathrm{yr^{-1}}$) or salinity budget ($\pm$2.6 μmol $\mathrm{O_2}$ $\mathrm{kg^{-1}}$ $\mathrm{yr^{-1}}$) based on mean-square errors as described in Chapter 3.

SL Region and Top 120 m

Prominent supersaturation was evident in the 10 m oxygen record during the months June-September 2008 and March-August 2009 (Fig. 4.12b). Gas exchange estimated from each of the four parameterizations was unifomly upward during June-September 2008, and uniformly downward in October 2008-February 2009 (Fig. 4.12b). There was less consistency between the four parameterizations regarding the rate of outgassing of O_2 in summer 2009 than in 2008. During the winter months, oxygen concentrations were weakly undersaturated or nearly saturated, yet strong flux of gas into the ocean was still estimated (Fig. 4.12). This is due to the effect of bubble injection during the stormy winter months, which raises the level of oxygen supersaturation at which the ocean is in gas exchange equilibrium with the atmosphere, and due to high wind speeds increasing the total gas exchange coefficient (Fig. 4.12a, [93]). The four parameterizations show systematic offsets in the rate of gas exchange throughout the time series, but in particular during the winter months. It is likely that these differences are due to variations in the parameterized bubble effect between the four algorithms.

Strong outgassing of 56.78 mmol O_2 m^{-2} d^{-1} was estimated in August 2008 under LEA13, which is intermediate in its estimation of outgassing rates in the summer season between the SEA09 (low outgassing) and LM86+WT91 (high outgassing) parameterizations, and in agreement with MD07 (Fig. 4.12c). The mean rate of upward surface gas flux under LEA13 in the months May-September excluding August 2008 was 20.11 mmol O_2 m^{-2} d^{-1}. Maximum downward flux of oxygen in winter was -44.22 mmol O_2 m^{-2} d^{-1} during October 2008 and -73.18 mmol O_2 m^{-2} d^{-1} in November 2009. Oxygen sensor drift on Seaglider 144 could not be evaluated after August 2008, so the latter rate is suspect (Appendix D).

Uncertainties in monthly-averaged gas exchange *within* parameterizations were largest during highly supersaturated August 2008 (when exchange is driven mainly by a few high-wind events, Fig. 4.12a) and in the winter months when wind speeds were high and the surface dissolved gas concentration was nearly at saturation, such that small uncertainties in

oxygen concentration result in large uncertainties in the gas exchange. Uncertainties *between* parameterizations, likely due to parameterization of the bubble effect, were also largest in the winter. Due to 1) the larger wintertime uncertainty within parameterizations, 2) the large discrepancies between gas exchange parameterizations when applied to wintertime, bubble-influenced gas fluxes, and 3) the long duration of deployment without comparison casts between September 2008-June 2009 and after August 2009, it was not considered feasible to determine rates of NCP in the SL in this study between October 2008-February 2009 and September 2009-onward.

Integrated vertically across the SL and throughout the growing seasons, the summer NCP is 1.8±0.4 mol O_2 m^{-2} (1.3±0.3 mol C m^{-2}, assuming ΔO_2:ΔC of 1.45, [70]) in the 2008 growing season and 1.5±0.8 mol O_2 m^{-2} (1.0±0.6 mol C m^{-2}) in 2009 (Fig. 4.13) using the intermediate exchange parameterization of LEA13. The largest monthly production of O_2 occured in August 2008, which coincides with a volcanic ash deposition event and fertilization of iron, which is a limiting micronutrient at OSP [67]. Under the LEA13 parameterization, this rate is estimated to be 45.1±7.1 mmol O_2 m^{-2} d^{-1} (31.1±4.9 mmol C m^{-2} d^{-1}). The mean rate of NCP in the SL is 16.0±3.4 mmol O_2 m^{-2} d^{-1} during summer 2008 and 8.3±4.5 mmol O_2 m^{-2} d^{-1} in summer 2009 (Fig. 4.13).

As discussed above, 120 m forms a natural depth of integration for the upper-ocean dissolved oxygen budget, because of its correspondence to the annual maximum extent of surface mixing. Although an incomplete knowledge of winter gas exchange prevents the complete closure of the top 120 m balance (as argued above), examination of the balance of terms in this zone is informative for whether horizontal and vertical advection account for signals comparable to the surface gas exchange in the top 120 m budget. Figure 4.14 shows the cumulative, vertically-integrated top 120 m budget, including the contributions of each resolved term to the integrated physical tendency, as was shown for the permanent pycnocline in Figure 4.11. Terms are labeled as in (4.12), though the net flux of O_2 through the ocean surface F_{surf} replaces diffusion at 120 m κ_{120} as the upper boundary condition for this zone, while κ_{120} is instead the lower boundary condition. In the top 120 m budget,

horizontal advection acts to import oxygen, though most of this occurs during the first three months of the array time series (Fig. 4.14). Vertical advection acts to remove oxygen, as does turbulent transport at 120 m. The largest resolved term is the surface gas exchange (Fig. 4.14). This net surface flux is shown for illustration of the relative strength of terms in the top 120 m budget only, since, as discussed in the previous section, the integrated gas exchange in the winter months is subject to a number of large uncertainties.

In this study, 1.4 mol O_2 m^{-2} were estimated to be diffused downward across 120 m depth (Fig. 4.14). Half of this downward diffusion was estimated to occur during months when the SL is deep and boundary layer turbulence penetrates to the halocline: 0.6 mol O_2 m^{-2} in winter 2009 (January-April), and 0.1 mol O_2 m^{-1} in December 2009-January 2010, giving a mean rate of downward diffusion during these months of 4.0 mmol O_2 m^{-2} d^{-1}. During the remaining months, the assumed $\kappa_{INT} = 10^{-5}$ m^2 s^{-1} gave a mean rate of downward O_2 diffusion of 1.8 mmol O_2 m^{-2} d^{-1}. If it is assumed that the elevated rate of diffusion occurs during ∼4 months of the year when the SL is deep, this gives an annual average rate of downward diffusion of 0.9 mol O_2 m^{-2} yr^{-1}.

4.4 Discussion

In order to estimate ANCP from the upper-ocean mass balance of dissolved oxygen at OSP, community metabolic rates must be resolved as a residual between local rates-of-change and physical tendency in essentially three distinct depth zones and time periods, or "boxes:" 1) the SL during the growing season, 2) the region in between the SL and 120 m, and 3) the SL outside the growing season. The winter season box 3 roughly spans the combined depth range of boxes 1 and 2, since the SL spans the depth from the surface to the permanent pycnocline for much of this time. The prevailing paradigm of the annual cycle of ocean metabolism at OSP from dissolved gas balances is that growing season production yields NCP of ∼3 mol O_2 m^{-2} (∼2 mol organic C m^{-2}) in box 1, and that respiration (negative NCP) in box 2 offsets ∼1 mol O_2 m^{-2} of this productivity. It is also thought that weak winter production (positive NCP in box 3) is also of the order of 1 mol O_2 m^2, thus cancelling the deep summer

respiration, and making an estimate of the summer production in box 1 essentially equal to the top 120 m ANCP [42].

In this study, NCP could be estimated with moderate errors in the surface layer in the growing season (box 1), and with small errors deeper than the surface layer and shallower than the depth of maximum winter mixing (box 2). Estimates of shallow respiration in this latter zone provide confirmation of the magnitude of OUR deeper than the mixed layer and bolster this portion of the existing paradigm of seasonal NCP at OSP. Given net annual C production estimated from mass balances or other methods of 1.6-2.6 mol C m^{-2} over a 150 d growing season [42], the respiration rates observed here imply that $1.17/1.45 = 0.81$ mol C m^{-2} of this summer production is respired deeper than the SL and shallower than the depth of winter mixing, and is thus re-equilibrated with the atmosphere rather than isolated from the surface ocean on an annual basis [80, 78]. This represents 30-50% of summer production under previously established rates. The rate of shallow respiration estimated here is also in good agreement with apparent oxygen utilization (AOU) deeper than the mixed layer in summer 2008 from unpublished data as quoted by Emerson and Stump [42].

It has been pointed out by Oschlies and Kähler [116] that, rather than the depth of maximum winter mixing, a still more accurate lower boundary of integration for boxes 2 and 3 would be the depth boundary beneath which water parcels will not be entrained in the SL the following winter, termed in this discussion the "depth of subduction." This depth may differ from the depth of maximum winter mixing because of net upwelling or downwelling along the path of water parcels following remineralization, or lateral flow to a region where the maximum SL thickness differs from that at OSP, or both [145, 176, 127]. This is important because organic carbon that is remineralized shallower than the depth of maximum winter mixing at OSP, but is then subducted into the permanent pycnocline while in inorganic form due to the above processes, still represents net export from the upper ocean and isolation from the atmosphere on an annual timescale [116]. Inversely, organic carbon remineralized deeper than the maximum mixing depth but then upwelled or transported horizontally while in inorganic form to a region where it can be re-exposed to the atmosphere

due to winter mixing would represent carbon that is not exported annually. An estimate of net J^{bio} integrated from the surface to the depth of subduction would more accurately account for carbon export from the surface ocean due to biological processes, regardless of whether the carbon is in inorganic or organic form when it crosses the appropriate depth horizon.

Measured at a fixed point (OSP), the minimum depth at which a unit of organic carbon must be remineralized to be exported from the upper ocean on an annual or longer time scale depends on the time of year at which the remineralization occurs and the horizontal and vertical flow along the trajectory of the water parcel following remineralization. An estimate of this minimum depth depends on a number of assumptions and is beyond the scope of the present study. However, it should be noted that OSP has previously been identified as a region of *obduction*, or net flow from the pycnocline into the upper ocean, due principally to wind stress curl-driven upwelling in the southeastern Gulf of Alaska [127]. This indicates that particles must be exported to a greater depth than the maximum SL depth in order to be isolated from the surface ocean over an annual cycle at OSP, and suggests that the estimates of net shallow respiration obtained in this study are lower bounds. Owing to their importance in setting the lower boundary of integration for upper-ocean ANCP in the dissolved oxygen mass balance, the processes of subduction or obduction in the annual cycle at OSP warrant further study.

The results of this study also suggest that estimates of net NCP in box 1 (SL in summer) are sensitive to the strength of the effect of bubbles in the parameterization of surface gas exchange; net NCP calculated using LEA13 in summers 2008 and 2009 is roughly half of previous estimates. Surface gas exchange estimates were too uncertain to formulate an estimate of NCP in box 3, and this remains a priority for future studies. However, the results of this study do offer an estimate of the bottom boundary condition in box 3 and box 2 (*i.e.*, the amount of oxygen diffused from the surface ocean to the pycnocline across the 120 m depth boundary), indicating that 0.9 mol O_2 m^{-2} yr^{-1} is diffused downward across 120 m depth, with half of this diffusion occurring during the months December-March when the SL

is thick and boundary layer turbulence penetrates to the upper pycnocline. The remaining half of this diffusion is driven by an assumed weak interior turbulent diffusivity ($\kappa_{\mathrm{INT}} = 10^{-5}$ $\mathrm{m^2\ s^{-1}}$).

Using the rates of NCP in boxes 1 and 2 in this study, it is possible to construct hypothetical estimates of top 120 m ANCP under two possible assumptions of winter production or respiration in box 3. These cases are chosen purely for illustrative purposes, in order to demonstrate possible ANCP ranges given plausible values for the unconstrained NCP in box 3. Under one case, winter NCP is assumed negligible, while in the second case, it is assumed to be positive and just sufficient to balance the summer shallow respiration, as assumed by [42]. In the first case, using the LEA13 gas transfer parameterization for summer SL productivity, the rates observed in this study would give an ANCP estimate in the top 120 m of 0.36±0.33 mol C $\mathrm{m^{-2}\ yr^{-1}}$ (using a mean rate of summer SL productivity of 7.8 mmol C $\mathrm{m^{-2}\ d^{-1}}$ over an assumed 150 d growing season, and respiration in the seasonal thermocline of 0.81 mol C $\mathrm{m^{-2}\ yr^{-1}}$). In the second case, if it is assumed that winter surface layer production is strong enough to balance summertime (box 2) shallow respiration, then the top 120 m ANCP estimate would be 1.16±0.32 mol C $\mathrm{m^{-2}\ yr^{-1}}$. The relatively weak time series-average ANCP estimated in these two hypothetical cases of ∼1 mol C $\mathrm{m^{-2}\ yr^{-1}}$ or less lies below the ANCP estimates from surface tracer balances (1.8-2.5 mol C $\mathrm{m^{-2}\ yr^{-1}}$) or those inferred from incubation rates or annual particle flux measurements (up to 4.5 mol C $\mathrm{m^{-2}\ yr^{-1}}$, [159]), though the hypothetical rate discussed here is sensitive to the choice of gas exchange parameterization; use of the LM86+WT91 would give higher rates of summer outgassing and greater inferred box 1 production, and SEA09 would give lower rates. MD07 would be comparable to LEA13 (Fig. 4.12). However, the hypothetical rates of organic carbon export under these assumptions, and using the LEA13 parameterization, is consistent with OUR estimated from AOU observed in the depth range 125-600 m, divided by chlorofluorocarbon and sulfur hexafluoride ages as described in Sonnerup et al. [141]. Their results show a decreasing trend of EP with latitude, with the OUR at 50°N in their study giving EP of ∼0.5 mol C $\mathrm{m^{-2}\ yr^{-1}}$ [141, *cf.* their Fig. 11], intermediate between the

hypothetical estimate that assumes negligible winter SL productivity and the estimate that assumes winter productivity fully compensates the shallow respiration in box 2.

Although significant particle export from the surface ocean continues into the winter season at OSP [159], it remains unclear if this corresponds to net autotrophy and positive NCP in the SL during this time. Contemporary independent studies at OSP of mixed layer dissolved inorganic carbon and alkalinity [51] and float-based oxygen mass balances using atmospheric standard for high gas exchange accuracy (Bushinsky and Emerson, submitted manuscript) find evidence for net heterotrophic conditions in the surface layer in autumn and winter and strong seasonality in SL NCP at Papa. Fassbender et al. [51] suggest that net respiration during this period could be fueled by a buildup of labile DOC or POC in the surface mixed layer that occurs during the summer growing season [121, 159]. The shallow respiration results of this study, along with confirmation of the presence of net heterotrophy in the SL for certain periods at OSP, could result in a downward revision of the accepted value of ANCP in this region. Further investigation of surface gas exchange during winter months is necessary to resolve this question if the dissolved oxygen balance is to be used.

The resolved terms in the monthly balances (Fig. 4.6) and the mean size of these terms across the time series (Fig. 4.7) indicate that horizontal advection of oxygen is weak in the SL at OSP. If an estimate of integrated productivity in the SL were formed without consideration of horizontal advection, the results would be 9.3% low in the first growing season, and 14.7% high in the second, a level of uncertainty that is less than the $\pm$21% (53%) associated with surface gas exchange (within a given parameterization) and errors in the least-squares solution in the 2008 (2009) growing seasons. This finding confirms the assumptions or inferences based on dissolved gas balances of previous investigators that horizontal advection is a weak contributor to the oxygen budget in the surface ocean at OSP [39, 42, 62]. However, when integrating across the top 120 m, the results of this study suggest that horizontal advection does become a leading term that must be accounted for if NCP is to be inferred as a residual (Fig. 4.14). Horizontal advection acted to import 2.9 mol O_2 m^{-2} during the Seaglider time series at OSP, though 63% of this occurred during the

first three months, when the edge of a mesoscale eddy was incident on the Seaglider survey pattern (Chapter 2). Computing a top 120 m budget in an Argo float-following frame of reference may reduce the effects of horizontal advection, since the weakly vertically-sheared horizontal velocities observed during the array time series imply that motion at 1000 m (the typical Argo float parking depth) will be qualitatively similar to that near the surface. For future Argo-type floats deployed specifically to examine surface oxygen cycles, the choice of a shallower parking depth could further ameliorate this problem.

The vertical profile of OUR deeper than the compensation depth in Figure 4.10 exhibits some similarities to OUR curves from individual optode-equipped Argo floats in the subtropical South Pacific Ocean [103, *cf.* their Fig. 11]. Both profiles show a subsurface minimum (or respiration rate maximum), and are of similar amplitude ($\sim$-0.1 μmol O_2 kg^{-1} d^{-1} peak respiration), though the peak respiration in the [103] curves appears to lie slightly deeper than the 60-100 m depth observed here. Feely et al. [52] report rates of organic carbon remineralization peaking at 6-7 μmol C kg^{-1} yr^{-1} (0.024-0.028 μmol O_2 kg^{-1} d^{-1}) near or shallower than 200 m depth in Pacific Subarctic Upper Water, which corresponds to a broad region of the North Pacific ocean north of $\sim$40°N. These rates correspond to those observed between 120-140 m depth in this study (Fig. 4.10). Though the shallower respiration maximum observed in this study is not present in the Feely et al. [52] results, this is likely due to the inability of CFC aging in their study to estimate the age of subsurface waters with $<$5 yr since ventilation, such as in the seasonal thermocline. As a result, their estimates of OUR shallower than the winter mixing depth in their study are likely not comparable to those obtained here.

Estimates of respiration of organic carbon deeper than the upper 120 m are valuable because, at sufficiently long time scales, vertically-integrated remineralization in this zone is coupled to net community production in the upper ocean. Thus, estimates of integrated respiration deeper than 120 m provide an independent, direct calculation of export production (EP$\sim$ANCP) that does not depend upon estimates of surface gas exchange. While circumventing the obstacle associated with net gas exchange, estimates of deep respiration face a

different challenge in that the biological signal deeper than the ventilated surface ocean is spread over a much larger vertical range, and hence is of a considerably weaker magnitude at any single depth. In the case of this study, the biological signal of EP was significantly smaller than the resolved physical terms and local rate-of-change in the permanent pycnocline (Fig. 4.7). Though some respiration was observed deeper than 120 m in this study, an insufficient fraction of the vertical profile of deep respiration could be resolved to draw any conclusions regarding the total magnitude of EP. The results of Figure 4.10, along with knowledge of the typical rates of respiration in mid-water column in the North Pacific Ocean [52] suggest that remineralization rates of organic carbon are probably not resolvable deeper than 150 m depth using the observations described here. As shown in the permanent pycnocline oxygen budget, horizontal advection was a large term during 2008-2010, importing >10 mol O_2 m^{-2} to the depth range 120-200 m and obscuring any seasonal signal in this zone (Fig. 4.11). This is likely a consequence of eddy circulation atypical of the usual North Pacific Current at OSP observed during this period, which imported warm, fresh, low-density water to the halocline during the Seaglider surveys (Chapters 2 and 3). Since dissolved oxygen concentration increases strongly with decreasing density in the permanent pycnocline (Fig. 4.4), there is a corresponding input of oxygen to the pycnocline. It is possible that future observations, collected during non-eddy conditions, could more feasibly extract a deep respiration signal in the halocline. Similar to this study, Tabata [147] found that non-seasonal variations dominated the dissolved oxygen content deeper than 125 m in his analysis of early Weathership data from 1956-1962.

In contrast to results from a similar array at HOT [111], although euphotic zone productivity deeper than the SL was evident at OSP (Fig. 4.10), it was not a substantial fraction of the total euphotic zone productivity (*cf.* integrated J^{bio} in top 25 m of TL in Fig. 4.13). The most prominent deep euphotic zone productivity was in mid-summer 2009, though preceding this period, respiration dominated in the upper TL such that the integrated NCP in this region over the growing season was negligible. The compensation depth of $\sim$40 m appears shallower than that at HOT, where productivity in the deep euphotic zone was evident as

deep as ∼100 m [111].

4.5 Summary and Conclusions

Observations from a combined Seaglider-moored array deployed for nearly 20 months in the Gulf of Alaska were used to investigate the kinematic fluxes of dissolved oxygen and rates of ocean metabolism in the upper ocean using the oxygen mass balance method. A least-squares method with inequality constraints provided estimates of the three-dimensional circulation and vertical diffusivities during the time series, which were formulated to minimize the time-integrated error in budgets of biologically inert tracers (Chapter 3). The circulation and diffusivity estimates were applied to the budget of dissolved oxygen, in order to estimate the net biological productivity or respiration as a residual between local rate-of-change and the physical tendency (the net convergence of advective and diffusive fluxes).

The most important result of this study is the measurement of respiration within the seasonal thermocline at OSP, which represents organic carbon that leaves the SL on a seasonal time scale and will be re-exposed to the atmosphere at the conclusion of the growing season as the SL deepens. It is estimated that 0.81 mol C m^{-2} yr^{-1} was respired deeper than the SL base and shallower than the maximum depth of winter mixing, taken in this study to be 120 m, during two growing seasons in 2008 and 2009. Using typical rates of productivity estimated from previous studies, this suggests that 30-50% of organic carbon produced in the surface layer in summer does not leave the upper ocean on an annual basis. As such, this number also represents a correction that must be applied to budgets of NCP computed solely in the surface layer, since this respiration is not detectable from a surface layer budget alone.

The results of this study also confirmed the vertical balance of terms in the surface layer, primarily between local storage, turbulent diffusion, and biology, with horizontal advection of secondary importance as previous studies had assumed. In summer, turbulent diffusion transfers oxygen from the thermocline to the SL where it is then outgassed to the atmosphere. In winter, turbulence acts to transport oxygen downward from the SL to the permanent

pycnocline. Horizontal advection of dissolved oxygen was an $\mathcal{O}(1)$ term in the transition layer and deeper during the array time series, although this may be due in part to the presence of a mesoscale eddy near the array, and corresponding strong horizontal gradients both on depth surfaces and along isopycnals – the effect observed here may not be representative of climatological conditions at OSP.

Rates of productivity during both resolved growing seasons were at the lower end of previously published rates, though these conclusions are sensitive to the choice of gas exchange parameterization. Observations during a volcanic ash deposition event confirmed rates of carbon production $\sim$3$\times$ the typical summer-average. Uncertainties on surface gas exchange during the cooling season, when mixed layer gas concentrations were increasing and surface supersaturations were near-neutral, were too large to specifically estimate winter surface layer NCP and thus complete a direct estimate of top 120 m ANCP. Estimates of turbulent transport of oxygen indicated 0.9 mol O_2 m^{-2} yr^{-1} is diffused downward across the 120 m depth boundary, though this estimate is based on an assumed weak interior diffusivity for 2/3 of the year. Respiration could not be resolved deeper than about 150 m, preventing a direct estimate of EP for comparison to upper-ocean ANCP. Observations during a period of weaker horizontal advection may better resolve respiration in this zone in the future.

This study is a successor to a similar Seaglider survey time series at HOT and further demonstrates the ability of an array of moored sensors and mobile autonomous profiling vehicles to resolve the dominant terms in the oxygen mass balance. The approach provides a depth-resolved description of NCP at ocean time series sites. Uncertainties in the surface gas exchange, both instrumental and theoretical, and turbulent diffusion remain the primary impediment to accurate estimates of ANCP from a single-tracer mass balance in the SL. When the budget of dissolved oxygen is integrated over the top 120 m at OSP, diffusion becomes less important, with the tradeoff that horizontal and vertical advection may become significant. Biological signals were effectively isolated from observed local rates of change where signals were large (in the surface layer in summer) and in regions of weak horizontal and vertical gradients (in the mid-seasonal thermocline). Although this study did not make

a concerted effort to resolve respiration deeper than 200 m, it seems unlikely that such a respiration profile could be computed from this array – at least, during the particular conditions observed at OSP during 2008-2010, when large horizontal gradients and changes in oxygen concentration were apparent at depth, making it imperative to estimate horizontal advection highly accurately. Furthermore, beneath the permanent pycnocline, the vertical structure in the pressure response of each optode instrument may become significant, especially compared to the small signals in the oxygen minimum zone near 1000 m at OSP. Computing a budget in an Argo float-following reference frame [*e.g.,* 103], or using many platforms, in which mesoscale noise is averaged out over a basin scale, may help address uncertainties when computing EP and complement fixed-point estimates of NCP such as those made here.

4.6 Tables

4.7 Figures

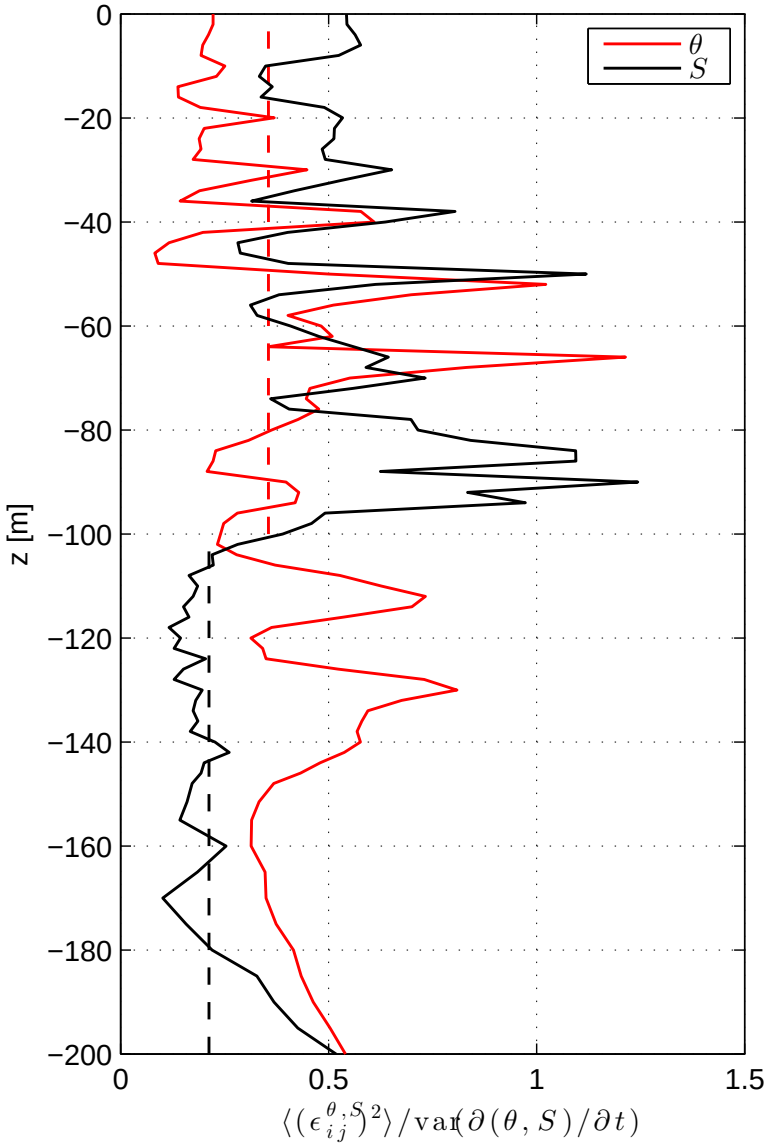

Figure 4.1: Mean square error ϵ in potential temperature θ (red) and salinity S (black) balances estimated in Chapter 3, normalized by the variance of $\partial\theta/\partial t$ and $\partial S/\partial t$ at each depth level. Red dashed line indicates mean normalized error for $\partial\theta/\partial t$ shallower than 100 m depth, while black dashed line indicates mean normalized error for $\partial S/\partial t$ deeper than 100 m.

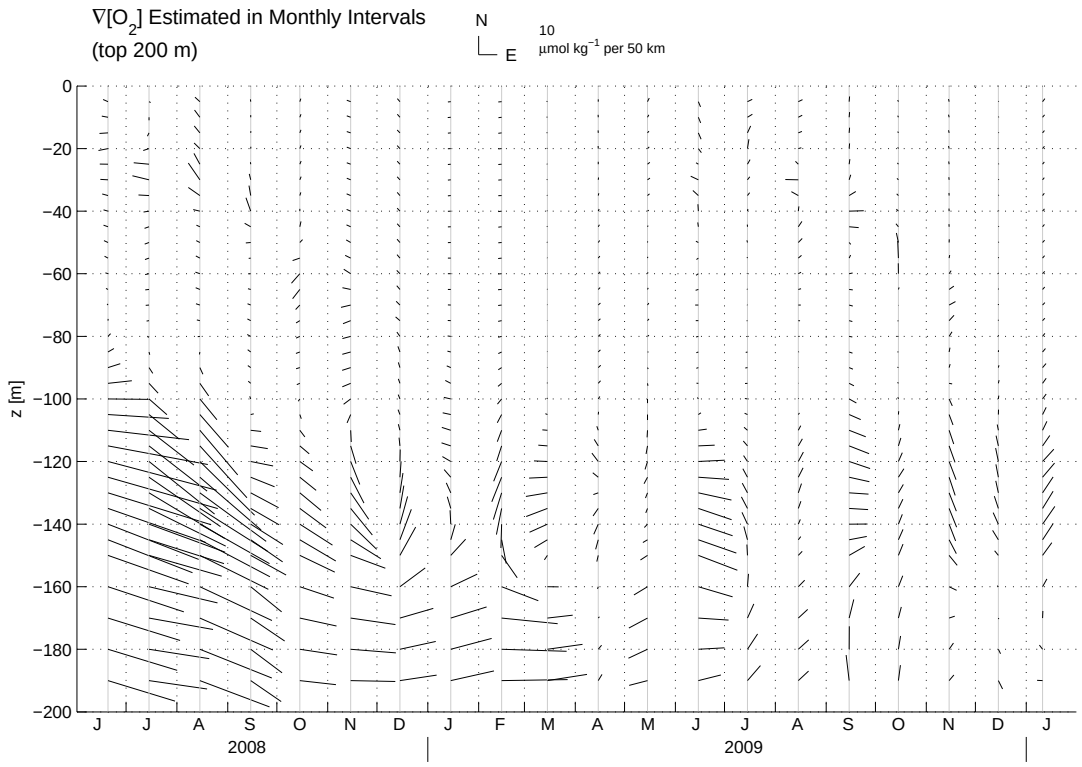

Figure 4.2: Horizontal gradients of dissolved oxygen concentration $\nabla[O_2]$ at monthly intervals (scale at top). Gradients are plotted at every 5 m shallower than 150 m and every 10 m deeper.

Vessel/Cruise	Cast Number	Latitude	Longitude	Date	SL-avg % Supersat
CCGS *John P. Tully*	75	144°49.95′W	50°08.28′N	10 June 2008 15:01UTC	5.32 (3 bottles)
2008-26 (Line P)	80	144°49.47′W	50°07.73′N	11 June 2008 19:27UTC	4.91 (4)
R/V *Thomas G. Thompson*	301	144°50.02′W	50°05.49′N	30 August 2008 12:09UTC	3.94 (1)
TN224 (UW Student Cruise 08)	302	144°48.35′W	50°05.54′N	30 August 2008 19:41UTC	3.94 (2)
Tully	65	144°50.12′W	50°07.96′N	14 June 2009 05:04UTC	5.14 (3)
2009-09 (Line P)	75	145°00.04′W	49°59.93′N	14 June 2009 20:15UTC	4.18 (1)
–	76	144°59.98′W	49°59.96′N	14 June 2009 22:17UTC	4.56 (1)
–	79	145°00.01′W	49°59.99′N	15 June 2009 02:31UTC	4.43 (3)
–	80	145°00.06′W	49°59.97′N	15 June 2009 05:02UTC	4.47 (3)
Tully	47	144°59.88′W	50°00.01′N	27 August 2009 19:57UTC	1.97 (3)
2009-10 (Line P)	48	144°59.90′W	50°00.00′N	27August 2009 22:16UTC	2.04 (5)
–	49	144°59.99′W	49°59.99′N	28 August 2009 00:34UTC	1.88 (1)
–	51	145°00.02′W	50°00.06′N	28 August 2009 03:28UTC	1.83 (1)
–	52	144°48.63′W	50°09.34′N	28 August 2009 07:29UTC	1.46 (5)

Table 4.1: Comparison casts with Winkler oxygen sampling used to postcalibrate Seaglider oxygen optodes at OSP in this study.

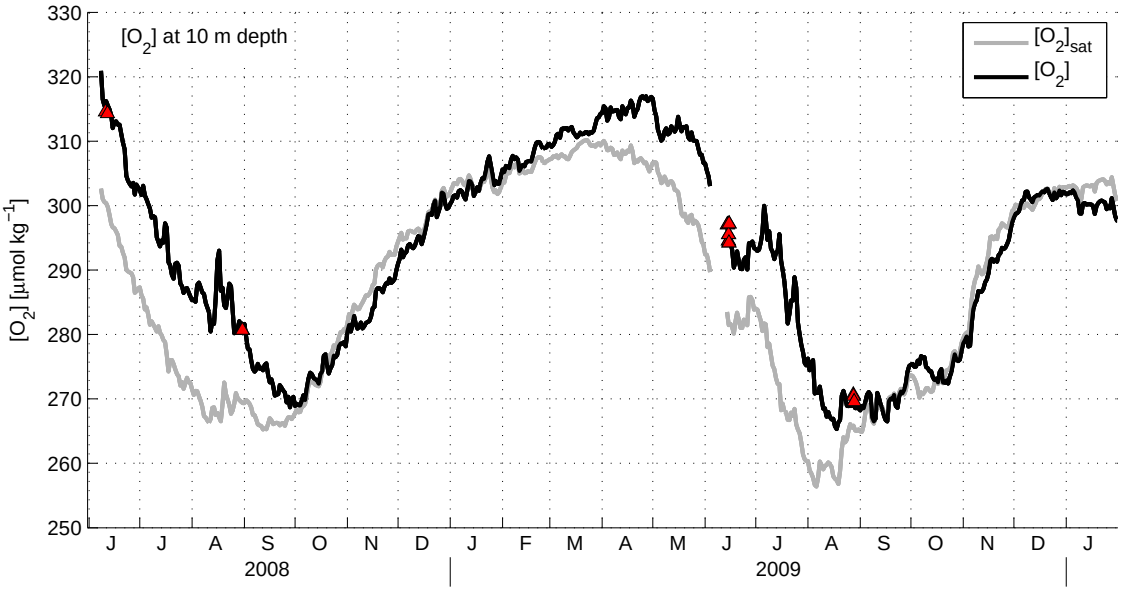

Figure 4.3: Near-surface measurements of dissolved oxygen from Seagliders at Ocean Station Papa. Black curve indicates daily-average oxygen concentration $[O_2]$ while gray curve indicates concentration at saturation equilibrium $[O_2]_{sat}$. Red triangles indicate surface-layer average oxygen concentrations reported from shipboard Winkler titrations from the CCGS *John P. Tully* or R/V *Thomas G. Thompson* during visits to Station Papa.

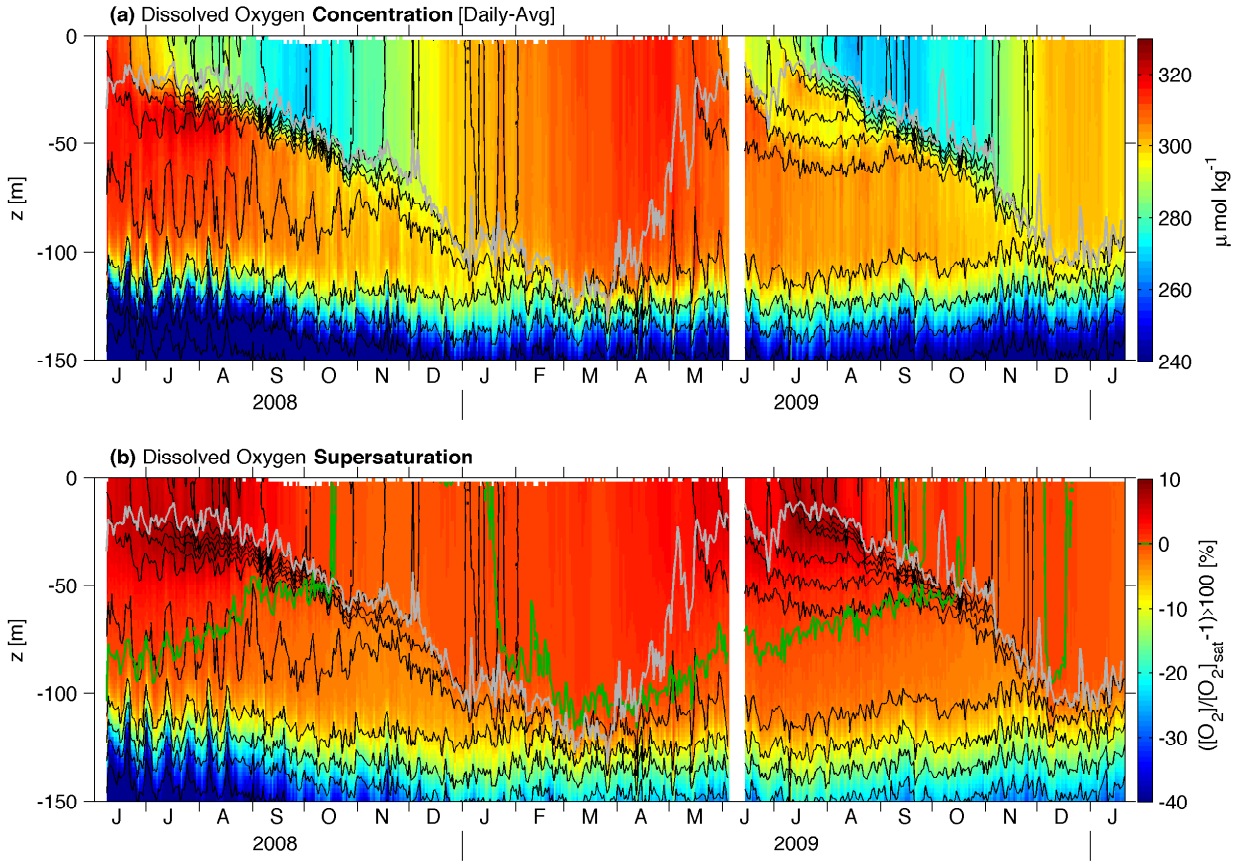

Figure 4.4: Daily-average dissolved oxygen concentration (a) and oxygen supersaturation ($[O_2]/[O_2]_{sat}$ - 1)×100 (b), where $[O_2]_{sat}$ is the concentration at saturation equilibrium. Gray line in (a) and (b) indicates the mixed-layer depth ($\Delta\sigma_\theta = 0.03$ kg m^{-3} from 10 m reference value) calculated from the daily-average density field. Green line in (b) indicates the 0% supersaturation contour. Black contours in (a) and (b) are isopycnals plotted at increments of $\Delta\sigma_\theta = 0.2$.

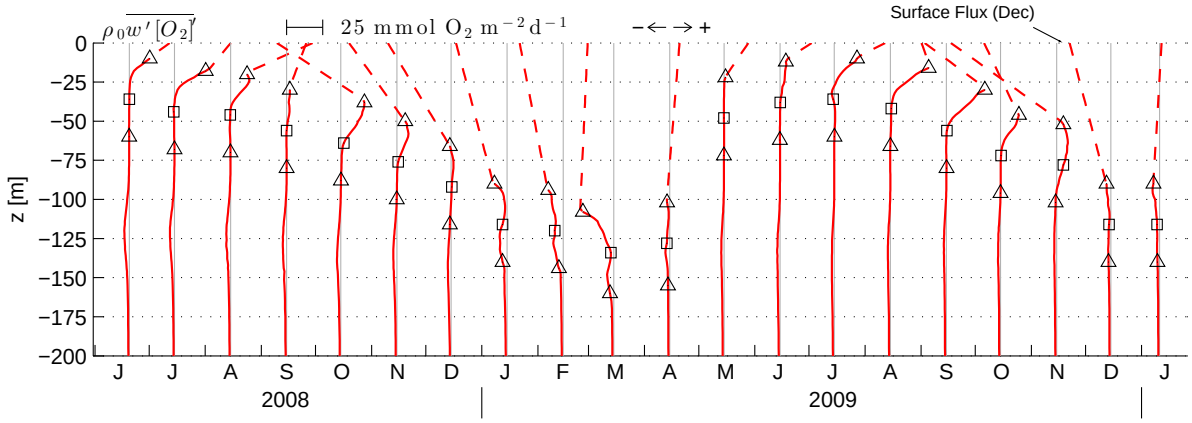

Figure 4.5: Profiles of turbulent dissolved oxygen flux $\rho_0 \overline{w'[\mathrm{O}_2]'}$ estimated in each monthly time interval. Profiles are offset from the center of each monthly bin; positive indicates upward turbulent transport (scale at upper left). Triangles plotted on each profile indicate the upper and lower boundaries of the 50 m-thick transition layer (TL); squares indicate its mid-point. The least-squares solution of Chapter 3 finds turbulent diffusivity only within the TL. Shallower than the top of the TL, the profile is interpolated between the value at the top of the TL and the value at the surface given by the mean rate of gas exchange in each monthly interval (dashed portion; Section 4.2.2).

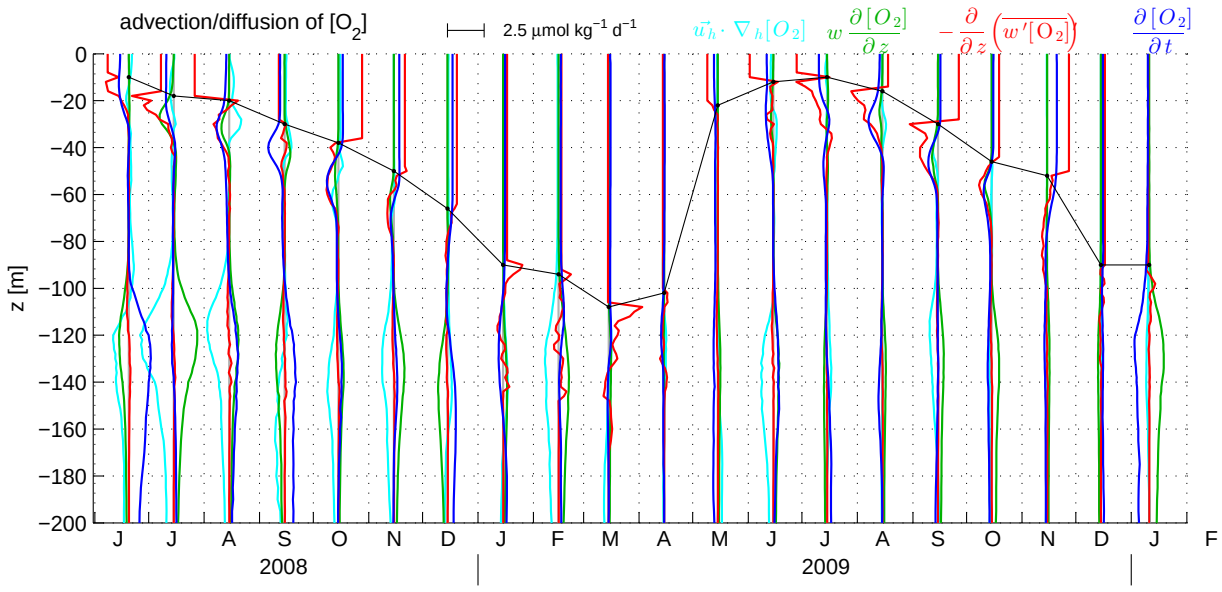

Figure 4.6: Vertical profiles of resolved terms in the dissolved oygen concentration ($[O_2]$) balance in each monthly time bin: horizontal advection (cyan), vertical advection (green), convergence of turbulent flux (red), and local rate-of-change (blue). Profiles are offset from the center of each monthly interval (scale at upper left). Advection and turbulent flux per unit density are derived from the least-squares solution estimates of velocity components and vertical diffusivities from Chapter 3. Black line indicates the surface layer depth in each monthly interval. In the surface layer, turbulent flux is assumed constant as the difference between diffusion at the surface layer base and surface gas exchange (Section 4.2.2).

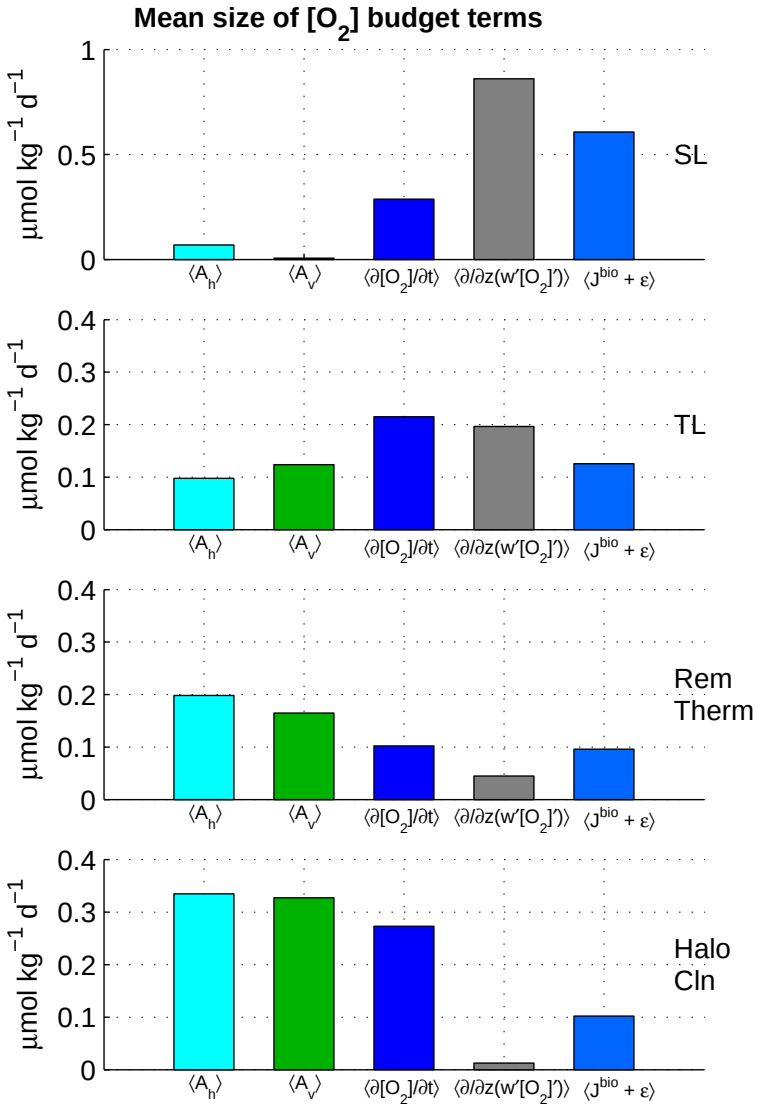

Figure 4.7: Mean size of terms in the dissolved oxygen balance in each of four vertical zones: surface layer (SL, top row), transition layer (TL, second row), remnant thermocline (RemTherm, third row), and halocline (HaloCln, fourth row). The remnant thermocline is defined as the region between the base of the transition layer and 120 m, while the halocline is the region between 200 m and either 120 m or the transition layer base, whichever is deeper. Vertical bars indicate the mean size of resolved terms (horizontal advection A_h, vertical advection A_v, local rate-of-change $\partial[\mathrm{O}_2]/\partial t$, and divergence of turbulent transport $\partial/\partial z\overline{w'[\mathrm{O}_2]'}$) and of unresolved terms, which are assumed to be due to biological activity and error (J^{bio} + err). Note the change of scale in the top row (SL) relative to all other rows. Divergence of turbulent transport in the SL is the difference between surface gas exchange and turbulent diffusion at the SL base (Section 4.2.2).

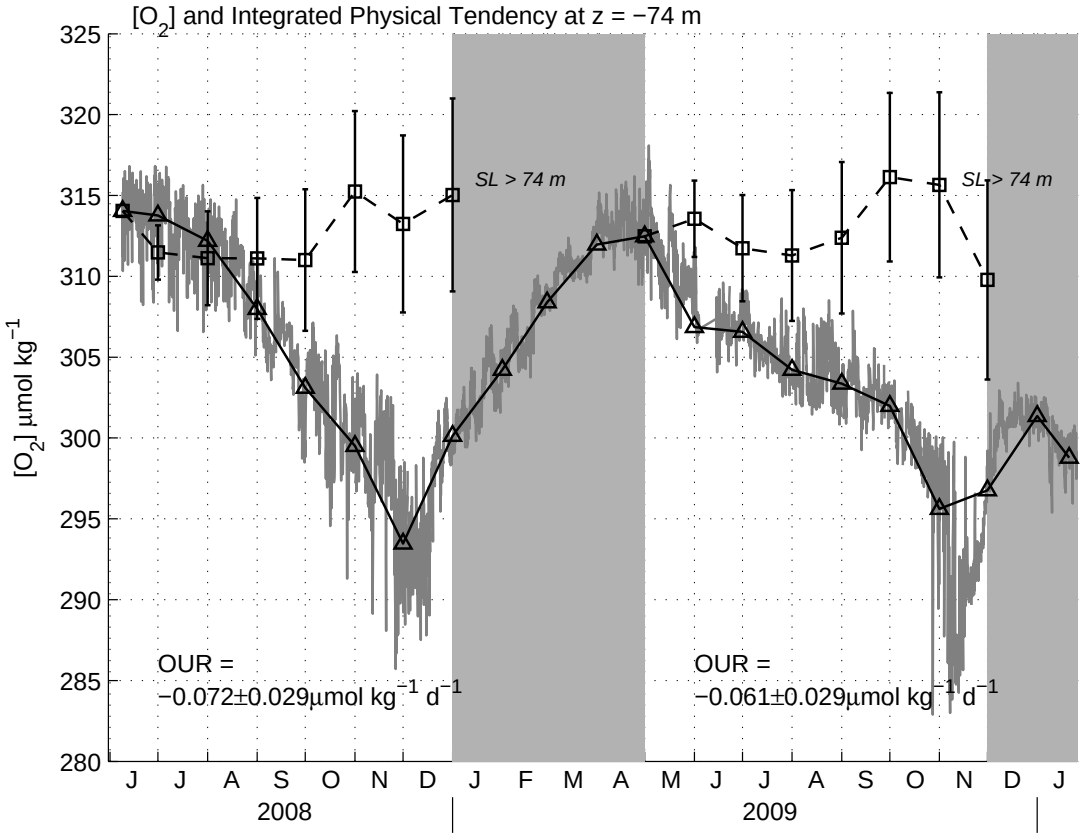

Figure 4.8: Observed dissolved oxygen concentration $[O_2]$ and integrated physical tendency at 74 m depth. The thin gray curve indicates observed $[O_2]$ in individual profiles. The solid black curve with triangle markers indicates $[O_2]$ estimated at the center of the survey region at the beginning and end of each monthly time interval. Dashed black curves with square markers indicate the integrated physical tendency of oxygen concentration. Integrated physical tendency is plotted during periods when the SL is shallower than 74 m depth (gray shaded portions indicate SL depth exceeds 74 m). During these times, estimates of diffusive transport are independent of surface gas exchange (Section 4.2.2). Whiskers indicate root-mean-square uncertainty bounds.

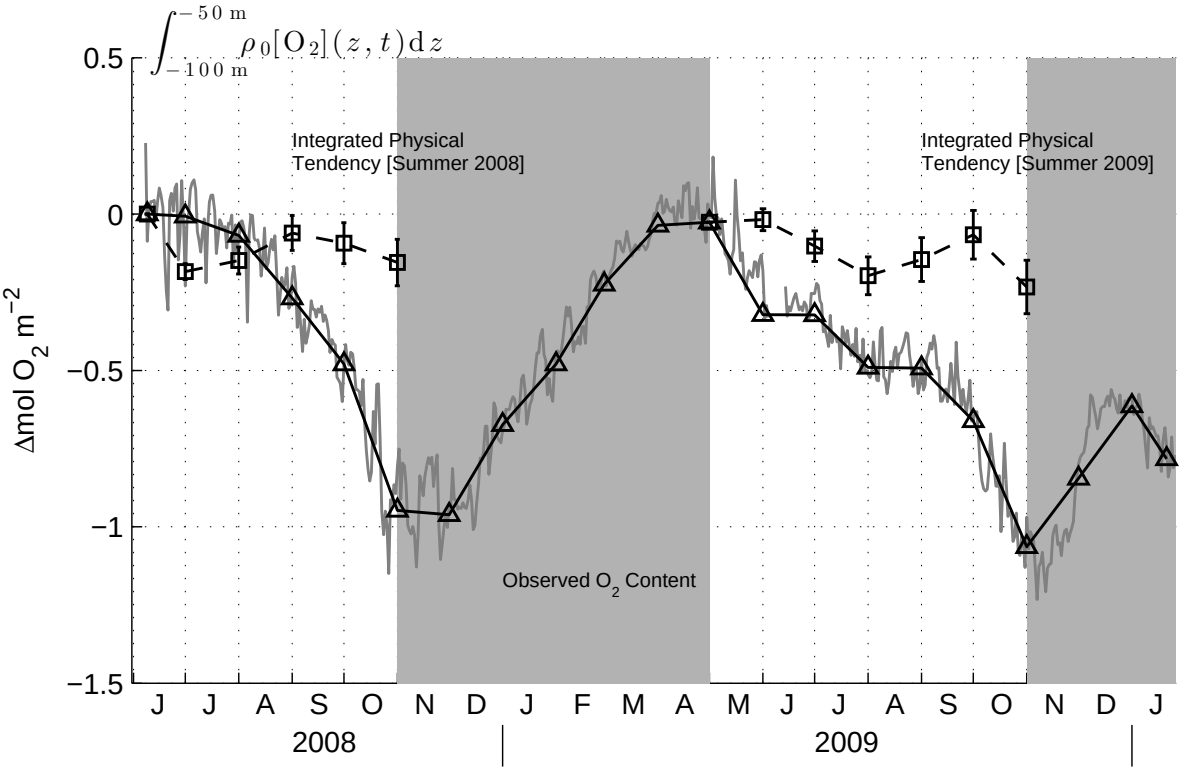

Figure 4.9: Observed dissolved oxygen content in the region -100 m $\leq z \leq$ -50 m depth (offset from initial oxygen content) and the integrated physical tendency. The thin gray curve indicates daily-average oxygen content in this region. The solid black curve with triangle markers indicates oxygen content estimated at the center of the survey region at the beginning and end of each monthly time interval. Dashed black curves with square markers indicate the integrated physical tendency of oxygen content. Integrated physical tendency is plotted during periods when the SL is shallower than 50 m depth, when estimated physical tendency is independent of surface gas exchange (Section 4.2.2). Gray shaded portions indicate SL depth exceeds 50 m. Whiskers indicate root-mean-square uncertainty bounds on the integrated physical tendency.

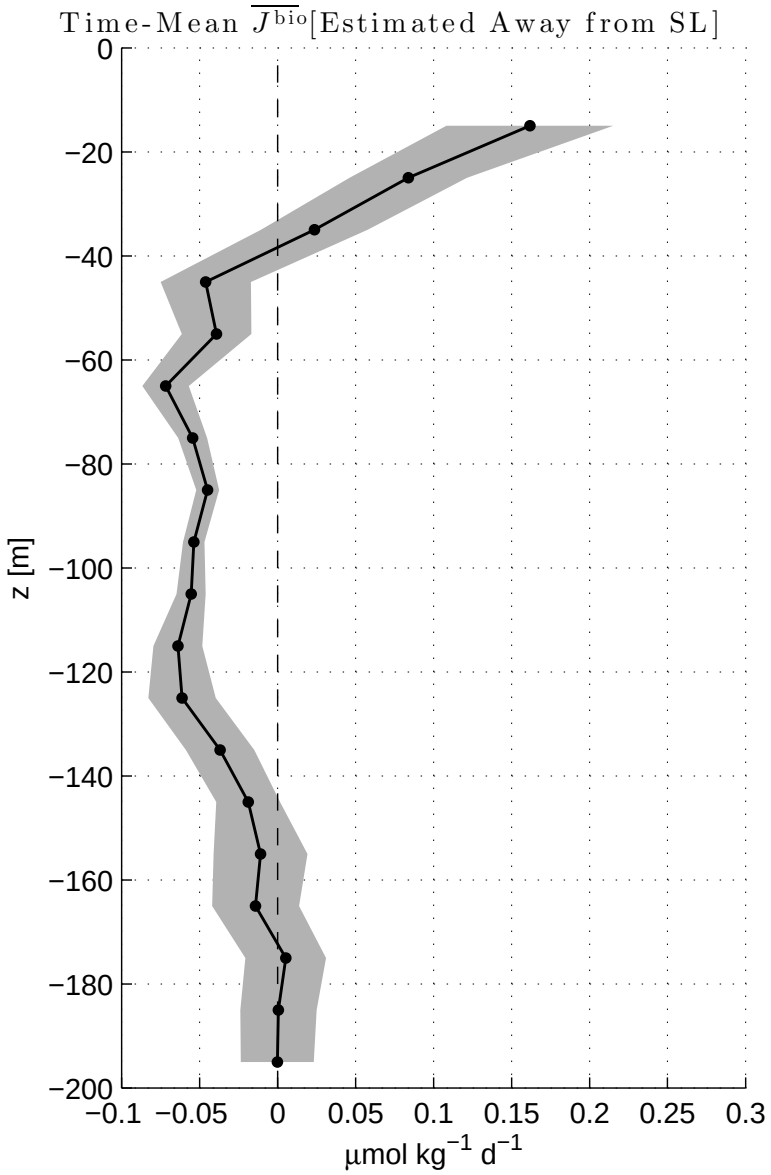

Figure 4.10: Time-series average of mean rate of change of oxygen concentration due to net community production or respiration J^{bio} in 10-m vertical intervals. The time-average at each depth only includes time bins where that depth is outside of the SL. Thus, the average reflects metabolic rate estimates that are independent of surface gas exchange. Shaded gray region indicates root-mean square uncertainty bounds.

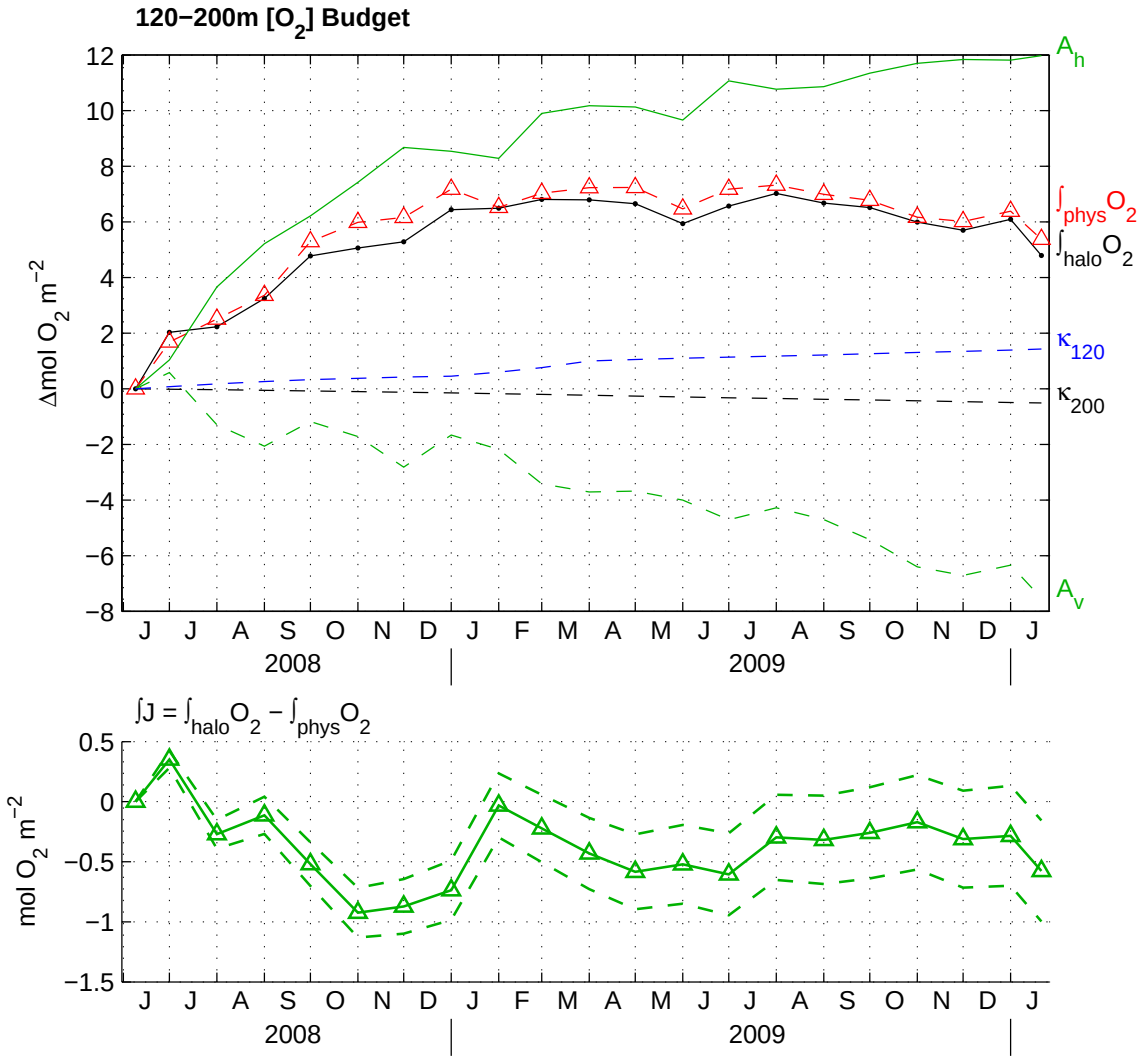

Figure 4.11: Vertically-integrated oxygen budget during the array time series for depths 120-200 m (the "halocline" or permanent pycnocline). All terms offset from the initial oxygen content. Horizontal advection (A_h, solid green line) adds oxygen to this zone during the time series while vertical advection (A_v) removes a comparable amount. Turbulent flux at 120 m (Kz_{120}, blue dashed line) adds oxygen mainly during the winter months, when boundary layer diffusion brings well-oxygenated surface water downward. Turbulent flux at 200 m (Kz_{200}, black dashed line) removes a small amount of oxygen. The integrated physical tendency (red dashed line, triangle markers) has a similar trend to the observed oxygen concentration ($\int_{halo} O_2$, solid black line). The difference between the observed oxygen content and the integrated physical tendency (green triangles, lower panel) is similar to the estimated root-mean square uncertainty (green dashed lines).

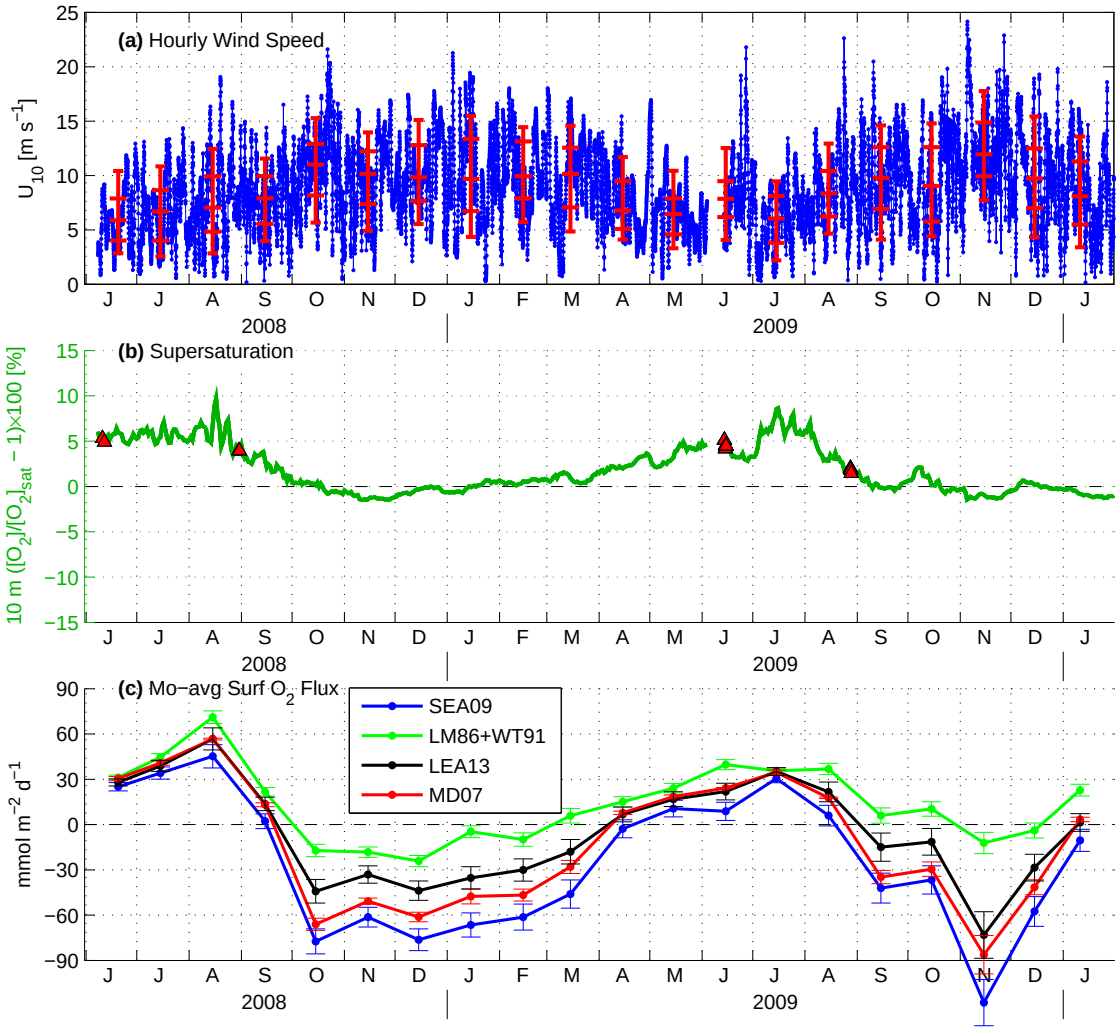

Figure 4.12: (a) Hourly-averaged 10 m neutral wind speed U_{10} (blue curve). Red horizontal dashes indicate the 10, 25, 50, 75, and 90th percentiles of wind speed in each month. (b) Daily-average supersaturation (%) of dissolved oxygen at 10 m depth from Seaglider optode measurements (green curve). Red triangles indicate surface-layer average measurements of supersaturation from shipboard Winkler samples. (c) Monthly-average gas exchange rates estimated using four different parameterizations; abbreviations defined in the text. Whiskers denote root-mean square uncertainty in gas exchange due to errors in optode accuracy.

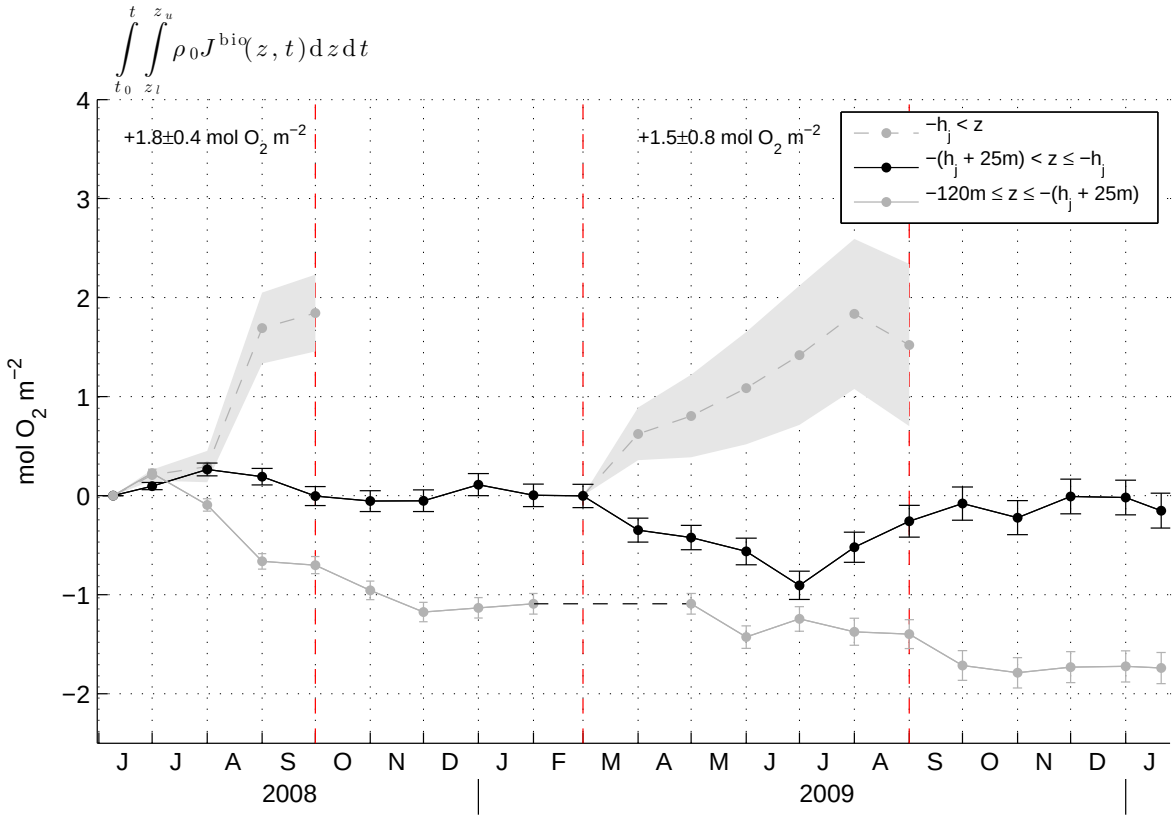

Figure 4.13: Vertically and temporally integrated rate of change of volumetric oxygen concentration due to production/respiration in three vertical zones. Curves indicate the cumulative productivity in each zone from the beginning of the Seaglider time series. Gray dashed curve indicates the surface layer (SL, $-h_j < z$, where h_j is the SL thickness in interval j), black line indicates the upper 25 m of the transition layer, and the gray solid line indicates the region from the lower 25 m of the TL to 120 m. For the deeper two zones, whiskers indicate the uncertainty bounds, which in these zones are due to errors in the least-squares solution. In the SL, gray shading indicates uncertainty due to the least-squares solution and surface gas exchange. Integrals for the SL are shown in the growing seasons; text indicates the integral of estimated NCP in this zone at the conclusion of each season.

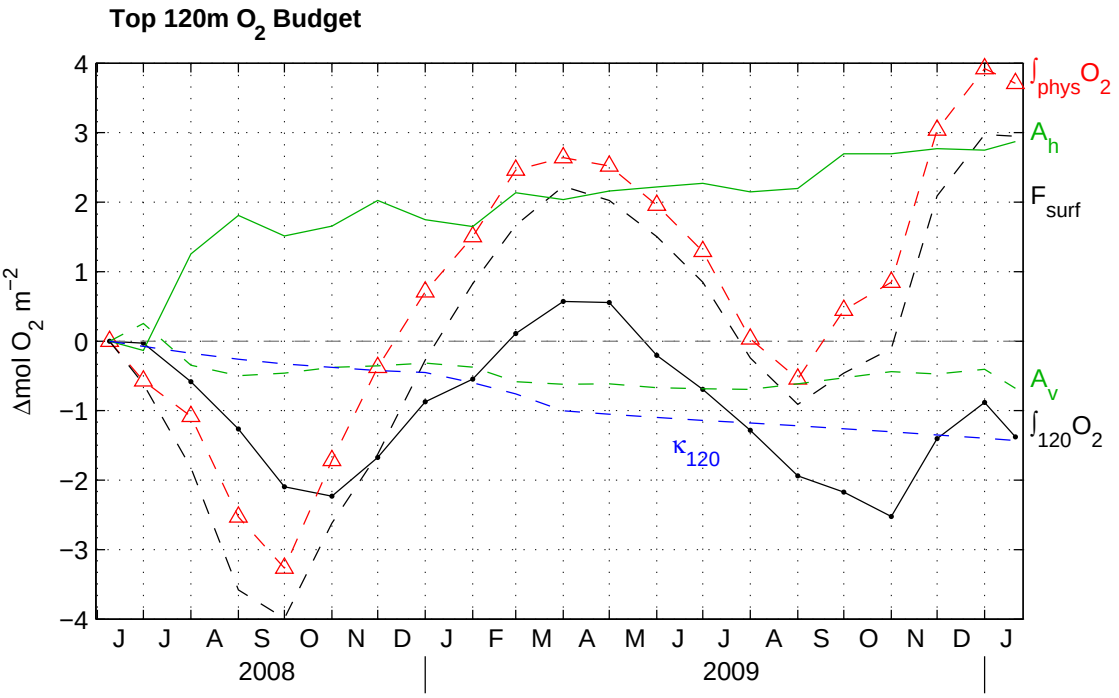

Figure 4.14: Time-integrated balance of resolved terms in the dissolved oxygen budget, integrated across the top 120 m. All terms offset from the initial oxygen content. Black curve indicates the time record of oxygen content in the top 120 m, while the red dashed curve ($\int_{phys} O_2$) indicates the integrated physical tendency. Other curves show the terms that compose $\int_{phys} O_2$: horizontal advection (A_h), vertical advection (A_v), diffusion at 120 m (κ_{120}), and surface gas exchange (F_{surf}). Dashed gray line indicates starting oxygen content. Surface gas exchange and integrated physical tendency are shown only to illustrate their approximate size, since these curves are highly sensitive to the choice of gas exchange parameterization.

BIBLIOGRAPHY

[1] K.A. Adams. *Influence of upwelling-season coastal currents on near-bottom dissolved oxygen concentrations over a submarine bank*. PhD thesis, Oregon State University, 2014.

[2] M.H. Alford, M.F. Cronin, and J.M. Klymak. Annual cycle and depth penetration of wind-generated near-inertial internal waves at Ocean Station Papa in the northeast Pacific. *Journal of Physical Oceanography*, 42(6):889–909, 2012.

[3] M.B. Alkire, E.D. D'Asaro, C. Lee, M.J. Perry, A. Gray, I. Cetinić, N. Briggs, E. Rehm, E. Kallin, J. Kaiser, and A. González-Posada. Estimates of net community production and export using high-resolution, Lagrangian measurements of O_2, NO_3^-, and POC through the evolution of a spring diatom bloom in the North Atlantic. *Deep-Sea Research I*, 64:157–174, 2012.

[4] D.M. Allen. The Relationship between Variable Selection and Data Augmentation and a Method for Prediction. *Technometrics*, 16(1):125–127, 1974.

[5] V.V. Anokhin, J. Imberger, G.N. Ivey, and J.R. Romero. Estimating net transport and mixing using a time-dependent inverse method. *Journal of Geophysical Research*, 113(C7):doi:10.1029/2006JC003705, 2008.

[6] T.E. Appleton. *Usque ad mare: A History of the Canadian Coast Guard and Marine Services*. Department of Transport, Ottawa, Canada. Available: `http://www.cc-gcc.gc.ca/eng/CCG/USQUE_Weather_Ships`, 1969.

[7] D. Archer, S. Emerson, T. Powell, and C.S. Wong. Numerical hindcasting of sea surface pCO_2 at Weathership Ocean Station Papa. *Progress in Oceanography*, 32:319–351, 1993.

[8] M. Aydin, Z. Top, R.A. Fine, and D.B. Olson. Modification of intermediate waters in the northeastern subpolar Pacific. *Journal of Geophysical Research*, 103(C13):30923–30940, 1998.

[9] M. Aydin, Z. Top, and D.B. Olson. Exchange processes and watermass modifications along the subarctic front in the North Pacific: Oxygen consumption rates and net carbon flux. *Journal of Marine Research*, 62:153–167, 2004.

[10] B.B. Benson and D. Krause. The concentration and isotopic fractionation of oxygen dissolved in freshwater and seawater in equilibrium with the atmosphere. *Limnology and Oceanography*, 29:620–632, 1984.

[11] S.J. Bograd, R.E. Thomson, A.B. Rabinovich, and P.H. LeBlond. Near-surface circulation of the northeast Pacific Ocean derived from WOCE-SVP satellite-tracked drifters. *Deep-Sea Research II*, 46:2371–2403, 1999.

[12] N.A. Bond, M.F. Cronin, H. Freeland, and N. Mantua. Causes and impacts of the 2014 warm anomaly in the NE Pacific. *Geophysical Research Letters*, page doi:10.1002/2015GL063306, 2015.

[13] P. Boyd and P.J. Harrison. Phytoplankton dynamics in the NE subarctic Pacific. *Deep-Sea Research II*, 46:2405–2432, 1999.

[14] T.P. Boyer, J.I. Antonov, O.K. Baranova, C. Coleman, H.E. Garcia, A. Grodsky, D.R. Johnson, R.A. Locarnini, A.V. Mishonov, T.D. O'Brien, C.R. Paver, J.R. Reagan, D. Seidov, I.V. Smolyar, and M.M. Zweng. World Ocean Database 2013. In S. Levitus and A. Mishonov, editors, *NOAA Atlas NESDIS 72*. NOAA, 209 pp., http://doi.org/10.7289/V5NZ85MT., 2013.

[15] H. Brix, N. Gruber, D. M. Karl, and N. R. Bates. On the relationships between primary, net community, and export production in subtropical gyres. *Deep-Sea Research II*, 53:698–717, 2006.

[16] C.G. Castro, F.P. Chavez, and C.A. Collins. Role of the California Undercurrent in the export of denitrified waters from the eastern tropical North Pacific. *Global Biogeochemical Cycles*, 15(4):819–830, 2001.

[17] M.A. Charette, S.B. Moran, and J.K.B. Bishop. Th–234 as a tracer of particulate organic carbon export in the subarctic northeast Pacific Ocean. *Deep-Sea Research II*, 46:2833–2861, 1999.

[18] D.M. Checkley Jr. and J.A. Barth. Patterns and processes in the California Current System. *Progress in Oceanography*, 83:49–64, 2009.

[19] D.B. Chelton, M.G. Schlax, and R.M. Samelson. Global observations of nonlinear mesoscale eddies. *Progress in Oceanography*, 91:167–216, 2011.

[20] T.K. Chereskin. Direct evidence for an Ekman balance in the California Current. *Journal of Geophysical Research*, 100(C9):18261–18269, 1996.

[21] T.K. Chereskin and D. Roemmich. A Comparison of Measured and Wind-derived Ekman Transport at 11°N in the Atlantic Ocean. *Journal of Physical Oceanography*, 21:869–878, 1991.

[22] W. Crawford, P. Sutherland, and P. van Hardenberg. Cold Water Intrusion in the Eastern Gulf of Alaska in 2002. *Atmosphere-Ocean*, 43(2):119–128, 2005.

[23] W.R. Crawford, P.J. Brickley, and A.C. Thomas. Mesoscale eddies dominate surface phytoplankton in northern Gulf of Alaska. *Progress in Oceanography*, 75:287–303, 2007.

[24] M.F. Cronin, N.A. Bond, J.T. Farrar, H. Ichikawa, S.R. Jayne, Y. Kawai, M. Konda, B. Qiu, L. Rainville, and H. Tomita. Formation and erosion of the seasonal thermocline in the Kuroshio Extension Recirculation Gyre. *Deep-Sea Research II*, 85:62–74, 2013.

[25] M.F. Cronin and M. J. McPhaden. Upper ocean salinity balance in the western equatorial Pacific. *Journal of Geophysical Research*, 103(C12):27567–27587, 1998.

[26] M.F. Cronin, R.A. Weller, S. Lampitt, and U. Send. Ocean Reference Stations. In R.B. Rustamov and S.E. Salahova, editors, *Earth Observation*. InTech. Available: `http://www.intechopen.com/books/earth-observation/ocean-reference-stations`, 2012.

[27] D.S. Crosby, L.C. Breaker, and W.H. Gemmill. A Proposed Definition for Vector Correlation in Geophysics: Theory and Application. *Journal of Atmospheric and Oceanic Technology*, 10:355–367, 1993.

[28] P.F. Cummins and H.J. Freeland. Variability of the North Pacific Current and its bifurcation. *Progress in Oceanography*, 75:253–265, 2007.

[29] P.F. Cummins and G.S.E. Lagerloef. Low-Frequency Pycnocline Depth Variability at Ocean Weather Station P in the Northeast Pacific. *Journal of Physical Oceanography*, 32:3207–3215, 2002.

[30] P.F. Cummins and D. Masson. Wind-driven variability of dissolved oxygen below the mixed layer at Station P. *Journal of Geophysical Research*, 117(C08015):doi:10.1029/2011JC007847, 2012.

[31] E.A. D'Asaro. Upper Ocean Temperature Structure, Inertial Currents, and Richardson Numbers Observed during Strong Meteorological Forcing. *Journal of Physical Oceanography*, 15:943–962, 1985.

[32] E.A. D'Asaro, C.C. Eriksen, M.D. Levine, P.P. Niiler, C.A. Paulson, and P. van Meurs. Upper-Ocean Inertial Currents Forced by a Strong Storm. Part I: Data and Comparisons with Linear Theory. *Journal of Physical Oceanography*, 25:2909–2936, 1995.

[33] E.A. D'Asaro and C. McNeil. Calibration and Stability of Oxygen Sensors on Autonomous Floats. *Journal of Atmospheric and Oceanic Technology*, 30:1896–1906, 2013.

[34] R.E. Davis, R. deSzoeke, D. Halpern, and P. Niiler. Variability in the upper ocean during MILE. Part I: The heat and momentum balances. *Deep-Sea Research*, 28A(12):1427–1451, 1981.

[35] R.E. Davis, R. deSzoeke, and P. Niiler. Variability in the upper ocean during MILE. Part II: Modeling the mixed layer response. *Deep-Sea Research*, 28A:1453–1475, 1981.

[36] K.L. Denman and M. Miyake. Upper Layer Modification at Ocean Station Papa: Observations and Simulation. *Journal of Physical Oceanography*, 3(2):185–196, 1973.

[37] A.J. Dodimead, F. Favorite, and T. Hirano. *Salmon of the North Pacific Ocean, Part II: Review of Oceanography of the Subarctic Pacific Region*. International North Pacific Fisheries Commission, Vancouver, Canada, 1963.

[38] K. Dohan and R.E. Davis. Mixing in the Transition Layer during Two Storm Events. *Journal of Physical Oceanography*, 41:42–66, 2011.

[39] S. Emerson. Seasonal oxygen cycles and biological new production in surface waters of the subarctic Pacific Ocean. *Journal of Geophysical Research*, 92(C6):6535–6544, 1987.

[40] S. Emerson, P. Quay, C. Stump, D. Wilbur, and M. Knox. O_2, Ar, N_2, and Rn–222 in surface waters of the subarctic ocean: net biological O_2 production. *Global Biogeochemical Cycles*, 5(1):49–69, 1991.

[41] S. Emerson, C. Sabine, M.F. Cronin, R. Feely, S. Cullison, and M. DeGrandpre. Quantifying the flux of $CaCO_3$ and organic carbon from the surface ocean using in situ measurements of O_2, N_2, pCO_2 and pH. *Global Biogeochemical Cycles*, 25:GB3008, doi:10.1029/2010GB003924, 2011.

[42] S. Emerson and C. Stump. Net biological oxygen production in the ocean—II: Remote in situ measurements of O_2 and N_2 in subarctic Pacific surface waters. *Deep-Sea Research I*, 57:1255–1265, 2010.

[43] S. Emerson, C. Stump, and D. Nicholson. Net biological oxygen production in the ocean: Remote in situ measurements of O_2 and N_2 in surface waters. *Global Biogeochemical Cycles*, 22(GB3023), 2008.

[44] S.R. Emerson. Annual net community production and the biological carbon flux in the ocean. *Global Biogeochemical Cycles*, 28:1–12, 2014.

[45] S.R. Emerson, P.D. Quay, D. Karl, C. Winn, L. Tupas, and M. Landry. Experimental determination of the organic carbon flux from open-ceaon surface waters. *Letters to Nature*, 389:951–954, 1997.

[46] J. Emile-Geay, M.A. Cane, N. Naik, R. Seager, A.C. Clement, and A. van Geen. Warren revisited: Atmospheric freshwater fluxes and "Why is no deep water formed in the North Pacific". *Journal of Geophysical Research*, 108(C6):doi:10.1029/2001JC001058, 2003.

[47] C.C. Eriksen, T.J. Osse, R.D. Light, T. Wen, T.W. Lehman, P.L. Sabin, J.W. Ballard, and A.W. Chiodi. Seaglider: A Long-Range Autonomous Underwater Vehicle for Oceanographic Research. *IEEE Journal of Oceanic Engineering*, 26(4):424–436, 2001.

[48] C.W. Fairall, E.F. Bradley, J.S. Godfrey, G.A. Wick, J.B. Edson, and G.S. Young. Cool-skin and warm-layer effects on sea surface temperature. *Journal of Geophysical Research*, 101(C1):1295–1308, 1996.

[49] C.W. Fairall, E.F. Bradley, J.E. Hare, A.A. Grachev, and J.B. Edson. Bulk Parameterization of Air-Sea Fluxes: Updates and Verification for the COARE Algorithm. *Journal of Climate*, 16:571–591, 2003.

[50] P. Falkowski, R.J. Scholes, E. Boyle, J. Canadell, D. Canfield, J. Elser, N. Gruber, K. Hibbard, P. Högberg, S. Linder, F.T. Mackenzie, B. Moore III, T. Pedersen, Y. Rosenthal, S. Seitzinger, V. Smetacek, and W. Steffen. The Global Carbon Cycle: A Test of Our Knowledge of Earth as a System. *Science*, 290:291–296, 2000.

[51] A.J. Fassbender, C.L. Sabine, and M.F. Cronin. Net community production and calcification from seven years of NOAA Station Papa mooring measurements. *Global Biogeochemical Cycles*, in press.

[52] R.A. Feely, C.L. Sabine, R. Schlitzer, J.L. Bullister, S. Mecking, and D. Greeley. Oxygen Utilization and Organic Carbon Remineralization in the Upper Water Column of the Pacific Ocean. *Journal of Oceanography*, 60:45–52, 2004.

[53] M. Feng, R. Lukas, P. Hacker, R. A. Weller, and S. P. Anderson. Upper-Ocean Heat and Salt Balances in the Western Equatorial Pacific in Response to the Intraseasonal Oscillation during TOGA COARE. *Journal of Climate*, 13:2409–2427, 2000.

[54] B. Fernández-Castro, B. Mouriño Carballido, V.M. Benítez-Barrio, P. Chouciño, E. Fraile-Nuez, R. Graña, M. Piedeleu, and A. Rodríguez-Santana. Microstructure turbulence and diffusivity parameterization in the tropical and subtropical Atlantic, Pacific and Indian Oceans during the Malaspina 2010 expedition. *Deep-Sea Research I*, 94:15–30, 2014.

[55] P. Flament. A state variable for characterizing water masses and their diffusive stability: spiciness. *Progress in Oceanography*, 54:493–501, 2002.

[56] H. Freeland. A short history of Ocean Station Papa and Line P. *Progress in Oceanography*, 75:120–125, 2007.

[57] H. Freeland, K. Denman, C.S. Wong, F. Whitney, and R. Jacques. Evidence of change in the winter mixed layer in the Northeast Pacific Ocean. *Deep-Sea Research I*, 44(12):2117–2129, 1998.

[58] H.J. Freeland. Vertical velocity estimates in the North Pacific using Argo floats. *Deep-Sea Research II*, 85:75–80, 2013.

[59] H.J. Freeland and P.F. Cummins. Argo: A new tool for environmental monitoring and assessment of the world's oceans, an example from the N.E. Pacific. *Progress in Oceanography*, 64:31–44, 2005.

[60] H.E. Garcia and L.I. Gordon. Oxygen Solubility in Seawater: Better Fitting Equations. *Limnology and Oceanography*, 37(6):1307–1312, 1992.

[61] P. Gaspar. Modeling the Seasonal Cycle of the Upper Ocean. *Journal of Physical Oceanography*, 18:161–180, 1988.

[62] K.E. Giesbrecht, R.C. Hamme, and S.R. Emerson. Biological productivity along Line P in the subarctic northeast Pacific: In situ versus incubation-based methods. *Global Biogeochemical Cycles*, 26:GB3028, 2012.

[63] A. Gill. *Atmosphere-Ocean Dynamics*. Academic Press, 1982.

[64] A.E. Gill. The stability of planetary waves on an infinite beta-plane. *Geophysical and Astrophysical Fluid Dynamics*, 6:29–47, 1974.

[65] A.L.M. Grant and S.E. Belcher. Wind-Driven Mixing below the Oceanic Mixed Layer. *Journal of Physical Oceanography*, 41:1556–1575, 2011.

[66] R.C. Hamme and S.R. Emerson. Constraining bubble dynamics and mixing with dissolved gases: Implications for productivity measurements by oxygen mass balance. *Journal of Marine Research*, 64:73–95, 2006.

[67] R.C. Hamme, P.W. Webley, W.R. Crawford, F.A. Whitney, M.D. DeGrandpre, S.R. Emerson, C.C. Eriksen, K.E. Giesbrecht, J.F.R. Gower, M.T. Kavanaugh, M. Angelica Peña, C.L. Sabine, S.D. Batten, L.A. Coogan, D.S. Grundle, and D. Lockwood. Volcanic ash fuels anomalous plankton bloom in subarctic northeast Pacific. *Geophysical Research Letters*, 37:L19604, doi:10.1029/2010GL044629, 2010.

[68] J.E. Hare, C.W. Fairall, W.R. McGillis, J.B. Edson, B. Ward, and R. Wanninkhof. Evaluation of the National Oceanic and Atmospheric Administration/Coupled-Ocean Atmospheric Response Experiment (NOAA/COARE) air-sea gas transfer parameterization using GasEx data. *Journal of Geophysical Research*, 109(C08S11):doi:10.1029/2003JC001831, 2004.

[69] G.H. Haug, D.M. Sigman, R. Tiedemann, T.F. Pedersen, and M. Sarnthein. Onset of permanent stratification in the subarctic Pacific Ocean. *Letters to Nature*, 401(779–782), 1999.

[70] J.I. Hedges, J.A. Baldock, Y. Gelinas, C. Lee, M.L. Peterson, and S.G. Wakeham. The biochemical and elemental compositions of marine plankton: A NMR perspective. *Marine Chemistry*, 45:47–63, 2002.

[71] R. Hervey. Are Moored Buoy Winds Too Low in High Seas? Technical Attachment 00-10. Technical report, NOAA Western Region, Available: `http://www.wrh.noaa.gov/media/wrh/online_publications/TAs/ta0010.pdf`, 2000.

[72] E. Howard, S. Emerson, S. Bushinsky, and C. Stump. The role of net community production in air-sea carbon fluxes at the North Pacific subarctic-subtropical boundary region. *Limnology and Oceanography*, 55(6):2585–2596, 2010.

[73] G.J. Huffman, R.F. Adler, M.M. Morrissey, D.T. Bolvin, S. Curtis, R. Joyce, B. McGavock, and J. Susskind. Global Precipitation at One-Degree Daily Resolution from Multisatellite Observations. *Journal of Hydrometeorology*, 2(1):36–50, 2001.

[74] J.C.R. Hunt, J.C. Kaimal, and J.E. Gaynor. Some observations of turbulence structure in stable layers. *Quarterly Journal of the Royal Meteorological Society*, 111:793–815, 1985.

[75] J.M. Jackson, P.G. Myers, and D. Ianson. An examination of advection in the northeast Pacific Ocean, 2001-2005. *Geophysical Research Letters*, 33:L15601, 2006.

[76] J.M. Jackson, P.G. Myers, and D. Ianson. An Examination of Mixed Layer Sensitivity in the Northeast Pacific Ocean from July 2001-July 2005 Using the General Ocean Turbulence Model and Argo Data. *Atmosphere-Ocean*, 47(2):139–153, 2009.

[77] G.C. Johnson, S. Schmidtko, and J.M. Lyman. Relative contributions of temperature and salinity to seasonal mixed layer density changes and horizontal density gradients. *Journal of Geophysical Research*, 117(C4):doi:10.1029/2011JC007651, 2012.

[78] L.W. Juranek, P.D. Quay, R.A. Feely, D. Lockwood, D.M. Karl, and M.J. Church. Biological production in the NE Pacific and its influence on air-sea CO_2 flux: Evidence from dissolved oxygen isotopes and O_2/Ar. *Journal of Geophysical Research*, 117:C05022, doi:10.1029/2011JC007450, 2012.

[79] E. Kalnay, M. Kanamitsu, R. Kistler, W. Collins, D. Deaven, L. Gandin, M. Iredell, S. Saha, G. White, J. Woollen, Y. Zhu, M. Chelliah, W. Ebisuzaki, W. Higgins, J. Janowiak, K.C. Mo, C. Ropelewski, J. Wang, A. Leetmaa, R. Reynolds, R. Jenne, and D. Joseph. The NCEP/NCAR 40-Year Reanalysis Project. *Bulletin of the American Meteorological Society*, 77(3):437–471, 1996.

[80] A. Körtzinger, U. Send, R. S. Lampitt, S. Hartman, D. W. R. Wallace, J. Karstensen, M. G. Villagarcia, O. Llinás, and M. D. DeGrandpre. The seasonal pCO_2 cycle at 49°N/16.5°W in the northeastern Atlantic Ocean and what it tells us about biological productivity. *Journal of Geophysical Research*, 113(C04020):doi:10.1029/2007JC004347, 2008.

[81] M. Kubota, N. Iwabe, M.F. Cronin, and H. Tomita. Surface heat fluxes from the NCEP/NCAR and NCEP/DOE reanalyses at the Kuroshio Extension Observatory buoy site. *Journal of Geophysical Research*, 113:C02009, doi:10.1029/2007JC004338, 2008.

[82] E. Kunze. Near-Inertial Wave Propagation in Geostrophic Shear. *Journal of Physical Oceanography*, 15:544–565, 1985.

[83] C. Ladd and N.A. Bond. Evaluation of the NCEP/NCAR reanalysis in the NE Pacific and the Bering Sea. *Journal of Geophysical Research*, 107(C10):doi:10.1029/2001JC001157, 2002.

[84] W.G. Large. An Observational and Numerical Investigation of the Climatological Heat and Salt Balances at OWS Papa. *Journal of Climate*, 9:1856–1876, 1996.

[85] W.G. Large and G.B. Crawford. Observations and Simulations of Upper-Ocean Response to Wind Events during the Ocean Storms Experiment. *Journal of Physical Oceanography*, 25:2831–2852, 1995.

[86] W.G. Large, J.C. McWilliams, and S.C. Doney. Oceanic Vertical Mixing: A Review and a Model with a Nonlocal Boundary Layer Parameterization. *Reviews of Geophysics*, 32:363–403, 1994.

[87] W.G. Large, J.C. McWilliams, and P.P. Niiler. Upper Ocean Thermal Response to Strong Autumnal Forcing of the Northeast Pacific. *Journal of Physical Oceanography*, 16:1524–1550, 1986.

[88] W.G. Large, J. Morzel, and G.B. Crawford. Accounting for Surface Wave Distortion of the Marine Wind Profile in Low-Level Ocean Storms Wind Measurements. *Journal of Physical Oceanography*, 25:2959–2971, 1995.

[89] W.G. Large and S. Pond. Open Ocean Momentum Flux Measurements in Moderate to Strong Winds. *Journal of Physical Oceanography*, 11:324–336, 1981.

[90] C.L. Lawson and R.J. Hanson. *Solving least squares problems*. Society for Industrial and Applied Mathematics, 1974.

[91] R.J. LeVeque. *Finite Difference Methods for Ordinary and Partial Differential Equations, Steady State and Time Dependent Problems*. Society for Industrial and Applied Mathematics, 2007.

[92] M. Li, P.G. Myers, and H. Freeland. An examination of historical mixed layer depths along Line P in the Gulf of Alaska. *Geophysical Research Letters*, 32(L05613):doi:10.1029/2004GL021911, 2005.

[93] J.-H. Liang, C. Deutsch, J.C. McWilliams, B. Baschek, P.P. Sullivan, and D. Chiba. Parameterizing bubble-mediated air-sea gas exchange and its effect on ocean ventilation. *Global Biogeochemical Cycles*, 27:doi:10.1002/gbc.20080, 2013.

[94] P.S. Liss and L. Merlivat. Air-sea gas exchange rates: Introduction and synthesis. In P. Buat-Menard, editor, *The Role of Air-sea Exchange in Geochemical Cycling*, pages 113–127. Springer, 1986.

[95] D. Lockwood, P.D. Quay, M.T. Kavanaugh, L.W. Juranek, and R.A. Feely. High-resolution estimates of net community production and air-sea CO_2 flux in the northeast Pacific. *Global Biogeochemical Cycles*, 26(4):doi:10.1029/2012GB004380, 2012.

[96] I. D. Lozovatsky, E. Roget, H. J. S. Fernando, M. Figueroa, and S. Shapovalov. Sheared turbulence in a weakly stratified upper ocean. *Deep-Sea Research I*, 53:387–407, 2006.

[97] J.M. Lyman and G.C. Johnson. Anomalous eddy heat and freshwater transport in the Gulf of Alaska. *Journal of Geophysical Research*, 120(2):1397–1408, 2015.

[98] A. Mahadevan, L.N. Thomas, and A. Tandon. Comment on "Eddy/Wind Interactions Stimulate Extraordinary Mid-Ocean Plankton Blooms". *Science*, 320:448, 2008.

[99] N. Mantua and S.R. Hare. The Pacific Decadal Oscillation. *Journal of Oceanography*, 58:35–44, 2002.

[100] P. Marchesiello, J.C. McWilliams, and A. Shchepetkin. Equilibrium Structure and Dynamics of the California Current System. *Journal of Physical Oceanography*, 33:753–783, 2003.

[101] A.P. Martin and K.J. Richards. Mechanisms for vertical nutrient transport within a North Atlantic mesoscale eddy. *Deep-Sea Research II*, 48:757–773, 2001.

[102] P.J. Martin. Simulation of the Mixed Layer at OWS November and Papa With Several Models. *Journal of Geophysical Research*, 90(C1):903–916, 1985.

[103] T.R. Martz, K.S. Johnson, and S.C. Riser. Ocean metabolism observed with oxygen sensors on profiling floats in the South Pacific. *Limnology and Oceanography*, 53(5):2094–2111, 2008.

[104] R.J. Matear. Circulation within the Ocean Storms Area Located in the Northeast Pacific Ocean Determined by Inverse Methods. *Journal of Physical Oceanography*, 23:648–658, 1995.

[105] C.R. McClain, K. Arrigo, K.-S. Tai, and D. Turk. Observations and simulations of physical and biological processes at ocean weather station P, 1951-1980. *Journal of Geophysical Research*, 101(C2):3697–3713, 1996.

[106] T.J. McDougall. The Relative Roles of Diapyncnal and Isopycnal Mixing on Subusurface Water Mass Conversion. *Journal of Physical Oceanography*, 14(10):1577–1589, 1984.

[107] D.J. McGillicuddy Jr., L.A. Anderson, N.R. Bates, T. Bibby, K.O. Buesseler, C.A. Carlson, C.S. Davis, C. Ewart, P.G. Falkowski, S.A. Goldthwait, D.A. Hansell, W.J. Jenkins, R. Johnson, V.K. Kosnyrev, J.R. Ledwell, Q.P. Li, D.A. Siegel, and D.K. Steinberg. Eddy/Wind Interactions Stimulate Extraordinary Mid-Ocean Plankton Blooms. *Science*, 316:1021, 2007.

[108] C.L. McNeil and E.A. D'Asaro. Parameterization of air-sea gas exchange at extreme wind speeds. *Journal of Marine Systems*, 66:110–121, 2007.

[109] J.C. McWilliams and E. Huckle. Ekman Layer Rectification. *Journal of Physical Oceanography*, 36:1646–1659, 2006.

[110] B.B. Nardelli. Vortex waves and vertical motion in a mesoscale cyclonic eddy. *Journal of Geophysical Research*, 118:doi:10.1002/jgrc.20345, 2013.

[111] D. Nicholson, S. Emerson, and C.C. Eriksen. Net community production in the deep euphotic zone of the subtropical North Pacific gyre from glider surveys. *Limnology and Oceanography*, 53(5):2226–2236, 2008.

[112] F.T.M. Nieuwstadt. The turbulent structure of the stable, nocturnal boundary layer. *Journal of Atmospheric Sciences*, 41:2202–2216, 1984.

[113] P.P. Niiler and J.D. Paduan. Wind-Driven Motions in the Northeast Pacific as Measured by Lagrangian Drifters. *Journal of Physical Oceanography*, 25:2819–2830, 1995.

[114] S.H. Nudds and J.A. Shore. Simulated eddy induced vertical velocities in a Gulf of Alaska model. *Deep-Sea Research I*, 58:1060–1068, 2011.

[115] D.J. Olbers, M. Wenzel, and J. Willebrand. The Inference of North Atlantic Circulation Patterns From Climatological Hydrographic Data. *Reviews of Geophysics*, 23(4):313–356, 1985.

[116] A. Oschlies and Kähler. Biotic contribution to air-sea fluxes of CO_2 and O_2 and its relation to new production, export production, and net community production. *Global Biogeochemical Cycles*, 18(GB1015):doi:10.1029/2003GB002094, 2004.

[117] M.J. Otte and J.C. Wyngaard. Stably stratified interfacial-layer turbulence from large-eddy simulation. *Journal of Atmospheric Sciences*, 58:3424–3442, 2001.

[118] J.D. Paduan and deSzoeke. Heat and Energy Balances in the Upper Ocean at 50°N, 140°W during November 1980 (STREX). *Journal of Physical Oceanography*, 16:25–38, 1986.

[119] J.D. Paduan and P.P. Niiler. Structure of Velocity and Temperature in the Northeast Pacific as Measured with Lagrangian Drifters in Fall 1987. *Journal of Physical Oceanography*, 23:585–600, 1993.

[120] C.A. Paulson and J.J. Simpson. Irradiance Measurements in the Upper Ocean. *Journal of Physical Oceanography*, 7:952–956, 1977.

[121] M. A. Peña and D.E. Varela. Seasonal and interannual variability in phytoplankton and nutrient dynamics along Line P in the NE subarctic Pacific. *Progress in Oceanography*, 75:200–222, 2007.

[122] H.J. Pearson, J.S. Puttock, and J.C.R. Hunt. A statistical model of fluid-element motions and vertical diffusion in a homogeneous stratified turbulent flow. *Journal of Fluid Mechanics*, 129:219–249, 1983.

[123] N.A. Pelland, C.C. Eriksen, and C.M. Lee. Subthermocline Eddies over the Washington Continental Slope as Observed by Seagliders, 2003-09. *Journal of Physical Oceanography*, 43:2025–2053, 2013.

[124] N.A. Pelland, J.T. Sterling, M.-A. Lea, N.A. Bond, R.R. Ream, C.M. Lee, and C.C. Eriksen. Fortuitous Encounters between Seagliders and Adult Female Northern Fur Seals (Callorhinus ursinus) off the Washington (USA) Coast: Upper Ocean Variability and Links to Top Predator Behavior. *PLoS ONE*, 9(8):e101268, 2014.

[125] M.J. Perry, B.S. Sackmann, C.C. Eriksen, and C.M. Lee. Seaglider observations of blooms and subsurface chlorophyll maxima off the Washington coast. *Limnology and Oceanography*, 53(5):2169–2179, 2008.

[126] S.G.H. Philander. El Niño Southern Oscillation phenomena. *Nature*, 302(24):295–301, 1983.

[127] B. Qiu and R.X. Huang. Ventilation of the North Atlantic and North Pacific: Subduction Versus Obduction. *Journal of Physical Oceanography*, 25(2374–2390), 1995.

[128] D.J. Raymond, S.K. Esbensen, C. Paulson, M. Gregg, C.S. Bretherton, W.A. Petersen, and R. Cifelli. EPIC2001 and the Coupled Ocean-Atmosphere System of the Tropical East Pacific. *Bulletin of the American Meteorological Society*, 85:1341–1354, 2004.

[129] L. Ren and S.C. Riser. Seasonal salt budget in the northeast Pacific Ocean. *Journal of Geophysical Research*, 114(C12004):doi:10.1029/2009JC005307, 2009.

[130] P.B. Rhines. Vorticity Dynamics of the Oceanic General Circulation. *Annual Reviews of Fluid Mechanics*, 18:433–497, 1986.

[131] M.-H. Rio, S. Mulet, E. Greiner, N. Picot, and A. Pascual. New global Mean Dynamic Topography from a GOCE geoid model, altimeter measurements and oceanographic in-situ data. OSTST 2013 Meeting, Boulder CO. Available: `http://www.aviso.altimetry.fr/fileadmin/documents/OSTST/2013/oral/mulet_MDT_CNES_CLS13.pdf`, 2013.

[132] A.R. Robinson and J.C. McWilliams. The Baroclinic Instability of the Open Ocean. *Journal of Physical Oceanography*, 4(3):281–294, 1974.

[133] G.I. Roden. Subarctic-Subtropical Transition Zone of the North Pacific: Large-Scale Aspects and Mesoscale Structure. In *Biology, Oceanography, and Fisheries of the North Pacific Transition Zone and Subarctic Frontal Zone*. NOAA Technical Report NMFS 105, Available: http://spo.nwr.noaa.gov/tr105.pdf, 1991.

[134] S. Rousseau, E. Kunze, R. Dewey, K. Bartlett, and J. Dower. On Turbulence Production by Swimming Marine Organisms in the Open Ocean and Coastal Waters. *Journal of Physical Oceanography*, 40:2107–2121, 2010.

[135] D.L. Rudnick. Observations of momentum transfer in the upper ocean: Did Ekman get it right? In P. Müller and D. Henderson, editors, *Near-Boundary Processes and Their Parameterization, Proceedings of the 13th 'Aha Huliko'a Hawaiian Winter Workshop*, pages 163–170, 2003.

[136] J.J. Schanze, R.W. Schmitt, and L.L. Yu. The global oceanic freshwater cycle: A state-of-the-art quantification. *Journal of Marine Research*, 68:569–595, 2010.

[137] Y.L. Serra, P. A'Hearn, H.P. Freitag, and M.J. McPhaden. ATLAS Self-Siphoning Rain Gauge Error Estimates. *Journal of Atmospheric and Oceanic Technology*, 18:1989–2002, 2001.

[138] J. Shao. Linear Model Selection by Cross-Validation. *Journal of the American Statistical Association*, 88(422):486–494, 1993.

[139] A.Y. Shcherbina, M.C. Gregg, M.H. Alford, and R.R. Harcourt. Characterizing Thermohaline Intrusions in the North Pacific Subtropical Frontal Zone. *Journal of Physical Oceanography*, 39:2735–2756, 2009.

[140] E.D. Skyllingstad, W.D. Smyth, and G.B. Crawford. Resonant Wind-Driven Mixing in the Ocean Boundary Layer. *Journal of Physical Oceanography*, 30:1866–1890, 2000.

[141] R.E. Sonnerup, S. Mecking, and J.L. Bullister. Transit time distributions and oxygen utilization rates in the Northeast Pacific Ocean from chlorofluorocarbons and sulfur hexafluoride. *Deep-Sea Research I*, 72:61–71, 2013.

[142] SSALTO/DUACS. User Handbook: (M)SLA and (M)ADT Near-Real Time and Delayed Time Products. Available: `http://www.aviso.altimetry.fr/fileadmin/documents/data/tools/hdbk_duacs.pdf`, 2015.

[143] R.H.R. Stanley, W.J. Jenkins, E.L. III Dempsey, and S.C. Doney. Noble gas constraints on air-sea gas exchange and bubble fluxes. *Journal of Geophysical Research*, 114(C11020), 2009.

[144] N. Steiner, S. Vagle, K. Kenman, and C. McNeil. Oxygen and nitrogen cycling in the northeast Pacific – Simulations and observations at Station Papa in 2003/2004. *Journal of Marine Research*, 65:441–469, 2007.

[145] H. Stommel. Determination of water mass properties of water pumped down from the Ekman layer to the geostrophic flow below. *Proceedings of the National Academy of Sciences*, 76(7):3051–3055, 1979.

[146] O. M. Sun, S. R. Jayne, K. L. Polzin, B. A. Rahter, and L. C. St. Laurent. Scaling Turbulent Dissipation in the Transition Layer. *Journal of Physical Oceanography*, 43:2475–2489, 2013.

[147] S. Tabata. Variability of oceanic conditions at Station "P" in the Northeast Pacific Ocean. *Transactions of the Royal Society of Canada*, 4:367–478, 1965.

[148] B. Taguchi, N. Schneider, and M. Nonaka. Decadal variability of upper ocean heat content in the western boundary currents regions. Abstract, International Union of Geodesy and Geophysics General Assembly, 2015.

[149] P.K. Taylor, E. Dunlap, F.W. Dobson, R.J. Anderson, and V.R. Swail. On the accuracy of wind and wave measurements from buoys. Technical Report 21-2002, Data Buoy Cooperation Panel, Available: `ftp://ftp.wmo.int/Documents/PublicWeb/amp/mmop/documents/dbcp/DBCP21-Perth-2001/DOCS_DBCP21/27-Taylor.doc`, 2002.

[150] P.K. Taylor and M.J. Yelland. On the Accuracy of Ocean Winds and Wind Stress– An Emperical Assesment. In *Wind Over Waves: Forecasting and Fundamentals of Applications*, volume 34. 2003.

[151] V. Thierry, D. Gilbert, T. Kobayashi, and C. Schmid. Processing Argo OXYGEN data at the DAC level, Version 1.3. Technical report, International Argo Program. Available: `http://www.argodatamgt.org/content/download/16300/106561/file/argo_oxygen_proposition_v1p3.pdf`, 2013.

[152] F. Thomas, V. Garcon, and J.-F. Minster. Modelling the seasonal cycle of dissolved oxygen in the upper ocean at Ocean Weather Station P. *Deep-Sea Research*, 37(3):463–491, 1990.

[153] J. Thomson, E.A. D'Asaro, M.F. Cronin, W.E. Rogers, R.R. Harcourt, and A.Y. Shcherbina. Waves and the equilibrium range at Ocean Weather Station P. *Journal of Geophysical Research*, 118:5951–5962, 2013.

[154] R.E. Thomson. On the Alaskan Stream. *Journal of Physical Oceanography*, 2:363–371, 1972.

[155] R.E. Thomson and I.V. Fine. A Diagnostic Model for Mixed Layer Depth Estimation with Application to Ocean Station P in the Northeast Pacific. *Journal of Physical Oceanography*, 39:1399–1415, 2009.

[156] R.E. Thomson and J.F.R. Gower. A basin-scale oceanic instability event in the Gulf of Alaska. *Journal of Geophysical Research*, 103(C2):3033–3040, 1998.

[157] R.E. Thomson and M.V. Krassovski. Poleward reach of the California Undercurrent extension. *Journal of Geophysical Research*, 115:doi:10.1029/2010JC006280, 2010.

[158] R.E. Thomson, P.H. LeBlond, and W.J. Emery. Analysis of Deep-Drogued Satellite-tracked Drifter Measurements in the Northeast Pacific. *Atmosphere-Ocean*, 28(4):409–443, 1990.

[159] D.A. Timothy, C.S. Wong, J.E. Barwell-Clarke, J.S. Page, L.A. White, and R.W. Macdonald. Climatology of sediment flux and composition in the subarctic North Pacific Ocean with biogeochemical implications. *Progress in Oceanography*, 116:95–129, 2013.

[160] A.J. Torruella. *The Fall Upper Ocean Heat Balance in the Northeast Pacific*. PhD thesis, Scripps Institute of Oceanography, University of California-San Diego, 1995.

[161] J.P. Tully, A.J. Dodimead, and S. Tabata. An Anomalous Increase of Temperature in the Ocean off the Pacific Coast of Canada through 1957 and 1958. *Journal of the Fisheries Research Board of Canada*, 17(1):61–80, 1960.

[162] J.S. Turner and E.B. Kraus. A one-dimensional model of the seasonal thermocline. *Tellus*, 19(1):88–97, 1967.

[163] E. Tziperman and A. Hecht. Circulation in the Eastern Levantine Basin Determined by Inverse Methods. *Journal of Physical Oceanography*, 18:506–518, 1988.

[164] H. Uchida, T. Kawano, K. Ikuo, and F. Masao. In Situ Calibration of Optode-Based Oxygen Sensors. *Journal of Atmospheric and Oceanic Technology*, 25:2271–2281, 2008.

[165] S. Vagle, C. McNeil, and N. Steiner. Upper ocean bubble measurements from the NE Pacific and estimates of their role in air-sea gas transfer of the weakly soluble gases nitrogen and oxygen. *Journal of Geophysical Research*, 115:C12054, doi:10.1029/2009JC005990, 2010.

[166] P. van Meurs and P.P. Niiler. Temporal Variability of the Large-Scale Geostrophic Surface Velocity in the Northeast Pacific. *Journal of Physical Oceanography*, 27:2288–2297, 1997.

[167] D.E. Varela and P.J. Harrison. Seasonal variability in nitrogenous nutrition of phytoplankton assemblages in the northeastern subarctic Pacific Ocean. *Deep-Sea Research II*, 46(11-12):2505–2538, 1999.

[168] B.A. Warren. Why is no deep water formed in the North Pacific? *Journal of Marine Research*, 41:327–347, 1983.

[169] C. Welch. Bizarre sea-life visitors arrive with North Pacific's historic warmth. *Seattle Times*, page 1 November 2014, 2014.

[170] C.B. Whalen, L.D. Talley, and J.A. MacKinnon. Spatial and temporal variability of global ocean mixing inferred from Argo profiles. *Geophysical Research Letters*, 39:L18612, 2012.

[171] F.A. Whitney. Anomalous winter winds decreases 2014 transition zone productivity in the NE Pacific. *Geophysical Research Letters*, 42:428–431, doi:10.1002/2014GL062634, 2015.

[172] F.A. Whitney, W.R. Crawford, and P.J. Harrison. Physical processes that enhance nutrient transport and primary productivity in the coastal and open ocean of the subarctic NE Pacific. *Deep-Sea Research II*, 52:681–706, 2005.

[173] F.A. Whitney and H.J. Freeland. Variability in upper-ocean water properties in the NE Pacific Ocean. *Deep-Sea Research II*, 46:2351–2370, 1999.

[174] F.A. Whitney, H.J. Freeland, and M. Robert. Persistently declining oxygen levels in the interior waters of the eastern subarctic Pacific. *Progress in Oceanography*, 75:179–199, 2007.

[175] H. W. Wijesekera, D.L. Rudnick, C.A. Paulson, S. D. Pierce, W. S. Pegau, J. Mickett, and M. C. Gregg. Upper ocean heat and freshwater budgets in the eastern Pacific warm pool. *Journal of Geophysical Research*, 110:1–27, 2005.

[176] R.G. Williams, J.C. Marshall, and M.A. Spall. Does Stommel's Mixed Layer "Demon" Work? *Journal of Physical Oceanography*, 25:3089–3102, 1995.

[177] G.E. Willis and J.W. Deardorff. A Laboratory Model of the Unstable Planetary Boundary Layer. *Journal of the Atmospheric Sciences*, 31:1297–1307, 1974.

[178] C.S. Wong, N.A.D. Waser, Y. Nojiri, F.A. Whitney, J.S. Page, and J. Zeng. Seasonal cycles of nutrients and dissolved inorganic carbon at high and mid latitudes in the North Pacific Ocean during the *Skaugran* cruises: determination of new production and nutrient uptake ratios. *Deep-Sea Research II*, 49:5317–5338, 2002.

[179] D.K. Woolf and S.A. Thorpe. Bubbles and the air-sea exchange of gases in near-saturation conditions. *Journal of Marine Research*, 49:435–466, 1991.

[180] C. Wunsch. *The ocean circulation inverse problem*. Cambridge University Press, 1996.

[181] J.C. Wyngaard and R.A. Brost. Top-Down and Bottom-Up Diffusion of a Scalar in the Convective Boundary Layer. *Journal of the Atmospheric Sciences*, 41(1):102–112, 1984.

[182] L. Yu and R.A. Weller. Objectively Analyzed Air-Sea Heat Fluxes for the Global Ice-Free Oceans (1981-2005). *Bulletin of the American Meteorological Society*, 88(4):527–539, 2007.

[183] X. Yuan and L.D. Talley. The subarctic frontal zone in the North Pacific: Characteristics of frontal structure from climatological data and synoptic surveys. *Journal of Geophysical Research*, 101(C7):16491–16508, 1996.

[184] Y. Zhang, W.B. Rossow, A.A. Lacis, V. Oinas, and M.I. Mishchenko. Calculation of radiative fluxes from the surface to top of atmosphere based on ISCCP and other global data sets: Refinements of the radiative transfer model and the input data. *Journal of Geophysical Research*, 109(D19105):doi:10.1029/2003JD004457, 2004.

Appendix A

POSTCALIBRATION OF SEAGLIDER CONDUCTIVITY SENSORS

Seaglider measurements of temperature are computed from thermistor frequency samples after subtracting the thermistor frequency offset and applying the manufacturer's polynomial with coefficients determined by factory calibration prior to each deployment. Seawater salinity is then determined from Seaglider temperature and conductivity samples using the UNESCO 1983 polynomial. For each Seaglider deployment, the accuracy of the factory-calibrated thermistor and conductivity sensors was assessed by comparing estimated temperature and salinity characteristics to those obtained from ship-based casts performed by the CCGS *John P. Tully* and R/V *Thomas G. Thompson* in the permanent thermocline, where T-S is stable and vertical temperature gradients are weak, hence the effect of thermal inertia of the conductivity cell and CT duct on estimated S is small.

Figure A.1a shows the deep T-S characterstics for Seaglider and ship-based profiles obtained during the first Seaglider deployment, 8 June-30 August 2008. The Seaglider profiles are uniformly saltier on constant temperature surfaces in comparison to those from the CCGS *Tully* and R/V *Thompson*. This offset is much larger than the estimated scatter in deep T-S during this period, which indicates that it is significant in comparison to any aliasing or apparent bias that may be due to the small number of CCGS *Tully* and R/V *Thompson* casts. If this offset is due to biases in conductivity samples alone, removal of a conductivity bias of 0.00208 S m^{-1} results in much better agreement between Seaglider and ship-based profiles (Fig. A.1b). The resulting profiles have a mean offset of -0.0010 in salinity between the temperatures 2.8-3.5°C.

It is not clear from the deep T-S characteristics alone that the bias should solely be at-

tributed to conductivity measurements; in fact, removal of a temperature bias has an effect on the Seaglider T-S cloud that is nearly collinear to that of the conductivity bias, since the salinity of a given sample is estimated from both temperature and conductivity. However, if the observed offset in deep T-S were corrected through removal or application of a temperature bias, it was found that the agreement between Seaglider and ship-based casts would worsen in the halocline region, when comparing casts collected over the first and last three days of the deployment (Fig. A.2). Thus, the available evidence supports only a conductivity bias in Seaglider measurements for this deployment. Applying a similar procedure to the second (August 2008-June 2009) and third (June 2009-January 2010) Seaglider deployments yielded conductivity biases of -0.0019 S m^{-1} and 0.0038 S m^{-1}, respectively. The mean offset in deep S along T surfaces after these conductivity corrections was 0.0007 for the second deployment and -0.0029 for the third. These offsets are on the order of 1% of the mean salinity changes observed in the top 120 m or in the permanent pycnocline over the 20 months of the Seaglider time series (*see* Chapter 3). After removal of conductivity biases and correction for the effects of thermal inertia, Seaglider salinity samples are estimated to be accurate to within 0.01, or 0.03 in regions of strong temperature gradient. The thermal inertia correction fails to completely remove the effects of thermal lag in the strongest vertical gradient regions in some profiles, and these are corrected by an interpolation procedure as described in the following Appendix.

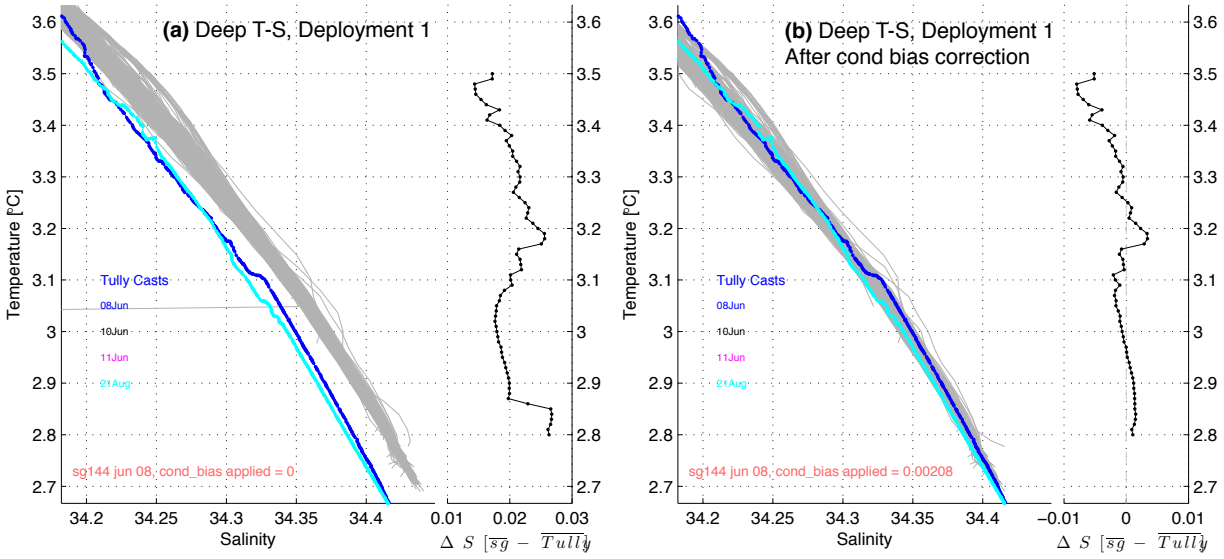

Figure A.1: Illustration of deep *in situ* temperature-salinity characteristics during Seaglider deployment 1 (8 June-30 August 2008) in comparison with those obtained from deep casts performed by the CCGS *John P. Tully* (June) and R/V *Thomas G. Thompson* (August). In panel (a), Seaglider profiles (gray curves) have not been corrected for any bias in temperature or conductivity samples; the ship-based profiles (blue and cyan curves) are fresher by ∼0.02 along surfaces of constant temperature (right axis in panel a). After correcting for a conductivity bias of 0.00208 S m^{-1} (b), Seaglider salinities have a bias of -0.0010±0.0026 (mean± standard deviation) on temperature surfaces compared to the CCGS *Tully* or R/V *Thompson* casts.

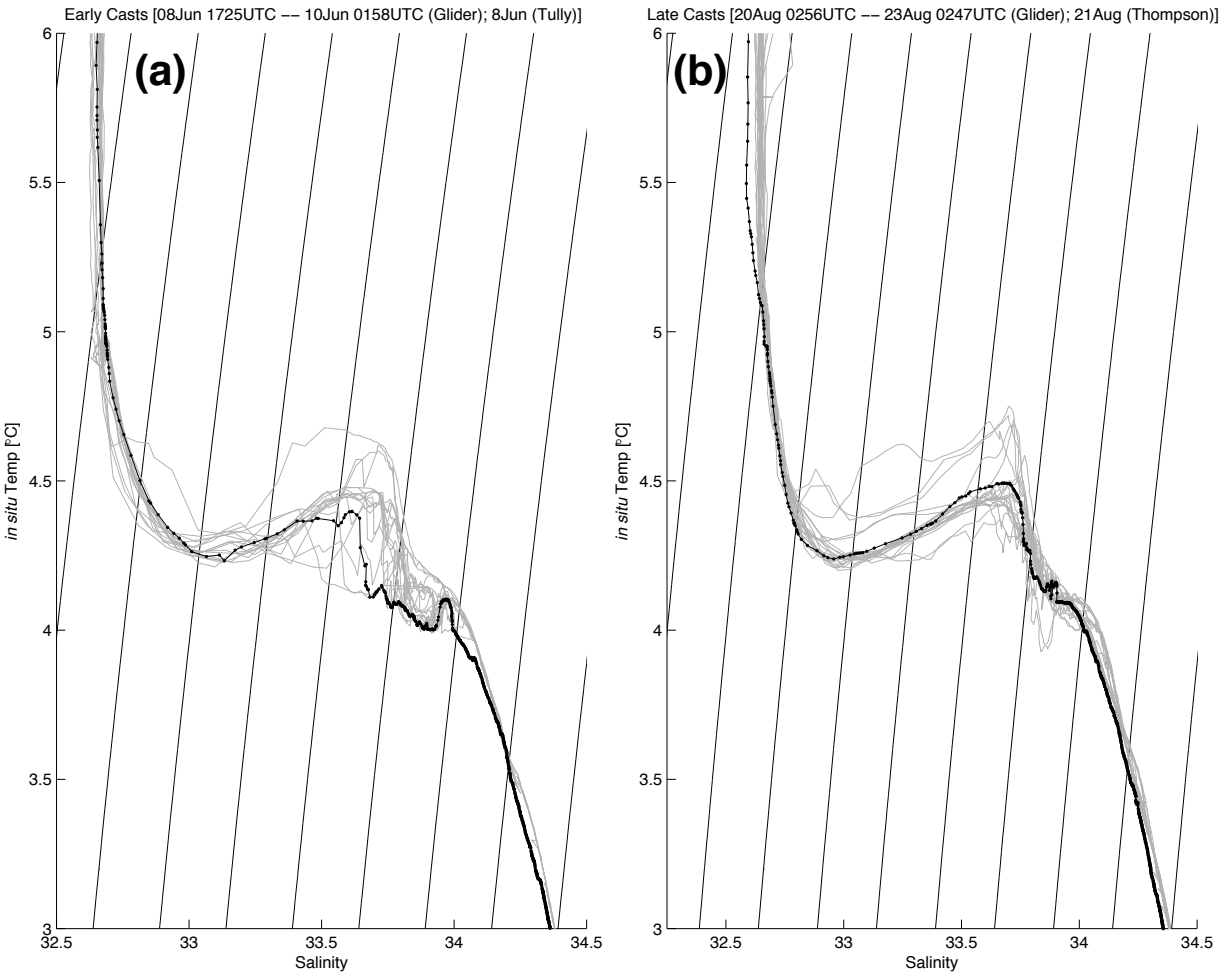

Figure A.2: Temperature-salinity characteristics of Seaglider (gray curves) and shipboard Conductivity-Temperature-Depth profiles (black curves) collected at the beginning (a) and end (b) of Seaglider (SG) 144's deployment at Ocean Station Papa, 8 June-30 August 2008. Each plot is centered on the halocline region, where vertical temperature gradients are weak. Seaglider profiles have not been corrected for any conductivity or temperature biases. Density contours (σ_t, black) are shown at 0.2 kg m^{-3} intervals.

Appendix B

INTERPOLATION OF SALINITY IN SEAGLIDER PROFILES

Seaglider estimates of salinity are computed using discrete, simultaneous samples of conductivity and thermistor temperature as the vehicle steadily profiles on ascent or descent. The thermistor temperature must be adjusted to account for the thermal lag of the conductivity sensor relative to the thermistor, which is modulated by the boundary layer within and around the conductivity cell duct, and is thus a function of vehicle speed and pitch. A form of this correction based on analytical solutions for flow surrounding the conductivity cell duct, developed by Eriksen (personal communication), was applied to Seaglider data at OSP and the results were bin-averaged in depth as described in Section 4.2.

Inspection of the T-S properties of the bin-averaged data revealed suspicious low- and high-salinity anomalies within the OSP seasonal thermocline, concentrated near the base of the well-mixed layer where vertical temperature gradients are typically the strongest throughout the entire water column in the subarctic North Pacific (gray lines in Fig. B.1a). These anomalies were suspicious because shipboard CTD casts performed by the CCGS *Tully* and R/V *Thompson* at OSP reveal a nearly linear T-S relation between the mixed layer endmember and the top of the permanent pycnocline/halocline at $\sigma_t = 25.8$ (black lines in Fig. B.1a). The interpretation of a linear T-S relationship in this zone is also supported by a number of previous investigations of the upper-ocean at OSP [*e.g.*, 147, 31, 118].

A late-summer profile from SG144 provides an example of the manifestation of such an anomaly in an individual profile (Fig. B.2). Contrary to typical ship-based CTD profiles at OSP, the minimum salinity is observed in this profile is near the base of the surface mixed layer. The corresponding T-S plot shows a weak sinuosity in the seasonal thermocline that is not apparent in profiles from the CCGS *Tully* and R/V *Thompson* (*c.f.* Figs. B.2c and B.1).

The maximum salinity anomaly occurs ∼5 m shallower than the maximum temperature gradient, consistent with a thermal lag during the vehicle ascent.

Examination of all profiles in the Seaglider OSP dataset revealed that such anomalies were prevalent during the summer months, when temperature gradients at the base of the surface mixed layer were strongest. However, the presence or absence of the anomalies could not be completely predicted by a simple threshold in temperature gradient strength or vehicle rate of ascent or descent. Given the unpredictable nature of the anomaly strength and character, and the resulting possible biases in computing mean salinity profiles or horizontal salinity gradients in the transition layer, it was elected to assume that water in the seasonal thermocline is a linear admixture between that in the surface mixed layer and that at the top of the halocline and interpolate S as a function of T within this region. This interpolation was performed following bin-averaging for all Seaglider profiles collected between June 2008-January 2009, and June 2009-January 2010. Outside of these months, temperature gradients at the base of the mixed layer were weak enough that salinity anomalies were rarely present.

Two separate vertical bins are needed to define S as a function of T in the transition layer in each profile. The shallower of these two bins (the "shallow anchor") is taken to be 15 m shallower than the isothermal layer depth (ILD), where the ILD is defined as the depth at which temperature decreases by 0.2°C from the value at 10 m. If the ILD is thinner than 25 m, the shallow anchor T/S is taken to be an average of these quantities within a portion of the ILD – on ascent, this average is taken in the top 8 m, while on descent, the average is the bottom 8 m. These vertical zones of averaging reflect the trusted regions within the Seaglider profile on each phase of the vehicle cycle; while ascending, the T/S samples within the upper mixed layer are the most trusted, since these samples are collected after the conductivity sensor has had time to equilibrate with the mixed layer temperature, while the opposite is true on descent.

The deeper of the two bins ("deep anchor") is taken to be the deeper of two points: either the ILD+4 m, or the first bin in which temperature is below a set temperature threshold, defined as 6° (June 2008-December 2008), 7°C (January 2009), or 5.75°C (June 2009-January

2010). These thresholds were chosen based on a compromise between a consistently stable deep anchor that had no salinity anomaly, and on the other hand avoiding unnecessarily interpolating over points without remnant thermal inertia error. Interpolation is performed only for profiles in which the ILD is less than 110 m and the difference in depth between the shallow and deep anchor bins is less than 100 m. These conditions were imposed to avoid interpolating into the halocline, where T-S is not linear.

Results of this interpolation procedure for the example profile from SG144 are shown in Figure B.2a, c. Following the application of the interpolation procedure to the bin-averaged OSP dataset, the bulk T-S properties in the seasonal thermocline are in much better agreement with those indicated by the shipboard CTD casts (Fig. B.1b). This procedure trades the error associated with uncorrected conductivity sensor thermal lag for error associated with the assumption of linearity in T-S in the seasonal thermocline. When this procedure was performed on the available shipboard CTD casts, 12 of 14 of the casts taken to a depth sufficient to reach a deep anchor point had maximum error induced by interpolation of less than 0.03. The error exceeded this amount in two casts in August 2009; the maximum error was 0.0842 for a cast from the CCGS *Tully* on 28 August 2009. The maximum amount by which Seaglider salinity was altered exceeded this amount in 99.3% of the casts in which interpolation was performed. This suggests that the error associated with remnant thermal inertia error is almost always greater than the error induced by assuming a perfectly linear T-S relationship in the seasonal thermocline.

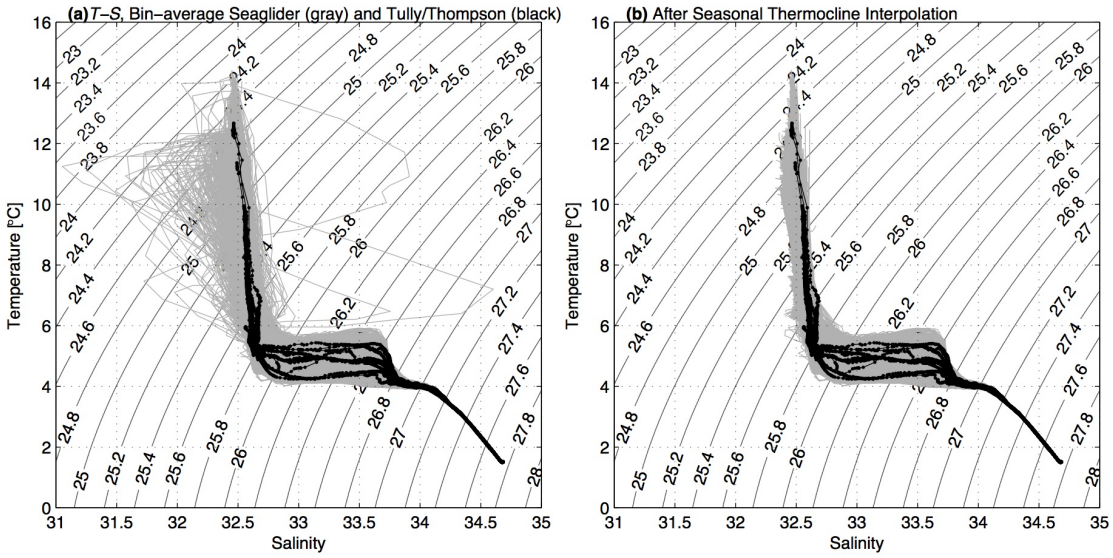

Figure B.1: Plot of temperature T versus salinity S from 16 Conductivity-Temperature-Depth profiles collected at Ocean Station Papa (OSP) from the R/V *Thomas G. Thompson* and CCGS *John P. Tully* (black) and all bin-averaged Seaglider profiles (gray curves) collected during the OSP surveys. Panel (a) shows bin-averaged profiles after correction for thermal inertia effects applied to Seaglider conductivity samples, but before salinity interpolation in the seasonal thermocline. Panel (b) shows bin-averaged profiles following salinity interpolation.

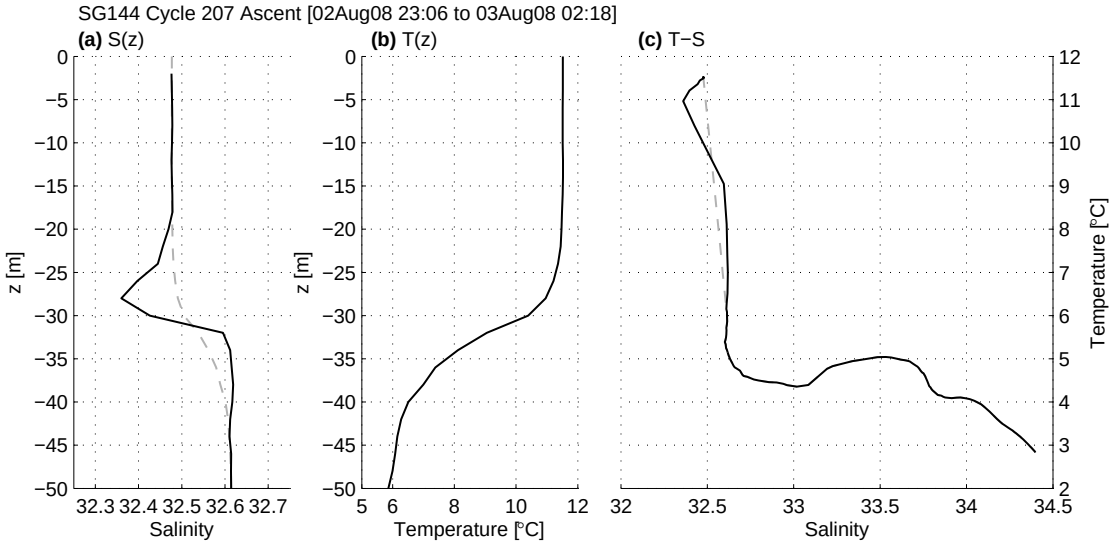

Figure B.2: Example salinity interpolation in seasonal thermocline, Seaglider (SG) 144 cycle 207, ascent profile. Panel (a) shows bin-averaged salinity S versus depth, panel (b) shows temperature T versus depth, and panel (c) shows T versus S. In panels (a) and (c), the black curve indicates profile of S obtained after correction for conductivity cell thermal inertia and bin-averaging. This profile has suspect salinity characteristics near the base of the well-mixed surface layer: abnormally fresh salinities near the mixed layer base (a) and nonlinear T-S within the seasonal thermocline (c). Note the strong vertical temperature gradient near this region in panel (b) (maximum of 0.57 °C m^{-1} at $z = -32$ m). The gray dashed curve in (a) and (c) indicates the profile obtained if S is linearly interpolated as a function of T between the mixed layer and the 6°C isotherm.

Appendix C

LINEAR REGRESSION MODEL SELECTION

Linear regression is used to estimate the horizontal gradients of all scalar variables in each depth bin and time interval during the Seaglider time series. The choice of predictors in the regression model to be used is motivated by a compromise between the ability of the model to adequately explain the variance in the scalar record while not "overfitting" the data. Overfitting may be defined as the inclusion of unnecessary predictors that do not add significant information, and whose coefficients are highly sensitive to errors in the data or inclusion of certain data points.

The statistical technique of *cross-validation* was used to evaluate the degree of compromise between variance explained and overfitting in each of several forms of linear model considered for performing regression fits to each scalar variable. Cross-validation involves evaluating the ability of a linear model to predict the observed value at points that are not used in the construction the estimates of linear regression model coefficients. That is, for one model configuration, given a set of n observations of a scalar variable, a subset n_c of these observations could be used to construct an estimate of the model coefficients. These coefficients are then used to predict the value of the observed variable at the remaining $n_v = n - n_c$ observation points. A model that achieves a compromise between explaining the variance in the observed variable without overfitting should minimize the square error over the n_v omitted observations.

One method of cross-validation useful for linear model selection developed is the Predicted Residual Sum of Squares [PRESS; 4], which takes $n_c = n-1$, and repeats the above procedure

for each of the n data points. Thus the PRESS score for a given model is

$$\text{PRESS} = \sum_{i=1}^{n} (Y_i - \hat{Y}_i)^2, \tag{C.1}$$

where Y_i is the observed variable at point i, and $\hat{Y}_i$ is the estimate of that variable given by a regression fit obtained from the dataset omitting point i. This study uses a modification of this technique as proposed by Shao [138], known as Monte Carlo Cross-Validation (MCCV), which was developed to address the asymptotic inconsistency present in the $n_v = 1$ method that led to overly conservative PRESS scores and consistent selection of overly complex linear model forms. Shao [138] suggests performing $b = 2n$ iterations, in each of which a subset of $n_c \approx n^{3/4}$ points are drawn randomly with replacement from the n original data points and the PRESS score evaluated using the fit constructed from these points. The best model configuration is the one that minimizes the mean PRESS score over b iterations.

Several model forms were considered for the linear regression performed in this study. The simplest includes linear terms in x', y', and t', where prime variables indicate anomalies from the center of the survey pattern or mid-point of each monthly interval as described in Section 2.2.3. For θ, this model has the form

$$\hat{\theta} = A + Bx' + Cy' + Dt', \tag{C.2}$$

while the most complex includes all the terms present in a second-order Taylor expansion about the center of the track pattern and mid-point of each month,

$$\hat{\theta} = A + \underbrace{Bx' + Cy' + Dt'}_{\text{linear}} + \underbrace{Ex'y' + Fx't' + Fy't'}_{\text{interaction}} + \underbrace{Hx'^2 + Iy'^2 + Jt'^2}_{\text{quadratic}}. \tag{C.3}$$

It was not considered reasonable for the Seaglider array configuration to resolve greater than second-order spatial terms, thus higher-order regression models were not considered. Four model forms intermediate to the two above were also considered: 1) all linear and interaction

terms, 2) all linear and quadratic terms, 3) all linear terms and a t quadratic only, and 4) all linear terms along with only those interaction and quadratic terms that involve t. For illustrative purposes, two models of reduced complexity in comparison to (C.2) were also evaluated, one including only x and y terms, and the other including only t.

In the dataset described here, it could be possible to use the above procedure to pick the model configuration appropriate for each variable, vertical depth bin, and time interval. However, for consistency and simplicity, it is desirable to use only a single linear regression model, outside of the upper ocean in the time period June 2009-January 2010 when the mooring was present as discussed in Section 4.2. To guide model selection, the PRESS score for each model was averaged across the monthly time intervals for each depth and variable (θ, S, σ_θ). Figure C.1a shows the results of this procedure for potential temperature; in this Figure, the time-mean depth profile of model PRESS scores are normalized by those of the model (C.2). In general, by this metric the lower-order models have the best predictive performance deeper than the permanent pycnocline, while the higher-order models are more successful near the surface. The model incorporating only linear terms (C.2) has the lowest mean score deeper than 500 m; the model incorporating only spatial terms ($\hat{\theta} \sim x', y'$) performed virtually as well in this depth range. Shallower than this depth, the model with only linear terms is consistently outperformed by the linear+quadratic beween 200-500 m depth, and by several higher-order configurations shallower than 150 m depth. The relative performance of the various models, including the space-only and time-only forms considered for illustrative purposes, provide an indication of the spatial versus temporal contribution to the total variance of θ at each depth. While the space-only model performed well at depths greater than 200 m, its mean PRESS score profile was much greater than all other models shallower than 100 m, indicating it had little predictive skill there. Inversely, the time-only model scored nearly as well as all others in the upper 100 m, but had little predictive skill deeper than this. Consistent with the plots of θ' as a function of depth and time in Figure 3.13, these results indicate that during the Seaglider time series the variance of θ was dominated by temporal variability shallower than 100 m, and by spatial variability in

the permanent pycnocline and deeper. In each time interval and depth bin, the models are ranked 1 to 8 according to their mean PRESS score over b resampling iterations, with lower ranks indicating lower score and better predictive ability. The depth profile of the time-mean of this rank is shown for θ in Figure C.1b. For θ, the model (C.2) and the $\hat{\theta} \sim x', y'$ model had the lowest mean rank deeper than 500 m. Shallower than 100 m, the model $\hat{\theta} \sim x', y', t', t'^2$ had the lowest mean rank.

Mean profiles of PRESS score for regression models of S and σ_θ showed largely similar results (Fig. C.2). In general, by both the time-mean PRESS score and rank, the full second-order model form (C.3) is clearly an overfit to the data, as expected. The simplest choice of predictors (C.2) has the best predictive ability for omitted points at depth, but is outperformed by higher-order models near the surface boundary layer. For the choice of a single model, this study uses the form $(\hat{\theta}, \hat{S}, \hat{\sigma_\theta}, \hat{\rho}) \sim x', y', t', t'^2$ for its compromise between performance in the surface boundary layer and at depth. For θ, this model had the second-lowest mean PRESS score and rank next to the simplest model (C.2) deeper than 500 m, and had among the best performance by mean score and rank in the top 100 m as well.

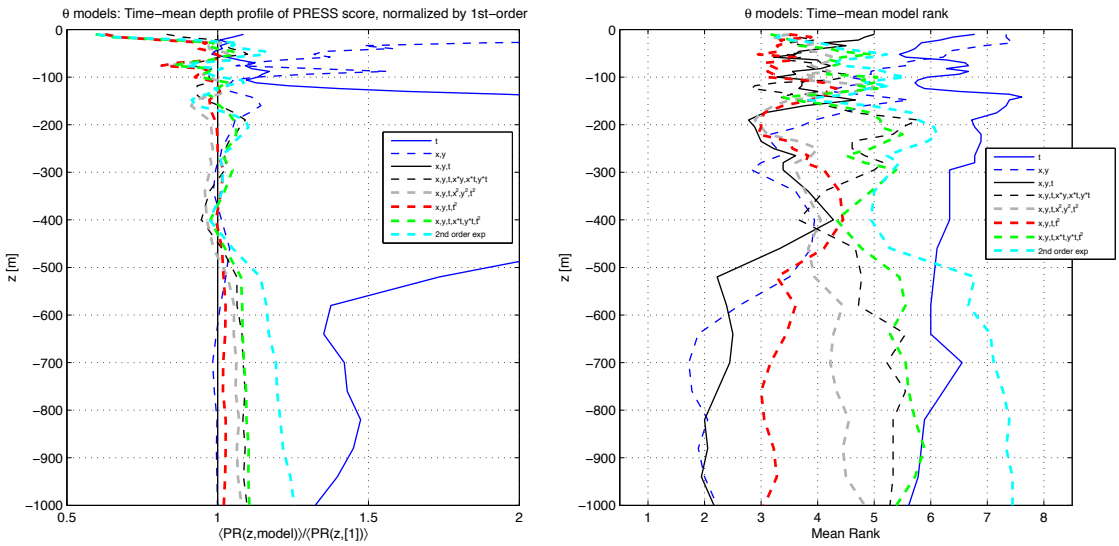

Figure C.1: Predicted Residual Sum of Squares (PRESS) score for various model configurations in regression modeling of potential temperature θ. Left panel shows the time-mean PRESS score for all model configurations considered, normalized by the model that includes only linear terms in x', y', and t' (C.2). The "2nd order exp" line indicates the model configuration (C.3) that includes all terms present in a 2nd-order Taylor expansion around the center of the survey pattern and mid-point of each monthly interval.

.

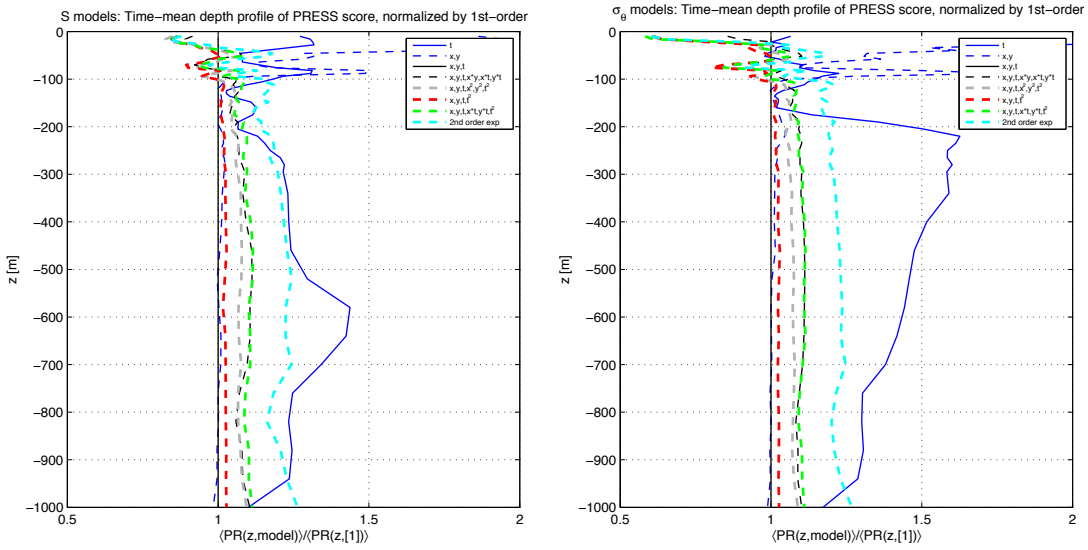

Figure C.2: Predicted Residual Sum of Squares (PRESS) score for various predictor configurations in linear regression modeling of salinity S (left panel) and potential density σ_θ (right panel). Each panel shows the time-mean PRESS score for all model configurations considered, normalized by the model that includes only linear terms in x', y', and t' (C.2). The "2nd order exp" line indicates the model configuration (C.3) that includes all terms present in a 2nd-order Taylor expansion around the center of the survey pattern and mid-point of each monthly interval.

.

Appendix D

POSTCALIBRATION OF OXYGEN OPTODE MEASUREMENTS

In addition to deploying and recovering the Seagliders and NOAA Ocean Climate Stations moorings used in this study, the CCGS *John P. Tully* and R/V *Thomas G. Thompson* performed multiple bottle and CTD casts at OSP during visits that overlapped with the Seaglider deployments: on 8-11 June 2008 (Tully), 30 August 2008 (Thompson), 14-16 June 2009 (Tully), and 27-28 August 2009 (Tully). Graduate students and technicians from the Hamme (Karina Giesbrecht, University of Victoria) and Emerson (Charles Stump and Seth Bushinsky, University of Washington) laboratories performed Winkler titrations from bottle samples and generously provided their results for the purposes of postcalibration of the optode sensors onboard the Seagliders. Table 4.1 describes the bottle casts used for comparison to Seaglider profiles during the array time series.

Obtaining accurate samples of dissolved oxygen in the surface mixed layer is important for calculating surface gas exchange. The diffusive component of surface gas exchange is proportional to surface saturation level of oxygen ($s = [O_2]/[O_2]_{sat}$) above 100%, where $[O_2]_{sat}$ is the concentration at saturation equilibrium at standard atmospheric temperature and pressure given as a function of seawater S and T by the polynomial of Garcia and Gordon [60] calibrated to the data of Benson and Krause [10]. The saturation level is also a useful metric by which to judge biases in optode output since it is proportional to the partial pressure of dissolved oxygen, which is the quantity that the optode instrument actually measures [33].

Optode and Winkler oxygen concentrations were converted to saturation s and samples were averaged within the SL on each glider and shipboard cast, where the SL base was in this

case defined as the depth at which density increases by 0.03 kg m^{-3} from the value at 10 m. Since Seaglider profiles were not immediately coincident with shipboard casts, to establish an initial offset in s between the optode and Winkler measurements, SL-average optode s measurements were interpolated to the shipboard sample times and latitude/longitudes using local regression curve fitting (commonly referred to as "LOESS"). Mixed layer-average optode s from the first 15 days of each Seaglider deployment were fit with a curve the form

$$\langle s\rangle_k = A + B(x_k - x_0) + C(y_k - y_0) + D(t_k - t_0) + E(t_k - t_0)^2 + \epsilon_k = X\vec{a} = \vec{s} + \vec{\epsilon}, \quad \text{(D.1)}$$

where $\vec{\hat{s}} = [\langle s\rangle_1 \langle s\rangle_2 \ldots \langle s\rangle_{n_k}]^{\mathrm{T}}$ is a vector of SL-average s from the n_k profiles during the first 15 days of the deployment and $\vec{a} = [A\,B\,C\,D\,E]^{\mathrm{T}}$ is the vector of regression coefficients. $(x - x_0)$, $(y - y_0)$ are zonal and meridional distances from OSP, and $(t - t_0)$ is the time since the mean time of the 15 d initial-deployment period. $\vec{\epsilon}$ is the vector of residuals from the least-squares fit, and X is a $n_k \times 5$ matrix of predictors, such that row k of X is $[1\,x'_k\,y'_k\,t'_k\,t'^2_k]$, $x'_k = (x - x_0)$, and the same notation is used for the other predictors. The regression model (D.1), also used to estimate horizontal gradients of all scalar variables during Seaglider surveys at OSP, was chosen based on its compromise between predictive ability at depth and in the surface boundary layer (Appendix C).

The best-fit coefficients for the regression are given by

$$\vec{a} = (X^{\mathrm{T}}X)^{-1}(X^{\mathrm{T}}\vec{s}). \quad \text{(D.2)}$$

These coefficients are then applied to the space and time coordinates of the shipboard casts, to estimate the s values that would have been measured had the glider performed a cast perfectly co-located with those from the ship:

$$\vec{\hat{s}} = X_{\mathrm{ship}}\vec{a}, \quad \text{(D.3)}$$

where X_{ship} is a matrix of predictors formed from the x', y', t' coordinates of the shipboard

casts. The vector of differences ($\Delta\vec{s}$) between shipboard SL-average s values ($\vec{s}_{\text{ship}}$) and those predicted by the LOESS regression is then

$$\Delta\vec{s} = \vec{s}_{\text{ship}} - \hat{\vec{s}}. \tag{D.4}$$

After evaluating this procedure for a given deployment, the mean of the vector $\Delta\vec{s}$ is taken to be the initial offset in saturation level for this optode. Figure D.1 shows the results of this procedure for SL-average optode saturation levels and *Tully* Winkler samples for the first Seaglider deployment in June 2008. This procedure determined initial offsets Δs_{init} that were universally low: 0.0271 for June 2008, 0.0295 for August 2008, and 0.0769 for June 2009.

For the first and third deployments, comparison casts were also available at the conclusion of the deployment (in August 2008 for deployment 1) or during the course of the deployment (August 2009 for deployment 3). The above procedure was repeated for these second set of calibration casts, after correcting the optode results by adding the initial offset Δs_{init}. This procedure revealed further residual low offsets between Winkler oxygen concentrations and optode measurements corrected for Δs^{init}. The mean of these residual offsets is denoted Δs_{resid}. Applying this procedure to deployments 1 and 3 gave Δs_{resid} of 0.0173 and 0.0097, respectively, again indicating both optodes reading low relative to Winkler measurements after correction for the initial offset.

It is assumed this residual offset is due to drift, and that this drift is linear in time between the beginning of the deployment and the second group of casts, for lack of better information regarding any functional form of time drift in optodes deployed on profiling Seagliders. D'Asaro and McNeil [33] find optode drift well-modeled by an exponential function in time for instruments experiencing varying combinations of deployment on profiling floats and storage time; for the multi-year scales of drift observed by [33], drift within an individual deployment could be considered approximately linear. The postcalibrated optode

supersaturations s_{cor} are then given by

$$s_{\mathrm{cor}}(t_d \leq t \leq t_{\mathrm{resid}}) = s_{\mathrm{uncor}} + \Delta s_{\mathrm{init}} + \frac{(t - t_d) \times \Delta s_{\mathrm{resid}}}{t_{\mathrm{resid}} - t_d}; \tag{D.5}$$

$$s_{\mathrm{cor}}(t_{\mathrm{resid}} < t) = s_{\mathrm{uncor}} + \Delta s_{\mathrm{init}} + \Delta s_{\mathrm{resid}}, \tag{D.6}$$

where t_d is the time at which the optode is deployed, t_{resid} is the time of the second set of comparison casts, and s_{uncor} are the optode saturations after correction for salinity and pressure effects, but prior to comparison to shipboard casts. Equation (D.6) applies only the instrument deployed June 2009, for which the second set of calibration casts are in the interior of the deployment. This equation states that the drift is not extrapolated beyond the second set of calibration casts in August 2009; doing so would result in unrealistically high concentrations in winter 2009-10.

The Seaglider deployed in August 2008 ceased sampling on 4 June 2009, 10 days prior to the arrival of the *Tully* on 14 June 2009. Given episodic increases of oxygen within the mixed layer and errors associated with extrapolation, it was not considered realistic to attempt to directly compare SL-average s from this vehicle to *Tully* samples obtained 10 days layer. However, after shoaling of the mixed layer in May, oxygen exhibits a steady decline within the seasonal thermocline (Fig. 4.4). This stable rate of decline allowed determination of $\Delta s_{\mathrm{resid}}$ for the second optode, by comparing s from this instrument – corrected for only for its initial offset Δs_{init} in August 2008 – to the fully-calibrated third instrument on the 6°C isotherm. This isotherm lies at 66±9 m depth during the late May-early July period, in the middle of the seasonal thermocline.

It is apparent from examination of s on the 6°C isotherm during this period that the second optode instrument, without correction for drift, reads too low compared to the saturation levels that would be expected from extrapolating backwards in time from the rate of decline observed on the fully-corrected third instrument (Fig. D.2). Furthermore, if NCP rates are estimated without correcting for any drift in the second instrument, positive NCP is inferred at all depths above 200 m in June 2009 (not shown), strongly indicating an erro-

neously high $\partial[O_2]/\partial t$ due to offset in the record of instruments 2 and 3. To estimate this offset, saturation levels s from both instruments sampled on the 6° isotherm were fit with a least-squares regression line of the form

$$s_k(T = 6°\text{C}) = A + Bx'_k + Cy'_k + Dt'_k + Ec_k, \tag{D.7}$$

where x'_k, etc. are defined as before, but a new predictor c_k is introduced. This predictor is set to 1 for samples taken from the second optode (deployed August 2008) and 0 for samples from the fully-corrected, third optode. This equation does not include the quadratic term in t' because of the steady decline observed within the seasonal thermocline, and because a quadratic could inadvertently account for some of the variance due to the offset between the instruments. The least-squares fit of the form (D.7) gives $E = 0.0140$, which is taken to be Δs_{resid} for the second instrument. Figure D.2 shows s values for the second optode after addition of this value of Δs_{resid}, which brings the saturation levels on the 6°C isotherm into agreement with those that would be expected from the record observed from the third instrument after 14 June.

The fact that three different instruments yielded similar levels of residual offset after varying lengths of time (three months in the case of deployments 1 and 3, nine months in the case of deployment 1) suggests that the drift may occur over some time within the first three months of each deployment before stabilizing thereafter. Precise functional forms for optode drift and optode drift at depth when deployed on long-duration, continuously-profiling vehicles have obvious implications for studies of ocean biogeochemistry from autonomous instruments and warrant further study.

Figure D.3 examines the oxygen concentration on the 6°C isotherm during summer 2008, near the interface between the end of the first deployment and the beginning of the third deployment. It is desirable that the corrections applied to two consecutive instruments are consistent such that there are no discontinuities in the time record of $[O_2]$, and thus no spurious inferred productivity or respiration (within the noise level) due to instrument

mismatch. The results of this figure demonstrate that the mixed-layer corrections applied to both instruments also succeed in bringing the time record of oxygen in the seasonal thermocline into alignment at the boundary between deployments on 30 August 2008.

For a similarly configured array at HOT, Nicholson et al. [111] used an extensive and high-resolution record of ship casts to effectively postcalibrate optode results at all depths, fitting a quadratic curve to a scatter plot of optode oxygen concentration vs. Winkler concentration, paired along isotherms. This method was initially attempted in this study, but abandoned due to a lack of sufficient comparison points for optode calibration deeper than 150 m, where oxygen concentrations vary rapidly in the vertical. With a lack of comparison points within the halocline, the quadratic curves were poorly constrained there, resulting in pronounced offsets between instruments within the halocline region. Furthermore, temperature inversions in the halocline during the array time series presented complications for comparison along isotherms.

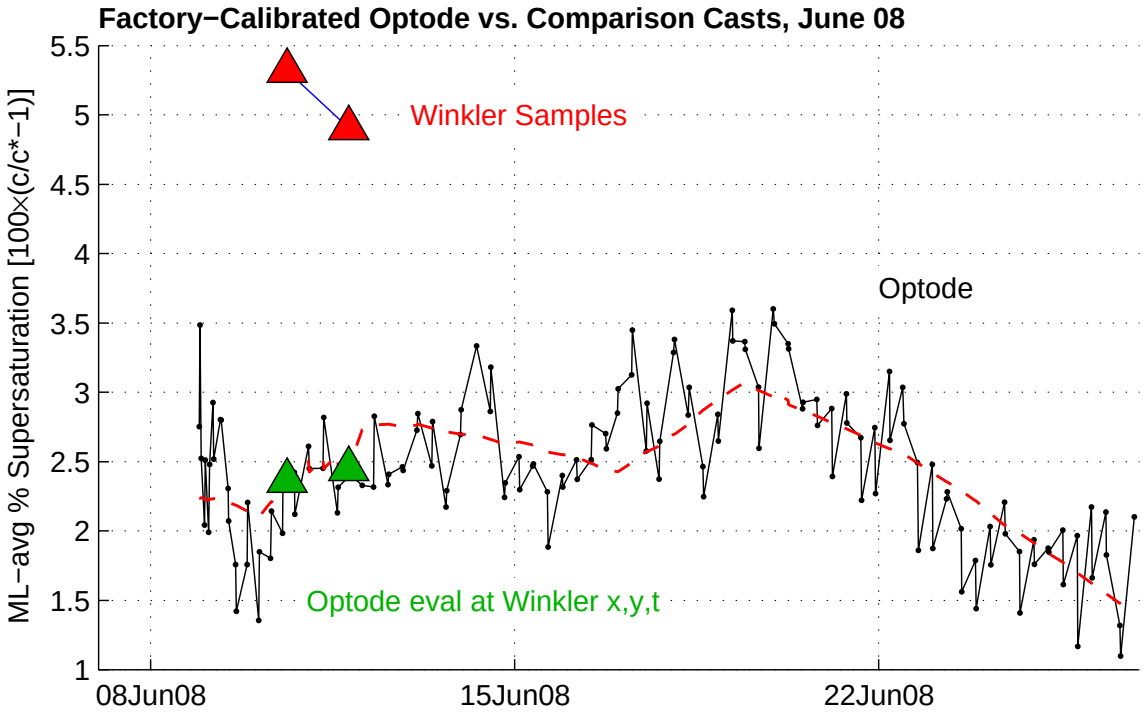

Figure D.1: Comparison of mixed layer-average saturation levels from Seaglider optode and Winkler-titrated bottle samples, June 2008. Black line indicates the time record of SL-average samples from Seaglider 144, and red dashed line is the least-squares fit of the form (D.1) applied to these data. Green triangles are the best-fit line evaluated at the times and spatial locations of the two ship casts available for comparison during June 2008. Red triangles show the SL-average saturation level from Winkler titrations performed on bottle samples from these casts.

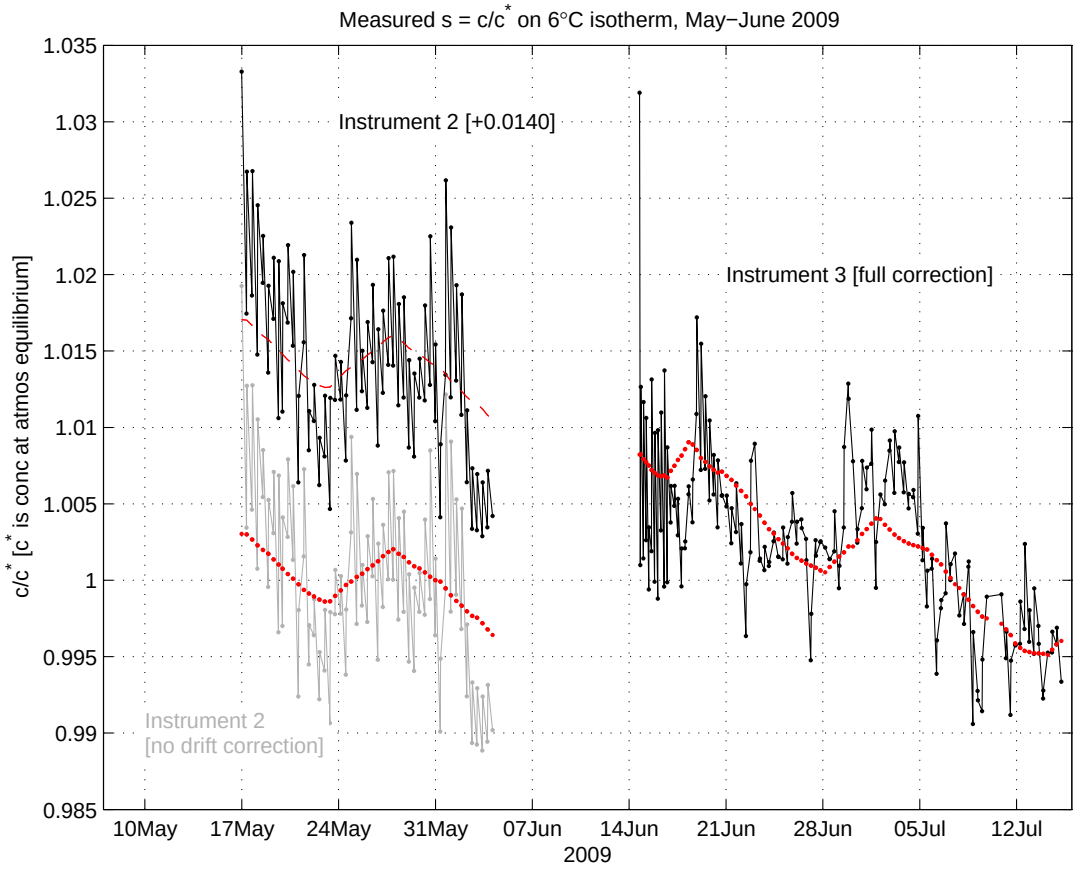

Figure D.2: Oxygen saturation level $s = [O_2]/[O_2]_{sat}$ measured on the 6°C isotherm near the end of Seaglider deployment 2 and beginning of Seaglider deployment 3, May-July 2009. Note the 10 d gap between measurements at the end of deployment 2 and the beginning of deployment 3. The black line after 14 June corresponds to samples collected from instrument 3, with corrections for initial offset and drift from comparison casts. The grey line prior to 14 June represents samples from instrument 2, with corrections for initial offset but not for drift. The solid red line indicates a best-fit line of the form (D.7) to the collective record from these two periods, which predicts a low offset for instrument 2 of 0.0140 relative to instrument 3. The instrument 2 record corrected for this offset (black line prior to 14 June) shows much better agreement with the linear decay observed in instrument 3 after 14 June, if it is assumed this rate of decay is constant throughout the period shown.

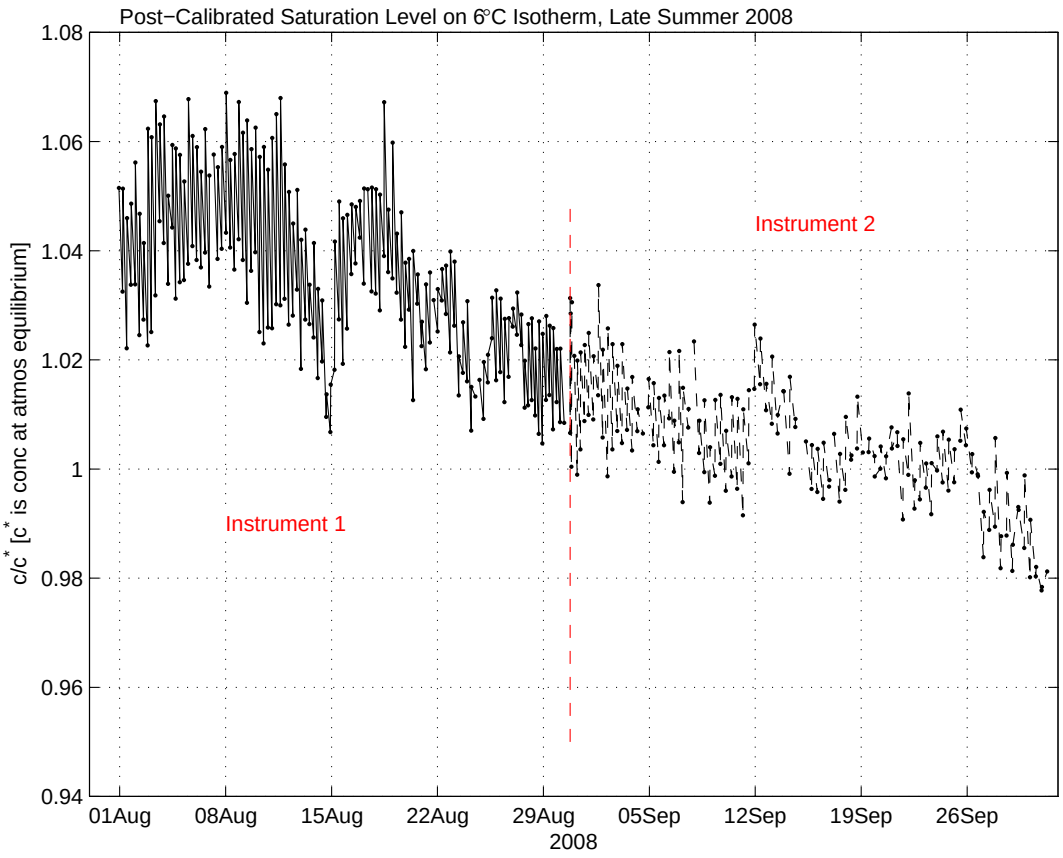

Figure D.3: Oxygen saturation level $s = [O_2]/[O_2]_{sat}$ measured on the 6 degree isotherm near the end of Seaglider deployment 1 and beginning of Seaglider deployment 2. Red dashed line marks the boundary between the two deployments. Dissolved oxygen saturation levels from both instruments have been corrected for initial offset from Winkler measurements and drift. This plot shows that, after all corrections have been applied, the time record of oxygen is continuous between the two instruments, minimizing error in inferred biological productivity that may be due to offset between the two instruments.

Appendix E

UNCERTAINTY ESTIMATES ON SURFACE GAS EXCHANGE

Uncertainty in the comparison between optode and shipboard oxygen concentrations is still significant relative to the observed surface supersaturation signal, in particular during the winter months. This section describes a Monte Carlo method for estimating the impact of these errors on the estimate of the surface gas exchange. The premise of the Monte Carlo simulation is to generate many iterations of the observed dataset, in each of which random errors are drawn and applied to the uncertain oxygen concentrations. These errors are drawn from a known distribution whose standard deviation is proportional to the assumed uncertainty of each postcalibration comparison point. In the simulation described here, 500 iterations were performed, and in each of these, randomly-sampled errors were applied to surface oxygen concentrations and the surface gas exchange re-calculated in every iteration. It is assumed that 500 iterations is a sufficient number to establish the statistics of the resulting errors in surface gas exchange and its integral over a growing season.

In each iteration, for the first and third instruments (deployed July 2008 and 2009), independent random errors are associated with with the postcalibration in saturation level Δs at both the initial and residual comparison casts. For the second instrument (deployed August 2008), a random error is applied to the initial comparison cast, but the error in drift is assumed to be the same as the initial comparison error for the third instrument, since its $\Delta s_{\mathrm{resid}}$ is derived from comparison to this instrument within the seasonal thermocline.

The noise level of the perturbations in optode accuracy at each iteration is assumed to reflect comparison error and assumed Winkler titration RMS error of $\pm 0.1\%$ supersaturation. Comparison error, due to errors in optode measurement scatter and the LOESS fitting used to estimate optode concentration at the Winkler x, y, t points, is adjudged by examination

of the individual comparison plots, for example Figure D.1. In this example, the comparison is considered accurate to ±0.4% supersaturation – the estimated supersaturations at the Winkler points are 2.4-2.5% and it is reasonable to conclude from Figure D.1 that the maximum window for these could be between 2% and 2.8%. The total ± bound for uncertainty on Δs_{init} for instrument 1 is thus $\gamma^{(1)}_{\mathrm{init}} = \sqrt{0.001^2 + 0.004^2} = 0.0041$. A similar uncertainty level was obtained at other comparison points.

At each iteration, a perturbation to Δs_{init} for instrument 1 is randomly drawn from a normal distribution with standard deviation of $\gamma^{(1)}_{\mathrm{init}}$. This process is repeated for Δs_{init} and $\Delta s_{\mathrm{resid}}$ for the remaining comparison points. When this process is completed, the postcalibration of the previous section is re-applied to produce a noise-perturbed optode O_2 dataset for that iteration. Note that the perturbation to $\Delta s_{\mathrm{resid}}$ applied to the second instrument is equal to the perturbation applied to Δs_{init} for the third, with additional 1% supersaturation error assumed in the comparison between second and third instruments along the 6°C isotherm.

The integral of surface gas flux over time bins $j = n_s$ to n_e in iteration k is then

$$\int F^{(k)} \approx \sum_{j=n_s}^{n_e} \Delta t_j F_j^{(k)} \tag{E.1}$$

and the RMS uncertainty on the observed integral between n_s and n_e is given by the standard deviation of $\int F^{(k)}$ across the $N_k = 500$ iterations. This procedure provides the gas exchange portion of the RMS uncertainty bounds on seasonal integrals of NCP shown in Figure 4.13 and seasonal and SL integrals quoted in Sections 4.3 and 4.4.

The above procedure does not take into account instrumental biases such as those potentially present in buoy wind speeds. This should be noted because, despite the fact that large-magnitude wind events are infrequent and of short duration in the OSP record, monthly-average estimates of surface gas exchange are sensitive to these events because of the nonlinear dependence in many parameterizations of bubble exchange on 10 m wind speed or friction velocity. Large et al. [88] found a low bias in buoy wind speed measurements rel-

ative to those predicted by numerical atmospheric reanalysis products at high wind speeds, and attributed this effect to the distortion of the marine atmospheric boundary layer when surface waves are large. However, support for this effect is not unequivocal in other datasets [150, 149, 71] and these corrections have not been applied to the results of this study.

If present, these effects could potentially induce large biases on estimates of surface gas exchange in this and other studies. Much of the previous literature regarding potential buoy wind speed biases involves comparison of buoy records to reanalysis products during high wind events, though this involves the assumption that reanalysis products can successfully replicate the frequency, magnitude, and duration of high wind events in the marine boundary layer, and are thus an effective choice of "true" wind speed records. However, a simple exercise undertaken with this dataset shows that this may be a tenuous assumption, depending on the reanalysis product employed. For comparison purposes, gas exchange was recomputed in this study using 10 m winds and SLP from the NCEP-Department of Energy Reanalysis 2 dataset (R2, likewise available from NOAA ESRL Physical Sciences Division at `http://www.esrl.noaa.gov/psd/`) instead of R1. This dataset estimated a much greater frequency of high winds than either the OSP mooring or R1, evident from the probability density function (PDF) of winds 2007-2010 from all three datasets (Fig. E.1). Corresponding rates of surface gas exchange were $\sim$30 mmol O_2 m^{-2} d^{-1} greater in magnitude in both summer (warming season/outgassing) and winter (cooling/downward gas flux; Fig. E.2). Both R1 and R2 cannot be correct in their representation of high wind speeds – demonstrating that reanalysis products may have substantial errors in the high-wind "tail" of the 10 m wind speed PDF, and that these errors are sufficient to substantially influence estimates of surface gas exchange, and likely inference of buoy wind speed bias as well.

Due to the potential bias of the sheltering effect, the agreement between R1 and the buoy could be coincidental. In absence of more conclusive evidence of bias from the sonic anemometer mounted on the NOAA OSP buoy at high wind speeds, this study does not employ any wind bias corrections and retains the use of R1 winds to fill in gap periods. Accurate experimental estimates of wind speed biases and bulk transfer of gases across the

air-sea interface in high winds remain critical priorities for reducing uncertainties in the oxygen mass balance.

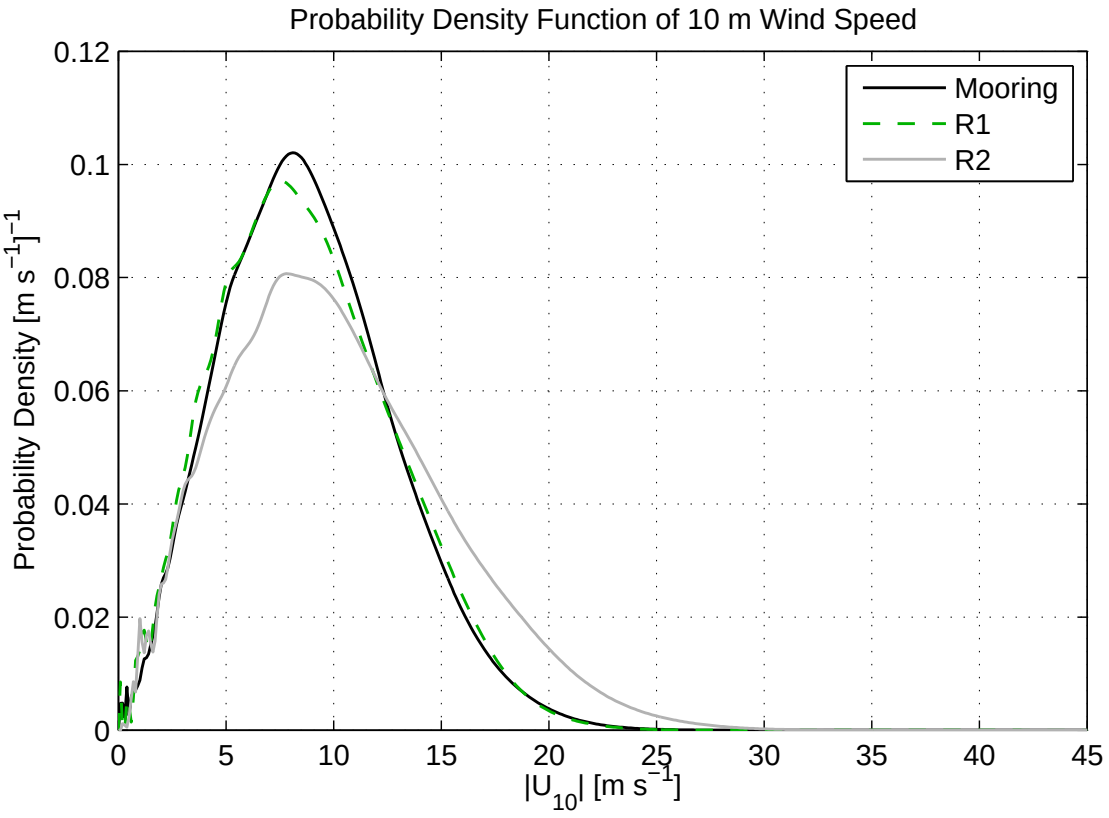

Figure E.1: Empirical probability density function (PDF) of 10 m neutral wind speed ($|U_{10}|$) from OSP mooring (black line), National Centers for Environmental Prediction (NCEP) Reanalysis 1 (R1) dataset, and NCEP-Department of Energy Reanalysis 2 (R2). There is good agreement between the buoy and R1 PDFs, despite the fact that the OSP mooring is not assimilated in the R1 model [83]. The R2 product predicts a greater probability of winds >12.5 m s^{-1} relative to the OSP mooring or R1. The probability density functions were computed from data July 2007-December 2010 inclusive, using a gaussian kernel smoothing estimator in log-space to ensure one-sided (positive only) PDFs.

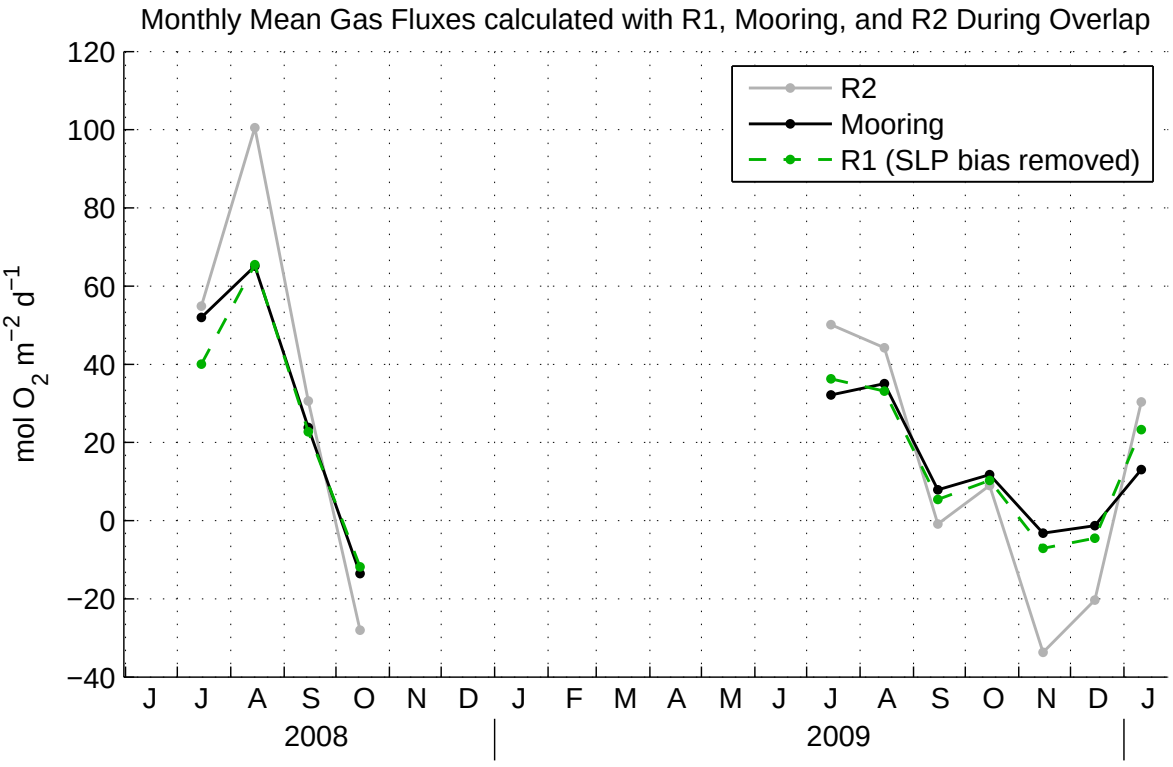

Figure E.2: Monthy-average rates of gas exchange computed using winds and sea level pressure (SLP) from three different sources: NOAA Ocean Station Papa mooring, National Centers for Environmental Prediction (NCEP) Reanalysis 1 (R1) dataset, and NCEP-Department of Energy Reanalysis 2 (R2). Rates are shown only for periods when data from all three sources are available. Rates of gas exchange agree between R1 and mooring, but R2 rates are of substantially larger magnitude, owing primarily to a greater probability of high winds. Rates of gas exchange shown are from the Liss and Merlivat [94] parameterization with Woolf and Thorpe [179] bubble flux modification. Sea level pressures from R1 have been corrected for an observed high bias relative to the mooring (Section 4.2.2). The R1 product is used as a replacement for the mooring when the latter is not available (November 2008-June 2009).

VITA

Noel A. Pelland

Education

Ph.D. Candidate (2012-present), Physical Oceanography, University of Washington

M.Sc. (2011), Physical Oceanography, University of Washington

B.Sc. (2005), *Cum laude*, Aeronautical and Astronautical Engineering, University of Washington

Research and Teaching

Doctoral Student (*Winter 2012-present*). Present work. University of Washington School of Oceanography. Supervisor: Dr. Charles C. Eriksen.

Master's Student (*Autumn 2008-Autumn 2011*). Subthermocline Eddies over the Washington Continental Slope as Observed by Seagliders, 2003-09. University of Washington School of Oceanography. Supervisor: Dr. Charles C. Eriksen.

Teaching Assistant (*Autumn 2009*). Introduction to Ocean Circulation. University of Washington School of Oceanography. Supervisor: Dr. Paul Quay.

Undergraduate Research Assistant (*Summer 2004-Spring 2005*). Camera Design for Three-Dimensional Particle Image Velocimetry of Flow over a Backwards-Facing Step. University of Washington Aeronautics and Astronautics. Supervisor: Dr. Dana Dabiri.

Peer-Reviewed Articles

Pelland N. A., C. C. Eriksen, and C. M. Lee (2013). Subthermocline eddies over the Washington continental slope as observed by Seagliders, 2003-09. Journal of Physical Oceanography 43, 20252053.

Giddings S. N., P. MacCready, B. M. Hickey, N. S. Banas, K. A Davis, S. A. Siedlecki, V. L. Trainer, R. Kudela, N. A. Pelland, and T. P. Connolly (2014). Hindcasts of harmful algal bloom transport on the Pacific Northwest coast. Journal of Geophysical Research, doi:10.1002/2013JC009622.

Sterling J. T., A. M. Springer, S. J. Iverson, S. P. Johnson, N. A. Pelland, D. S. Johnson, M. A. Lea, and N. A. Bond (2014). The sun, moon, wind, and biological imperative shaping contrasting wintertime migration and foraging strategies of adult male and female northern fur seals. PLoS ONE, doi: 10.1371/journal.pone.0093068.

Pelland N. A., J. T. Sterling, M. A. Lea, N. A. Bond, R. R. Ream, C. M. Lee, and C. C. Eriksen (2014). Fortuitous encounters between Seagliders and adult female northern fur seals (*Callorhinus ursinus*) off the Washington (USA) coast: upper ocean variability and links to top predator behavior. PLoS ONE, doi: 10.1371/journal.pone.0101268.

Jaeger K. L., J. D. Olden, and N. A. Pelland (2014). Climate change poised to threaten hydrologic connectivity and endemic fishes in dryland streams. Proceedings of the National Academy of Sciences 111(38), 13894-9.

Presentations

Pelland N. A., C. C. Eriksen, and C. M. Lee. Cross-shore structure off the Washington Coast: Observations of the California Undercurrent and Other Prominent Features from the Cascadia Seaglider Time Series. 2010 Eastern Pacific Ocean Conference, Timberline Lodge, OR.

Pelland N. A., J. T. Sterling, N. Bond, and M. A. Lea. Fur Seals and Seagliders: Potential Applications to Climate-Ecosystem Coupling in the North Pacific. 2010 University of Washington Graduate Climate Conference, Pack Forest Conference Center, WA.

Pelland N. A., C. C. Eriksen, and C. M. Lee. The California Undercurrent and Beyond: Five Years of Seaglider Observations of Cross-Shore Structure in the Pacific Northwest Coastal Zone. 2010 American Geophysical Union Fall Meeting, San Francisco, CA.

Pelland N. A., C. C. Eriksen, and C. M. Lee. Subthermocline Eddies over the Washington Slope, 2003-09.

- 2011 Eastern Pacific Ocean Conference, Fallen Leaf Lake, CA.
- 2012 Ocean Sciences Meeting, Salt Lake City, UT.
- 2012 Line P Meeting, Institute of Ocean Sciences, Sidney, BC (Canada).
- Oregon State University College of Earth, Ocean and Atmospheric Sciences Physical Oceanography Seminar, April 2013

Pelland N. A., J. T. Sterling, M. A. Lea, N. A. Bond, R. R. Ream, C. C. Eriksen, and C. M. Lee. Fortuitous Encounters Between Seagliders and Adult Female Northern Fur Seals:

Linking Upper Ocean Biophysical Variability to Top Predator Behavior.

- 2012 Eastern Pacific Ocean Conference, Timberline Lodge, OR.
- 2013 Alaska Marine Sciences Symposium, Anchorage, AK.

Pelland N. A., C. C. Eriksen, M. F. Cronin, and S. R. Emerson. The 18-Month Seaglider Time Series at Ocean Station P: Application to Budgets of Heat, Salt, and Oxygen.

- 2013 Line P Meeting, Institute of Ocean Sciences, Sidney, BC (Canada).
- Woods Hole Oceanographic Institution Physical Oceanography Seminar, August 2013.
- 2013 Eastern Pacific Ocean Conference, Fallen Leaf Lake, CA.
- 2014 Ocean Sciences Meeting, Honolulu, HI.
- 2014 Line P Meeting, Institute of Ocean Sciences, Sidney, BC (Canada).

Field Experience

Deployment and recovery of Seagliders on the Washington continental shelf (1 day), F/V Tommycod (*Autumn 2008, Spring 2014*).

Numerous deployments and recoveries of Seaglider shakedown missions in Port Susan, Washington (*2009-present*).

Mission design, planning, monitoring, and control for Cuddy Decay Seaglider survey experiment (*Autumn 2013-present*). Along with supervisor C. C. Eriksen, contributed to Seaglider deployment scheduling and search planning, identification of isolated vortices, Seaglider survey pattern, and interpretation of real-time data during a survey mission dedicated to persistent tracking of an isolated California Undercurrent eddy (Cuddy) by multiple autonomous Seagliders over an extended period. Led effort to automate Cuddy tracking through use of the extended Kalman filter for glider data assimilation and automated glider targeting using Kalman filter prediction of eddy state.

Service Activities

Treasurer, Eastern Pacific Ocean Conference (*2012-Present*).

Reviewer, Journal of Geophysical Research, Oceans.

Reviewer, Geophysical Research Letters.

Awards

Roy and Irene Grossman Scholarship (2004), University of Washington Aeronautics and Astronautics.

Mary Gates Research Training Grant (2004-05), University of Washington.

Best Student Poster, 2010 Eastern Pacific Ocean Conference.

Best Student Presentation, 2011 Eastern Pacific Ocean Conference.

Outstanding Student Presentation Award, 2012 Ocean Sciences Meeting.

Best Student Poster, 2012 Eastern Pacific Ocean Conference.

Mary Landsteiner Scholarship (2013), For excellence in research at the intersection of interdisciplinary ocean science with advanced computing, University of Washington School of Oceanography.